



VNIVERSITAT ID VALÈNCIA

Instituto de Ciencia Molecular
Departamento de Química Orgánica
Doctorado en Química Sostenible

Ph.D. Thesis

***Organic-inorganic Lead Bromide Perovskites Nanoparticles:
Synthesis, Stability and Photophysical Properties***

Ph. D. Candidate:

Soranyel González Carrero

Supervisors:

Prof. Dra. Julia Pérez Prieto

Dra. Raquel E. Galian

Septiembre 2018

Dra. Julia Pérez Prieto, Profesora Catedrática de Química Orgánica de la Universitat de València y la Dra. Raquel E. Galian, Investigadora de la Universitat de València

CERTIFICAN

Que la presente Tesis Doctoral, titulada: *Organic-inorganic Lead Bromide Perovskites Nanoparticles: Synthesis, Stability and Photophysical Properties*, se ha realizado bajo su dirección en el Instituto de Ciencia Molecular (ICMol) de la Universitat de València por la Licenciada en Química Soranyel González Carrero y autorizan su presentación para ser calificada como tesis doctoral internacional.

En Valencia, 20 de Septiembre de 2018

Fdo. Dra. Julia Pérez Prieto
Directora y Tutora

Fdo. Dra. Raquel E. Galian
Directora

Dedicado a mi familia

Agradecimientos

A la Prof. Julia Pérez Prieto un especial agradecimiento por brindarme la oportunidad de desarrollar este interesante proyecto en su grupo de investigación, por su constante apoyo, paciencia, confianza y motivación para abordar cada uno de los retos planteados.

A la Dra. Raquel E. Galian por su confianza, paciencia y consejos. Así como también por motivarme a emprender actividades de divulgación científica, las cuales me han enseñado a disfrutar aún más de la ciencia.

A todos los que a través de trabajos en colaboración han contribuido en este proyecto. En especial a la Dra. María González Béjar y Dra. Luciana Smidth por su disponibilidad y colaboración.

A todos los miembros del grupo por su amistad, apoyo y por hacer del laboratorio un entorno agradable en el cual hacer ciencia. En especial a Carlos, Laura, Néstor, Ignacio y Juan.

A mi compañero, colega y mejor amigo Néstor Estébanez, por su apoyo incondicional, paciencia y cariño. Han sido muchas las etapas que hemos compartido juntos y estoy feliz de poder seguir haciéndolo.

A mis amigos Mary, Diana, Faber, Jorge, Rosy y Manuel, con quienes compartí momentos muy agradables llenos de risas y cenas a lo largo de estos años. Un especial agradecimiento a mis compañeras Mary y Diana por apoyarme, compartir este trayecto con ustedes fue mucho más divertido.

A mi familia dedico mi más profundo y sincero agradecimiento. En especial a mi abuela por su amor incondicional, su apoyo y su fe en mí cuando emprendí esta carrera.

Al ministerio de Educación, Cultura y Deporte por su financiación a través de la FPI.

Table of Contents

Chapter 1. Introduction	1
1.1 Organic-inorganic metal halide perovskites	4
1.1.1 Crystal structure	4
1.1.2 Optical properties	8
1.2 Methods of preparation	14
1.3 Organic-inorganic lead halide perovskites nanoparticles	17
1.3.1 Three-dimensional CH ₃ NH ₃ PbX ₃ perovskite nanoparticles	18
1.3.2 Two-dimensional perovskites nanoparticles	20
1.4 Optoelectronic applications	21
Chapter 2. Aim	25
2.1 Motivation of the thesis	27
2.2 Aim	28
Chapter 3. Characterization Techniques for Perovskite Nanoparticles	29
3.1. Optical characterization	31
3.1.1 Ultraviolet–visible absorption spectroscopy	31
3.1.2 Photoluminescence	31
3.1.3 Photoluminescence quantum yield	32
3.1.4 Photostability assays	32
3.2. Structural and morphological characterization	33
3.2.1 Powder X-ray diffraction	33
3.2.2 High Resolution Transmission Electron Microscopy	34
3.2.3 Scanning Electron Microscopy	34
3.3. Chemical composition analysis	34
3.3.1 X-ray photoelectron spectroscopy	34
3.3.2 Thermogravimetric analysis	35
3.3.3 Proton nuclear magnetic resonance spectroscopy	35
3.3.4 Attenuated Total Reflection-Fourier Transform Infrared spectroscopy	36
3.4. Preparation of nanoparticles solid film	36
3.5. Preparation of electroluminescent devices	37
3.6. Atomic Force Microscopy	39
Chapter 4. Synthesis and Characterization of Colloidal CH₃NH₃PbBr₃ Perovskite Nanoparticles	43
4.1. Introduction	45
4.2. Synthesis of colloidal CH ₃ NH ₃ PbBr ₃ perovskite nanoparticles by a non-template strategy	46
4.3. Photoluminescent enhancement of colloidal CH ₃ NH ₃ PbBr ₃ perovskite nanoparticles	51
4.4. Conclusions	59

4.5.	Experimental section	60
Chapter 5. Synthesis and Optical Properties of Dispersible Two-dimensional (RNH₃)₂PbBr₄ Perovskites		63
5.1.	Introduction	65
5.2.	Synthesis and optical properties of (RNH ₃) ₂ PbBr ₄ perovskite	66
5.3.	Characterization of (RNH ₃) ₂ PbBr ₄ perovskites	69
5.4.	Processability of perovskites	71
5.5.	Conclusions	73
5.6.	Experimental section	73
Chapter 6. Surface Engineering to Yield Highly Luminescence CH₃NH₃PbBr₃ Perovskite Nanoparticles and Dense Solid Films		75
6.1.	Introduction	77
6.2.	Efficient surface passivation of colloidal CH ₃ NH ₃ PbBr ₃ perovskite nanoparticles	80
6.3.	Photoluminescence lifetime and nanoparticle aggregation effect	85
6.4.	Surface engineering	87
6.5.	Delayed luminescence	92
6.6.	CH ₃ NH ₃ PbBr ₃ nanoparticle solid films	95
6.6.1	Preparation of the nanoparticle solid films	95
6.6.2	Conductive properties of CH ₃ NH ₃ PbBr ₃ nanoparticle solid films	97
6.7.	Conclusions	99
6.8.	Experimental section.	100
Chapter 7. Ligand-free CH₃NH₃PbBr₃ Perovskite Nanoparticles and their Solid Film Deposition		103
7.1.	Introduction	105
7.2.	Synthesis and characterization of naked CH ₃ NH ₃ PbBr ₃ perovskite nanoparticles	107
7.3.	Preparation and characterization of nanoparticle solid films	110
7.4.	Conclusions	113
7.5.	Experimental section	114
Chapter 8. Conclusions		117
Chapter 9. Resumen de la Tesis Doctoral		121
References		151
List of Publications		157
List of Abbreviation		293

Chapter 1. Introduction

Hybrid organic-inorganic metal halide perovskites semiconductors have shown unique properties, such as magnetic, electrical conductivity, photoconductivity, photoluminescence and electroluminescence, among others, which make them promising candidates for photovoltaic and related optoelectronic devices. ^[1]

The hybrid lead halide perovskite ($\text{CH}_3\text{NH}_3\text{PbX}_3$; X= halide ions) in particular, have emerged as exceptional semiconductor materials for photovoltaic applications, owing to their outstanding optical and electrical properties, such as broad absorption spectra (which is tunable from ultraviolet to near infrared with the composition), small exciton binding energy and long carrier diffusion length.^[2-4] Moreover, they are easily prepared from abundant and low cost starting compounds.

Since the first report of perovskite solar cell in 2009,^[5] based on $\text{CH}_3\text{NH}_3\text{PbX}_3$ nanoparticulate material into mesoporous TiO_2 film as light absorber and exhibiting moderate power efficiency (PCE less than 4 %), the configuration of the solar cells have been optimized by using thin film of bulk perovskite and the PCE thus it reached 15% in 2013, i.e. approaching that of commercial solar cells (ca. 20%).^[2,6] The fast and continuous improvement has been driven by a concerted worldwide research effort to develop new sustainable technologies, using renewable sources, and lowering the production costs.

Furthermore, the photoluminescence of hybrid lead halide perovskites nanoparticles into mesoporous films^[7] attracted great interest owing to their potential for optoelectronic applications, such as light-emitting devices.

This thesis is focused on hybrid organic-inorganic lead halide perovskite nanoparticles, whose inorganic framework present a three or two (3D or 2D) dimensionality. This chapter summarizes the crystal structure, the optical properties and the methods used for the preparation of these hybrid perovskites as single crystals, thin films and nanoparticles. Finally, their application in optoelectronic devices is described.

1.1 Organic-inorganic metal halide perovskites

1.1.1 Crystal structure

The perovskites present a general formula of AMX_3 . In the case of metal halide perovskites, M is a divalent metal (Pb^{+2} , Sn^{+2} or Ge^{+2}) and X is a halogen (Cl^- , Br^- , I^- , or a combination of them). According to the nature of the cation A, the metal halide perovskite can be further divided into two large groups: *alkali-metal halide perovskites* and *hybrid organic-inorganic metal halide perovskites (HOIP)*. The first category is mainly formed from the monovalent alkali metal A^+ (Li^+ , Na^+ , K^+ , Rb^+ , Cs^+), while in the second type, A is a small organic cation, mostly methylammonium ($CH_3NH_3^+$) or formamidinium ($CH(NH_2)_2^+$).

The AMX_3 perovskite consists in an extended *three-dimensional (3D)* framework, in which the cation M is coordinated to six halide ions in an $[MX_6]^{-4}$ octahedra. The octahedra are all-corner connected and the cation A is occupying the 12-fold coordinated holes within those cuboctahedral configuration, thus counterbalancing the charge of the whole framework, figure 1.1. Only small organic and inorganic cations can fit in the A-site of the perovskite framework, according to the Goldschmidt tolerance factor (t) described in Eq. 1,^[8] where r_A , r_M , and r_X are the ionic radii for the corresponding ions (table 1.1).^[9]

$$t = \frac{r_A + r_X}{\sqrt{2} r_M + r_X} \quad \text{Eq. 1}$$

Table 1. 1 Ionic radii of A, M and X ions

Ionic radii (Å)					
A	r_A	M	r_M	X	r_X
Cs^+	1.88	Pb^{+2}	1.19	Cl^-	1.81
$CH_3NH_3^+$	2.17	Sn^{+2}	0.69	Br^-	1.96
$CH(NH_2)_2^+$	2.53			I^-	2.20

The structure and properties of methylammonium lead halide perovskites, $CH_3NH_3PbX_3$, were reported for first time by Weber et al. in 1978,^[10] These

perovskites adopt a cubic 3D perovskite framework at the highest temperature phase. The cubic space group is $Pm\bar{3}m$ and the cubic lattice constants are $a = 5.657(2) \text{ \AA}$, $a = 5.901(1) \text{ \AA}$ and $a = 6.3285(4) \text{ \AA}$ for Cl, Br and I, respectively (figure 1.1).^[1,11]

The structural phase of the $\text{CH}_3\text{NH}_3\text{PbX}_3$ perovskite change with the temperature. There is a relationship between the methylammonium cation orientations and phase transitions, as well as a dependence of the respective phase with respect to volume change. At low temperatures the motion of the organic cation is restricted (lower than 237 K for $\text{CH}_3\text{NH}_3\text{PbBr}_3$) and the material adopt a tetragonal ($I4/mcm$) or orthorhombic ($Pnma$) phase.^[11-13]

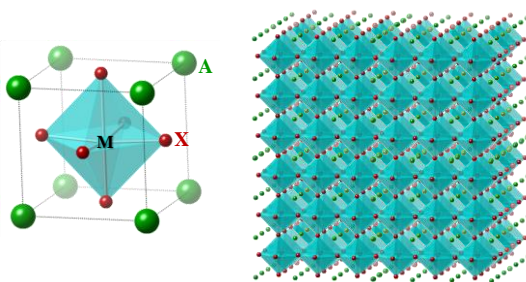


Figure 1. 1. Representation of the basic AMX_3 perovskite structure (left) and the extension of the structure in a 3D perovskite framework (right). The atoms A, M and X are shown as green, grey and red spheres, respectively.

If the organic cation A is too large, the 3D perovskite framework will be inappropriate and the dimensionality of the inorganic framework changes to 2D, 1D or 0D (figure 1.2). Thus, perovskites with *low-dimensional* inorganic framework can be obtained by making slices along different crystallographic directions of the 3D perovskite structure.

In the 2D perovskite inorganic framework, the $[\text{MX}_6]^{-4}$ octahedra are connected at the corner in layered sheets, while in 1D they are connected in a chain (the octahedra are connected at the corners, edges, or faces), finally, in 0D the $[\text{MX}_6]^{-4}$ octahedra are isolated (figure 1.2). In all cases, the organic cations are counterbalancing the anionic charge from the inorganic framework through ionic and

hydrogen bonding interactions. Hence, the selection of the organic cation A is an influential parameter on the resultant perovskite inorganic framework. These low-dimensional perovskites compounds have been comprehensively reviewed by Mitzi et al.^[1,14-16] The reduction of the framework dimensionality has a great impact on their physical properties; one of the most relevant is the increase of the band gap (see below).

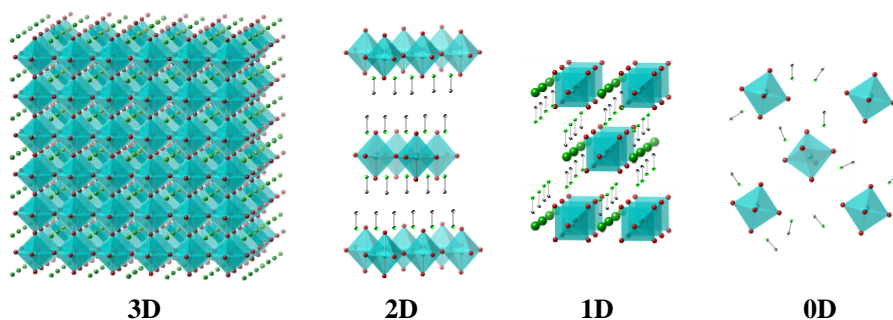


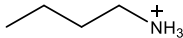
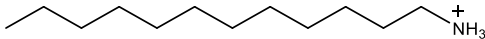
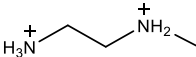
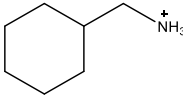
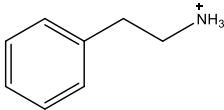
Figure 1. 2. Schematic representation of perovskite inorganic frameworks with different dimensionalities (3D, 2D, 1D, and 0D). A, M, and X atoms are shown as green, grey and red spheres, respectively.

The HOIP with a 2D inorganic framework have the general formula $(\text{RNH}_3)_2\text{A}_{n-1}\text{M}_n\text{X}_{3n+1}$ ($n = 1, 2, 3, \dots$), where R is a medium/long alkyl chain or aryl-alkyl ammonium cation (e.g. 2-phenylethylammonium); and n represents the number of inorganic framework layers. Therefore, 2D perovskite combine an extended inorganic framework with a network of organic molecules. The ammonium head of the cations bind the halogens of the inorganic sheets by hydrogen-bonds and the organic alkyl moieties are extended into the space between the inorganic layers (figure 1.2).

The most studied 2D perovskites are $(\text{RNH}_3)_2\text{MX}_4$ or $(\text{NH}_3\text{RNH}_3)\text{MX}_4$. There is no important restrictions for the length of the interlayer organic cation in the 2D perovskites family. However, there is restriction for the width of the organic cation, since it fit into an area defined by the terminal halides from four adjacent corner-sharing octahedra.^[14,16] Different properties are observed with the length

of the organic alkyl chain and the temperature, which causes phase transitions due to the dynamic rotation of the organic layer.^[17] Table 1.2 summarizes some of the organic ammonium cations that have been used to prepare perovskites with 2D inorganic framework.^[18]

Table 1. 2. Chemical structures of the organic cations used for the preparation of low-dimensional 2D perovskite.

Organic cation	Chemical structure	Ref.
n-butylammonium		[19,20]
n-dodecylammonium		[17,19,21]
N-methylethane-1,2 diamonium		[22]
Cyclohexylmethylammonium		[23,24]
2-phenylethylammonium		[23,24]

Perovskites with 1D and 0D inorganic framework remain relatively unexplored. Perovskites with 1D framework and general formula $A_2A_mM_mX_{3m+2}$ have been obtained using the iodoformamidinium cation $[\text{NH}_2\text{C}(\text{I})=\text{NH}_2]_3\text{MX}_5$; $M = \text{Pb}, \text{Sn}$],^[25,26] *N*-(3-aminopropyl)-imidazolium $[(\text{C}_6\text{H}_{13}\text{N}_3)\text{PbBr}_4]$,^[27] and cyclooctylammonium $[(\text{RNH}_3)_2\text{PbI}_4]$.^[28] There are few examples of 0D perovskites, such as the prepared with methylamine $(\text{CH}_3\text{NH}_3)_4\text{PbI}_6 \cdot 2\text{H}_2\text{O}$ and butylamine, $(\text{C}_4\text{H}_8\text{N}_2\text{H}_4)_2\text{PbBr}_6 \cdot 2\text{H}_2\text{O}$.^[29-31] This thesis is focused on the study of perovskites with 3D and 2D inorganic frameworks.

1.1.2 Optical properties

The terms 3D, 2D, 1D, and 0D used above refers to the dimensionality of the inorganic framework of perovskites not to the dimensionality of the material. In this regard, the materials can be classified as bulk 3D materials ($x,y,z > 100$ nm), bulk low-dimensional (1D only $x > 100$ nm; 2D both $x,y > 100$ nm), and nanomaterials (0D), figure 1.3.^[18] The latter group is defined as any material with the three dimensions (x,y,z) within the nanoscale ($x,y,z \leq 100$ nm), independently of its shape (e.g. spherical nanoparticles, nanoplates and nanowires). The optical properties of the HOIP depend on their chemical composition, the dimensionality of the inorganic framework and the material dimensionality.

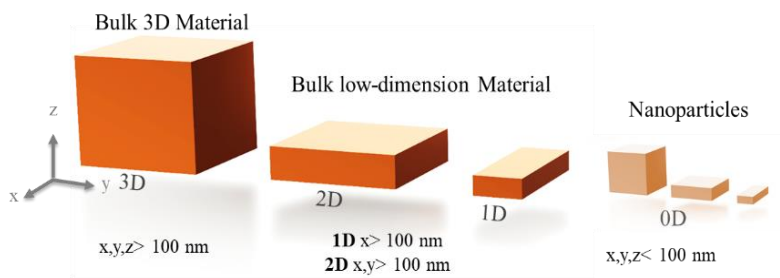


Figure 1. 3. Representation of the material dimensionality, which can be bulk 3D, bulk low-dimensional (1D, 2D), and nanoparticles (0D).

Three-dimensional perovskites. The HOIP are semiconductors, therefore their electronic structure is organized in two bands, the valence band (VB) and the conduction band (CV). The *band gap energy* (E_g) refers to the minimum energy needed for an electron to be excited from the VB to the CB and determines the light absorption and emission wavelengths of the material (figure 1.4). The photoexcitation of semiconductors leads to an electron and hole pair, known as *exciton*. Hence, the exciton is a bound state of an electron and a hole which are attracted to each other by the electrostatic Coulomb interaction and has a significant impact on the charge carrier mobility in semiconductors.

The excitons are classified into Frenkel excitons, with a small-radius comparable to the unit cell dimension, and Wannier-Mott exciton, which describes the exciton

as a bound electron-hole pair that is not localized at a crystal position but diffuses across the crystal. As a result, the Wannier-Mott type excitons have a large *Bohr radius* (a_B) that embrace many atoms, and the *exciton binding energy* (E_b) is usually small. The a_B depends on the chemical nature of the semiconductor.

The excitons in a 3D perovskite framework are Wannier-Mott excitons. The a_B and E_b values calculated experimentally for $\text{CH}_3\text{NH}_3\text{PbBr}_3$ crystal are 14–20 Å and 76 meV, respectively; whereas for $\text{CH}_3\text{NH}_3\text{PbI}_3$ they are 22–28 Å and 50 meV, respectively.^[32] Comparatively, other inorganic semiconductors, such as CdSe, possess an a_B and E_b in the 30–100 Å and 10–30 meV range, respectively.^[33]

In the HIOP semiconductor the electronic structure is mainly determined by the divalent metal cation M and the X anion of the $[\text{MX}_6]^{4-}$ octahedra framework. In the $\text{CH}_3\text{NH}_3\text{PbI}_3$ perovskite, the VB consists of Pb(6s)–I(5p) orbitals, while the CB is derived from Pb(6p)–I(5p) antibonding (σ^*) interactions, figure 1.4.^[34] Moreover, the organic cation CH_3NH_3^+ does not contribute directly to the band structure, but it provides structural stability by charge compensation with the $[\text{PbI}_6]^{4-}$ octahedra through electrostatic (Van der Waals) interactions.

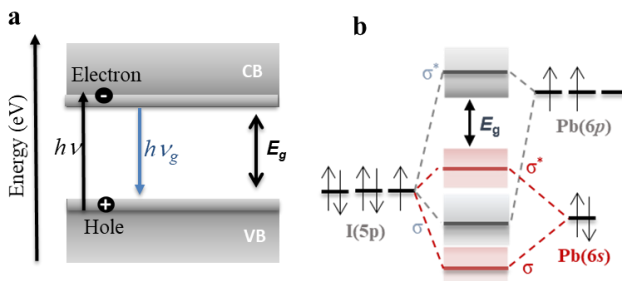


Figure 1. 4. a) Energy band diagram of a bulk semiconductor with band gap E_g , and the CB and VB. b) Simplified representation of the bonding orbitals in $\text{CH}_3\text{NH}_3\text{PbI}_3$ semiconductor.

Therefore, the E_g of the HOIP are sensitive to the anion X, $E_{g,Cl} > E_{g,Br} > E_{g,I}$ within a homologous set of compounds. The main impact of halide substitution is the modulation of the upper VB as a result of the large halide p orbitals contribution at these energies.^[35] As a result, the band gap of the cubic $CH_3NH_3PbI_3$ of 1.55 eV (800 nm) increases with the halide substitution to 2.3 eV (540 nm) and 3.1 eV (400 nm) for $CH_3NH_3PbBr_3$ and $CH_3NH_3PbCl_3$, respectively. Table 1.3 summarizes the band gap values of HOIP with different composition and dimensionality.

The $CH_3NH_3PbX_3$ perovskites exhibits strong and broad absorption spectra ranging from the ultraviolet (UV) to visible (VIS). The solids are white, orange and black for X= Cl, Br and I, respectively. Figure 1.5 shows the absorption and photoluminescence (PL) emission spectra of $CH_3NH_3PbX_3$ platelets, showing the blue shift in the optical spectra with the halide variation from I to Cl.^[36]

Table 1. 3. Comparison of the optical band gap of reported 3D, 2D, quasi-2D, 1D, and 0D perovskites.

Perovskite formula	Dimension	Band gap energy E_g		Ref.
		(eV)	(nm)	
$CH_3NH_3PbCl_3$	3D	3.11 ^b	398	[37]
$CH_3NH_3PbBr_3$		2.2-2.35 ^b	535-568	[32,36,37]
$CH_3NH_3PbI_3$		1.51-1.57 ^{a,b}	789-821	[38-40]
$CH_3NH_3SnI_3$		1.20 ^b	1000	[40]
$HC(NH_2)_2PbBr_3$		2.23 ^a	555	[39]
$HC(NH_2)_2PbI_3$		1.48 ^a	840	[39]
$CsPbI_3$		1.73 ^a	716	[39]
$(C_4H_9NH_3)_2PbBr_4$	2D	3.33 ^a	372	[19]
$(C_{12}H_{25}NH_3)_2PbBr_4$		3.52 ^a	352	[19]
$(C_4H_9NH_3)_2PbI_4$		2.40 ^a	516	[20]
$(C_7H_{15}NH_3)_2PbI_4$		3.80 ^a	326	[20]
$(C_4H_9NH_3)_2SnI_4$		2.04 ^b	607	[41]
$(C_{12}H_{25}NH_3)_2SnI_4$		2.14 ^b	580	[41]
$(C_6H_{13}NH_3)_2PbBr_2$		3.13 ^a	395	[42]
$(C_6H_{13}NH_3)_2(CH_3NH_3)Pb_2Br_7$	q -2D	2.87	431	
$(C_6H_{13}NH_3)_2(CH_3NH_3)_2Pb_3Br_{10}$	q -2D	2.77	450	
$(NH_2C(I)=NH_2)_3PbI_5$	1D	3.10	400	[29]
$(CH_3NH_3)_4PbI_6 \cdot 2H_2O$	0D	3.87	320	[29]

Perovskite prepared as ^a thin film and ^b single crystals (see section 1.2)

The $\text{CH}_3\text{NH}_3\text{PbI}_3$ perovskite exhibits a broad absorption spectrum, and high absorption coefficient ($1.5 \times 10^4 \text{ cm}^{-1}$), which enable the use of this material as the light absorber in photovoltaic applications. The band gap of $\text{CH}_3\text{NH}_3\text{PbCl}_3$ limits its use as single light absorber, whereas $\text{CH}_3\text{NH}_3\text{PbBr}_3$ perovskites have shown lower efficiency than the iodide counterparts but they have been studied because of their photoluminescence and stability under humidity conditions.

Notably, the band gap of $\text{CH}_3\text{NH}_3\text{PbX}_3$ perovskites can be tuned over the whole visible spectra range by using mixed halide perovskites.^[37] The variation of the Br content in $\text{CH}_3\text{NH}_3\text{Pb}(\text{I}_{1-x}\text{Br}_x)_3$ allows a band gap tuning from 1.57 eV (for $x=0$) to 2.27 eV (for $x=1$).^[43]

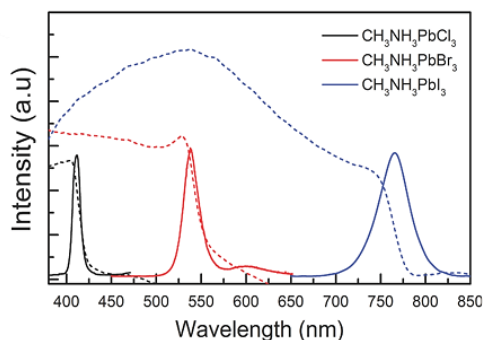


Figure 1. 5. Absorption (dashed line) and room temperature PL emission spectra (solid line) of $\text{CH}_3\text{NH}_3\text{PbX}_3$ perovskite platelets showing a band gap of 400 nm for $X = \text{Cl}$, 530 nm for $X = \text{Br}$ and 770 nm for $X = \text{I}$. Reprinted with permission of Ref. ^[36] Copyright 2014 John Wiley and Sons.

The organic cation determines the dimensionality of the perovskite framework as was discussed above. Furthermore, it has an important effect on the stability of the solid material. The increase of the cation size, ionic radius $\text{Cs} < \text{CH}_3\text{NH}_3^+ < \text{HC}(\text{NH}_2)_2^+$ expands the crystal lattice and induce a small band gap shift, which is small in comparison with that produced by halide substitution. In lead iodide thin films, the band gap decreases from 1.73 eV to 1.48 eV for CsPbI_3 and $\text{HC}(\text{NH}_2)_2\text{PbI}_3$, respectively.^[39]

In addition, replacing Pb^{+2} by the smaller divalent cation Sn^{+2} results in a decrease of the band gap to 1.20 eV (1000 nm) for $\text{CH}_3\text{NH}_3\text{SnI}_3$, thus extending the optical

absorption to the near infrared range (table 1.3).^[40] Nevertheless, this material exhibits low stability, which has limited (up to now) its application as light absorber in solar cells.

Two-dimensional perovskites. Additional band gap tunability is observed with the reduction in the inorganic framework from 3D to 0D. The band gap energy increases in the trend $E_{g,3D} < E_{g,2D} < E_{g,1D} < \text{HOMO-LUMO}_{0D}$ for a homologous set of perovskite compounds (table 1.3).^[29,35]

In the HOIP with a 2D inorganic framework, the exciton is confined within the inorganic framework layer. Such quantum confinement, in combination with the surrounding organic cations spacers, induce a strong electron-hole Coulomb interaction and larger E_b than in 3D perovskites. The E_b reported for 2D perovskites are in the 200-500 meV range.^[44,45] Because of this, the 2D perovskites are usually photoluminescent at room temperature and exhibit a narrow emission band and small Stokes shift. Their optical properties depend on the length and the features of the organic cation, the halide and the metal (table 1.3).

In general, the exciton band is blue-shifted with the increase of the length of the alkyl chain organic cation.^[19-21,46] In $(C_nH_{2n+1}NH_3)_2PbBr_4$, for instance, the exciton absorption shifts from 3.33 eV (372 nm) to 3.52 eV (352 nm) for butylammonium ($n=4$) and dodecylammonium ($n=12$), respectively.^[19] The change in the length of the alkyl chain varied the distance between the inorganic layer and the orientation of the organic group.

Analogous to 3D perovskites, the band gap of 2D perovskites can be tuned by the halide substitution.^[47,48] Thus, $(C_{18}H_{37}NH_3)_2PbX_4$ perovskite exhibit the exciton peak at ca. 500 nm, 393 nm, and 328 nm for I, Br, and Cl, respectively.^[48] Additional band gap tunability can be achieved by mixing the halides.^[45,49-51]

The confinement in 2D perovskite decreases with the increase in the number of inorganic framework layers, this means that additional degrees of electronic

tunability are afforded by modifying the number of adjacent inorganic sheets $(\text{RNH}_3)_2\text{A}_{n-1}\text{M}_n\text{X}_{3n+1}$ ($n = 1, 2, 3, \dots, \infty$) along the crystallographic axis. This intermedia dimensionality structure between 3D ($n = \infty$) and 2D ($n = 1$) is termed as quasi-2D (q-2D). For example, the absorption peak maximum of 2D perovskite thin films prepared with hexylammonium ($\text{C}_6\text{H}_{13}\text{NH}_3^+$) and CH_3NH_3^+ cations, $(\text{C}_6\text{H}_{13}\text{NH}_3)_2(\text{CH}_3\text{NH}_3)_{n-1}\text{Pb}_n\text{Br}_{3n+1}$, red-shifted from 395 nm to 450 nm as the number of inorganic layers increases from $n = 1$ to $n = 3$, figure 1.6.^[42]

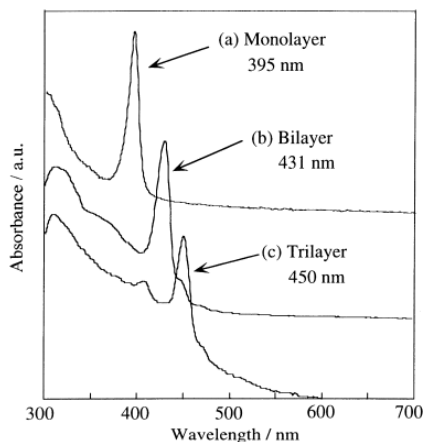


Figure 1.6. Absorption spectra of spin-coated film of $(\text{C}_6\text{H}_{13}\text{NH}_3)_2(\text{CH}_3\text{NH}_3)_{n-1}\text{Pb}_n\text{Br}_{3n+1}$ ($n = 1-3$). Reproduced with permission from ^[42] Copyright 2000, Elsevier.

In summary, the chemical variability of HOIP offers significant opportunities for the tuning of their physical and optical properties by the appropriate choice of metal atom, halogen and the dimension of the inorganic framework.

1.2 Methods of preparation

HOIP, either 3D or 2D perovskites, have been prepared with high purity as single crystals and thin films by using solution-processing methods. These perovskite exhibit a low energy barrier of formation; the mixture of the organic cation with metal halide, react even at room temperature in solid state or by gridding. Although this method is easy and fast, the lack of experimental control yields a mixture of the product and unreacted precursors.

Single crystals. Single crystals have been used for the study of the HOIP structure and their intrinsic properties. In general, the synthesis of bulk single crystals are carried out by classical solution crystal growth methods such as cooling-induced crystallization, inverse temperature crystallization, anti-solvent vapor-assisted crystallization, layered solution growth method and slow solvent evaporation of a saturated precursor solution.^[11]

In the cooling-induced crystallization the process for $\text{CH}_3\text{NH}_3\text{MX}_3$ ($\text{X} = \text{Cl}, \text{Br}, \text{I}$; and $\text{M} = \text{Pb}, \text{Sn}$) has usually been carried out by dissolving the inorganic salt (e.g. lead acetate) in concentrated aqueous solution of the halide acid, followed by heating the mixture in a water or oil bath. Afterwards, the organic amine (e.g. methylamine) is added to the solution. The mixture was cooled from $100\text{ }^\circ\text{C}$ to ca. $40\text{ }^\circ\text{C}$, over several hours.^[38,40,52] The slow decrease of the temperature induces the saturation of the perovskite precursor in the solution and the HOIP crystals growth slowly. A large crystal is obtained by cooling the solution over days. 2D perovskites with butylammonium $(\text{C}_4\text{H}_9\text{NH}_3)_2\text{ML}_4$ ($\text{M} = \text{Ge}, \text{Sn}, \text{and Pb}$) and phenylethylammonium $(\text{C}_6\text{H}_5\text{C}_2\text{H}_4\text{NH}_3)_2\text{PbX}_4$ ($\text{X} = \text{Cl}, \text{Br}, \text{and I}$) have been prepared by using this method.^[53]

The inverse temperature crystallization is a different approach for the crystal preparation of materials whose solubility in certain solvents is high at room temperature but decreases with the increase of the temperature.^[54] Bakr, O. M et al. studied the solubility of $\text{CH}_3\text{NH}_3\text{PbX}_3$ ($\text{X} = \text{Cl}, \text{Br}$ and I) in different solvents,

and demonstrated the preparation of high quality millimeter-sized crystal using dimethylformamide/dimethyl sulfoxide (1:1; at 50 °C), dimethylformamide (at 80 °C) and γ -butyrolactone (at 60 °C) as the solvent for X = Cl, Br and I, respectively.^[54,55]

The anti-solvent vapor-assisted crystallization has been used to grow materials that are highly soluble in a good solvent but have poor solubility in other solvents, which is slowly diffused into a solution containing the HOIP crystal precursors. The layered solution growth method, on the other hand, is a similar method in which two solvents of different density are in contact; its suitability is due to the different solubility of the crystallizing material in both solvents; $(\text{C}_6\text{H}_5\text{C}_2\text{H}_4\text{NH}_3)_2\text{PbCl}_4$ single crystals have been prepared using this approach.^[56]

Thin film. Different methods have been developed for the preparation of HOIP thin films, based on the degree of surface coverage together with crystal and film quality.^[57] The *one-step solution-processed technique* is one of the most used to prepare HOIP in the form of polycrystalline films, due to its simplicity and low-cost. In this technique a specific ratio of the perovskites precursor (PbX_2 and organic cation) are dissolved in an organic solvent, and then the resultant precursors are applied onto substrates followed by spin-coating. The excess of the precursor solution is removed by centrifugal force. Then, the crystallized perovskite thin film is obtained after annealing (40-160 °C), figure 1.7.

Additional control over the morphology can be achieved by using a *two-step method*, in which first the metal halide (PbX_2) is deposited (or infiltrated into mesoporous film) and sequentially, the as-prepared film is exposed to a solution of the organic cation.^[2] After removing residual solvent by annealing, dense perovskite film is formed.

The preparation of uniform films with good coverage is essential to get high performance devices in optoelectronic applications. The relevant parameters for the HOIP crystallization control and the film formation include the selection of

the substrate, the solvent, the concentration of the HOIP precursor, the annealing temperature, the atmosphere used during spinning and the spin speed.

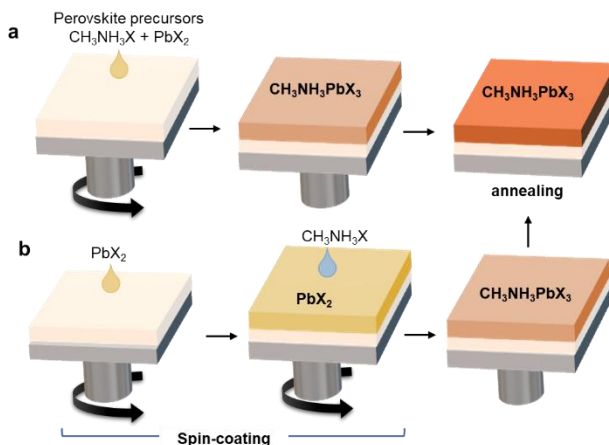


Figure 1. 7. Schematic representation of the preparation of $\text{CH}_3\text{NH}_3\text{PbX}_3$ thin films by a) one- and b) two-step solution-processed technique

The HOIP precursor solubility is limited to polar aprotic solvents, such as dimethylformamide, dimethyl sulfoxide, γ -butyrolactone and acetonitrile.

An important factor during the deposition, spinning and processing it is to work under dry atmosphere. This is due to the fact that the organic and inorganic components are often susceptible to oxidation and water adsorption. In particular, Pb and Sn metal halide perovskites exhibit low stability under moisture conditions, which is one of the main challenges to be addressed. Under ambient conditions, $\text{CH}_3\text{NH}_3\text{PbI}_3$ films decompose into PbI_2 and volatile components (i.e. $\text{CH}_3\text{NH}_3\text{I}$, HI) thus leading to an irreversible decomposition process.^[58] Consequently, some processes are performed in a dry inert (nitrogen or argon) atmosphere to minimize the sample degradation. Additional factors, such as oxygen, high temperature and UV light can also degrade the HOIP material.^[59]

In addition, polycrystalline HOIP films can be prepared by a *vapor-phase deposition technique*.^[57,60] Films have been prepared by i) simultaneous evaporation of the metal halide and organic cation, or ii) deposition of the PbX_2

film using the techniques described above followed by the evaporation of the organic cation.^[6,61] Thus, uniform and flat films of mixed halide $\text{CH}_3\text{NH}_3\text{PbI}_{3-x}\text{Cl}_x$ perovskites have been prepared by simultaneous evaporation of $\text{CH}_3\text{NH}_3\text{I}$ and PbCl_2 , from separated sources.^[6] Moreover, highly photoluminescent films of 2D perovskites $(\text{C}_6\text{H}_5\text{C}_2\text{H}_4\text{NH}_3)_2\text{PbX}_4$ (X= Br and I) and $(\text{C}_6\text{H}_5\text{C}_2\text{H}_4\text{NH}_3)_2\text{SnI}_4$ have been prepared following this strategy.^[60]

1.3 Organic-inorganic lead halide perovskites nanoparticles

Nanoparticles are materials with their dimension in the range of a few nanometers (0D material, $x,y,z \leq 100$ nm). The electron-hole pair is confined when the particle size becomes comparable to the exciton Bohr diameter of the material. A strong confinement occurs when the diameter of the nanoparticle is lower than threefold the Bohr diameter of the material, and a weak confinement occurs when the diameter of the nanoparticle is in the three to tenfold the Bohr diameter of the material. As a consequence, the optoelectronic properties of inorganic semiconductor nanoparticles (e.g. CdSe) show a strong size and shape dependence, and the degree of confinement may be different in the three dimensions of the nanoparticle.

Quantum size effects are manifested as changes in the optical absorption spectra with an increase in the E_g , i.e. shift of the excitonic peaks to higher energies (in comparison with that of the bulk material), and enhancement of their oscillator strength as the particle size decreases.

The nanoparticles can be prepared as colloids by using organic molecules which play a key role in their synthesis, colloidal stability, functionality and optical features.^[62] These molecules can act as solvents, surfactants, reactants and ligands. Colloidal nanoparticles of inorganic semiconductors, such as II–VI (CdSe, CdTe, CdS, ZnSe) and III–V (ZnP, InAs) semiconductors, have been extensively studied. The ligands, commonly referring to organic molecules (such as trioctylphosphine, trioctylphosphine oxide, long-chain alkylamines, long-chain

carboxylic acid and alkylthiols), enable control over the stability of semiconductor nanoparticles dispersions in polar or nonpolar solvents via steric and electrostatic interactions.^[63,64]

Semiconductor nanoparticles can be suitable for many applications such as catalysis, sensing, imaging, photovoltaics and optoelectronic devices.^[65-67] Despite the interesting optical properties and the easy and low cost preparation of the HOIP material, the synthesis of nanoparticles had been scarcely developed before 2013 when this thesis started (see below).

1.3.1 Three-dimensional $\text{CH}_3\text{NH}_3\text{PbX}_3$ perovskite nanoparticles

The preparation of perovskite nanoparticles with a 3D inorganic framework, namely $\text{CH}_3\text{NH}_3\text{PbX}_3$, was firstly explored by using mesoporous TiO_2 , Al_2O_3 , and ZrO_2 films as templates, and a one-step solution-processed technique.^[5,68-71]

The pioneer work of Miyasaka et al. in 2009 reported the preparation of $\text{CH}_3\text{NH}_3\text{PbX}_3$ ($\text{X} = \text{Br}$ and I) nanoparticles onto mesoporous TiO_2 film, as light absorbers in solar cells.^[5] Specifically, a stoichiometric ratio solution of $\text{CH}_3\text{NH}_3\text{X}$ and lead halide (PbX_2) in a polar solvent (dimethylformamide or γ -butyrolactone) was spin coated on the mesoporous film. The porosity of the TiO_2 film allowed the formation of $\text{CH}_3\text{NH}_3\text{PbBr}_3$ and $\text{CH}_3\text{NH}_3\text{PbI}_3$ nanoparticles with a size of 2-3 nm and an absorption spectrum response up to 550 nm and 800 nm, respectively.

Nanoparticles of $\text{CH}_3\text{NH}_3\text{PbI}_3$ on TiO_2 film were prepared by spin-coating of an equimolar ratio solution of $\text{CH}_3\text{NH}_3\text{I}$ and PbI_2 in γ -butyrolactone on the TiO_2 film, followed by annealing at a different temperatures (from 40 °C to 160 °C). The $\text{CH}_3\text{NH}_3\text{PbI}_3$ nanoparticles (average diameter of 2.5 nm) were distributed homogeneously within the pores and on the surface of the TiO_2 nanoparticles.^[68]

In addition, using a two-step sequential method, $\text{CH}_3\text{NH}_3\text{PbI}_3$ nanoparticles were prepared by first spin-coating a solution of PbI_2 on a nanoporous TiO_2 film (anatase, thickness of 500 nm), thus forming 22 nm-sized PbI_2 nanoparticles into the porous film.^[2] Then, this material was transformed into the $\text{CH}_3\text{NH}_3\text{PbI}_3$ film

by dipping the TiO₂/PbI₂ nanocomposite film in a solution of CH₃NH₃I in 2-propanol. The confinement of PbI₂ in the nanopores of the TiO₂ film facilitated the conversion, while limited the CH₃NH₃PbI₃ perovskite to adopt a morphology confined to the nanoscale.

The green photoluminescence of CH₃NH₃PbBr₃ nanoparticles prepared into mesoporous Al₂O₃ film was reported by Miyasaka et al. in 2012.^[7] The nanoparticles were prepared by spin-coating of a precursor solution (CH₃NH₃Br plus PbBr₂ in dimethylformamide at different concentrations, 1-10 wt %) onto an Al₂O₃ mesoporous film. The high resolution scanning electron microscopy (SEM) images showed the formation of 5 nm-sized CH₃NH₃PbBr₃ nanoparticles on the Al₂O₃ surface. An intense PL emission peak at 523 nm was observed when 1 wt % of the precursor solution was used. However, the PL intensity decreased at higher concentrations, attributed to the formation of the CH₃NH₃PbBr₃ bulk material. No luminescent nanoparticles were obtained in mesoporous TiO₂ and SnO₂ films.

Factors such as concentration of the perovskites precursors, solvent, spin-coating speed and drying temperature can affect the infiltration of precursor solution into the porous films, and, as a consequence, the formation of the nanoparticles. Although the template method provides an interesting tunability of the average size of CH₃NH₃PbX₃ perovskites nanoparticles through the pore size control of the mesoporous matrix, the stability and integrability of CH₃NH₃PbX₃ nanoparticles into functional devices beyond solar cells were not studied until 2013.

Remarkably, no strategy to prepare colloidal perovskites nanoparticles with 3D inorganic framework had been reported before 2013. Therefore, this was the first objective of this doctoral thesis.

1.3.2 Two-dimensional perovskites nanoparticles

Contrary to perovskite with 3D inorganic framework, there were several strategies reported to prepare perovskite with 2D inorganic framework, both as suspension and powder, by the time of this thesis was initiated.

Boissière et al.^[72] reported in 2009 the preparation of $(RNH_3)_2PbX_4$ ($X = Br, I$; $R =$ phenylethyl, cyclohexylmethyl, and 1-adamantylmethyl) by fast nebulization and subsequent lyophilization of the perovskites precursor in dimethylformamide solutions. The polydispersed spherical nanoparticles (average size of 60 nm) proved to be dispersible in hexane and photoluminescent at room temperature, in addition they showed good stability under UV irradiation. The optical properties of these nanoparticles were similar to those of the bulk prepared as thin films. However, this method lacked of morphology and size control of the HOIP nanoparticles; this was ascribed to the polydisperse character of the sprayed droplets.

Later on, Prakash et al.^[73] reported the preparation of $(C_{12}H_{25}NH_3)_2PbI_4$ and $(C_6H_5C_2H_4NH_3)_2PbI_4$ nano- and micro-crystals (size range from 20 nm to several microns) through intercalation of the organic moiety into vacuum deposited PbI_2 nano-/micro-crystals by using short intercalation times. The 2D perovskite exhibited a considerable photoluminescence at room temperature in methanol, ethanol, and acetonitrile (PL maximum centered at 497 nm and 517 nm, respectively). Comparison between the PL of $(C_{12}H_{25}NH_3)_2PbI_4$ nanocrystals and that of the thin film showed that the nanocrystals preserved all the optical features of the thin films.

Nanocrystalline/microcrystalline materials based on $Pb(Br_xX_{1-x})_3$ and $Pb(Cl_xX_{1-x})_3$ ($X = Cl, Br, I$; $x=0-1$) were reported by Papavassiliou et al.^[74] They were prepared by injection of solutions or by using melts of the corresponding perovskite bulk material with 2D and 3D inorganic frameworks, such as $(CH_3C_6H_4CH_2NH_3)_2PbBr_4$ and $CH_3NH_3PbBr_3$ for preparation of

$(\text{CH}_3\text{NH}_3)(\text{CH}_3\text{C}_6\text{H}_4\text{CH}_2\text{NH}_3)_2\text{Pb}_2\text{Br}_7$, into toluene or toluene/poly-methylmethacrylate (PMMA), under vigorous stirring at room temperature. The corresponding nano/microparticles were obtained in the form of powders by centrifugation and decantation from the suspensions in toluene. Besides, films were prepared by the drop-casting, deep-coating and/or spin-coating techniques, from suspensions in toluene/PMMA. Thus, this strategy made it possible to obtain blue to red emitters as suspensions, powders, and films by varying the halide composition of the bulk.

Soon after the same group reported the preparation of nanocrystalline/microcrystalline (100-200 nm) $(\text{CH}_3\text{NH}_3)(1\text{-naphthylmethyl ammonium})_2\text{Pb}_2\text{Cl}_7$ particles by using a mixture of $\text{CH}_3\text{NH}_3\text{PbCl}_3$ and $(1\text{-naphthylmethyl ammonium})_2\text{PbCl}_4$.^[75] The suspensions and thin films of $(\text{CH}_3\text{NH}_3)(1\text{-naphthylmethyl ammonium})_2\text{Pb}_2\text{Cl}_7$ showed a broad phosphorescence band (at ca. 500, 536, and 577 nm), which was ascribed to the organic chromophore.

1.4 Optoelectronic applications

The incorporation of HOIP with a 3D framework as the light absorber in liquid dye-sensitizer solar cells started in 2009, when Miyasaka et al. demonstrated the preparation of $\text{CH}_3\text{NH}_3\text{PbI}_3$ and $\text{CH}_3\text{NH}_3\text{PbBr}_3$ dye-sensitized solar cells, with power conversion efficiency (PCE) ca. 4 %.^[5] Interestingly, these HOIP were prepared as nanomaterial into mesoporous film. The PCE was improved up to 6.5 % by optimization of perovskite deposition.^[68]

Nevertheless, these early reports showed the low stability of the $\text{CH}_3\text{NH}_3\text{PbI}_3$ under continuous irradiation.^[5,68] In 2012, the stability of the $\text{CH}_3\text{NH}_3\text{PbI}_3$ films was addressed by Grätzel and Park et al.^[70] by using a solid-state organic hole conductor in the solar cell configuration, which reached a 9.7 % of PCE and proved to be stable for 500 h. Almost at the same time, Snaith et al.^[71] improved the devices stability by using a thin layer of mixed lead halide $\text{CH}_3\text{NH}_3\text{PbI}_2\text{Cl}$

perovskites on a mesoporous Al_2O_3 thin film surface, with a PCE of 10 %. These breakthroughs in solar cells attracted the interest of many research focused in device engineering, thus a PCE of 15 % was obtained in 2013 by using perovskite bulk thin films prepared by vapor deposition.^[2,6]

Figure 1.8 shows the structural evolution of solar cell configuration until 2013, from nanoparticles onto the TiO_2 surface to a mesoporous film-free solar cell structure in which the perovskite is capable of transporting charge.^[76]

Hybrid lead halide perovskites can be prepared with remarkable properties, such as wide absorption spectrum (up to 1.55 eV), high absorption coefficient, low exciton binding energy, long electron and hole diffusion length ($> 1 \mu\text{m}$).^[77] Therefore, they have emerged as new solar cell absorbers, comparable with the most efficient materials used in solar cell technologies such as GaAs, copper indium gallium (di) selenide, crystalline silicon and CdTe, with efficiencies up to 25 %.^[78]

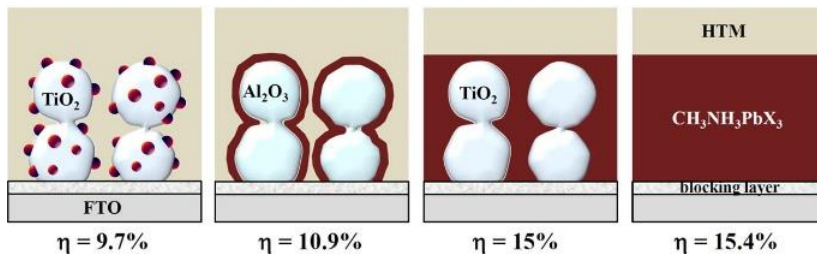


Figure 1. 8. Evolution of device configuration in perovskite solar cells. From left to right: the dye-sensitized solar cell, the thin layer of perovskite deposited on mesoporous scaffold layer, the perovskite infiltration into mesoporous film and the planar structure. Reprinted with permission from Ref. ^[76] Copyright (2014) American Chemical Society.

In the case of electroluminescent devices, the first attempt of preparing HOIP-based LEDs was reported by Era et al. in 1994 using the 2D $(\text{C}_6\text{H}_5\text{C}_2\text{H}_4\text{NH}_3)_2\text{PbI}_4$ perovskite. The device, with a layer architecture of indium tin oxide (ITO) anode, 2D perovskite emitter, an electron transport layer (oxadiazole derivative, OXD7) and Mg/Ag cathode, showed an electroluminescence (EL) emission peak at 520

nm with an intensity higher than 10 000 cdm^2 (turn-on at 24 V). However, this strong EL was observed at the temperature of liquid nitrogen. [79,80]

Later, in 1999 Chondroudīs, K. and Mitzi D. B. [81] reported a LED device using $(\text{AEQT})_2\text{PbCl}_4$, where the organic molecule R was designed based on the oligothiophene moiety and ethylammonium ($\text{H}_2\text{NC}_2\text{H}_4\text{C}_{16}\text{H}_8\text{S}_2\text{C}_2\text{H}_4\text{NH}_2$; AEQT). The device ITO/ $(\text{AEQT})\text{PbCl}_4$ /OXD7/ Mg_{20}Ag /Ag (figure 1.9) exhibited a room temperature green PL and EL emission (peak at ca. 530 nm) and a low turn-on voltage as low as 5.5 V.

In 2011 Koutselas et al. [48] reported the LED device of $(\text{OL})_2\text{PbX}_4$ (X= Cl, Br and I; OL is oleylammonium). The device exhibited an EL peak at 360 nm, 415 nm and 475 nm for Cl, Br and I based perovskite, respectively.

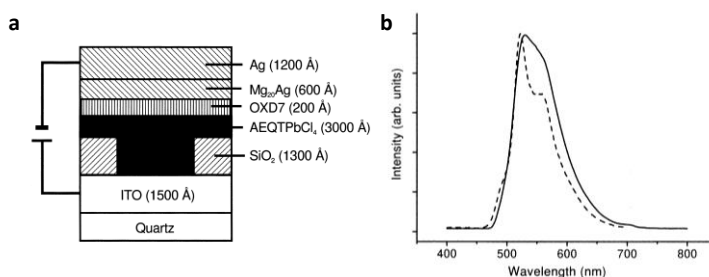


Figure 1. 9. a) Schematic representation of the cross-section of the device structure, b) electroluminescence (solid line) and photoluminescence (broken line, excited at 360 nm) spectra of $(\text{AEQT})\text{PbCl}_4$. Adapted from Ref. [81] Copyright (1999), American Chemical Society

Chapter 2. Aim

2.1 Motivation of the thesis

By the time of this thesis started, hybrid organic-inorganic metal perovskites were receiving a considerable attention as a result of their chemical flexibility, allowing a band gap tuning in the visible spectrum through the appropriate choice of metal atom and halogen atoms, or framework dimensionality. Moreover, they were prepared easily at low temperatures by solution processing strategies. Methylammonium lead halide perovskite ($\text{CH}_3\text{NH}_3\text{PbX}_3$, X= Br, I) in particular, emerged as novel sensitizer materials for photovoltaic and optoelectronic applications, due to their optical and electronic properties. The power conversion efficiency in solar cells based on perovskites kept increasing since the first report with the formation of $\text{CH}_3\text{NH}_3\text{PbX}_3$ nanoparticulate material on mesoporous metal oxides, such as titania and alumina.

The optimization of the device structure had led to solar cells with efficiencies around 15 % by using $\text{CH}_3\text{NH}_3\text{PbI}_3$ bulk thin films. $\text{CH}_3\text{NH}_3\text{PbX}_3$ perovskites, both as confined nanomaterial and as bulk thin film, proved to function not only as light absorber but also as electrons and/or holes carriers.

The particular properties of perovskites in the form of nanoparticles attracted great interest due to their potential relevance in optoelectronic applications. The studies of nanoparticles into mesoporous film demonstrated the formation of photoluminescent $\text{CH}_3\text{NH}_3\text{PbBr}_3$ perovskite nanoparticles, attributed to the quantum and dielectric confinement effect on the nanoscale. Nevertheless, the use of mesoporous scaffolds limited the integrability of the nanoparticles into functional devices.

The lack of a suitable synthetic procedure to obtain colloidal perovskite nanoparticles, either 3D or 2D inorganic framework, with sizes as small as several nanometers (0D materials), motivated our interest in their preparation since colloidal $\text{CH}_3\text{NH}_3\text{PbX}_3$ nanoparticles could enable among other applications, the

preparation of new optoelectronic devices, with enhanced performance and/or stability.

2.2 Aim

The aim of this thesis is the synthesis of highly photoluminescent colloidal organic-inorganic lead bromide perovskite nanoparticles by means of a non-template approach and exploration of their processability into conductive materials.

The objectives developed in this thesis are:

- To synthesize colloidal 3D-methylammonium lead bromide nanoparticles, $\text{CH}_3\text{NH}_3\text{PbBr}_3$, with high photoluminescent quantum yield and (photo)stability.
- To explore the preparation and processability of two-dimensional hybrid lead bromide $(\text{RNH}_3)\text{PbBr}_4$ perovskites.
- To explore the self-assembly of colloidal $\text{CH}_3\text{NH}_3\text{PbBr}_3$ nanoparticles into nanoparticles solid films and evaluate their conductive properties.
- To synthesize colloidal, organic ligand-free $\text{CH}_3\text{NH}_3\text{PbBr}_3$ nanoparticles and explore their assembly and conductive properties.

***Chapter 3. Characterization Techniques for Perovskite
Nanoparticles***

In this chapter, the techniques used to characterize the optical properties, crystalline structure, morphology and elemental composition of the colloidal perovskite nanoparticles, as well as those used for the conductive characterization of the nanoparticles solid films, are presented.

3.1. Optical characterization

3.1.1 Ultraviolet–visible absorption spectroscopy

The ultraviolet–visible (UV-vis) absorption spectra of the colloidal nanoparticles were recorded to characterize their optical properties as well as to obtain information on their colloidal stability in organic solvents. The spectra were registered using secoman Uvi Ligth XT5 spectrophotometer. Moreover, the UV-Vis spectra of nanoparticles solid films described in *chapter 6* and *7* were registered in a JASCO V-670 spectrometer with horizontal integrating sphere (PIV-757).

3.1.2 Photoluminescence

Steady-state photoluminescence (PL) spectra. The PL spectra of the nanoparticles were recorded in order to study the intrinsic recombination processes. The PL spectrum of the colloids were measured in a quartz cuvette (10 mm) under air atmosphere (unless otherwise indicated) by using a spectrofluorometer PTI (LPS-220B, motor driver (MD-5020), Brytebox PTI), equipped with a Xenon lamp (75 W). The Felix 32 analysis software was used to register the data. The excitation wavelength (λ_{exc}) used for these measurement was 350 nm (330 nm in *chapter 5*).

The PL spectra of the nanoparticles solid films on a glass substrate were registered on a Hamamatsu C9920-02 absolute PL Quantum Yield Measurement System ($\lambda_{\text{exc}} = 350$ nm).

Time resolved PL. The PL kinetic decay of colloidal nanoparticles and films were recorded using a compact fluorescence lifetime spectrometer C11367, Quantaaurus-Tau with a pulse light emission diode source of 340 nm. The average lifetime was obtained from the tri-exponential fitting, with a function of time (t),

Eq. 2, where τ_i and α_i represent the lifetime and the amplitude of each exponential component, respectively.

$$I(t) = \sum_i \alpha_i \left(-\frac{t}{\tau_i}\right) \quad \text{Eq. 2}$$

The average recombination lifetime (τ_{av}) was estimated with the τ_i and α_i values from the fitted curve data according to Eq. 3.

$$\tau(av) = \frac{\sum \alpha_i \tau_i^2}{\sum \alpha_i \tau_i} \quad \text{Eq. 3}$$

3.1.3 Photoluminescence quantum yield

Photoluminescence quantum yield (PLQY) is defined as the ratio between the photon emitted and the photon absorbed by the sample. To measure the PLQY, diluted dispersions of nanoparticles in toluene (absorbance ca. 0.1 at 350 nm) were prepared. In addition, dye solutions of 9,10-diphenylanthracene (PLQY = 91 % in cyclohexane at $\lambda_{exc} = 355$ nm) and fluorescein (PLQY = 86 % in NaOH 0.1 M at $\lambda_{exc} = 465$ nm) were used as fluorescence standards.^[82]

The PLQY of the colloids and films were recorded using a Hamamatsu absolute PL Quantum Yield Measurement System (C9920-02), equipped with monochromatic light source (150 W) and an integrating sphere. The excitation wavelength used was 350 nm.

3.1.4 Photostability assays

Studies on the photostability of the colloidal nanoparticles under continuous UV-Vis irradiation (described in *chapter 4, 5 and 6*) were carried out at room temperature using three different irradiation sources:

- *Fluorimeter Xenon lamp*: the toluene dispersion of nanoparticles in quartz cuvettes (10 mm) was placed in the sample-holder of a PTI- LPS-220B spectrometer equipped with a xenon lamp (75 W). The samples were irradiated with UV-light ($\lambda_{exc} = 350$ nm and 330 nm in *chapter 4 and 5*,

respectively). The Felix 32 analysis software was used to register the data of the PL intensity as a function of the irradiation time.

- *Visible lamps (UV-A)*: In *chapter 4* (section 4.2) the toluene dispersion of nanoparticles in quartz cuvettes (10 mm) was irradiated with eight UV-A lamps (316-400 nm, maximum at 351 nm); intensity 5.3 mWcm⁻², in a Luzchem photoreactor. The PL spectra ($\lambda_{\text{exc}} = 350$ nm) were recorded at room temperature every 3 min.
- *Visible lamps*: In *chapter 4* (section 4.3) the toluene dispersion of nanoparticles in quartz cuvettes (10 mm) were irradiated with eight visible lamps (380-490 nm, maximum at 419 nm), intensity 70.02 Wm⁻² (in the 401-700 nm range) in a Luzchem photoreactor equipped. The PL spectra ($\lambda_{\text{exc}} = 350$ nm) were recorded at room temperature every 5 min.

3.2. Structural and morphological characterization

3.2.1 Powder X-ray diffraction

The analysis of the crystalline structure, phase, lattice parameters and crystalline grain size of the nanoparticles was performed by using powder X-ray diffraction (PXRD). The diffraction spectra were recorded on a Bruker D8 Advance A25 diffractometer using Cu K α ($\lambda = 1.54060$). The powder diffraction pattern was scanned over the angular range of 2-80° (2 θ) with a step size of 0.020°, at room temperature.

The crystalline grain size of the nanoparticles were estimated by the Debye–Scherrer equation (Eq. 4), where D is the average crystallite size, λ is the X-ray wavelength, k is the Scherrer constant, β is the full width at half maximum (fwhm) of the diffraction peak (in radians) and θ is the angle at which that reflection occurs.

$$D = \frac{k \lambda}{\beta \cos \theta} \quad \text{Eq. 4}$$

3.2.2 High Resolution Transmission Electron Microscopy

The analysis of the size and shape homogeneity and the crystalline structure of the nanoparticles were performed using high resolution transmission electron microscopy (HRTEM). The samples were prepared by drop casting (about 20 μL) of the nanoparticles dispersion in toluene on a carbon-coated copper grid (200 mesh). The images were acquired using a Field Emission Gun (FEG) TECNAI G2 F20 microscope, operated at 200 kV.

3.2.3 Scanning Electron Microscopy

The morphology of the surface of nanoparticles solid films and their thickness were analyzed by scanning electron microscopy (SEM). The images were recorded using a field emission scanning electron microscope HITACHI S-4800, at 20 kV. In addition, the chemical microanalysis of the nanoparticles and films were performed by energy-dispersive spectroscopy (EDX) on HITACHI S-4800, equipped with XFlash 5030 Bruker detector and acquisition software QUANTAX 400.

3.3. Chemical composition analysis

3.3.1 X-ray photoelectron spectroscopy

The X-ray photoelectron spectroscopy (XPS) technique measures the kinetic energy of photoelectrons originating from core and valence band energy levels and is highly sensitive to atoms at or near the surface of the material. The energy of the photoelectrons, i.e. the peak position in binding energy scale (in eV), is used for elemental analysis. In the core-level spectra, the position of atoms from different chemical elements is different. Moreover, the differences (in eV), i.e. the chemical shift, in the binding energy of a specific element enables to identify its local chemical environment and the electronic structure. Furthermore, a quantitative analysis of the surface composition can be performed from the peak intensity or area of the spectrum of the photoelectrons detected, which is proportional to the amount of the element in the sample.

In this thesis, the XPS technique was used to study the surface properties and to determine the molar ratio of the elements in nanoparticles capped with different organic ligands (*chapter 4 and 6*). The core-level spectra of Pb 4f, Br 3d, N 1s, C 1s and O1s were analyzed. The Pb/Br ratio in the nanoparticle was quantified through the analysis of the peak area of the Pb and Br bands. The analysis of the other elements can provide information about the nature of the ligand and the kind of interaction between the ligand and the perovskite nanoparticle surface.

The measurements were carried out in solid state, using an X-ray photoelectron spectrometer Phoibos 150-9MCD. The incident radiation was 50 W. The C 1s peak at 285 eV was set as a reference for all the XPS peak positions.

3.3.2 Thermogravimetric analysis

Thermogravimetric analysis (TGA) measures the amount of weight change of a material as a function of the temperature. The percentage of organic and inorganic components of the nanoparticles (and supernatants) was studied by TGA. The heating curves were recorded on Mettler Toledo TGA/SDTA 851e system. The samples were heated from 25 to 800 °C, with an increase of 10 °C/min, under nitrogen flux of 40 mL/min.

The heating curves of individual perovskite precursors ($\text{CH}_3\text{NH}_3\text{Br}$, PbBr_2), organic ligands, solvent, as well as the amines used for the ammonium salt preparation, were used as standards for the analysis of the perovskite nanoparticles composition.

3.3.3 Proton nuclear magnetic resonance spectroscopy

The quantification of the organic cations in the perovskite nanoparticles was performed using ^1H NMR. The spectra were collected at room temperature in a Bruker DPX300 spectrometer, with a 300 MHz Bruker magnet (7 T). The chemical shifts (δ) are reported in ppm relative to tetramethylsilane.

First, the colloidal nanoparticles were precipitated by centrifugation (at 7000 rpm) and the resulting nanoparticles powder was reverted back into the precursors by dissolving it in deuterated dimethyl sulfoxide.

Then, the ^1H NMR spectra were analyzed to determine the molar ratio of the different organic components of the nanoparticles. Finally, the composition of the perovskite nanoparticles was possible by combining these results with the contribution of the inorganic material (i.e. PbBr_2) in the TGA.

The supernatants were also analyzed by TGA and ^1H -NMR. The resulting data made it possible to determine the chemical yield of the perovskite nanoparticles.

3.3.4 Attenuated Total Reflection-Fourier Transform Infrared spectroscopy

The attenuated total reflection-fourier transform infrared spectroscopy (ATR-FTIR) technique provides information related to molecular structures and interactions. Hence, the interaction of the host-guest system described in *chapter 6* was studied using this technique. The spectra were recorded using a FTIR Thermo Nicolet Nexus spectrometer at room temperature with 64 scans and a resolution of 4 cm^{-1} between 400 and 4000 cm^{-1} . The nanoparticles were deposited by drop casting from hexane dispersion at room temperature, whereas the cucurbit[7]uril powder was directly deposited on the crystal.

3.4. Preparation of nanoparticles solid film

Spin-coating. The photoluminescent films described in *chapter 4* and *5* were prepared by following a similar procedure to that of the one-step solution processed technique described in *chapter 1*, figure 1.7. First, the quartz substrates used were cleaned using a detergent solution, demineralized water and isopropyl alcohol, followed by treatment with UV-ozone for 90 min and oxygen plasma treatment for 10 min. Then, a dispersion of the nanoparticles in toluene was spin-coated on top of the quartz substrate at 1000 rpm during 30 seconds and the film was dried at room temperature.

Centrifugal casting. In *chapter 6* and *7* the preparation of nanoparticle solid films was attempted by the centrifugal casting method.^[83] To prepare the film, first a dispersion of the nanoparticle in toluene was prepared with a final volume of 5 mL (or 10 mL in *chapter 7*), then the colloid was added to a conical centrifuge tube (50 mL) containing a glass slide substrate (1.5 cm²) at the bottom, and the sample was centrifuged (6 min at 6000 rpm) in an Eppendorf Centrifuge 5804 R. Thereafter, the supernatant was pipetted out and the glass substrate with the deposited nanoparticle was carefully washed with toluene and allowed to dry under saturated toluene atmosphere (or ethyl acetate in *chapter 7*), at room temperature.

Moreover, the nanoparticles solid films used for the analysis of conductive atomic force microscopy (AFM), were prepared on indium-doped tin-oxide (ITO) substrate. All the glass substrates were first cleaned ultrasonically in detergent solution, then in demineralised water and finally in 2-propanol baths. Finally, they were dried under nitrogen and immediately placed into the conic tube.

3.5. Preparation of electroluminescent devices

The electroluminescent devices described in this thesis were prepared and characterized by the research members of the group directed by Dr. Hendrick Jan Bolink, from the Instituto de Ciencia Molecular (ICMoL) of the Universitat de València.

The devices described in *chapter 4* were prepared as follows:

Materials: The commercial materials used for the preparation of the devices were used as received: aqueous dispersion of PEDOT:PSS [poly(3,4-ethylenedioxythiophene): poly(styrenesulfonate)] Clevios PVP AI 4083 from Heraeus); aluminium oxide nanoparticles (particle size <50 nm, 20 wt. % in isopropanol, Aldrich); SPPO13 (2,7-bis(diphenylphosphoryl)-9,9'-spirobi[fluorene], Luminescence Technology Corp.) and pTPD (Poly[*N,N'*-bis(4-butylphenyl)-*N,N'*-bis(phenyl)-benzidine], American Dye Source Inc.).

- *Control device:* A layer of Al₂O₃ nanoparticles was coated by spin-coating (at 2000 rpm) on ITO substrate from a dispersion of 1:2 isopropanol:ethanol v/v. Then, the sample was sintered at 300 °C during 2 hours. Then, the CH₃NH₃PbBr₃ perovskite layer was coated using a two-step process: first, a solution of PbBr₂ (50 mg/mL) in dimethylformamide was spin-coated (at 1500 rpm) on the Al₂O₃ nanoparticle layer; second the substrate was dipped in a CH₃NH₃Br solution in 2-propanol (10 mg/mL). Finally, the SPPO13 layer was prepared by spin-coating (1000 rpm for 60 s) of a solution of 10 mg/mL in anisole.
- *Nanoparticles device:* A layer of PEDOT:PSS (80 nm) was spin-coated on the ITO-glass substrate. Then, a chlorobenzene solution of pTPD (7 mg/mL) was used to coat the layer (at 2000 rpm during 30 s), which was annealed at 180 °C (30 min) and subsequently washed (3 times) with chlorobenzene at 2000 rpm. The perovskite layer was prepared from toluene dispersion of CH₃NH₃PbBr₃ (P_{OA}) nanoparticles in toluene (4 mg/mL).

Finally, all the devices were transferred into an inert atmosphere glove-box, where the barium/silver electrode was thermally evaporated using a shadow mask. The size of the device was 6.5 mm².

The LED device described in *chapter 6* was prepared as follows:

- The ITO substrate was coated with a 40 nm thick PEDOT:PSS film in air, and annealed at 150 °C for 15 minutes. After deposition of the nanoparticle films by centrifugal casting, the electron transport layer (1,3-bis[3,5-di(pyridin-3-yl)phenyl]benzene, BmPyPhB) and the top metal electrode (5 nm Ba layer capped with 100 layer nm Ag) were thermally evaporated in a high vacuum chamber with a base pressure of 10⁻⁶ mbar.

The devices were characterized in a nitrogen filled glove box. The current density and luminance versus voltage characteristics were measured using a Keithley 2400 Source-Meter and a photodiode coupled to a Keithley 6485 pico-ammeter.

All the substrates used were cleaned ultrasonically in detergent solution, water and isopropyl alcohol baths. After drying, the substrates were placed in a UV-ozone cleaner (Jelight 42-220) for 20 min. In addition, the transport measurement described in *chapter 7* were performed using substrates of pre-patterned interdigitated ITO electrodes (Naranjosubstrates) coated on glass. The electrical characterization was performed in the dark. The current density has been calculated taking into account the channel width and the film thickness.

3.6. Atomic Force Microscopy

The atomic force microscopy (AFM) enables to correlate changes in optoelectronic properties with morphological features at the nanoscale. This technique measures the interacting forces between the cantilever equipped with a probe (sharp tip with radius <10 nm) and the sample. Piezoelectric drives control the sample and the cantilever, and the bending is quantified by a laser, which is reflected off by the cantilever during the scan. The AFM can be operated in three different modes: contact, tapping and non-contact mode. The operating mode is selected based on the degree of proximity between the probe and the sample, the physical properties and the stability of the sample to be studied.

Topographic AFM. The topographic analysis is used to characterize the morphology of substrate or nanoparticles. The average grain size and root mean square (RMS) roughness are two parameters that provide information about the morphology uniformity and quality of a film. These features are important in the study of HOIP films. Moreover, this technique provides information about the stability of the sample by following the morphological changes over time.

In *chapter 5* the morphology, size and aggregation dependence of the nanoparticles deposited on silicon substrate were studied. The topographic AFM images were recorded in tapping mode using a Di NanoScope IVa Controller (resonance frequency of 300 KHz, force constant of 40 N/m). A tip radius of 10 nm and tip-to-face angle (γ) of 19.4° was used to estimate the experimental width.

The nanoparticles were deposited on silicon wafer by drop casting at two concentrations in toluene i) 2 mg/mL and ii) fiftyfold more diluted. These substrates were previously sonicated for 10 minutes in a freshly prepared $\text{H}_2\text{O}_2:\text{NH}_4\text{OH}:\text{H}_2\text{O}$ (1:1:2) solution and the process was repeated three times using new solutions. Then, they were sonicated for 10 minutes in deionized water and dried under a nitrogen stream.

Conductive AFM. The conductive atomic force microscopy (c-AFM) allows the simultaneous determination of local conductivity and topographic maps of the same area of a sample. This technique measures the current between the conducting cantilever and the sample. The correlation between the local conductivity and the surface morphology of nanoparticle solid films prepared by centrifugal casting is commented in *chapter 6* and *7*. The topographic and current mapping were registered in dark and at room temperature, using an atomic force microscope Park Systems NX20, equipped with Pt-Ir coated Si tips (CONTSCPt, diameter of 7 nm).

Two different operating modes were selected:

- *Contact mode:* In *chapter 6* the topographic and current mapping of nanoparticle solid films were measured in contact mode, using a resonance frequency of 31.998 kHz and a spring constant of 0.2 Nm^{-1} . We first tested the suitability of the contact mode scanning. As no tip-sample deterioration was observed, the measurements were performed using this scanning mode. The c-AFM mapping was recorded at different voltages bias (from $\pm 0.5 \text{ V}$ to $\pm 4.5 \text{ V}$) and at scan rates of 0.6 Hz.
- *PinPoint conductive mode:* In *chapter 7* we use the *PinPoint* scanning mode after observing the deterioration of the nanoparticle solid film when using the contact mode. The *PinPoint* is a gentle scanning mode that allows acquiring reproducible and reliable topography and c-AFM images of film surfaces, operating in an approach-retract manner, figure 3.1. The difference with tapping mode is that the contact mode tip used is not oscillating and the tip

retracts and approaches at each pixel rather than adjusting the tip height to maintain a constant oscillation amplitude, bringing highly reproducible images.

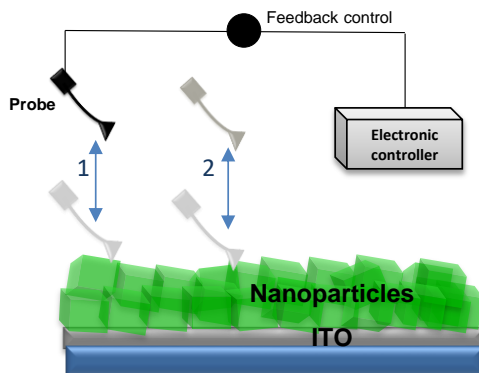


Figure 3. 1. Simplified diagram of conductive AFM in PinPoint conductive mode, the tip approaches to the surface of the nanoparticles film (deposited on conductive substrate) until a predefined threshold point is reached, and then retracts at each pixel point.

Experimentally, the measurement were carried out approaching the tip to the film over a period of 2 ms to achieve an interaction force of 0.24 nN, the force was held constant while the current was registered (twice) at 17 kHz. Then the tip retracted (over a period of 2 ms) and moved to the next pixel. The control height (set to 0.15 μm) at constant force is also recorded to generate a simultaneous topographic image. Different voltages bias were applied (from ± 1.5 V to ± 5.5 V) using a scan rates of 0.23 Hz. The current intensity as a function of the voltaje (I-V) were registered using a current compliance of 10 nA and sample bias from +6 V to -6 V with a period of 1.0 sec.

The current was measured directly after the tip approach by using a preamplifier with a gain of 1011 V/A (ULCA). Data acquisition was carried out using SmartScan software (version 1.0) and XEI Data Processing and Analysis software (version 4.3.0) Build2 (Park Systems Corp). The NX20 equipment is supported by an Active Vibration Isolation System (AVIS) model AVI-200S/LP (Table Stable Ltd).

***Chapter 4. Synthesis and Characterization of Colloidal
CH₃NH₃PbBr₃ Perovskite Nanoparticles***

4.1. Introduction

The first objective of this thesis was the synthesis of colloidal $\text{CH}_3\text{NH}_3\text{PbBr}_3$ perovskite nanoparticles by a non-template strategy. The preparation of the colloidal nanoparticles was based on the synthetic procedure already reported for colloidal inorganic semiconductors, such as CdSe.^[63,64,84] The general approach for the synthesis of colloidal CdSe nanoparticles includes the heating of specific high-boiling point organic solvents (such as octadecene), and the organic ligand (such as oleic acid and oleylamine), followed by the injection of the semiconductor inorganic precursors. The solvent acts as stabilizing agent at high temperatures. The organic ligand acts as capping ligand, controls the growth of the nanoparticle, prevents their agglomeration and makes them dispersible in organic solvents.

We envisaged that the mixing of a good capping agent with perovskite precursors (i.e. $\text{CH}_3\text{NH}_3\text{Br}$ and PbBr_2) would favor the formation of perovskite nanoparticles. The ligand would limit the growth of the 3D inorganic framework at the nanometric scale and, at the same time, passivate the surface of the nanoparticles. To this aim, a binary ligand system consisting of a medium- to long-alkyl chain ammonium cation and oleic acid was chosen.

In this chapter, the conditions studied for the preparation of green photoluminescent colloidal $\text{CH}_3\text{NH}_3\text{PbBr}_3$ nanoparticles under mild conditions, as well as the composition and morphology characterization of the nanoparticles are presented.

The effect of the components molar ratio and the length of the alkyl chain ammonium, as well as of the non-coordinating solvent on the synthesis, stability and unique optical properties of colloidal $\text{CH}_3\text{NH}_3\text{PbBr}_3$ nanoparticles are described. Furthermore, their fully characterization by a combination of different techniques such as UV-Vis absorption, time-resolved and steady state spectroscopy, as well as HRTEM, PXRD, TGA and ^1H NMR, is included.

4.2. Synthesis of colloidal $\text{CH}_3\text{NH}_3\text{PbBr}_3$ perovskite nanoparticles by a non-template strategy

The synthesis of the colloidal nanoparticles was carried out by a hot-injection method. Briefly, a mixture of oleic acid (OLA) in 1-octadecene (ODE) was stirred and heated at 80 °C. Then, the alkyl chain ammonium bromide was added, followed by the addition of $\text{CH}_3\text{NH}_3\text{Br}$ and lead bromide dissolved in dimethylformamide. Finally, acetone was added to induce the precipitation of nanoparticles and the unreactive material was separated by centrifugation, see experimental section for further details.

To determine the best molar ratio between the ammonium salts, preliminary assays were performed by using octadecylammonium bromide (ODABr). Thus, the suitability of the ODABr: $\text{CH}_3\text{NH}_3\text{Br}$ molar ratios of 0.5:0.5, 0.6:0.4 and 0.7:0.3 was studied, whereas the molar ratio between the total ammonium salt ($\text{CH}_3\text{NH}_3\text{Br}$ plus ODABr) and lead bromide (PbBr_2) was fixed at 1:1. The optimal molar ratio was 0.6:0.4.

The perovskite nanoparticles, P_{ODA} (P refers to perovskite and ODA to octadecylammonium cation), dispersed in toluene showed the absorption peak maximum at ca. 525 nm, in agreement with the value reported for nanoparticles into mesoporous film.^[5] The PL emission spectrum exhibited a symmetrical peak at 526 nm (figure 4.1), and additional peaks at lower wavelength (below 500 nm); this is consistent with the competitive formation of low-dimension perovskites by the presence of the long alkyl chain of ODA.^[30,42,85,86]

Strikingly, when using medium length octylammonium bromide (OABr), the spectrum of the nanoparticles did not show any additional peaks, figure 4.1. These nanoparticles, termed as P_{OA} (OA refers to octylammonium), exhibited high dispersibility in toluene, a symmetric and narrow PL emission peak at 530 nm (fwhm = 21 nm) and a PLQY of 17 % (figure 4.1 and 4.2). The blue-shifted absorption peak (at 527 nm) of P_{OA} , compared with that of $\text{CH}_3\text{NH}_3\text{PbBr}_3$ bulk

(~540 nm), was attributed to the particle-size quantum confinement effect in the $\text{CH}_3\text{NH}_3\text{PbBr}_3$ nanoparticles.

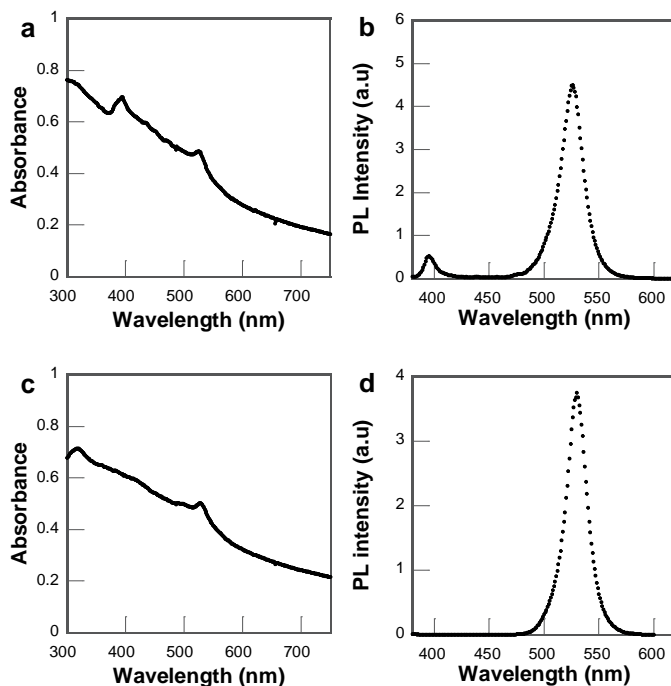


Figure 4. 1. a,c) Absorption and b,d) PL emission spectra of the $\text{CH}_3\text{NH}_3\text{PbBr}_3$ nanoparticles P_{ODA} (a,b) and P_{OA} (c,d) dispersed in toluene.

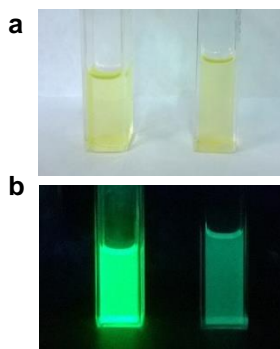


Figure 4. 2. Comparative images of toluene dispersion of $\text{CH}_3\text{NH}_3\text{PbBr}_3$ nanoparticles P_{OA} (left) and P_{ODA} (right) under a) lab light and b) UV-light.

The HRTEM images of P_{OA} confirmed the formation of highly crystalline spherical nanoparticles with an average size of 6 nm, figure 4.3. The PXRD pattern of P_{OA} fit to the cubic phase of $\text{CH}_3\text{NH}_3\text{PbBr}_3$ perovskite ($a = 5.9334$ (5) Å, space group = $Pm\bar{3}m$).^[11,13,87,88] This result was consistent with the lattice spacing and fast Fourier transform (FFT) patterns observed in the HRTEM image of individual nanoparticles (figure 4.3).

Furthermore, the EDS analysis showed a Br/Pb ratio of 77/23, which is consistent with a $\text{CH}_3\text{NH}_3\text{PbBr}_3$ stoichiometry. This was the first example of the preparation of 3D hybrid lead halide perovskites nanoparticles (i.e. 0D material) using a non-template strategy (*Journal of the American Chemical Society* **2014**, 136, 850-853). Additionally, it showed that, contrary to CdSe, these nanoparticles did not need a shell of inorganic material to achieve a PLQY of ca. 20 %.

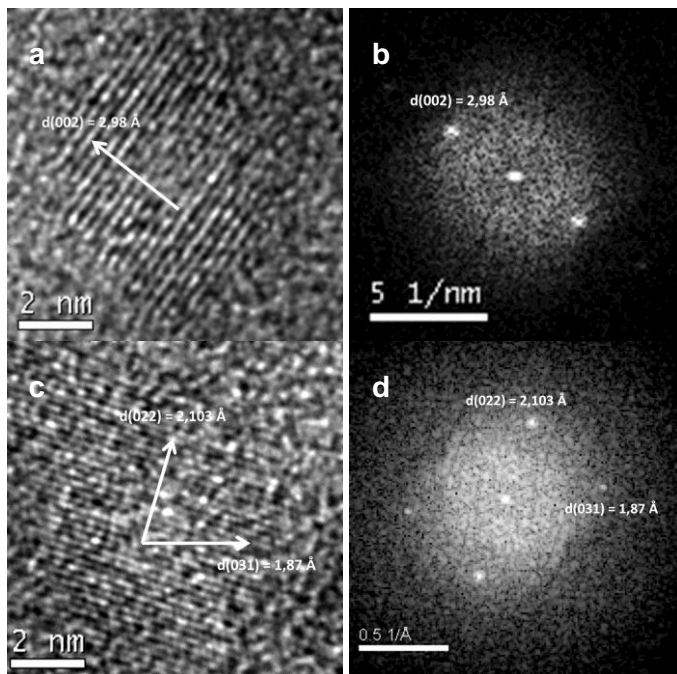


Figure 4. 3. a,c) HRTEM images of individual $\text{CH}_3\text{NH}_3\text{PbBr}_3$ nanoparticles (P_{OA}); and b,d) their corresponding FFT analyses, showing the interplanar distance from fringes of about 2.98 Å (image a, b), 2.103 Å and 1.87 Å (image c,d), attributed to (002), (022) and (031) family planes of cubic phase structure of $\text{CH}_3\text{NH}_3\text{PbBr}_3$ with $Pm\bar{3}m$ space group, respectively.

The main features of $\text{CH}_3\text{NH}_3\text{PbBr}_3$ nanoparticles prepared in this study using OA as ligand are: i) improved emissive properties compared with those with ODA; this indicates the key role of the alkyl chain length of the ammonium ligand, ii) high dispersibility in aprotic solvents (such as toluene, hexane, tetrahydrofuran, chloroform and ethyl acetate); iii) stability in the solid state for more than three months and iv) a remarkable stability under continuous UV irradiation (figure 4.4).

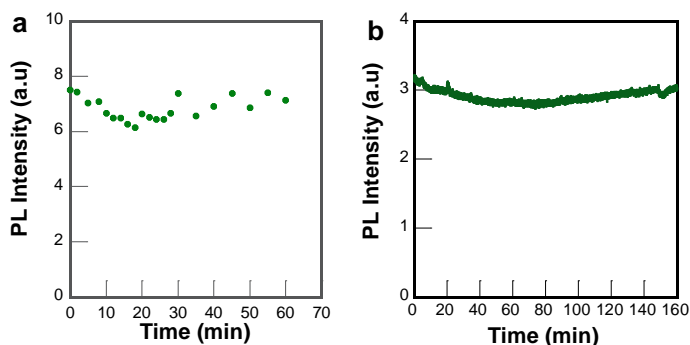


Figure 4.4. PL intensity as a function of irradiation time of P_{OA} nanoparticles in toluene ($\lambda_{\text{em}} = 528 \text{ nm}$): a) under UV-A lamp irradiation (λ_{exc} maximum at 351 nm) for 60 minutes; b) Under continuous fluorimeter excitation lamp ($\lambda_{\text{exc}} = 350 \text{ nm}$) for 160 minutes.

In collaboration with Dr. Hendrik Jan Bolink, we prepared thin films from colloidal nanoparticles. Interestingly, the nanoparticle thin film, prepared by spin-coating from the dispersion of P_{OA} nanoparticles in toluene, exhibited a narrow PL emission peak at 533 nm (fwhm 22 nm) and a PLQY of 23% (figure 4.5 a).

Later on, a light-emitting device was prepared in an architecture of ITO/PEDOT:PSS/pTPD/ $\text{CH}_3\text{NH}_3\text{PbBr}_3$ nanoparticles/Ba/Ag. For comparative purposes a device with a $\text{CH}_3\text{NH}_3\text{PbBr}_3$ bulk film was prepared with an architecture of ITO/ Al_2O_3 / $\text{CH}_3\text{NH}_3\text{PbBr}_3$ -bulk/SPPO13/Ba/Ag (see chapter 3). Remarkably, the electroluminescent device based on the photoluminescent

$\text{CH}_3\text{NH}_3\text{PbBr}_3$ nanoparticles film exhibited an improved EL, up to 10 times, than that of the $\text{CH}_3\text{NH}_3\text{PbBr}_3$ bulk. The device based on nanoparticles exhibited an EL emission peak centered at 528 nm (figure 4.5 b) and this was the first example of an electroluminescent device from 3D perovskite nanoparticles.

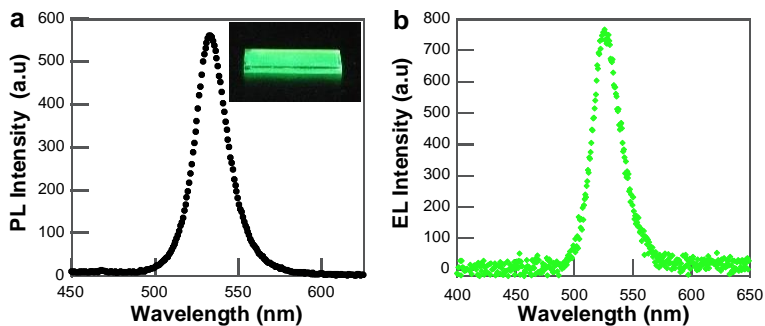


Figure 4. 5. a) Room temperature PL emission spectrum of a thin film prepared using colloidal $\text{CH}_3\text{NH}_3\text{PbBr}_3$ nanoparticles (P_{OA}). b) Room temperature electroluminescent spectrum of the device $\text{ITO}/\text{PEDOT}:\text{PSS}/\text{pTPD}/\text{CH}_3\text{NH}_3\text{PbBr}_3$ nanoparticles/ Ba/Ag registered at 6 V.

4.3. Photoluminescent enhancement of colloidal $\text{CH}_3\text{NH}_3\text{PbBr}_3$ perovskite nanoparticles

The hot-injection method^[89] was subsequently adopted by several groups to study the applications of the nanoparticles in the preparation of chemical sensor^[90] and light-emitting electrochemical cells.^[91]

Encouraged by our previous results in the synthesis of colloidal $\text{CH}_3\text{NH}_3\text{PbBr}_3$ perovskite nanoparticles, we then focused on improving their optical properties and dispersibility, taking into account the fact that surface states would be highly accessible for passivation treatment.^[62,64] The role of the molar ratio of the perovskite precursors ($\text{CH}_3\text{NH}_3\text{Br}$, PbBr_2) and the organic ligands (OLA and alkyl ammonium salt) was studied. In addition, the effect of the length of the alkyl chain ammonium ligand was evaluated by using different organic cations such as ethylammonium (EA), hexylammonium (HA) and octadecylammonium (ODA), instead of OA (*Journal of Materials Chemistry A* **2015**, 3, 9187-9193).

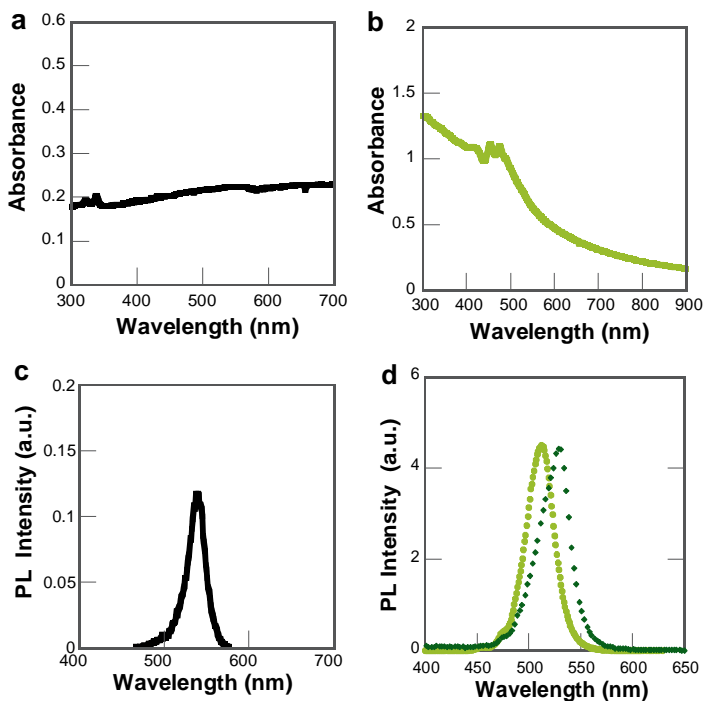
We envisaged that an increase in the $\text{CH}_3\text{NH}_3\text{Br}/\text{PbBr}_2$ molar ratio used in the hot-injection method could be advantageous for the passivation of the nanoparticle surface. Hence, following our strategy, first the molar ratio between the total ammonium salts ($\text{CH}_3\text{NH}_3\text{Br}$ plus OABr) and PbBr_2 was increased to 4:1, keeping the $\text{OLA}:\text{PbBr}_2$ and $\text{ODE}:\text{PbBr}_2$ molar ratio of 3:1 and 63:1, respectively.

Table 4.1 summarizes the component molar ratio used and the optical features of the $\text{CH}_3\text{NH}_3\text{PbBr}_3$ nanoparticles. Comparatively, a control sample (P_c) was prepared under the same reaction conditions without adding any alkyl chain ammonium ligand. As expected, the solid obtained was hardly dispersible in toluene (figure 4.6). The colloid showed a PL peak maximum at 538 nm, i.e. at a wavelength close to that of the bulk $\text{CH}_3\text{NH}_3\text{PbBr}_3$. This result re-emphasizes the importance of the alkyl ammonium in the formation and dispersibility of the nanoparticles.

Table 4.1. Components molar ratio used in the synthesis of $\text{CH}_3\text{NH}_3\text{PbBr}_3$ perovskites nanoparticles and the optical properties of the nanoparticles

P	Ligand ^a		$\text{CH}_3\text{NH}_3\text{Br}$ (mmol)	PbBr_2 (mmol)	ODE (mmol)	OLA (mmol)	PL ^b (nm)	PLQY ^d (%)	PLQY ^c (%)
	(mmol)								
Pc	-	-	0.24	0.1	6.26	0.3	538	-	-
P _{OA1}	OA	0.16	0.24	0.1	6.26	0.3	513	67	34
P _{OA2}							520	83	72
P _{OA3}							525	52	41
P _{HA}	HA	0.16	0.24	0.1	6.26	-	526	58	38
P _{EA}	EA	0.16	0.24	0.1	6.26	-	^c	-	-

^a Long alkyl chain ammonium salt used in the synthesis. ^bPL emission spectra ($\lambda_{\text{exc}}=350$ nm) of toluene dispersion. The perovskites prepared fit to cubic phase of $\text{CH}_3\text{NH}_3\text{PbBr}_3$ structure. ^cAn orange solid not dispersible in toluene was obtained. ^dPLQY recorded at $\lambda_{\text{exc}}=350$ nm. ^ePLQY of the nanoparticle thin films.

Figure 4. 6. Absorption spectra of the toluene dispersion of a) Pc b) P_{OA1} . PL emission spectra ($\lambda_{\text{exc}}=350$ nm) of c) Pc toluene solution and b) P_{OA1} in toluene (\bullet) and film (\blacklozenge).

A more dispersible and emissive perovskites was obtained when using an $\text{OABr}:\text{CH}_3\text{NH}_3\text{Br}:\text{PbBr}_2$ molar ratio of 1.6:2.4:1.0. The perovskite, labelled as P_{OA1} (1 refer to the synthesis with OLA addition) exhibited a PL peak at 513 nm (fwhm 31 nm), figure 4.6, and a remarkable increase of the PLQY (67 %).

Interestingly, an enhancement in the optical properties of $\text{CH}_3\text{NH}_3\text{PbBr}_3$ nanoparticles was observed when the synthesis was carried out in the absence of OLA, P_{OA2} . Specifically, we found that i) the colloidal P_{OA2} absorption spectrum showed a negligible scattering (figure 4.7), ii) the PLQY increased to 83 % for the colloidal solution and 72 % for the film, and iii) the emission band of the P_{OA2} film was similar to that of the colloidal dispersion.

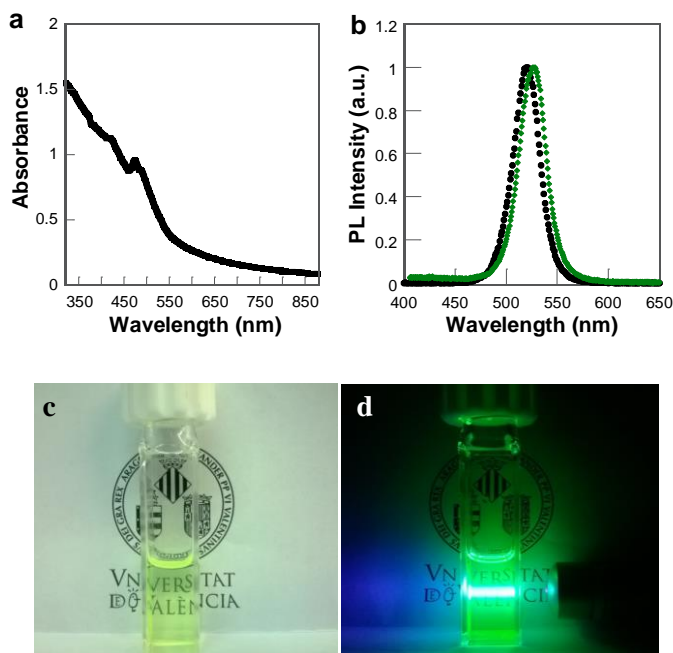


Figure 4. 7. a) Absorption spectrum of $\text{CH}_3\text{NH}_3\text{PbBr}_3$, P_{OA2} , dispersed in toluene. b) PL emission spectra of P_{OA2} in toluene (\bullet) and deposited on thin film (\blacklozenge). c,d) Image of toluene dispersion of P_{OA2} nanoparticles under the lab light (c) and UV-laser pointer excitation (d).

Less emissive colloids were formed in the absence of ODE (P_{OA3} , 52 %) and with the shorter alkyl ammonium HA (P_{HA} , 58 %); in addition, the films showed lower PLQY than the colloid (38-41 %), table 4.1. Nevertheless, these PLQY values

were still higher than those of our previous results (section 4.2). Moreover, a non-dispersible solid was obtained when using EA, while ODA led to a perovskite with a low-dimensionality.

Time-resolved photoluminescence spectroscopy analysis showed that $\text{P}_{\text{OA}2}$ exhibited a considerably longer lifetime average (τ_{av}) than $\text{P}_{\text{OA}1}$, reaching values close to 600 ns in solution and ca. 410 ns in film (table 4.2). Furthermore, similar to our previous result, the toluene dispersion of the perovskite exhibited a high photostability under continuous UV irradiation; the PL intensity only decreased ca. 10 % after 540 minutes of continuous irradiation (figure 4.8).

Table 4. 2. Photoluminescence data of $\text{P}_{\text{OA}1}$ and $\text{P}_{\text{OA}2}$ toluene colloids and films.

Sample	PL (nm)	fwhm (nm)	τ_{av} ^a (ns)	PLQY (%)
$\text{P}_{\text{OA}1}$	513	31	415	67
$\text{P}_{\text{OA}1}$ film	526	36	344	34
$\text{P}_{\text{OA}2}$	520	32	594	83
$\text{P}_{\text{OA}2}$ film	526	30	412	72

^aPL decay traces recorded at $\lambda_{\text{exc}} = 340$ nm, in air.

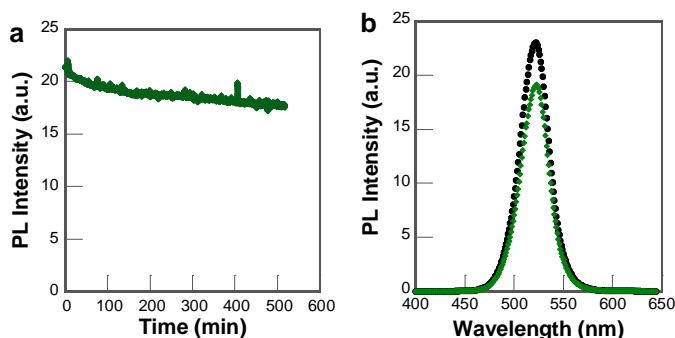


Figure 4. 8. a) PL intensity as a function of the irradiation time of $\text{P}_{\text{OA}2}$ nanoparticles in toluene ($\lambda_{\text{em}} = 520$ nm), b) PL emission spectra before and after 540 minutes of irradiation; using continuous fluorimeter excitation lamp ($\lambda_{\text{exc}} = 350$ nm).

The HRTEM images of the perovskites prepared by using this approach confirmed the formation of nanoparticles with an average size of 7 ± 1.5 nm and 5.5 ± 1.5

nm for the most emissive samples P_{OA1} and P_{OA2} , respectively, figure 4.9. The nanoparticles were embedded into amorphous material forming plaques.

X-ray photoelectron spectroscopy (XPS) analysis was performed to gain further information of the nanoparticles. Table 4.3 summarizes the core-level binding energies (in eV) of the peaks observed and their assignment. Overall, the XPS spectrum of P_{OA2} showed slightly shifted peaks to higher binding energy than P_{OA1} , as it is shown in figure 4.10 for Pb 4f, Br 3d and N 1s. This could be indicative of a higher stability of P_{OA1} than P_{OA2} . The XPS quantification analyses revealed a Pb/Br atomic ratio of 68:32 and 73:28 for P_{OA1} and P_{OA2} , respectively, which are in agreement with the PXRD result for the cubic phase of the $\text{CH}_3\text{NH}_3\text{PbBr}_3$ structure (space group = $Pm\bar{3}m$), figure 4.9.

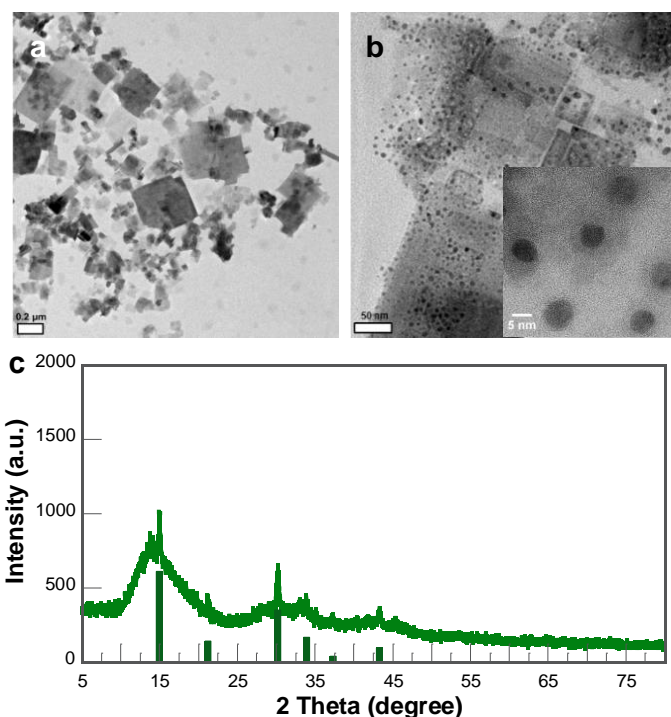


Figure 4. 9. HRTEM images of P_{OA2} ; scale bar of $0.2 \mu\text{m}$ (a) and 50 nm (b); inset image b: HRTEM image of P_{OA2} nanoparticles (scale bar 5 nm). c) PXRD pattern of P_{OA2} ; the vertical bars correspond to the standard peaks of cubic phase of $\text{CH}_3\text{NH}_3\text{PbBr}_3$.

Table 4. 3. XPS core-level peaks and deconvolution in their components of $\text{P}_{\text{OA}2}$ nanoparticles.

Element Core-level	$\text{P}_{\text{OA}2}$ BE (eV) ^a	Assignment
Pb 4f	143.6	<i>Pb 4 f_{5/2}</i>
	138.7	<i>Pb 4 f_{7/2}</i>
	136.8	<i>Metallic Lead</i>
Br 3d	69.1	<i>Br 3d</i>
N 1s	402.6	<i>-NH₃⁺</i>
	400.0	<i>-NH₂</i>
C 1s	285.7	<i>C-C /C-H; C=C</i>
	285.0	<i>C-N⁺</i>
O 1s	532.9	<i>O 1s</i>
	528.8	<i>PbO</i>

^a The XPS spectra were analyzed using the C peak at 285.0 eV as the reference.

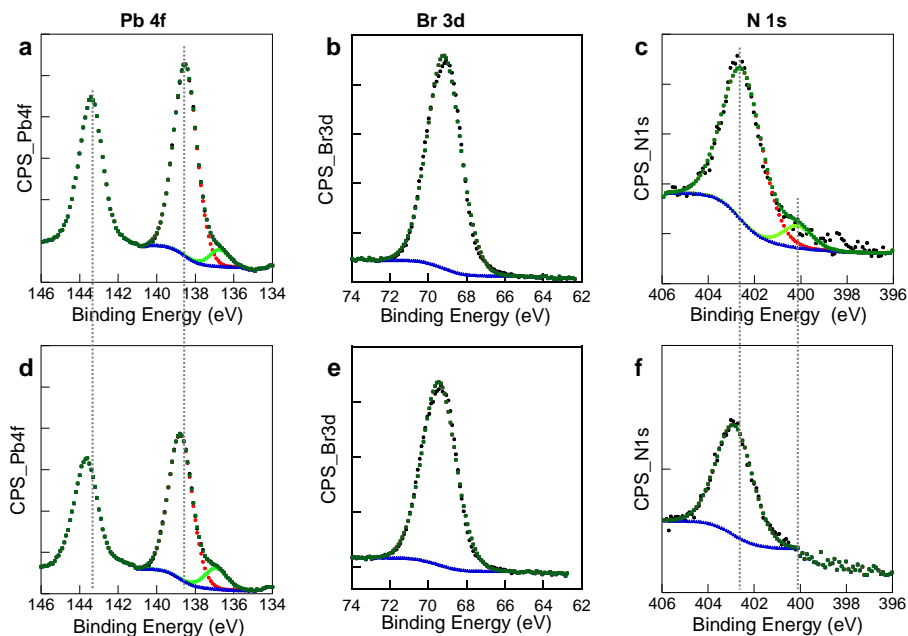


Figure 4. 10. Comparison of the XPS spectra of $\text{P}_{\text{OA}1}$ (top) and $\text{P}_{\text{OA}2}$ (down) for Pb 4f (a,d), Br 3d (b,e) and N 1s (c,f). The dotted line indicate the slight shift of the $\text{P}_{\text{OA}2}$ peaks to higher binding energies.

Additional information of the perovskite composition was obtained from the TGA and ^1H NMR spectra. Whereas the TGA heating curve provided information on the organic and inorganic weight percentage in the isolated mass, the ^1H NMR

was used to obtain information about the molar ratio between the organic components in the perovskite nanoparticles (see chapter 3). Figure 4.11 shows the comparative TGA heating curves and their corresponding 1st derivative of P_{OA1} and P_{OA2} . The three weight losses observed were attributed to octylamine at ~ 200 °C, ODE plus the remaining ammonium salts (plus OLA in the case of P_{OA1}) at ~ 360 °C and lead bromide at ca. 600 °C (weight loss 56.6 %). Interestingly, P_{OA2} solid weight loss shifted to higher temperatures, suggesting a higher stability of the nanoparticles components in the absence of OLA.

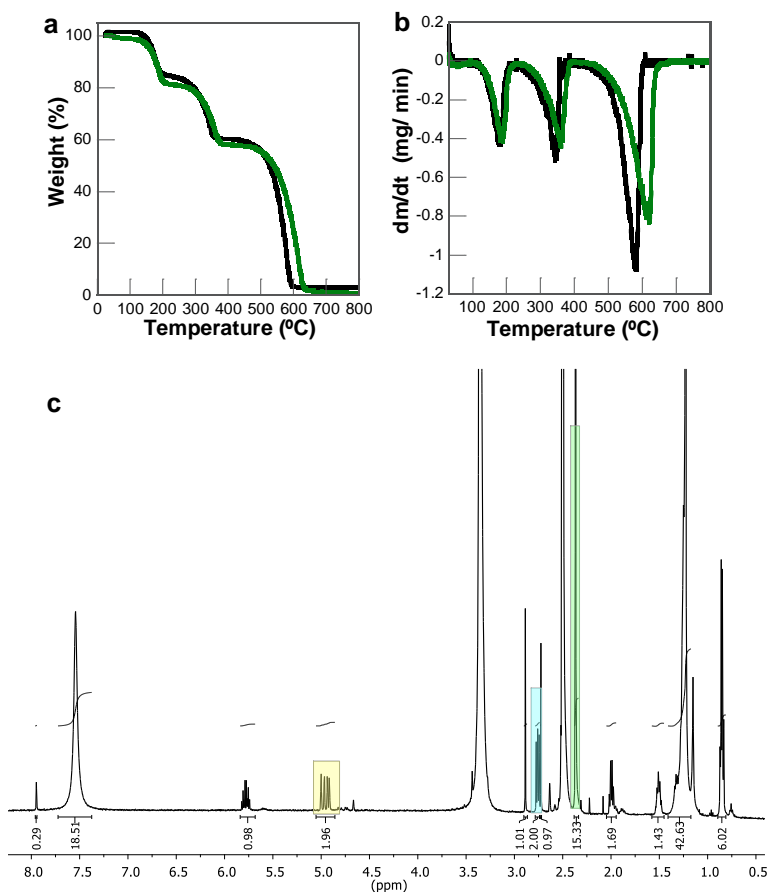


Figure 4. 11. a,b) TGA heating curves of P_{OA1} (-) and P_{OA2} (-), and their corresponding 1st derivatives. c) ¹H NMR spectrum of P_{OA2} in deuterated dimethyl sulfoxide; the signal of $\text{CH}_3\text{NH}_3\text{Br}$, OA, and ODE used for the quantification are in indicated in green, cyan and yellow rectangle, respectively.

The ^1H NMR spectrum showed the signals of OA, $\text{CH}_3\text{NH}_3\text{Br}$ and ODE (figure 4.11). The molar ratios were in agreement with the weight loss of the components observed in the TGA curves. Taken together, we were able to determinate the composition of the perovskite nanoparticles (table 4.4).

Table 4. 4 Components molar ratio in $\text{P}_{\text{OA}2}$ obtained from the TGA and ^1H -RMN data

	synthesis (mmol) ^a	Reagent	
		$\text{P}_{\text{OA}2}$ (mmol) ^b	Molar ratio ^c Component/ PbBr_2
OABr	0.24	0.011	0.11
$\text{CH}_3\text{NH}_3\text{Br}$	0.16	0.131	1.37
ODE	6.17	0.025	0.26
PbBr_2	0.10	0.088	1.00

^a Reagent added in synthesis. ^bComponents determinate in $\text{P}_{\text{OA}2}$ nanoparticles. ^cThe moles of PbBr_2 was calculated by TGA.

In 2014, it was reported that the passivation of mixed $\text{CH}_3\text{NH}_3\text{PbI}_{3-x}\text{Cl}_x$ perovskite films with electron rich weak Lewis bases, such as thiophene and pyridine, played a relevant role on their emissive properties by binding the under-coordinated lead atoms, thus enhancing the photoluminescence and solar cell performance of the perovskite.^[92,93] Therefore, we hypothesized that the ammonium moiety of octylammonium would bind the under-coordinated bromide ions of the perovskite nanoparticles, while ODE would bind to under-coordinated lead ions (via its double bond), thus passivating these defect sites and decreasing the rate of non-radiative recombination processes at the perovskite surface, as well as cooperating in their stability and dispersability in organic solvents.

4.4. Conclusions

In summary, we reported for the first time the synthesis of colloidal CH₃NH₃PbBr₃ nanoparticles. A medium alkyl chain ammonium salt was used to limit the growth of the array that extends in 3D and to provide colloidal stability to the nanoparticles. Green photoluminescent colloidal nanoparticles were prepared under mild conditions with a photoluminescent quantum yield ca. 20 %. They proved to be stable and dispersible in aprotic and moderate polarity organic solvent and highly stable in solid state (up to three months).

In addition to this, photo- and electroluminescent thin films were prepared from the colloidal nanoparticles. Interestingly, the nanoparticles film preserved the optical properties of the colloid. These pioneer results opened the possibility of multiple applications of the photoluminescent perovskite nanoparticles for the preparation of optoelectronic devices by using low cost processing techniques.

Finally, CH₃NH₃PbBr₃ perovskite nanoparticles with a photoluminescence quantum yield of 83 % was demonstrated through the fine tuning of the molar ratio between the alkyl ammonium salts and lead bromide, in the absence of oleic acid. The nanoparticles preserved their emissive properties in solid state and exhibited high photostability under continuous UV irradiation of the colloid.

4.5. Experimental section

Reagents. Lead bromide (99.999 %), methylamine (40 % in water), ethylamine (≥ 99.5 %), hexylamine (99 %), octylamine (≥ 99.5 %), octadecylamine (≥ 99 %), hydrobromic acid (47 %), oleic acid, 1-octadecene and the solvents used were purchased from Sigma-Aldrich and used as received.

Synthesis of alkyl ammonium salts. The alkyl ammonium bromide salts were prepared by the equimolar addition of an aqueous hydrobromic acid (HBr) solution to the amine $\text{C}_n\text{H}_{2n+1}\text{NH}_2$ ($n = 1, 2, 6$ and 8) in round bottom flask at 0°C . The mixture was stirred for 2 hours. Then the precipitate was filtered and the solid washed with diethyl ether (three times). After filtration, the solid was collected and dried at 40°C in vacuum for 24 h.

In the case of the octadecylammonium bromide ($\text{C}_{18}\text{H}_{37}\text{NH}_3\text{Br}$), it was prepared by using a similar methodology but the amine was previously dissolved in acetonitrile at 60°C and then hydrobromic acid (HBr) was added. The precipitate was washed several times with diethyl ether and dried under vacuum (at 40°C).

Synthesis of $\text{CH}_3\text{NH}_3\text{PbBr}_3$ perovskite nanoparticles by hot-injection method. The colloidal perovskite nanoparticles P_{OA} described in section 4.1 were prepared as follows: a solution of oleic acid (OLA, 85 mg, 0.3 mmol) in 2 ml of 1-octadecene (ODE, 6.26 mmol, 2.0 mL) was stirred and heated at 80°C and then, octylammonium bromide (OABr, 12.6 mg, 0.06 mmol) was added. Subsequently, methylammonium bromide ($\text{CH}_3\text{NH}_3\text{Br}$, 4.4 mg, 0.04 mmol) and lead bromide (36.7 mg, 0.1 mmol) dissolved in dimethylformamide (100 μL) were added. The molar ratio between the components OABr: $\text{CH}_3\text{NH}_3\text{Br}$: PbBr_2 was 0.6:0.4:1.0

Thereafter, the nanoparticles were precipitated by addition of acetone and a yellow dispersion was observed. Finally, the perovskite was separated by centrifugation (7000 rpm, 10 min) and the solid was dispersed in toluene

Synthesis of $\text{CH}_3\text{NH}_3\text{PbBr}_3$ nanoparticles by a modified method. The colloidal perovskite nanoparticles P_{OA1} described in section 4.2 and summarized in table

4.1 were prepared as follows: a solution of oleic acid (OLA, 0.30 mmol, 85 mg) in 1-octadecene (ODE, 6.26 mmol, 2.0 mL) was heated at 80°C under stirring. Then octylammonium bromide (OABr, 0.16 mmol, 33.5 mg) followed by methylammonium bromide ($\text{CH}_3\text{NH}_3\text{Br}$, 0.24 mmol, 26.4 mg, dissolved in 100 μL of dimethylformamide) and lead bromide (0.10 mmol, 36.7 mg, dissolved in 200 μL of dimethylformamide) were added. The molar ratio between the components OABr: $\text{CH}_3\text{NH}_3\text{Br}$: PbBr_2 was 1.6:2.4:1.0. The solution was cooled down to 60 °C and immediately the precipitation of the nanoparticles was induced by the addition of acetone (5 mL). The unreactive material was separated by centrifugation (7000 rpm, 10 min, 20°C). Finally, the nanoparticles were dispersed in toluene. The colloidal nanoparticles $\text{P}_{\text{OA}2}$ were prepared following the procedure described for $\text{P}_{\text{OA}1}$ but in the absence of oleic acid. The colloidal perovskite nanoparticles P_{EA} and P_{HA} were prepared following the procedure described for $\text{P}_{\text{OA}2}$ but using EABr or HABr instead of OABr and keeping the same molar ratios of the other components.

Contribution of the Author:

- Schmidt, L. C.; Pertegás, A.; **Gonzalez-Carrero, S.**; Malinkiewicz, O.; Agouram, S.; Mínguez Espallargas, G.; Bolink, H. J.; Galian, R. E.; Pérez-Prieto, J., Nontemplate Synthesis of $\text{CH}_3\text{NH}_3\text{PbBr}_3$ Perovskite Nanoparticles. *Journal of the American Chemical Society* **2014**, *136* (3), 850-853.
Impact Factor (JCR): 12.113, Quartile: Q1, Cited by: 475
- **Gonzalez-Carrero, S.**; Galian, R. E.; Pérez-Prieto, J., Maximizing the emissive properties of $\text{CH}_3\text{NH}_3\text{PbBr}_3$ perovskite nanoparticles. *Journal of Materials Chemistry A* **2015**, *3* (17), 9187-9193.
Invited contribution of special issue “perovskite solar cell”.
Impact Factor (JCR): 8.262, Quartile: Q1, Cited by: 160

***Chapter 5. Synthesis and Optical Properties of
Dispersible Two-dimensional $(RNH_3)_2PbBr_4$
Perovskites***

5.1. Introduction

As was previously described, the HOIP with 2D inorganic framework $(\text{RNH}_3)_2\text{PbBr}_4$ have been extensively studied mostly as single crystals and thin films.^[23,46,59,94] They show a facile preparation and structure tunability by varying the organic cation and the inorganic layer composition. Few strategies have been reported on the preparation of photoluminescent 2D perovskites as nano-microcrystals. Polycrystalline particles with size from 20 nm to several microns have been prepared by nebulization/lyophilization, intercalation and precipitation from bulk powder.^[72-74] These particles proved to be dispersible in organic solvents and showed similar optical features to those observed in thin films, such as a narrow excitonic peak and intense photoluminescence.

After the successful synthesis of highly luminescent colloidal perovskites nanoparticles with a 3D framework, we pursued the extension of the hot-injection strategy to the synthesis of dispersible 2D perovskites nanoparticles. But in this case, the alkyl ammonium salt would play a dual role: be part of the 2D inorganic framework and act as ligand. The alkyl ammonium salts hexylammonium (HA), octylammonium (OA) and octadecylammonium (ODA) were selected for this study.

In this chapter, the synthesis and optical properties of colloidal blue-photoluminescent 2D $(\text{RNH}_3)_2\text{PbBr}_4$ perovskites as well as their processability are presented (*Journal of Materials Chemistry A* **2015**, 3, 14039-14045). The effect of the organic RNH_3^+ cations and the oleic acid addition on the synthesis, optical properties and stability are described.

5.2. Synthesis and optical properties of $(\text{RNH}_3)_2\text{PbBr}_4$ perovskite

The synthesis of $(\text{RNH}_3)_2\text{PbBr}_4$ was carried out by using the hot injection method described previously.^[89] Briefly, a mixture of OLA and ODE was heated under stirring at 80 °C, then the alkyl ammonium bromide (RNH_3Br) followed by PbBr_2 were added. The $\text{RNH}_3\text{Br}:\text{PbBr}_2$ molar ratio was 2:1. Finally, the precipitation of the nanoparticles was induced by addition of acetone and the nanoparticles were purified by centrifugation.

The perovskites with the longest alkyl ammonium ODA, P_{ODA1} (1 refers to the above mentioned conditions), exhibited high dispersibility in toluene. The absorption and PL emission spectra showed a sharp and intense peak at 389 nm and 397 nm (fwhm 13 nm), respectively. Moreover, the colloid showed a remarkable PLQY ca. 21 % vs 12 % as thin film. The excitonic peak was consistent with that of a perovskite with 2D inorganic framework (chapter 1, table 1.3). In contrast, much less emissive (PLQY not measurable) and dispersible perovskites were obtained with the shortest ammonium cations OA and HA (P_{OA1} , P_{HA1}). They showed a broader absorption peak (ca. 400 nm), wider PL emission with maximum at ca. 408 nm and a considerable long tail extending up to ca. 600 nm.

In order to study the effect of OLA on the optical properties of the perovskites, the synthesis was carried out under the same conditions but in the absence of OLA. Similar absorption and emission spectra features as well as dispersibility were observed for the 2D perovskites (figure 5.1 and table 5.1); however, the perovskite with a shorter alkyl ammonium, P_{OA2} and P_{HA2} (2 refers to synthesis in the absence of OLA), exhibited a measurable PLQY (ca. 1 %). Figure 5.2 shows the picture of P_{ODA2} perovskite (PLQY of ca. 20 %) dispersed in toluene under lab light and UV laser pointer excitation.

Additionally, the synthesis was carried out under the same conditions that P_{ODA1} but i) in absence of ODE and ii) halving the amount of ODE and OLA. The

perovskites were less emissive (PLQY lower than 14 %); thus confirming the importance of the ODE in the preparation of these 2D perovskite, similar to our previous results with 3D perovskite nanoparticles (chapter 4). The optimal condition for the synthesis of 2D perovskite nanoparticles in this study was in the absence of OLA.

Table 5. 1 Optical properties of $(\text{RNH}_3)_2\text{PbBr}_4$ toluene colloid

$(\text{RNH}_3)_2\text{PbBr}_4$	Alkyl ammonium salt ^a	A ^b (nm)	PL ^c (nm)	PLQY ^d (%)
P_{ODA1} (ODA) ₂ PbBr ₄	<i>ODABr</i>	389	397	22.9
		389	397	20.1 ^e
P_{ODA2} (ODA) ₂ PbBr ₄	<i>ODABr</i>	390	397	19.8
		390	397	21.4 ^e
P_{OA2} (OA) ₂ PbBr ₄	<i>OABr</i>	396	409	0.5
		396	409	0.7 ^e
P_{HA2} (HA) ₂ PbBr ₄	<i>HABr</i>	398	408	0.5
		398	408	0.5 ^e

^a Long alkyl chain ammonium salt used in the synthesis. ^b Absorption maximum. ^c PL emission maximum ($\lambda_{\text{exc}} = 330$ nm). ^d PLQY ($\lambda_{\text{exc}} = 330$ nm). ^e PLQY measured under N₂ atmosphere.

The effect of the length of the organic RNH_3^+ cations on the optical properties followed the trend observed previously in thin films, i.e the excitonic absorption peak blue shifts with the increase of the alkyl chain length, from 398 nm to 389 nm for P_{HA2} and P_{ODA2}, respectively (table 5.1).^[19,24,95]

The time-resolved PL spectroscopy analysis of the three $(\text{RNH}_3)_2\text{PbBr}_4$ perovskites dispersed in toluene ($\lambda_{\text{exc}} = 337$ nm), under both nitrogen and air atmosphere, showed a short lifetime τ_1 of ca. 2.6 ns (contribution >97%), with a negligible dependence on the presence of oxygen.

The photostability of the colloidal perovskites was studied by measuring the evolution of its PL intensity as a function of the irradiation time using fluorimeter lamps as the irradiation source ($\lambda_{\text{exc}} = 330$ nm). Figure 5.3 shows that the PL intensity decreases less than 7% for P_{ODA2} and P_{OA2}; but more than 30 % for P_{HA2}, after 200 min of continuous UV irradiation under nitrogen atmosphere. These results indicated that our synthetic approach yielded highly photostable P_{ODA2} colloids.

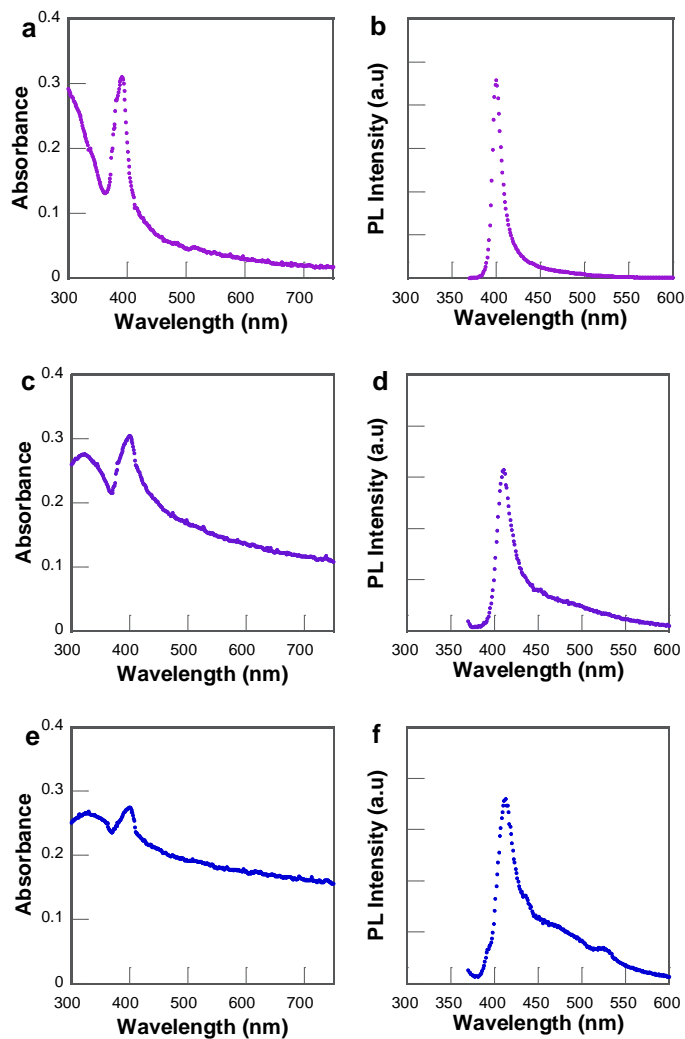


Figure 5. 1. Absorption and PL emission ($\lambda_{\text{exc}} = 330 \text{ nm}$) spectra of colloidal solutions of a,b) $P_{\text{ODA}2}$; c,d) $P_{\text{OA}2}$ and e,f) $P_{\text{HA}2}$ in toluene.

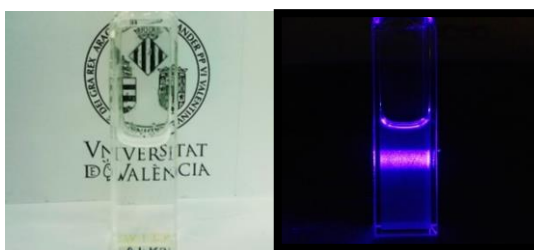


Figure 5. 2. Picture of toluene dispersion of $P_{\text{ODA}2}$ under the lab light (left) and UV-laser pointer excitation.

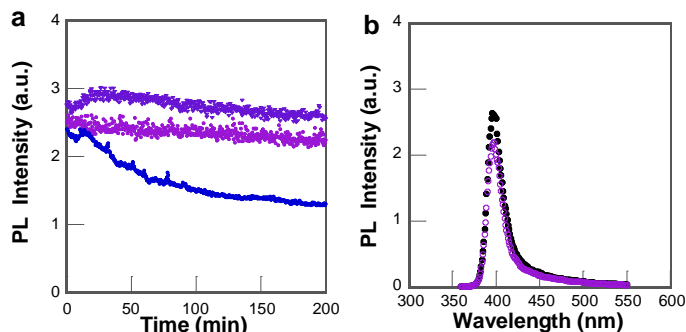


Figure 5. 3. Comparison of the PL intensity as a function of the irradiation time ($\lambda_{\text{exc}} = 330 \text{ nm}$) of $P_{\text{HA}2}$ (\blacksquare), $P_{\text{OA}2}$ (\blacktriangledown) and $P_{\text{ODA}2}$ (\blacklozenge) dispersed in toluene. b) PL emission spectra of $P_{\text{ODA}2}$ before (\bullet) and after (\circ) 240 minutes of UV irradiation.

5.3. Characterization of $(\text{RNH}_3)_2\text{PbBr}_4$ perovskites

The HRTEM images of the perovskites showed the formation of small nanoparticles coexisting with material forming plaques. The PXRD analysis, performed in collaboration with Dr. Guillermo Mínguez Espallargas, indicated the formation of highly crystalline perovskites with intense diffraction peaks ascribed to the (0 0 2l) reflections (figure 5.4), which appear at lower 2θ values as the alkyl chain of the ammonium cation increases. The diffraction pattern of the three perovskites fit to the orthorhombic phase model of the 2D inorganic framework $(\text{R-NH}_3)_2\text{PbBr}_4$; space group $Pbca$.^[96] The calculated unit cell lattice constants are described in table 5.2.^[87,88] The increase of the organic cations lengths does not alter the in-plane lattice parameters, a and b , however the interlayer spacing c increases linearly with increasing the alkyl chain length.^[13,95]

Table 5. 2. Calculated unit cell lattice constant of orthorhombic single-phase model of 2D $(\text{R-NH}_3)_2\text{PbBr}_4$ perovskites

$(\text{RNH}_3)_2\text{PbBr}_4$		Lattice parameters (\AA)		
		a	b	c
$P_{\text{HA}2}$	$(\text{HA})_2\text{PbBr}_4$	8.19243	8.22189	37.73297
$P_{\text{OA}2}$	$(\text{OA})_2\text{PbBr}_4$	8.19642	8.24638	42.34463
$P_{\text{ODA}2}$	$(\text{ODA})_2\text{PbBr}_4$	8.18840	8.27068	72.44761

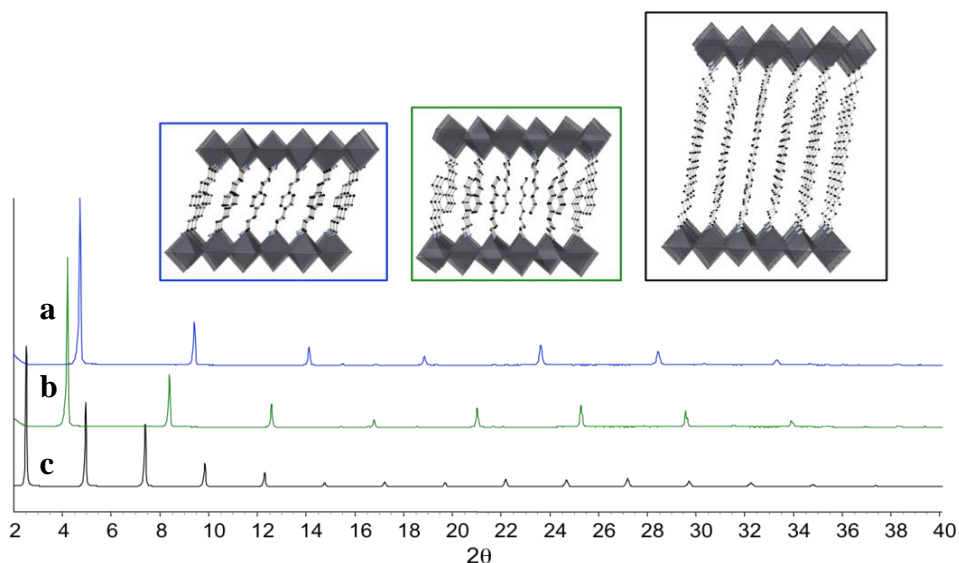


Figure 5. 4. PXRD pattern of a) P_{HA2} , b) P_{OA2} and c) P_{ODA2} . The top images are the schematic representations of the $(RNH_3)_2PbBr_4$ perovskites frameworks.

Further analysis of the composition of the $(RNH_3)_2PbBr_4$ perovskites were performed by using TGA and 1H NMR. The TGA heating curves and their corresponding first derivative of P_{ODA2} and P_{OA2} showed three weight losses before reaching i) 250 °C (41%), ii) 400 °C (35 %) and iii) 580 °C (20 %), figure 5.5. They were attributed to the organic ligand (the alkyl ammonium plus ODE), the ammonium in the perovskite framework and the lead bromide, respectively. This result in combination with the 1H NMR analysis of the perovskites (after their precipitation and purification) and their supernatant, indicated that the dispersible $(RNH_3)_2PbBr_4$ perovskites nanoparticles were capped with the ammonium salt and ODE, and that the perovskites nanoparticles were obtained with a chemical yield higher than 44 %.

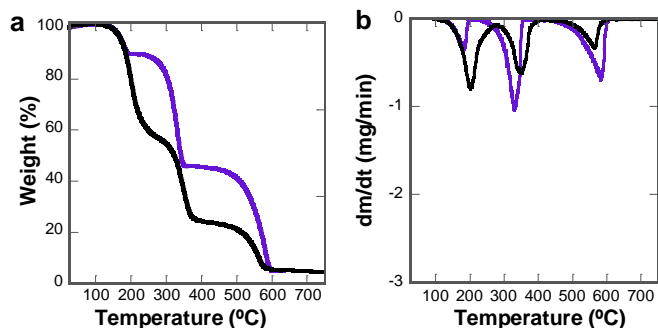


Figure 5. 5. Comparison of a) the TGA heating curves expressed as weight % as a function of temperature and b) their corresponding 1st derivatives of $P_{\text{ODA}2}$ (black) and $P_{\text{OA}2}$ (purple).

5.4. Processability of perovskites

In order to show the versatility of the $P_{\text{ODA}2}$, the perovskite was subjected to different processes as pictured in figure 5.6, without losing its optical properties. First, the stability of the colloidal $P_{\text{ODA}2}$ perovskite after three separation/redispersion in toluene was demonstrated, figure 5.6 (1 ↔ 2).

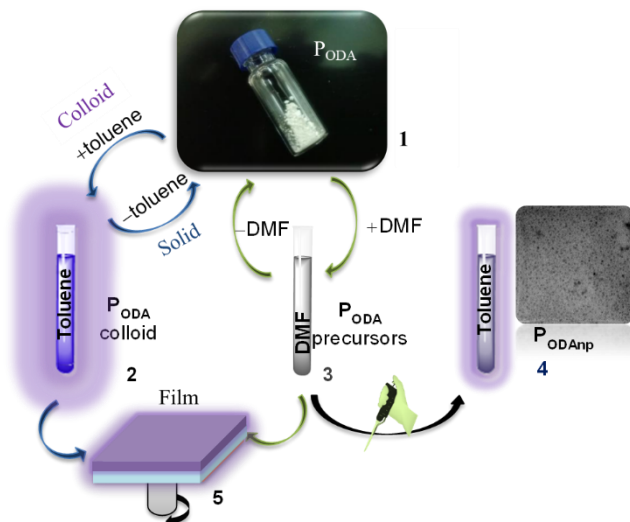


Figure 5. 6. Picture showing the processability of the $P_{\text{ODA}2}$ perovskite

We also demonstrated that $P_{\text{ODA}2}$ can be dissolved back to the precursor in dimethylformamide and then rebuilt after solvent evaporation (1 ↔ 3) or injection into toluene (3 → 4). In the latter case, the formation of nanoparticles increased and

the size of the plaques was smaller than 100 nm (see P_{ODA2nm} in figure 5.7). The colloidal P_{ODA2nm} exhibited a narrower PL emission peak at 396 nm (fwhm 10 nm) than P_{ODA2} (figure 5.7), but the PLQY was lower (7 %).

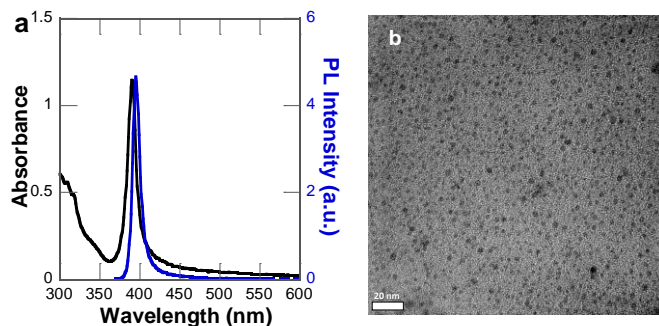


Figure 5. 7. Absorption (black) and PL emission (blue, $\lambda_{exc}= 330$ nm) spectra of P_{ODA2np} dispersion in toluene. b) HRTEM image (Scale bar = 20 nm).

Finally, perovskite films were prepared from the toluene dispersion of P_{ODA2} on a glass substrate was demonstrated (2→5). The thin film of P_{ODA2} showed narrow PL emission peak at 398 nm and PLQY of ca. 6 % (table 5.3). Similar features were obtained for a film prepared from a dissolution of P_{ODA2} back to the precursors in dimethylformamide (3→5) (see P_{ODA2np} table 5.3).

Table 5. 3. Photoluminescence data of $(RNH_3)_2PbBr_4$ perovskites films

Films	OA ^a (nm)	PL ^b (nm)	fwhm (nm)	PLQY (%)
P_{ODA1}	389	398	21	11.9
P_{ODA2}	389	398	19	5.8
P_{ODA2np}	390	403	22	6.3

^a Optical absorption maximum. ^bPL emission maximum ($\lambda_{exc}= 330$ nm).

5.5. Conclusions

In conclusion, we demonstrated the preparation of highly crystalline, blue photoluminescent and dispersible perovskite with 2D inorganic framework $(\text{RNH}_3)_2\text{PbBr}_4$ by using the non-template approach. The length of ammonium alkyl chain proved to be crucial not only in the 2D inorganic framework but also in the colloidal stability of the perovskite.

The 2D inorganic framework perovskite prepared with the longer ammonium cation, showed high dispersibility, photoluminescence (PLQY 20%) and photostability under continuous UV irradiation of the colloid. These materials proved to be easily processed and therefore of interest in optoelectronic devices.

5.6. Experimental section

Synthesis of dispersible perovskites. For the synthesis of $\text{P}_{\text{ODA}1}$, OLA (0.3 mmol) and 2 mL ODE (6.26 mmol) were stirred and heated at 80 °C. Then octadecylammonium bromide (ODABr, 0.2 mmol,) and lead bromide (0.10 mmol, 36.7 mg) dissolved in 200 μL of dimethylformamide were added. Finally, acetone (5 mL) was added to induce the precipitation of the nanoparticles.

The colloidal $\text{P}_{\text{ODA}2}$ nanoparticles were prepared following the procedure described for $\text{P}_{\text{ODA}1}$ but in the absence of OLA. The perovskite nanoparticles $\text{P}_{\text{HA}2}$ and $\text{P}_{\text{OA}2}$ were prepared following the procedure described for solid $\text{P}_{\text{ODA}2}$ but using HABr or OABr instead of ODABr and keeping the same molar ratios of the other components.

Preparation of perovskites by different solution processes. The films were prepared from perovskite nanoparticle dispersion (3 mg mL^{-1}) by spin-coating. The experiment of dis-assemble/assemble was carried out by dissolving $\text{P}_{\text{OA}2}$ back to the precursors in dimethylformamide in a concentration of 4 mg mL^{-1} , then 100 μL of this precursor solution was injected into toluene (4 mL), leading the immediately formation of a blue photoluminescent dispersion ($\text{P}_{\text{OA}2\text{nm}}$). Finally,

the film from the precursor solution was prepared by spin-coating on glass substrate.

Contribution of the Author

- **Gonzalez-Carrero, S.**; Espallargas, G. M.; Galian, R. E.; Pérez-Prieto, J., Blue-luminescent organic lead bromide perovskites: highly dispersible and photostable materials. *Journal of Materials Chemistry A* **2015**, 3 (26), 14039-14045.
Invited contribution of special issue “Perovskite Solar Cell”.
Impact Factor (JCR): 8.262, Quartile: Q1, Cited by: 46

***Chapter 6. Surface Engineering to Yield Highly
Luminescence $\text{CH}_3\text{NH}_3\text{PbBr}_3$ Perovskite
Nanoparticles and Dense Solid Films***

6.1. Introduction

As discussed in chapter 4, we demonstrated that crystalline $\text{CH}_3\text{NH}_3\text{PbBr}_3$ nanoparticles can be prepared with high dispersibility and photoluminescence (PLQY up to 83 %) by using the hot-injection method and medium alkyl chain ammonium ligands.^[89,97]

In 2015 Zhang et al.^[98] reported another interesting strategy for the preparation of highly photoluminescent $\text{CH}_3\text{NH}_3\text{PbBr}_3$ nanoparticles (PLQY of 70 %), termed as ligand assisted re-precipitation (LARP) method. This method consists in the injection of a precursor solution, composed by a mixture of $\text{CH}_3\text{NH}_3\text{Br}$, PbBr_2 and the organic ligands dissolved in a good solvent (e.g. polar solvent dimethylformamide), into a bad solvent (such as toluene) at room temperature, followed by the removal of large particles via centrifugation. Thus, $\text{CH}_3\text{NH}_3\text{PbBr}_3$ nanoparticles with an average diameter ca. 3 nm were prepared by using n-octylamine and oleic acid as ligands.^[98]

Soon after Rogach et al.^[99] demonstrated the size-tunability of the band gap of $\text{CH}_3\text{NH}_3\text{PbBr}_3$ nanoparticles by using the LARP strategy with slight modifications. Nanoparticles were prepared with an average size of 1.8 nm-3.6 nm and remarkably PLQY up to 93 %, using oleylamine and oleic acid as ligands and by varying the temperature of the toluene in the 0-60 °C range. The chemical yield of $\text{CH}_3\text{NH}_3\text{PbBr}_3$ nanoparticles by LARP method is limited due to the formation of bulk material in combination with the nanoparticles.

Encouraged by these results, our first objective was to reach the maximum in the emissive properties of the $\text{CH}_3\text{NH}_3\text{PbBr}_3$ nanoparticles as well as to prepare them with a high chemical yield.

Colloidal nanoparticles with such properties could be further used to prepare nanoparticles solid films. Bulk perovskite films are commonly prepared from their precursors by using a solution-processed technique. They are polycrystalline films with many grain boundaries, which may act as recombination centers, thus

hindering their performance in optoelectronic devices.^[100] Several strategies, such as passivation with different species (e.g chloride ions, pyridine and lead halides), as well as using excess of methylammonium iodide, have been reported to minimize the non-radiative recombination of perovskite films to achieve high efficient optoelectronic devices.^[100-104]

The use of perovskite nanoparticles colloids for films preparation, which are well passivated by ligands, could improve the morphology of perovskite films. The challenge was to retain their confined structures and properties into the nanoparticles solid film. In addition, the charge transport properties specially when are passivated with organic ligands was also a challenge. In this regard, we hypothesized that the organic ligand selected, besides providing an effective passivation of the nanoparticle surface, should i) provide them with a low tendency to aggregate, ii) enable their assembly in densely-packed solid films by inter-particle coupling and iii) be charge transport compatible.

To address these objectives, first the quasi-spherical shaped 2-adamantylammonium bromide (2ADBr) was chosen as the only organic ligand and the LARP method, with slight modifications based on our previous results, was adopted for the synthesis of the colloidal nanoparticles. The formation of cucurbit[7]uril-adamantylammonium host-guest complexes (2AD-CB) as ligands on the nanoparticle surface was also explored together with its effect on the optical properties and photostability of colloids under humid conditions.

The synthesis of $\text{CH}_3\text{NH}_3\text{PbBr}_3$ nanoparticles with 2AD as capping ligand resulted in the formation of outstandingly photoluminescent nanoparticles with a PLQY of 100 % (*Small* **2016**, *12*, 5245-5250). However, the nanoparticles manifested a considerable aggregation in solution and long-lived photoluminescence.

Additional ligand surface engineering using binary ligand systems composed of adamantylamine (ADA) and a short chain alkyl carboxylic acid was studied in order to reduce the tendency of the nanoparticles to aggregate in solution, with the

final aim of preparing densely-packed nanoparticles solid films with enhanced optical and electronic properties (*Journal of Materials Chemistry C* **2018**, *6*, 6771-6777).

The effect of the length of the alkyl carboxylic acid and shape of the ADA ligand on the synthesis and optical properties of highly dispersible $\text{CH}_3\text{NH}_3\text{PbBr}_3$ perovskite nanoparticles are described. Furthermore, the preparation as well as the optical and conductive characterization of nanoparticle solid films are included.

6.2. Efficient surface passivation of colloidal $\text{CH}_3\text{NH}_3\text{PbBr}_3$ perovskite nanoparticles

We attempted the synthesis of colloidal $\text{CH}_3\text{NH}_3\text{PbBr}_3$ perovskite through combination of: i) 2 adamantylammonium and ii) 2 adamantylammonium and cucurbit[7]uril (CB) as organic ligands (figure 6.1), using both the hot-injection and LARP method. Interestingly, the LARP yielded the most luminescent colloids. Briefly, the synthesis with 2AD was carried out by injection of a mixture of $\text{CH}_3\text{NH}_3\text{Br}$, 2ADBr and PbBr_2 in dimethylformamide into toluene while stirring at room temperature. After 1 h of stirring, the dispersion was purified by centrifugation and the precipitate was separated and dispersed in toluene. The optimal molar ratio between the perovskite precursors and the organic ligand $\text{CH}_3\text{NH}_3\text{Br}:2\text{ADBr}:\text{PbBr}_2$ was 1.2:0.8:1.0.

Strikingly, the $\text{CH}_3\text{NH}_3\text{PbBr}_3$ nanoparticles prepared with 2AD, labelled as P_{AD} (AD refers to 2-adamantylammonium) crested the summit in their emissive efficiency with a PLQY $\approx 100\%$. The PL emission peak was centered at 520 nm (fwhm 22 nm), figure 6.1.

Taking into the account the high binding affinity constant of CB portals for cations such as the 2-adamantylammonium cation ($K = 1.00 \pm 0.3 \times 10^{14} \text{ M}^{-1}$),^[105,106] colloidal nanoparticles were synthesized using the same condition described for P_{AD} but in the presence of CB. Interestingly, the nanoparticles, labelled as $\text{P}_{\text{AD-CB}}$, were dispersible in toluene and showed a PL peak maximum at 519 nm (fwhm 24 nm) and a PLQY of 89 % (figure 6.1, Table 6.1).

Table 6. 1. Photoluminescence data of P_{AD} and $\text{P}_{\text{AD-CB}}$ toluene colloids

P_{AD}	PL ^a (nm)	fwhm (nm)	PLQY ^b (%)	τ_1 ^c (ns)	τ_2 ^c (ns)	τ_3 ^c (ns)
P_{AD} Air	520	22	99	19.9 (76)	185.2 (20)	1082.0 (4)
P_{AD} N_2	520	24	99	23.1 (73)	205.0 (22)	1161.4 (6)
$\text{P}_{\text{AD-CB}}$ Air	519	24	89	23.3 (73)	201.5 (22)	1142.4 (5)
$\text{P}_{\text{AD-CB}}$ N_2	519	25	82	23.5 (74)	203.7 (21)	1233.7 (5)

^{a,b} Registered at λ_{exc} 340 nm. ^c % Contribution of the component to the total PL decay in brackets.

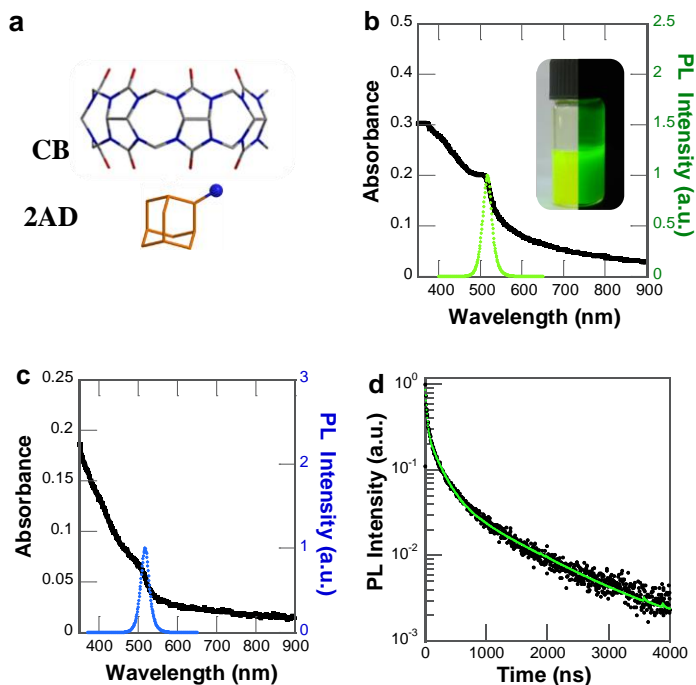


Figure 6. 1. a) Molecular structure of CB and 2AD compounds used as organic ligands of nanoparticles. Absorption and PL emission spectra of colloidal a) P_{AD} (inset: image of toluene dispersion) and c) P_{AD-CB} in toluene. d) Photoluminescence decay trace of P_{AD} in toluene.

Time-resolved photoluminescence spectroscopy analysis of the colloidal nanoparticles showed that the PL decay fitted to a tri-exponential function (figure 6.1), with a short-lived component of $\tau_1 \approx 20$ ns, attributed to charge carrier recombination, and two extraordinarily long-lived components (contribution of about 20 % and 5 % to the total PL). Likewise, long-lived components were obtained for P_{AD-CB} (table 6.1). Further studies were conducted in order to gain insight into the nature of the long-lived photoluminescence, see below.

The PXRD pattern of the nanoparticles was consistent with the crystalline cubic phase of $\text{CH}_3\text{NH}_3\text{PbBr}_3$ perovskite nanoparticles previously reported,^[5,98] figure 6.2. The diffraction peaks corresponding to the organic ligand 2AD were also observed (figure 6.2). The calculated crystalline sizes from the PXRD spectrum were 53 nm and 34 nm for P_{AD} and P_{AD-CB} , respectively.

The HRTEM images exhibited the formation of nanoplatelets (44 nm x 35 nm) unstable under the e-beam irradiation. Formation of spherical Pb nanoparticles after short exposure times to the electron beam was clearly observed, this was consistent with previous reports on perovskite instability.^[107]

Further analysis of the nanoparticles morphology was performed by using topographic AFM, figure 6.3. Large aggregates of nanoparticles were observed when a concentrated solution (2 mg/mL) of P_{AD} was used for the deposition. The aggregates were smaller using diluted solution of P_{AD} (50 fold). The height and the lateral size of the nanoplatelets was 21 nm and 60 nm, respectively. These size values were in agreement with those calculated in PXRD analysis.

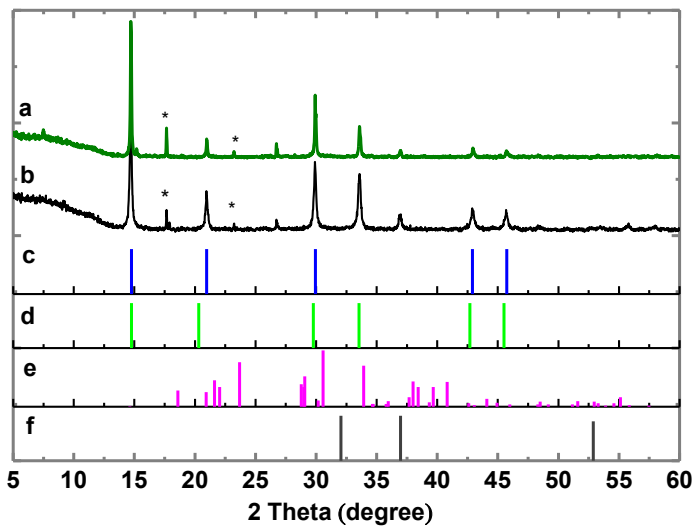


Figure 6. 2. Comparison of PXRD pattern of: a) P_{AD} and b) $\text{P}_{\text{AD-CB}}$. c,d) Reference lines for specified reflections derived from XRD patterns reported for $\text{CH}_3\text{NH}_3\text{PbBr}_3$ nanoparticles; e) lead bromide (PDF 05-0608) and f) metallic lead (PDF 00-003-1156). Signals corresponding to 2AD are marked with an asterisk.

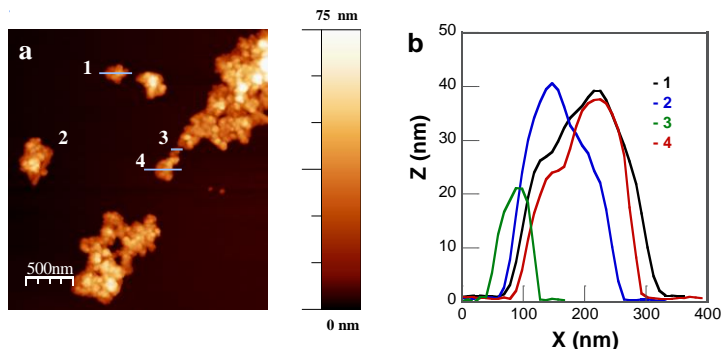


Figure 6. 3. a) Representative topographic AFM image of P_{AD} showing the presence of aggregates. b) Height profile of the aggregates identified in the horizontal lines inset AFM image (a).

The composition of the nanoparticles was studied by TGA and ^1H NMR. The inorganic component was determined by TGA. The molar ratio between the organic components in P_{AD} was calculated by dissolving the perovskite back to the precursors and then analyzing the mixture by ^1H NMR spectroscopy (see details in chapter 3). These studies revealed that molar ratio between the components $2\text{ADBr}:\text{CH}_3\text{NH}_3\text{Br}:\text{PbBr}_2$ in P_{AD} nanoparticles was 0.29:0.68:1.0. Moreover, indicated that nanoparticles were obtained in a high chemical yield (76 %).

Furthermore, the ^1H NMR analysis of P_{ADA-CB} nanoparticles after dissolution into the precursors showed that the 2AD/CB molar ratio was 6.83. The attachment of CB to the nanoparticle surface in P_{ADA-CB} was corroborated by ATR-FTIR and the spectrum was compared with those of CB, AD@CB and P_{AD} , figure 6.4. The strong band assigned to CB $\nu_{\text{as}}(\text{C}=\text{O})$ shifted to higher values in P_{AD-CB} (1734 cm^{-1} vs 1710 and 1716 cm^{-1} for CB and AD@CB). This is indicative of the interaction of the CB with the nanoparticle surface through the carbonyl groups.^[108]

The photostability of the colloidal perovskites were studied by measuring the evolution of its PL intensity as a function of the irradiation time using fluorimeter lamps as the irradiation source ($\lambda_{\text{exc}} = 350\text{ nm}$), figure 6.5. A decrease of ca. 25%

on the PL intensity was observed for P_{AD} after 180 min irradiation. This result indicated that, although the quasi-spherical shaped 2AD ligand allows the perovskite nanoparticles to reach the maximum emission efficiency; it cannot stop the photodarkening process, which has been associated with the presence of water in the environment.

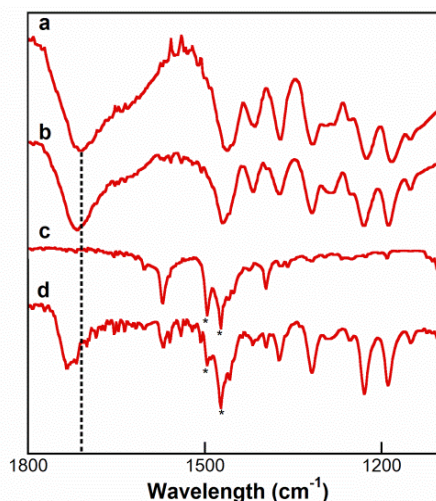


Figure 6. 4. Comparison between the ATR-FTIR spectra of: a) CB, b) 2AD@CB, c) P_{AD} and d) $\text{P}_{\text{AD-CB}}$. The dotted line represent the band assigned to CB ν_{as} ($\text{C}=\text{O}$). The signals corresponding to the remaining hexane are marked with an asterisk (*).

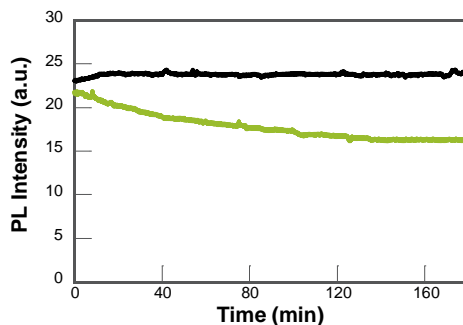


Figure 6. 5. PL intensity as a function of the irradiation time of colloidal P_{AD} (\blacklozenge) and $\text{P}_{\text{AD-CB}}$ (\blacksquare) dispersed in aerated toluene ($\lambda_{\text{exc}}=340$ nm, $\lambda_{\text{em}} = 520$ nm).

Notably, colloidal $\text{P}_{\text{AD-CB}}$ showed an initial photoactivation stage, leading to a slight enhancement of the PL intensity (up to 4 %) in the first 20 min, and then

the PL intensity remained unaltered during the following 160 min (figure 6.5). Moreover, after 24 h of irradiation their PL intensity only decreased 13%. This improved photostability suggests that CB reduces the efficiency of the moisture effect. Remarkably, the colloidal $\text{P}_{\text{AD-CB}}$ showed higher stability than P_{AD} when exposed to direct contact with water and under continuous UV irradiation (figure 6.6).

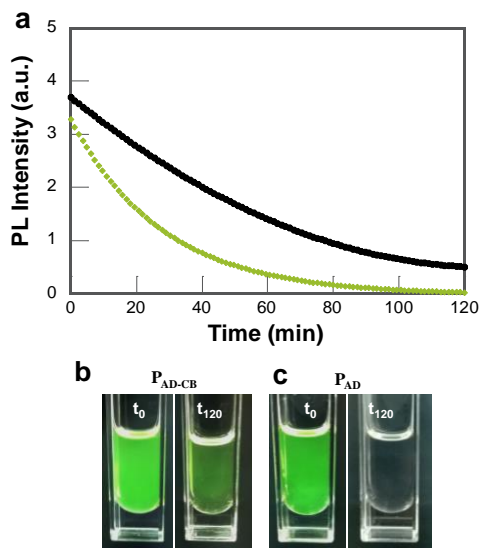


Figure 6. 6. a) PL intensity as a function of the irradiation time of colloidal $\text{P}_{\text{AD-CB}}$ (■) and P_{AD} (◆) in toluene and in contact with water ($\lambda_{\text{exc}} = 350 \text{ nm}$, PL registered at 520 nm under air atmosphere); b,c) Images of $\text{P}_{\text{AD-CB}}$ and P_{AD} colloidal dispersions immediately after addition of water (left) and 120 min afterward (right).

6.3. Photoluminescence lifetime and nanoparticle aggregation effect

Although the 2AD organic ligand improved the photoluminescent properties up to 100 % it induced a considerable aggregation of the nanoparticles, as was demonstrated by AFM images. Such aggregation affected their optical properties, specifically the PL lifetime, which was extraordinarily long (table 6.1).

Therefore, additional centrifugation/separation steps of the P_{AD} nanoparticles were conducted. The PL features of the precipitates obtained after the

centrifugation (termed as P_1 and P_2) and that of the supernatant (S_{P2}) were analysed, figure 6.7. The absorption and PL emission peaks of the colloidal nanoparticles preserved after the centrifugation/separation process (PL maximum at 521-523 nm) and their PLQY was higher than 90 %, indicating the high stability of the nanoparticles prepared with 2AD. However, the longest-lived component decreased (up to 5 times) compared to those of the initial P_{AD} (table 6.1) but the PL lifetime was still quite long (ca. 200 ns) in comparison with the few nanoseconds expected for the direct band gap recombination of semiconductors.

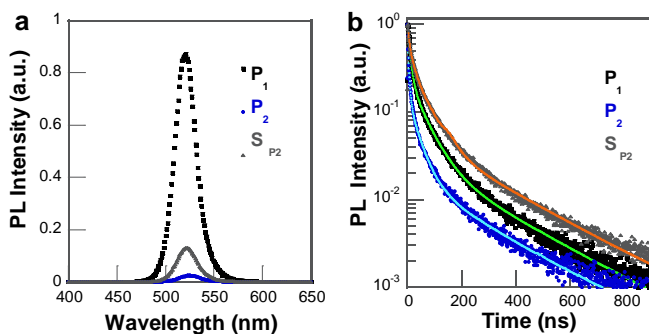


Figure 6. 7. b) PL emission spectra and c) PL decay traces of P_{AD} precipitate (P_1) obtained after centrifugation of the initial dispersion at 3000 rpm for 5 min, (ii) the precipitate obtained after centrifugation of supernatant at 9000 rpm for 10 min (P_2) and (iii) the final supernatant (S_{P2}). The decay traces were registered using $\lambda_{exc} = 340$ nm, $\lambda_{em} = 521$ nm for P_1 and S_{P2} and 523 nm P_2 .

6.4. Surface engineering

To address the preparation of uniform and highly photoluminescent dense solid film from perovskite colloids it is imperative to use highly luminescent but non-aggregated colloidal nanoparticles. The $\text{CH}_3\text{NH}_3\text{PbBr}_3$ perovskite nanoparticles with 2-adamantylammonium as capping ligand resulted in the formation of strongly luminescent nanoparticles (PLQY ca. 100 %).^[109] Nevertheless, a considerable aggregation in solution was observed, indicating the low capacity of the capping to provide the required steric hindrance between the nanoparticles, attributed to the Van der Waals attraction between adamantyl moieties.^[110-112]

Surface engineering of the extraordinary emissive P_{AD} nanoparticles was then directed towards decreasing their aggregation tendency in solution by interfering slightly in their interaction. To this aim the use of binary ligand systems consisting of an adamantylamine (ADA) and alkyl chain carboxylic acid was explored.

First, the effect of the binary ligand system in the optical properties of colloidal nanoparticles was studied. The organic ligands selected were: i) the amines 1-adamantylamine (1ADA) and 2-adamantylamine (2ADA) and ii) linear alkyl carboxylic acids with 3, 6, 8, 10 and 18 carbon atoms, and the branched isobutanoic acid and 1-adamantanecarboxylic acid, figure 6.8.

This combination of the two types of organic ligands allowed the study of the effect of the adamantylamine shape and the length of the alkyl carboxylic acid on the colloid stability and the optical properties of the nanoparticles. The synthesis of the nanoparticles was carried out following a similar procedure to that described previously for P_{AD} . In short, a dimethylformamide precursor solution containing PbBr_2 , $\text{CH}_3\text{NH}_3\text{Br}$, 1ADA (or 2ADA) and the alkyl carboxylic acid in a molar ratio of 1.0:1.1:0.8:9.5 respectively, was injected dropwise into toluene while stirring. The green photoluminescent dispersion provided a solid after centrifugation. The final solid was easily dispersed in toluene.

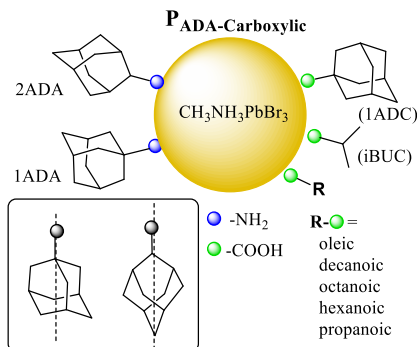


Figure 6. 8. Schematic representation of $\text{CH}_3\text{NH}_3\text{PbBr}_3$ nanoparticles capped with ADA and carboxylic acid

The optical properties of the colloidal nanoparticles (P_{ADA}-carboxylic acid) are summarized in tables 6.2 and 6.3 for 1-ADA and 2ADA ligands, respectively. All the colloidal nanoparticles synthesized showed a crystalline structure that fit to the cubic phase of $\text{CH}_3\text{NH}_3\text{PbBr}_3$ perovskite. The colloidal nanoparticles prepared with 1ADA and alkyl carboxylic acids as ligands exhibited PL emission maximum between 521 nm and 526 nm (fwhm 27 nm) and PLQY up to 87 % (table 6.2). Moreover, the colloids prepared with 2-ADA and alkyl carboxylic acids as the binary ligand system exhibited PL emission peak at shorter wavelength than 521 nm and a remarkable high PLQY (ca. 100 %), figure 6.9 and table 6.3.

Table 6. 2. Photoluminescence data of $\text{CH}_3\text{NH}_3\text{PbBr}_3$ colloidal nanoparticles prepared with 1-ADA and alkyl carboxylic acids.

Amine	Carboxylic Acid	PL ^a (nm)	fwhm (nm)	PLQY (%)	τ_{av} ^{b,c} (ns)
1	Oleic acid	521	24	87	30
2	Decanoic acid	523	24	81	47
3	Octanoic acid	523	23	85	116
4	Hexanoic acid	525	22	82	93
5	Isobutanoic acid	526	22	78	181
6	Propanoic acid	526	22	66	125
7	1-Adamantanecarboxylic acid	522	23	72	78

^a PL emission peak maximum. ^b Average photoluminescence lifetime; ^c the PL decays were registered at the PL peak maximum and fitted with a triexponential function of time. The PL spectrum, PLQY and τ_{av} were registered using $\lambda_{\text{exc}} = 365$ nm.

Table 6. 3. Photoluminescence data of $CH_3NH_3PbBr_3$ colloid prepared with 2ADA and alkyl carboxylic acids.

Amine	Carboxylic Acid	PL ^a (nm)	fwhm (nm)	PLQY (%)	$\tau_{av}^{b,c}$ (ns)
8	Oleic acid	518	26	94	32
9	Decanoic acid	521	26	94	76
10	Octanoic acid	517	26	98	34
11	Hexanoic acid	519	27	96	40
12	Isobutanoic acid	519	27	95	50
13	Propanoic acid	516	27	98	33
14	1-Adamantanecarboxylic acid	516	26	97	41

^a PL emission peak maximum. ^b Average photoluminescence lifetime; ^c PL decays were registered at the PL peak maximum and fitted with a triexponential function of time. The PL spectrum, PLQY and τ_{av} were registered using $\lambda_{exc} = 365$ nm.

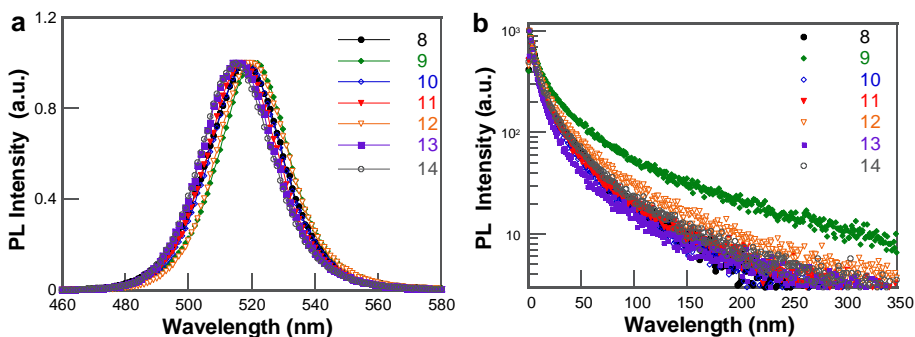


Figure 6. 9. a) PL emission spectra and b) PL kinetic decay traces of $CH_3NH_3PbBr_3$ nanoparticles capped with 2ADA and carboxylic acid. See details in table 6.3.

Interestingly, the $P_{ADA-carboxylic\ acid}$ exhibited an extraordinary shorter average PL lifetime (τ_{av}) than of P_{AD} (section 6.2). The τ_{av} of the colloidal nanoparticles using 1ADA varied from 30 ns to 182 ns, with oleic acid and the branched acid isobutanoic acid, respectively. No trend was observed with the alkyl chain length of the carboxylic acid used.

Moreover, shorter τ_{av} were observed with 2ADA. The nanoparticles prepared with oleic, octanoic and propionic acid (τ_{av} of 30 ns, 34 ns and 33 ns, respectively), proved to be the most effective alkyl carboxylic acid to provide additional colloidal stability and reduce the aggregation of the nanoparticles in solution.

These findings demonstrated the positive synergy between the carboxylic acid and 2ADA ligand: while the 2ADA steric hindrance enables a good passivation of the nanoparticle surface, thus reaching the high PLQY of P_{AD} (section 6.2), the anchored carboxylic acid impedes the aggregation of the nanoparticles in solution.

The $\text{CH}_3\text{NH}_3\text{PbBr}_3$ nanoparticles prepared with the shortest alkyl-chain carboxylic acid, propionic acid, showed the desired photophysical features for the preparation of nanoparticles solid film here proposed, i.e. high PLQY (98%), short τ_{av} (33 ns) and the PL emission peak at about 516 nm (fwhm of 27 nm). Therefore, these nanoparticles, labelled as $\text{P}_{2\text{ADA-Propionic}}$ (2ADA-propionic refers to the binary ligand system) were fully characterized.

The size of $\text{P}_{2\text{ADA-Propionic}}$ nanoparticles was estimated by SEM images as about 22 nm. The TEM analysis was limited due to the instability of the nanoparticles under the electron beam irradiation, as has previously been described.^[109,113]

The interaction of the organic ligand with the nanoparticles surface and the stoichiometry was studied by XPS. Figure 6.10 shows the XPS core-level spectra of Pb 4f, Br 3d, N1s, O 1s and C 1s. The XPS spectrum of Pb 4f shows two peaks at 138.1 eV and 143.0 eV attributed to Pb 4f_{7/2} and Pb 4f_{5/2}, respectively.^[97,114] The XPS spectrum of Br 3d shows two peaks centered at 67.9 eV and 69 eV corresponding to the inner and surface Br anions.^[98,115] The N 1s spectrum has two peaks centered at 399.8 eV and 401.5 eV, which can be ascribed to 2ADA and methylammonium cation, respectively.^[97,116]

Moreover, the O 1s spectrum exhibits three peaks. The typical band at 530.0 eV together with two peaks at higher energies (figure 6.10d). The peak at 531.8 eV ascribed to two non-equivalent oxygen atoms of the carboxylic acid and the peak at 533.4 eV attributed to the two chemically equivalent oxygen atoms of the carboxylate species.^[97] The C 1s XPS spectrum also shows three peaks, the peak at 284.6 eV assigned to C-C and C-H bonds, the peak at 285.9 eV assigned to the C-N bond of the amine and the C-O bond of the carboxylic acid. Finally, the peak

at 288.4 eV can be assigned to the C=O bond of the carboxylic acid.^[117] These results revealed the presence of amine and carboxylic acid on nanoparticles surface and confirmed that the 2ADA and propionic acid act as binary ligand system. The quantification of the perovskite components by XPS showed that the atomic ratio of Br:Pb and N:Pb was 2.7 and 1.1, respectively.

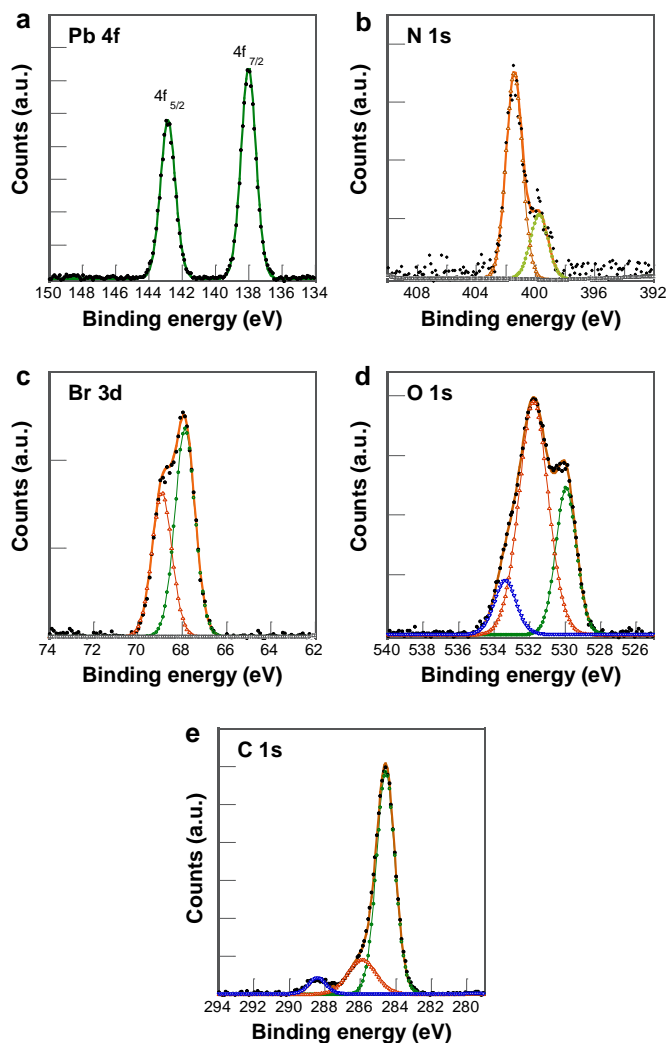


Figure 6. 10. XPS spectra corresponding to: a) Pb 4f; b) Br 3d; c) N 1s, d) O 1s and e) C 1s of $\text{P}_2\text{ADA-Propionic}$ nanoparticles.

6.5. Delayed luminescence

Similar to II-VI semiconductors quantum dots (QDs), such as CdSe, the HOIP nanoparticles have shown outstanding properties such as wide absorption spectrum, narrow emission peak and high absorption coefficients. Moreover, their optical properties are tunable with the composition and size of the nanoparticles.^[99,118,119]

The HOIP nanoparticles exhibits high PLQY, up to 100 % for $\text{CH}_3\text{NH}_3\text{PbBr}_3$ nanoparticles.^[109] Contrary to conventional semiconductors, the high PLQY are reached without electronic passivation with wider band gap inorganic materials, as it is required for CdSe semiconductor. This feature, termed *defect-tolerance*, have been attributed to the formation of shallow defects, which are not recombination active, near a band edge, figure 6.11.^[34,120] In a conventional *defect-intolerant* semiconductor, the intrinsic defects are deep in the middle of the gap and they trap carriers and quench the semiconductor photoluminescence.

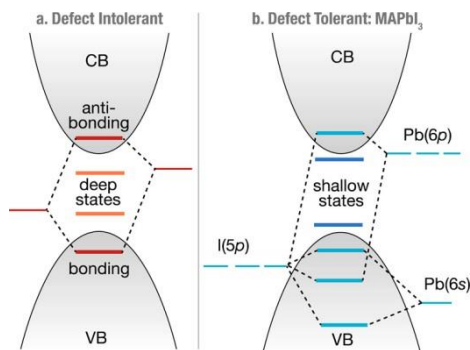


Figure 6. 11. Schematic representation of a) the electronic structure of typical III–V, II–VI, or group IV semiconductors, b) compared to the lead halide perovskite crystal structure. Reprinted with permission from ref^[120] Copyright 2017 American Chemical Society.

Direct gap semiconductor nanoparticles with high absorption coefficient, such as CdSe and HOIP, should exhibit a short luminescence lifetime, in the order of few nanoseconds.^[121] However, CdSe and HOIP nanoparticles exhibit lifetimes of a few tens of nanoseconds.

Chirvony, V. S et al.,^[122] in collaboration with our research group, studied the excitation deactivation processes in $\text{CH}_3\text{NH}_3\text{PbBr}_3$ nanoparticles in order to understand the long-lived photoluminescence for this material. To this end, the $\text{CH}_3\text{NH}_3\text{PbBr}_3$ perovskite nanoparticles capped with adamantylammonium with a PLQY ca. 100 % (see section 6.2) were investigated.

Interestingly, it was found that the PL decay kinetics of the $\text{CH}_3\text{NH}_3\text{PbBr}_3$ perovskite nanoparticles was temperature independent in the 20-300 K range and it consisted of a minor component with a lifetime of 2 ns, attributed to the prompt-luminescence and a long-lived component of around 20 ns, ascribed to a delayed luminescence, both with the same photoluminescence spectra. The later was a result of a fast multiple trapping and detrapping of excited carrier by shallow traps combined with a slower release back to the conduction band, see scheme in figure 6.12.

In this model, termed as *delayed luminescence model* by the authors, the 0 , I and T states correspond to the valence band edge, the excitonic state and the trap state, respectively. The model describes the delayed luminescence of nanoparticles as a charge-carrier trapping/detrapping process, in which k_{I0} is the rate of the spontaneous radiative recombination of excitons and k_{T0} corresponds to the trap mediated non-radiative recombination of excitons, while k_{IT} and k_{TI} are the rate constant that describe the circular trapping–detrapping of electrons, respectively.

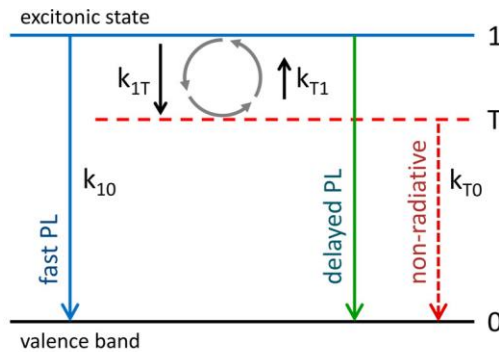


Figure 6.12. Energy diagram describing the delayed luminescence mechanism. Reprinted with permission from ref. ^[122] Copyright (2017) American Chemical Society

The delayed luminescence is the emission by spontaneous recombination of a multiple trapping–detrapping processes (gray arrows in figure 6.12). The condition for the formation of long-lived PL decay kinetics within the proposed scheme is that $k_{1T} \gg k_{10}, k_{T0}$. Because of the high PLQY of the nanoparticles studied, the contribution of k_{T0} is negligible, that means that all trapped carrier return back to the excitonic state and recombine radiatively. Therefore, the traps act as carrier storages during long times (up to tens of nanoseconds), in which the dark states (traps) and bright excitonic states are in dynamic equilibrium, resulting in a long-lived emission.^[122]

The temperature independent PL decay kinetics are ascribed to a continuous distribution of trap states. Within the proposed model, the factor responsible for the delayed PL kinetics is the ratio between the trapping and detrapping rate constants, k_{1T} and k_{T1} , which are related by the Boltzmann factor. The ratio k_{1T}/k_{T1} will remain unchanged if the temperature decrease is accompanied by a corresponding decrease of the energy difference (ΔE) between the excitonic (1) and trap (T) states.

6.6. $\text{CH}_3\text{NH}_3\text{PbBr}_3$ nanoparticle solid films

6.6.1 Preparation of the nanoparticle solid films

The preparation of films from nanoparticles in suspension has been accomplished by using different strategies, such as drop-casting and spin-coating. The challenge is to obtain uniform and defect free films. Though nanoparticles of CdSe and PbSe have been self-assembled successfully into thick films,^[123,124] the same has been considerably less studied for hybrid perovskites.

We attempted the preparation of dense nanoparticles solid film from $\text{P}_{\text{ADA-carboxylic acid}}$ nanoparticles by using the centrifugal casting technique, which take advantage of the centrifugal acceleration to distribute and cast the material onto a large surface.^[83,125,126] Briefly, the substrate was placed at the bottom of a conic centrifuge tube; then, a freshly-prepared $\text{P}_{2\text{ADA-propionic}}$ colloid in toluene was added and centrifuged. Thus colloidal nanoparticles started to settle and assemble on the substrate. Finally, the supernatant solvent was removed and the film was dried under toluene atmosphere.

This technique permitted significant control over the uniformity and the thickness of the nanoparticles solid films by adjusting the concentration of the colloid. Figure 6.13 shows the cross-sectional SEM images of the films prepared at different concentrations (25, 50, and 100 % v/v) of $\text{P}_{2\text{ADA-propionic}}$ colloids, labelled as P_{film1} , P_{film2} and P_{film3} (the number 1,2,3 indicated increasing concentration). Interestingly, the SEM images demonstrated the formation of densely-packed nanoparticle solid films of increasing thickness of 260 ± 30 nm, 396 ± 28 nm, and 670 ± 44 nm for P_{film1} , P_{film2} and P_{film3} , respectively.

Figure 6.14 shows the UV-Vis absorption and PL spectra of the as-prepared nanoparticles solid films. The films exhibited narrow PL emission peaks between 527 nm and 529 nm (fwmh 26-28 nm), high PLQY (up to 80 %) and short average lifetime, which only changed from 33 ns (colloidal nanoparticles) to 52 ns for P_{film1} , table 6.4.

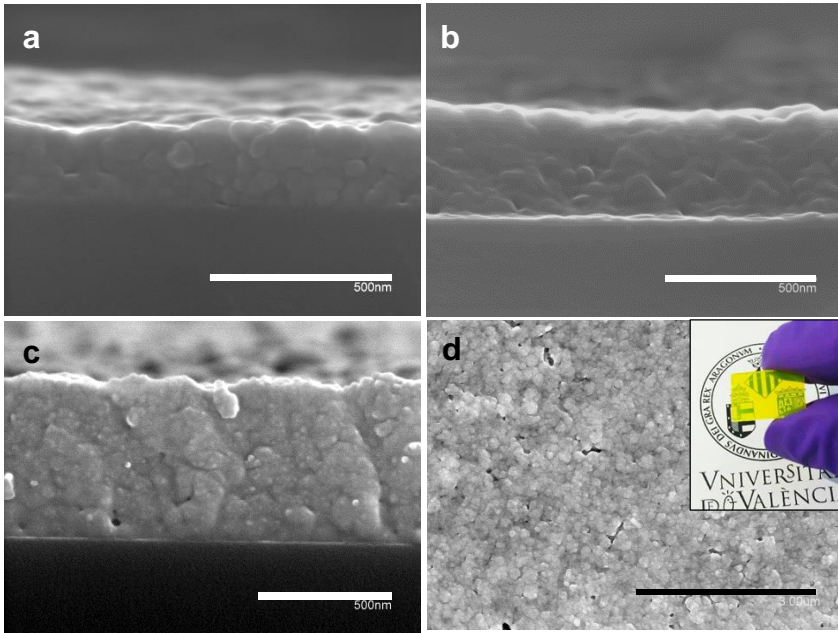


Figure 6. 13. a-c) Cross-sectional SEM images of $\text{P}_{2\text{ADA-Propanoic}}$ nanoparticle solid films on glass substrate with different thicknesses: a) P_{film1} , b) P_{film2} and c) P_{film3} (scale bar= 500 nm). d) Top view SEM image of P_{film1} (Scale bar = 3 μm), inset: image of nanoparticle solid film.

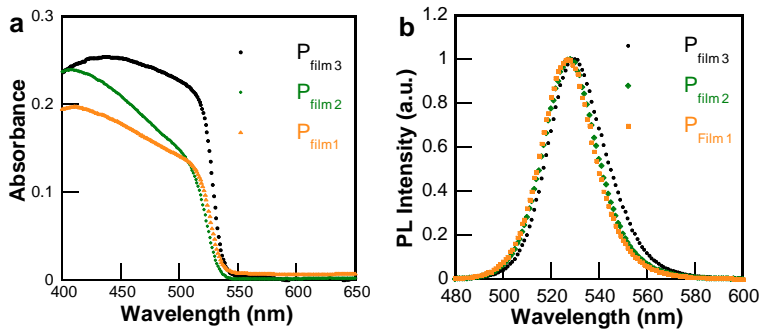


Figure 6. 14. a) Absorption and b) normalized PL spectra of $\text{P}_{2\text{ADA-Propanoic}}$ films

Further composition analysis of the nanoparticle solid film P_{film1} was performed by energy dispersive X-ray spectroscopy (EDS), which showed a Br:Pb average atomic ratio of 3.1. Moreover, the XRD pattern confirmed the formation of crystalline nanoparticle solid film that fit to the cubic phase of $\text{CH}_3\text{NH}_3\text{PbBr}_3$.^[52]

Table 6. 4 Photoluminescence data of the $\text{P}_{2\text{ADA-propanoic}}$ colloids and nanoparticle solid films

	Thickness (nm)	PL ^a (nm)	fwhm (nm)	PLQY	τ_{av} ^{b,c} (ns)
$\text{P}_{2\text{ADA-Propanoic}}$		516	27	0.98	33
P_{film1}	260	527	26	0.80	52
P_{film2}	396	528	26	0.72	58
P_{film3}	670	529	28	0.53	93

^a PL emission peak maximum ^b Average photoluminescence lifetime; ^c PL decays were registered at the PL peak maximum and fitted with a tri-exponential function of time. The PL spectrum, PLQY and τ_{av} were registered using $\lambda_{\text{exc}} = 365$ nm.

6.6.2 Conductive properties of $\text{CH}_3\text{NH}_3\text{PbBr}_3$ nanoparticle solid films

We then turned to perform a preliminary study on the charge transport properties of the nanoparticles solid films. In a first approach, a multi-layer diode was fabricated in collaboration with Dr. Michele Sessolo. The layer architecture of the device was: ITO/PEDOT:PSS/nanoparticle solid P_{film1} /BmPyPhB/Ba/Ag. The electrical characteristics revealed a high-quality diode, with a low leakage current and a moderate electroluminescence (about 20 cd/m^2 , turn-on about 2V). This means that both electrons and holes are injected into, and transported within, the nanoparticle solid film.

The moderate electroluminescence can be attributed to a non-optimal device configuration, i.e. lack of the electron blocking layer in between PEDOT:PSS and the perovskite, or to spatial inhomogeneities on the perovskite morphological and optoelectronic properties. Accordingly, conductive atomic force microscopy (c-AFM) analysis was carried out to further investigate the topography and local electronic properties of a nanoparticles solid film. Thus the nanoparticle solid film on a conductive ITO-coated glass ($\text{P}_{\text{film1}^*}$) was prepared with a thickness of 291 ± 18 nm (see figure 6.15). The c-AFM measurements were carried out in the dark using the conventional contact mode (chapter 3).

The topographic image of the $\text{P}_{\text{film1}^*}$ (area $25 \mu\text{m}^2$) showed protrusions and depressions in the film morphology (range of ± 80 nm), with a RMS of about 25

nm, figure 6.16. Similar RMS values have been reported for PbSe quantum dot films (RMS of 19 nm) of a similar thickness.^[124] The conductive image of the same area, revealed low conductive regions and high conductive domains, with a maximum current magnitude of 100 pA on the brighter domains (figure 6.16). Such results suggested that the spatial inhomogeneity observed in film probably hinders the charge carrier distribution within the diode, thus leading to an inefficient electroluminescence.

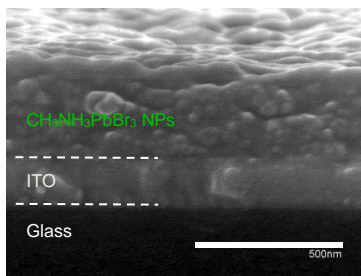


Figure 6. 15. Cross-sectional SEM image of nanoparticle solid $P_{\text{film}1^*}$ showing each layer (scale bar 500 nm).

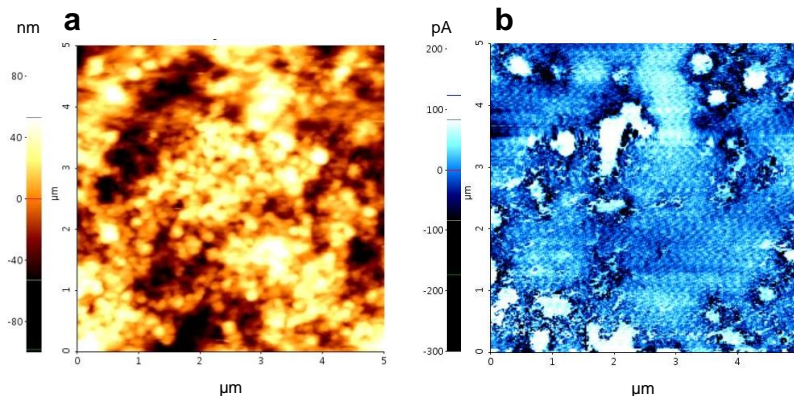


Figure 6. 16. a) Topographic and c) conductive AFM images of nanoparticle solid $P_{\text{film}1^*}$ obtained at a bias voltage (-3.5 V) in the dark. AFM image scale: $5 \mu\text{m} \times 5 \mu\text{m}$.

Despite the spatial inhomogeneity, the high conductive domains observed in the nanoparticle solid film support the formation of high-density regions of nanoparticles with an efficient connectivity between them. This can be related to the unique properties of the adamantyl moiety, in particular to the strong ADA-

ADA interactions, which minimize the inter-particle distance and improve the assembly of the nanoparticles in the film. These results are promising and we envisage that the interparticle connectivity on the thick nanoparticle solid film here studied could be further improved by improving the procedure of the film preparation.

6.7. Conclusions

In summary, we demonstrated that the surface passivation of the $\text{CH}_3\text{NH}_3\text{PbBr}_3$ nanoparticles by using 2-adamantylammonium bromide as the only capping ligand results in an effective surface trap passivation, allowing the exceptional photoluminescence quantum yield of 100 %. Moreover, the colloidal nanoparticles were prepared with high chemical yield and colloidal stability, keeping their stability after six months at room temperature.

The photostability studies showed that the 2-adamantylammonium capped nanoparticles experiment a considerable photodarkening effect under continuous UV irradiation in solution. The capacity of the adamantyl moiety to form supramolecular system with cucurbit[7]uril portal demonstrated the enhancement of the nanoparticles photostability even under the drastic conditions of direct contact with water and under continuous UV irradiation.

Although the adamantylammonium organic ligand improved the photoluminescent properties of nanoparticles, a considerable aggregation in solution and as a consequence an extraordinarily long-lived photoluminescence was observed. The surface engineering by using 2-adamantylamine and different alkyl carboxylic acids as a binary ligand systems enabled the preparation of highly dispersible and photoluminescent $\text{CH}_3\text{NH}_3\text{PbBr}_3$ colloids, with a photoluminescence quantum yield of ca. 100 % and shorter photoluminescence lifetime. These properties proved the good passivation of the nanoparticle surface and the low tendency of nanoparticles to aggregate, mainly when using a short alkyl chain carboxylic acid.

The optimal $\text{CH}_3\text{NH}_3\text{PbBr}_3$ nanoparticles colloid was that with a short carboxylic acid, namely propionic acid, and they were successfully assembled into densely packed solid films with thicknesses up to several hundreds of nanometers. The films retained the pre-engineered confined morphologies as well as their optical properties, in particular a high photoluminescence quantum yield (up to 80 %), and showed good charge transport properties.

6.8. Experimental section.

The colloidal nanoparticles described in section 6.2 were prepared as follows:

Synthesis of P_{AD} nanoparticles. First, concentrated solutions of 2-adamantylammonium bromide (2ADBr, 0.043 M), methylammonium bromide ($\text{CH}_3\text{NH}_3\text{Br}$, 0.089 M) and lead bromide (0.027 M) were prepared in dimethylformamide. Then, a precursor solution was prepared by mixing 2ADBr (50 μL , 2.18 μmol), $\text{CH}_3\text{NH}_3\text{Br}$ (37 μL , 3.24 μmol) and lead bromide (100 μL , 2.7 μmol) in dimethylformamide and stirred for 15 minutes. The final molar ratio between all components $\text{CH}_3\text{NH}_3\text{Br}$:2ADBr:PbBr₂ was 1.2:0.8:1.0.

This precursor solution was dropped into toluene (5 mL) and stirred at room temperature for 1 hour. Finally, the strong green photoluminescent dispersion was centrifuged (7000 rpm; 6300 g) at 20 °C for 4 minutes and the solid obtained was dispersed in toluene.

Synthesis of P_{AD-CB} nanoparticles. The nanoparticles were prepared following the procedure described for P_{AD} , except that after stirring the precursor solution for 15 minutes, CB (0.18 μmol , dissolved in dimethylformamide) was added (molar ratio 2ADBr:CB = 12:1), and then the mixture was stirred during 30 minutes before it was dropped into toluene

Variation in the separation method of P_{AD} nanoparticles. Colloidal P_{AD} perovskites were centrifuged at 3000 rpm at 20 °C for 5 minutes and the precipitate (P_1) was separated. The supernatant was centrifuged at 9000 rpm at 20 °C for 10 minutes, leading to a new precipitate (P_2) and supernatant (S_{P_2}). The

precipitates (P_1 and P_2) were dispersed in toluene and maintained as colloidal dispersions.

The colloidal nanoparticles described in section 6.4 were prepared as follows:

Synthesis of $\text{P}_{2\text{ADA-propionic}}$ nanoparticles. The precursor solution was prepared by mixing lead bromide (50 mg, 0.136 mmol), $\text{CH}_3\text{NH}_3\text{Br}$ (18 mg, 0.160 mmol), 2-adamantylamine (2ADA, 16.4 mg, 0.108 mmol) and propionic acid (97 μL , 1.30 mmol) in 5 mL of dimethylformamide. The $\text{PbBr}_2:\text{CH}_3\text{NH}_3\text{Br}:2\text{ADA}:\text{propionic acid}$ molar ratio was 1.0:1.1:0.8:9.5. Then, 100 μL of precursor solution was injected into toluene (5 mL) while stirring. The unreactive material was separated by centrifugation at 7000 rpm (6,300 g) at 20 °C for 7 minutes. The solid obtained was dispersed in toluene (5 mL) and maintained as colloidal dispersion.

The colloidal nanoparticles comprising a different carboxylic acid as ligand were prepared following the same procedure described for $\text{P}_{2\text{ADA-propionic}}$, but replacing the propionic acid with the corresponding alkyl carboxylic acid (table 6.3), preserving the molar ratio between the reagents.

The colloidal nanoparticles comprising 1-adamantylamine and different alkyl carboxylic acid as ligands were prepared following the procedure described for $\text{P}_{2\text{ADA-propionic}}$ but using 1-adamantylamine and the corresponding alkyl carboxylic acid (table 6.2) preserving the molar ratio between the reagents.

Preparation of nanoparticle solid films. The procedure for the preparation of nanoparticle solid films, and the techniques used for the conductive characterization are described in chapter 3

Contribution of the author:

- **Gonzalez-Carrero, S.;** Francés-Soriano, L.; González-Béjar, M.; Agouram, S.; Galian, R. E.; Pérez-Prieto, J., The Luminescence of $\text{CH}_3\text{NH}_3\text{PbBr}_3$ Perovskite Nanoparticles Crests the Summit and Their Photostability under Wet Conditions is Enhanced. *Small* **2016**, *12* (38), 5245-5250.
Impact Factor (JCR): 8.643, Quartile: Q1, Cited by: 27
- **Gonzalez-Carrero, S.;** Martínez-Sarti, L.; Sessolo, M.; Galian, R. E.; Pérez-Prieto, J., Highly photoluminescent, dense solid films from organic-capped $\text{CH}_3\text{NH}_3\text{PbBr}_3$ perovskite colloids. *Journal of Materials Chemistry C* **2018**, *6* (25), 6771-6777.
Impact Factor (JCR): 5.976, Quartile: Q1, Cited by: 1

***Chapter 7. Ligand-free $\text{CH}_3\text{NH}_3\text{PbBr}_3$ Perovskite
Nanoparticles and their Solid Film Deposition***

7.1. Introduction

The HOIP materials have been extensively studied due to their exceptional optoelectronic properties as well as the easy processability using, for example solution-processing techniques for the preparation of bulk thin films from solutions of perovskite precursors. As was previously mentioned, this technique yields polycrystalline films and often suffers from a lack of reproducibility of the film morphology. Therefore, there is a great interest in the direct film preparation from colloidal perovskite nanoparticles aimed at higher reproducibility of the film morphology as well as improvement of their optoelectronic properties. Nevertheless, the passivation of perovskite nanoparticles with organic ligand often hindering the preparation of conductive thin films. Post-synthesis removal of the surface ligand result in nanoparticle aggregation and dramatically decreases their PLQY.

There are important challenges to be overcome for achieving that goals in the case of lead halide perovskites, such as the preparation of organic ligand-free perovskite nanoparticles with low tendency to aggregate in solution and their efficient self-assembly on a substrate to lead to conductive nanoparticle solid films.

The synthesis of the ligand-free nanoparticles is challenging, and there were few methods to prepare ligand-free $\text{CH}_3\text{NH}_3\text{PbBr}_3$ nanoparticles. A mixture of ligand-free crystalline $\text{CH}_3\text{NH}_3\text{PbBr}_3$ nano- and microcubes have been prepared by injecting the perovskites precursors in dimethylformamide into organic solvents such as diethyl ether, 1,2,4-trichlorobenzene and isopropanol.^[127-129]

In addition, the top-down methodology by laser ablation has been used to prepare $\text{CH}_3\text{NH}_3\text{PbBr}_3$ colloids in organic solvents without addition of organic ligands.^[130,131] The strategy consisted in the laser irradiation of a $\text{CH}_3\text{NH}_3\text{PbBr}_3$ bulk powder dispersed in chloroform. The yellow colloid exhibited a PL emission at 525 nm and was stable during several hours.^[130] Almost at the same time, a two-

step approach was reported for the preparation of $\text{CH}_3\text{NH}_3\text{PbX}_3$ (X= Br, I) colloids of 100 nm to 1 μm , depending of the nature of X. It consisted in the mixing of PbX_2 (X= Br, I) nanoparticles, prepared by laser ablation in iodobenzene or bromobenzene, with an isopropanol solution of $\text{CH}_3\text{NH}_3\text{X}$ (X= Br, I) under sonication.^[131]

Our aim was to explore the preparation of naked $\text{CH}_3\text{NH}_3\text{PbBr}_3$ colloidal nanoparticles by a one-step procedure and their assembly in conductive solid films. To this aim, the preparation of colloidal nanoparticles was attempted by using an excess of $\text{CH}_3\text{NH}_3\text{Br}$ in the perovskite precursor solution and an inorganic salts as confinement agent, specifically potassium hexafluorophosphate (KPF_6), whose anion (PF_6^-) is both more lipophilic and less coordinating than the bromide anion. The purpose was to replace the excess of CH_3NH_3^+ at the $\text{CH}_3\text{NH}_3\text{PbBr}_3$ nanoparticle surface with K^+ cation on the basis of the higher enthalpy formation of KBr than that of $\text{CH}_3\text{NH}_3\text{Br}$ (-394 kJ/mol vs -259 kJ/mol),^[132,133] with the final aim to produce confined and colloidal stable nanoparticles (*ACS Omega* **2018**, *3*, 1298-1303).

In this chapter we report the synthesis of naked green photoluminescent $\text{CH}_3\text{NH}_3\text{PbBr}_3$ nanoparticles and their self-assembly on a substrate by centrifugal casting method to lead to conductive solid films.

7.2. Synthesis and characterization of naked $\text{CH}_3\text{NH}_3\text{PbBr}_3$ perovskite nanoparticles

The synthesis of $\text{CH}_3\text{NH}_3\text{PbBr}_3$ nanoparticles was carried out by using the re-precipitation strategy and the moderately polar solvent ethyl acetate as the bad solvent. Briefly, a precursor solution in dimethylformamide composed of a mixture of $\text{CH}_3\text{NH}_3\text{Br}$, KPF_6 and PbBr_2 with a molar ratio of 2:2:1 was prepared. Then, an aliquot of the precursor solution was added dropwise to ethyl acetate under vigorous stirring. Finally, the colloidal nanoparticles were separated by centrifugation and re-dispersed in ethyl acetate (see experimental section).

Interestingly, the nanoparticles were dispersible in a polar solvent (ethyl acetate) and exhibited an absorption and emission peak maximum at 505 nm and 525 nm (fwhm = 28 nm), respectively (figure 7.1). The absorption peak is blue shifted compared to that of the $\text{CH}_3\text{NH}_3\text{PbBr}_3$ bulk (absorption peak at about 540 nm) indicating the confinement of the material. These nanoparticles exhibited a PLQY of 17 % and an average lifetime (τ_{av}) of 29 ns. Moreover, they were considerably stable as colloid, remaining dispersible in ethyl acetate for about 3h, thereafter a complete precipitation of the solid is observed, but it was easily redispersed by hand shaking.

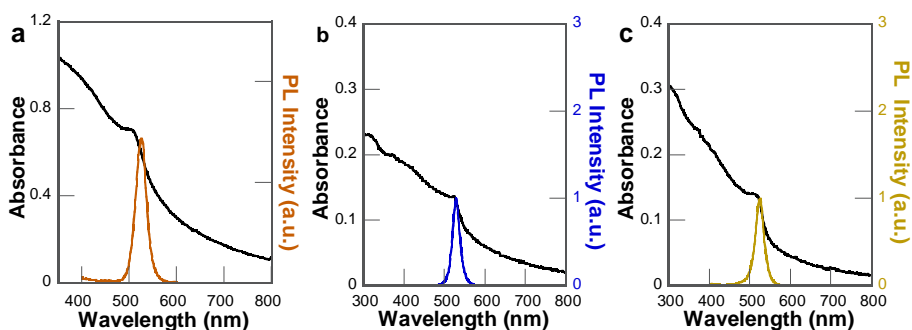


Figure 7. 1. Absorption and PL emission spectra of colloidal MAP@K prepared in a) ethyl acetate, b) toluene and c) chlorobenzene.

Comparatively, green photoluminescent $\text{CH}_3\text{NH}_3\text{PbBr}_3$ colloid, PL peak ca. 527 and 525 nm, were also obtained using toluene and chlorobenzene as bad solvents, respectively (figure 7.1); however it showed lower colloidal stability and only the colloid in ethyl acetate was fully characterized (see below).

Interestingly, no additional absorption peaks were observed in the UV-Vis spectrum of the $\text{CH}_3\text{NH}_3\text{PbBr}_3$ perovskite; their presence would indicate the partial substitution of CH_3NH_3^+ for K^+ in the crystalline structure.^[134]

The composition of the nanoparticles was studied by ^1H and ^{19}F NMR. The analysis was carried out by dissolving the perovskite nanoparticles and the supernatant back to the precursors in deuterated dimethyl sulfoxide. Moreover, the spectra were compared with that of the KPF_6 inorganic salt (figure 7.2). ^{19}F NMR spectra showed that the PF_6^- anions were in the supernatant in the form of two different salts, KPF_6 and $\text{CH}_3\text{NH}_3\text{PF}_6$. The presence of the CH_3NH_3^+ cation in the supernatant was also confirmed by ^1H NMR.

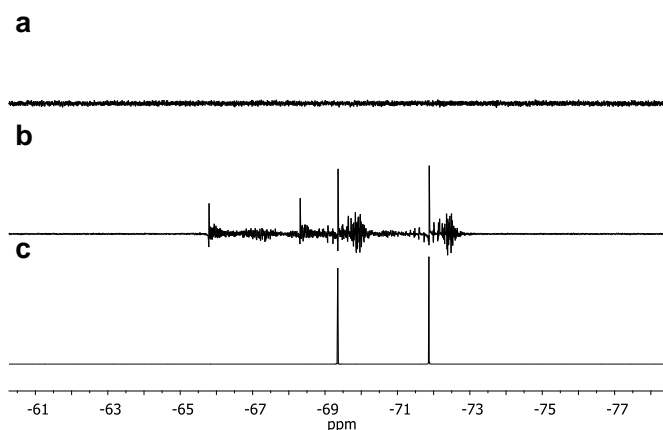


Figure 7. 2. ^{19}F NMR spectra of a) MAP@K nanoparticles, b) the residual material obtained after solvent evaporation of the supernatant and c) KPF_6 inorganic salt, in deuterated dimethyl sulfoxide.

The PXRD pattern of the nanoparticles confirmed the formation of crystalline cubic phase of $\text{CH}_3\text{NH}_3\text{PbBr}_3$ with an exclusive (001) film orientation and a crystalline average size of 69 nm, figure 7.3.^[52,135-137] These data suggested the passivation of the nanoparticles surface with potassium. Moreover, the SEM images showed the formation of cubic nanoparticles, and the energy dispersive X-ray (EDS) spectrum revealed a K/Pb/Br molar ratio of 0.5:1.0:3.4. Therefore, the $\text{CH}_3\text{NH}_3\text{PbBr}_3$ perovskite nanoparticles are capped with KBr and were termed as MAP@K (MA refers to CH_3NH_3^+).

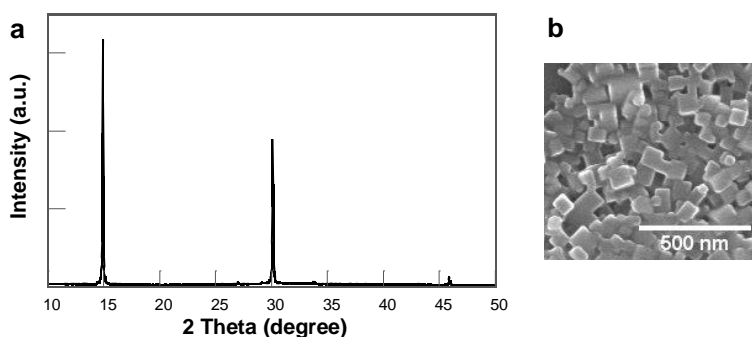


Figure 7. 3. a) PXRD of the MAP@K nanoparticles deposited on quartz showing lattice diffraction peaks at 14.9° , 30.1° and 45.9° and a (001) exclusive orientation, b) SEM image of nanoparticles.

In order to gain further insight into the role of K^+ cation in the stability of MAP@K nanoparticles, a control sample was prepared under the same experimental conditions but in the absence of KPF_6 . The orange colloid obtained showed a low dispersibility in ethyl acetate and its absorption spectrum exhibited a poor absorption band and high scattering. This is consistent with the formation of $\text{CH}_3\text{NH}_3\text{PbBr}_3$ bulk with arbitrary size.

These results demonstrated that K^+ cation not only passivates the nanoparticle surface and permits the colloidal stabilization of the $\text{CH}_3\text{NH}_3\text{PbBr}_3$ nanoparticles in a moderately polar solvent, but also prevents their collapse.

7.3. Preparation and characterization of nanoparticle solid films

Taking into account the successfully assembly of perovskite nanoparticles into solid films by using the centrifugal casting strategy (chapter 6), we explored the preparation of densely packed nanoparticle solid films from the colloidal MAP@K in ethyl acetate. Briefly, the colloidal nanoparticles were added to a centrifugal tube with the glass substrate at the bottom and then centrifuged for 7 min. Finally, the supernatant was pipetted out and the film MAP@K_{F1} was dried under ethyl acetate atmosphere at room temperature. The as-prepared film showed an incomplete substrate coverage, figure 7.4. Consequently, different deposition conditions were studied in order to obtain homogeneous films, such as i) increasing the volume of the MAP@K colloid (film MAP@K_{F2}) and ii) using a mixture of ethyl acetate and toluene for the dispersion of MAP@K nanoparticles (film MAP@K_{F3}), figure 7.4.

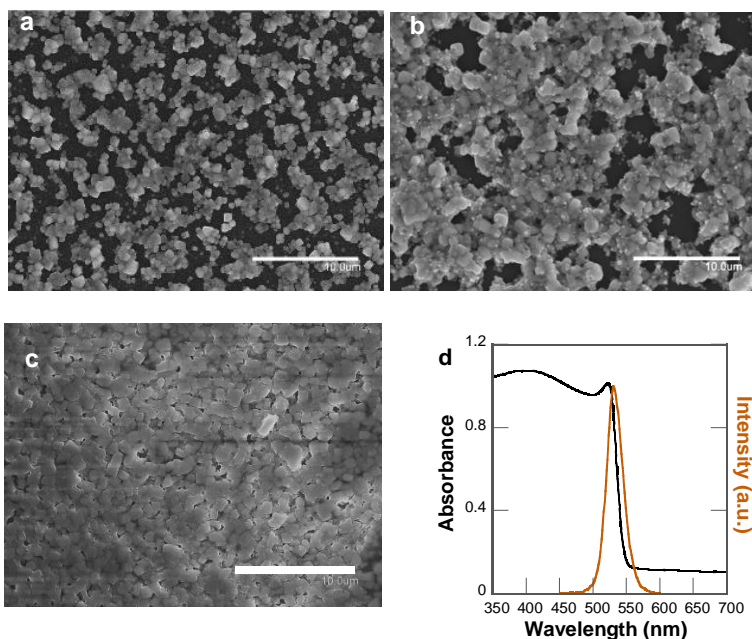


Figure 7. 4. SEM images of nanoparticles solid films a) MAP@K_{F1} b) MAP@K_{F2} and c) MAP@K_{F3}. Scale bar 10 μm . d) Absorption and PL emission spectra of the MAP@K_{F3}

Interestingly, a homogeneous distribution of nanoparticles over the substrate was obtained in $\text{MAP@K}_{\text{F}_3}$. The film showed an absorption peak at 526 nm and a slightly red-shifted PL emission peak at 530 nm (fwhm = 30 nm) compared to that of the colloid in ethyl acetate (figure 7.4 d). In addition, the film showed a PLQY of 7%.

Conductive atomic force microscopy (c-AFM) technique was used to gain further insight into the local electronic properties and morphology of the nanoparticle solid film. Therefore, a nanoparticle solid film was prepared by centrifugal casting on ITO coated-glass, termed as $\text{MAP@K}_{\text{F}_4}$, following the strategy described for $\text{MAP@K}_{\text{F}_3}$. Figure 7.5 shows the densely packed nanoparticle solid film $\text{MAP@K}_{\text{F}_4}$, with an average thickness of 881 ± 78 nm.

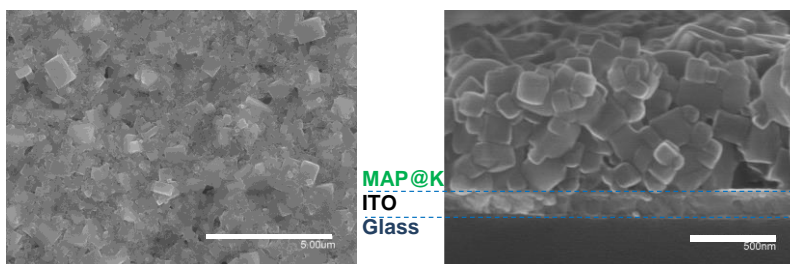


Figure 7. 5. Top (left) and cross-sectional (right) SEM images of $\text{CH}_3\text{NH}_3\text{PbBr}_3$ nanoparticle solid $\text{MAP@K}_{\text{F}_4}$. Scale bar 5 μm and 500 nm, respectively.

The topographic and conductive AFM measurements were carried out in the dark using the PinPoint mode to prevent the nanoparticle film damage after each scan. The topographical AFM image of the film $\text{MAP@K}_{\text{F}_4}$ showed protrusions and depressions in the range of ± 100 nm, figure 7.6. Moreover, high and low current magnitude regions were observed in the c-AFM image of the same area, figure 7.6b. This behavior can be observed in detail in the cross-sectional profile image of height and current along the white line in the topographic and c-AFM image (figure 7.6c), in which high magnitude current domains, between -8.4 and 2.1 nA (average current magnitude of -0.447 nA), were observed. The high conductive

domains were ascribed to high-density regions of nanoparticles dispersed in the film with an effective electrical connectivity between them.

Overall, the c-AFM measurement showed that the vertical current transport was heterogeneous on the nanometer scale. A similar behavior has been reported in c-AFM studies of $\text{CH}_3\text{NH}_3\text{PbX}_3$ ($\text{X} = \text{Br}, \text{I}$) bulk thin films prepared by spin-coating of the precursor solution.^[103,138,139] Notably, MAP@K_{F4} exhibited higher conductivity than the dense solid film prepared from colloidal nanoparticles capped with organic ligands (chapter 6).

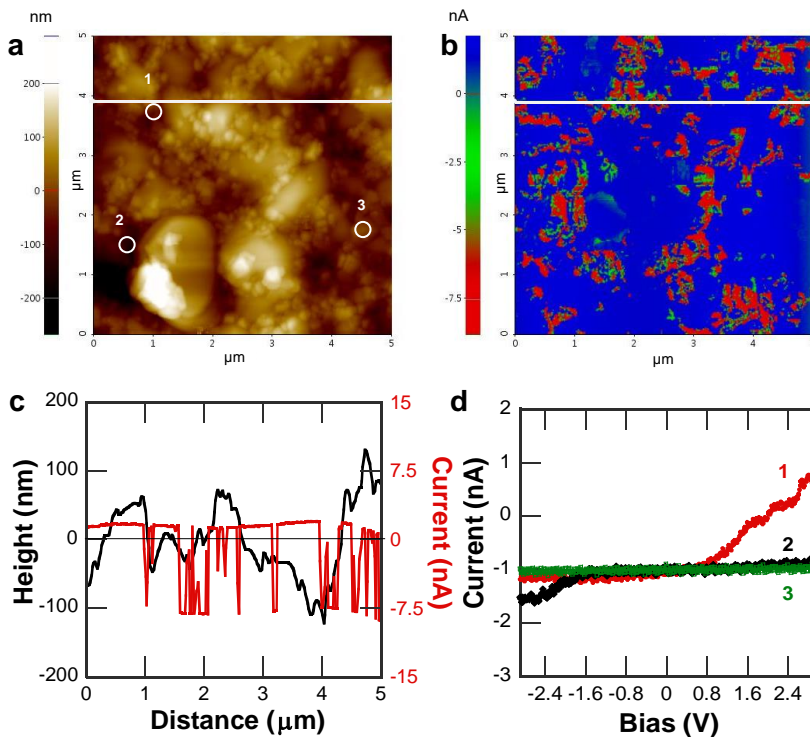


Figure 7.6. a) Topographical and b) conductive AFM images of nanoparticle solid film MAP@K_{F4} (bias = -1.5 V); image scale $5 \mu\text{m} \times 5 \mu\text{m}$. c) Cross-sectional profile of height and current along the white line in images a and b. d) I - V curve as a function of applied bias ($+6 \text{ V}$ to -6 V) for grains marked in the topographic AFM image a.

Complementary local current versus bias (I-V) measurement were performed by c-AFM. The local I-V curves of selected topographic areas of MAP@K_{F4} showed a diode behavior (figure 7.6a and 7.6d), as it has previously been observed for millimeter-sized $\text{CH}_3\text{NH}_3\text{PbBr}_3$ crystals,^[140,141] i.e. a linear ohmic region at low voltages, a step-up in current at intermediate voltages where the traps are filled and an abrupt increase in current where the carriers move freely (figure 7.6d).

Comparatively, in collaboration with Dr. Michele Sessolo, the charge transport properties of the nanoparticles solid films were further investigated at a larger scale by depositing the nanoparticles onto interdigitated ITO electrodes. The results were compared with a polycrystalline $\text{CH}_3\text{NH}_3\text{PbBr}_3$ film prepared by direct spin-coating of the precursor solution. The current density versus voltage (J-V) curves of the nanoparticle solid film showed a current injection in both reverse and forward bias, with current up to 100 nA at voltages as low as 5 V. Moreover, the charge transport properties of MAP@K_{F4} were comparable to those of polycrystalline $\text{CH}_3\text{NH}_3\text{PbBr}_3$ thin film.

7.4. Conclusions

In summary, we demonstrated the easily preparation of organic ligand-free $\text{CH}_3\text{NH}_3\text{PbBr}_3$ nanoparticles by adding a potassium salt to the perovskite precursor solution. The potassium cations acted as the confinement agent and provided colloidal stability in moderately polar solvent. In addition, they enabled the assembly of $\text{CH}_3\text{NH}_3\text{PbBr}_3$ nanoparticles on substrates to lead densely packed nanoparticle solid films.

The conductive atomic force microscopy studies revealed the formation of high-density regions of nanoparticles dispersed in the film with high conductivity. These are preliminary results but it is expected that they promote the interest in naked lead halide perovskites nanoparticles due to the new opportunities offered by the corresponding solid films.

7.5. Experimental section

Synthesis of MAP@K nanoparticles. The colloidal nanoparticles were prepared by the re-precipitation method in ethyl acetate. First, a precursor solution was prepared by mixing lead bromide (25 mg, 0.068 mmol), $\text{CH}_3\text{NH}_3\text{Br}$ (15.3 mg, 0.14 mmol) and KPF_6 (25 mg, 0.14 mmol) in 2.5 mL of dimethylformamide. The molar ratio between the components $\text{PbBr}_2:\text{CH}_3\text{NH}_3\text{Br}:\text{KPF}_6$ was 1:2:2. Then, an aliquot of the precursor solution (100 μL) was added dropwise into ethyl acetate (10 mL) under vigorous stirring, at room temperature. Thereafter, the yellowish dispersion was centrifuged (7000 rpm for 7 min), and the supernatant was discarded. The green photoluminescent precipitate obtained was redispersed in 5 ml of ethyl acetate.

The nanoparticle solid films were prepared by using a centrifugal casting method (chapter 3), as follow:

Nanoparticles solid MAP@K_{F1}. First colloidal MAP@K nanoparticles were prepared following the above-mentioned method. Then, the colloid (10 mL) was added to a conical centrifuge tube (50 mL), with a glass slide substrate at its bottom. The mixture was centrifuged at 8000 rpm for 7 min. Finally, the supernatant was pipetted out and the glass substrate with the deposited nanoparticle solid film was allowed to dry in ethyl acetate atmosphere, at room temperature.

Nanoparticles solid MAP@K_{F2}. The film was prepared following the method described above but increasing the volume of the freshly prepared MAP@K colloid in ethyl acetate, i.e. using 20 mL instead of 10 mL.

Nanoparticles solid MAP@K_{F3}. The film was prepared following the method describe for MAP@K_{F2}, but toluene (10 mL) was added to freshly prepared MAP@K colloid (20 mL) in ethyl acetate.

Nanoparticles solid MAP@K_{F4}. The film was prepared following the method described for MAP@K_{F3} but using an ITO-glass coated substrate. In addition, a film was prepared in the same conditions on interdigitated ITO substrate.

Preparation of polycrystalline CH₃NH₃PbBr₃. The precursor solution was prepared mixing PbBr₂ and CH₃NH₃Br (molar ratio 1:2, respectively) in dimethylformamide (concentration of 100 mg/mL). The solution was spin-coated at 3000 rpm for 60 s. The film was annealed on a hot plate at 90 °C for 30 minutes in a nitrogen atmosphere glove-box.

Contribution of the Author:

- **Gonzalez-Carrero, S.;** Schmidt, L. C.; Rosa-Pardo, I.; Martínez-Sarti, L.; Sessolo, M.; Galian, R. E.; Pérez-Prieto, J., Colloids of Naked CH₃NH₃PbBr₃ Perovskite Nanoparticles: Synthesis, Stability, and Thin Solid Film Deposition. *ACS Omega* **2018**, 3 (1), 1298-1303.
Invited contribution; Impact Factor (JCR): --, Quartile: --, Cited by: 1

Chapter 8. Conclusions

The conclusions of this thesis, focused in the synthesis of colloidal organic-inorganic lead bromide perovskite nanoparticles, can be summarized as follows:

- Colloidal $\text{CH}_3\text{NH}_3\text{PbBr}_3$ perovskite nanoparticles were prepared for the first time by using a hot-injection, a non-template approach and they exhibited a photoluminescence quantum yield of 20 %. A medium alkyl chain ammonium salt together with a surfactant, namely oleic acid, controlled the growth and dispersibility of the nanoparticles. The ligands play a crucial role in the dispersibility, photoluminescence, photostability and stability in solid state of the nanoparticles. In addition, the dispersion of nanoparticles in organic solvents enabled the effective preparation of photoluminescent thin films and a light emitting device. The electroluminescence of the device based on the nanoparticles film was higher than that of the bulk perovskite.
- Later on, colloidal $\text{CH}_3\text{NH}_3\text{PbBr}_3$ perovskite nanoparticles with photoluminescent quantum yield of up to 83 % were produced by following the same strategy. The length of the alkyl ammonium cation and the perovskite components molar ratio, together with the absence of oleic acid, played a key role on the optical properties of the $\text{CH}_3\text{NH}_3\text{PbBr}_3$ nanoparticles. Moreover, the nanoparticles exhibited good photostability under continuous UV irradiation of the colloidal dispersion and preserved their emissive properties as a solid.
- Blue-photoluminescent and dispersible perovskites with a 2D inorganic framework, $(\text{RNH}_3)_2\text{PbBr}_4$, were also successfully prepared by the hot injection method. The colloids obtained with octadecylammonium bromide showed a photoluminescent quantum yield of 21 % and were ease of processing.
- The passivation of the $\text{CH}_3\text{NH}_3\text{PbBr}_3$ nanoparticles surface with adamantylammonium bromide as the only organic ligand led to colloids with

an outstanding photoluminescence (quantum yield of 100 %). The colloidal nanoparticles were prepared with a high chemical yield. The photostability of the nanoparticles in solution under continuous photoirradiation and in contact with water was improved through the formation of adamantylammonium-cucurbit[7]uril complexes at the nanoparticle surface. However, these colloids showed a high trend to aggregate and, as a consequence, exhibited an extraordinarily long photoluminescence lifetime.

- The synthesis of $\text{CH}_3\text{NH}_3\text{PbBr}_3$ nanoparticles using adamantylamine/alkyl carboxylic acid organic combinations as the ligands drastically decreased the aggregation trend of the nanoparticles in solution, and as a consequence the photoluminescence lifetime of the colloid, while preserving their high photoluminescence quantum yield. In addition, the synergy between the organic ligands allowed the assembly of the nanoparticles into densely packed nanoparticles solid films with thicknesses up to several hundreds of nanometers. Notably, the nanoparticles solid films retained the pre-engineered confined morphologies of the nanoparticles as well their optical properties and they exhibited good charge transport properties.
- Finally, organic ligand-free $\text{CH}_3\text{NH}_3\text{PbBr}_3$ nanoparticles were successfully prepared by adding potassium hexafluorophosphate to the perovskite precursor solution together with an excess of $\text{CH}_3\text{NH}_3\text{Br}$. The potassium cation on the nanoparticle surface stabilizes the nanoparticles and the colloid in a moderately polar solvent and enables the assembly of the nanoparticles on substrates to lead to densely packed films. Moreover, conductive atomic force microscopy measurements demonstrated the presence of highly conductive domains that can be attributed to nanoparticles with an effective electrical connectivity between them. The charge transport properties of the nanoparticles solid film proved to be comparable to those of a polycrystalline bulk thin film.

Chapter 9. Resumen de la Tesis Doctoral

Capítulo 1. Introducción

Las perovskitas híbridas orgánicas-inorgánicas de haluros de plomo, $\text{CH}_3\text{NH}_3\text{PbX}_3$ (X= halógeno) son materiales semiconductores que han sido extensamente estudiados para aplicaciones optoelectrónicas, debido a sus interesantes propiedades tales como elevado coeficiente de absorción, amplio espectro de absorción, el cual puede modificarse por cambios en su composición, baja energía de enlace del excitón y elevada difusión de la carga.^[1-4] Además se preparan a partir de compuestos de partida abundantes y de bajo coste. Desde su primera aplicación en células solares en 2009 como sensibilizador,^[5] la estabilidad del material y la eficiencia de las células solares ha aumentado rápidamente llegando a alcanzar una eficiencia similar a la de las células solares comerciales (20 %) en 2013.^[2,6] Además, se demostró que las perovskitas híbridas en forma de nanopartículas son luminiscentes, lo cual atrajo la atención sobre estos materiales para aplicaciones en dispositivos electroluminiscentes.^[7] En este trabajo nos enfocamos en el estudio de las perovskitas híbridas de bromuro de plomo confinadas a la escala nanométrica.

Las perovskitas híbridas orgánicas-inorgánicas de haluros metálicos (HOIP, por sus siglas en inglés) presentan la fórmula general AMX_3 , en la cual M es un catión metálico divalente (por ejemplo Pb^{+2} o Sn^{+2}), X es un haluro (Cl^- , Br^- , I^-) y A es un catión monovalente que puede ser orgánico como metilamonio (CH_3NH_3^+) o inorgánico como el cesio (Cs^+). Estos materiales adoptan una estructura cristalina tridimensional (3D) en la cual el octaedro formado por el haluro metálico $[\text{MX}_6]^{-4}$ se extiende en 3D y el catión orgánico A ocupa los intersticios entre los octaedros para compensar la carga de la estructura (figura 1.1, tabla 1.1).^[8-10] Las perovskitas con cationes orgánicos de mayor tamaño forman estructura con una dimensionalidad inferior a la 3D, como la estructura bidimensional (2D), monodimensional (1D) y cero dimensional (0D), figura 1.2. En todos los casos, la carga de la estructura inorgánica formada por los octaedros $[\text{MX}_6]^{-4}$ se compensa con la de los cationes orgánicos (figura 1.2, tabla 1.2). En la estructura de las

perovskitas 2D, los octaedros están unidos formando una estructura inorgánica en forma de láminas separadas por los cationes orgánicos. La fórmula general de la perovskita 2D más estudiada es $(\text{RNH}_3)_2\text{MX}_4$, en la que RNH_3^+ es un catión orgánico de cadena alquílica (tabla 1.2).^[1,14-16]

Las propiedades ópticas de las HOIP dependen de su composición, de la dimensionalidad de su estructura inorgánica y de la dimensión del material (tabla 1.3, figura 1.3). La estructura electrónica de las HOIP está determinada por la interacción entre los orbitales del metal y del halógeno (figure 1.4). En consecuencia, la energía de la banda prohibida (*band gap*) de $\text{CH}_3\text{NH}_3\text{PbI}_3$ de 1.5 eV (800 nm) aumenta con la sustitución del halógeno a 2.3 eV (540 nm) y 3.2 eV (400 nm) para $\text{CH}_3\text{NH}_3\text{PbBr}_3$ y $\text{CH}_3\text{NH}_3\text{PbCl}_3$, respectivamente (figura 1.5).^[36] Estas perovskitas presentan por tanto un amplio espectro de absorción, el cual puede modularse notablemente en todo el espectro de absorción visible mezclando los halógenos (tabla 1.3).^[43] La reducción de la dimensionalidad de la estructura inorgánica de las HOIP también tiene un efecto en las propiedades ópticas, siendo el más importante el aumento de energía de la banda prohibida con la reducción de la dimensión de 3D hasta 0D (tabla 1.3, figura 1.6).^[19-21,23,24,29,35,46-48]

Estos materiales han sido estudiados mayoritariamente como cristales y películas sólidas delgadas.^[11,38,40,52-55] Estas últimas se pueden preparar por una variedad de técnicas, siendo las más utilizadas las técnicas de deposición a partir de una disolución de los precursores y las de evaporación al vacío (figure 1.7).^[2,57] Factores como selección del sustrato, disolvente, concentración de los precursores, temperatura y atmosfera a la que se lleva a cabo la preparación, influyen la morfología de las películas y por tanto su aplicación. Las perovskitas de $\text{CH}_3\text{NH}_3\text{PbX}_3$, particularmente las de I, son sensibles a la humedad,^[58] por lo que su preparación o caracterización se lleva a cabo en atmosfera inerte (de nitrógeno o argón). La baja estabilidad a la humedad es una de las principales desventajas que presenta este material.

En el caso de nanopartículas de perovskitas (materiales 0D; $x, y, z < 100$ nm), solo unos pocos ejemplos habían sido publicados antes del 2013. El primer ejemplo de nanopartículas de perovskita con estructura inorgánica 3D, $\text{CH}_3\text{NH}_3\text{PbX}_3$ ($X = \text{Br}, \text{I}$) con un tamaño de 2-3 nm, se publicó en 2009 utilizando los poros de una película mesoporosa de TiO_2 .^[5] Dicha porosidad actúa como plantilla y permite el confinamiento del material $\text{CH}_3\text{NH}_3\text{PbX}_3$ en las tres dimensiones a escala nanométrica, sin embargo el material no presentaba luminiscencia.^[2,5,68-71] Interesantemente, en 2012 se publicó la preparación de nanopartículas luminiscentes de $\text{CH}_3\text{NH}_3\text{PbBr}_3$ (tamaño de 5 nm) dentro de los poros de una película mesoporosa de Al_2O_3 , las cuales mostraron un máximo de la banda de emisión en 523 nm.^[7] Por otra parte, antes del año 2013 no se había publicado ninguna estrategia para la síntesis de nanopartículas coloidales de perovskita con estructura 3D.

A diferencia de las perovskitas 3D, la preparación de nano/micropartículas de perovskita con estructura 2D, $(\text{RNH}_3)_2\text{PbX}_4$, se habían descrito en el momento en que se inició esta tesis utilizando métodos tales como nebulización, intercalación y precipitación.^[72-75] De esta forma se prepararon partículas luminiscentes poli-dispersas (tamaño desde 20 nm a varias micras), en forma de sólidos y como suspensiones en solventes orgánicos.

Capítulo 2. Objetivos.

Motivación de las tesis. En el momento en que se inició esta tesis, las perovskitas híbridas orgánicas-inorgánicas de haluros metálicos recibían una considerable atención debido a sus propiedades ópticas y eléctricas. Además, la luminiscencia de las nanopartículas de $\text{CH}_3\text{NH}_3\text{PbBr}_3$ dentro del material mesoporoso atrajo un gran interés por su potencial en aplicaciones optoelectrónicas. Sin embargo, el uso de material mesoporoso podría limitar la aplicación de las nanopartículas. La falta de un procedimiento de síntesis para obtener nanopartículas de perovskita coloidales con estructura 3D motivó nuestro interés en su preparación, ya que las nanopartículas coloidales podría permitir la preparación de nuevos dispositivos optoelectrónicos con un mejor rendimiento y estabilidad.

Objetivo general.

El objetivo general de la tesis doctoral es la síntesis de nanopartículas coloidales y luminiscentes de perovskitas híbridas orgánicas-inorgánicas de bromuro de plomo mediante un método sin plantilla y además explorar su procesabilidad como materiales conductores.

Objetivos específicos.

Los objetivos específicos de la tesis son:

- Sintetizar nanopartículas coloidales híbridas de bromuro de plomo y metilamonio con estructura 3D, $\text{CH}_3\text{NH}_3\text{PbBr}_3$, con una elevada luminiscencia y (foto)estabilidad
- Explorar la preparación y procesabilidad de perovskitas híbridas bidimensionales de haluros de plomo $(\text{RNH}_3)\text{PbBr}_4$.
- Explorar el auto-ensamblaje de nanopartículas coloidales de $\text{CH}_3\text{NH}_3\text{PbBr}_3$ en forma de películas sólidas de nanopartículas y estudiar sus propiedades conductoras.
- Sintetizar nanopartículas coloidales de $\text{CH}_3\text{NH}_3\text{PbBr}_3$ sin ligandos orgánicos y explorar su ensamblaje y propiedades conductoras.

Capítulo 3. Metodología

A continuación se describen las técnicas utilizadas en la tesis para la caracterización de las propiedades ópticas, la estructura cristalina, la morfología y la composición de las nanopartículas y las películas sólidas.

Caracterización de las propiedades ópticas. Se han utilizado las siguientes técnicas: espectroscopia de absorción ultravioleta-visible (UV-Vis), espectroscopia de fluorescencia en estado estacionario y resuelto en el tiempo. Mediante estas técnicas se midieron los espectros de absorción, de emisión y los tiempos de vida de las nanopartículas. En todos los casos se prepararon dispersiones de nanopartículas en cubetas de cuarzo (10 mm de paso óptico). Además, los rendimientos cuánticos de emisión (PLQY, por sus siglas en inglés) se midieron utilizando los colorantes orgánicos 9,10 difenil-antraceno y fluoresceína como patrones. Para los estudios de fotoestabilidad se utilizaron dos fuentes de irradiación: a) lámpara de Xenon del fluorímetro, con máximo de emisión en 350 nm (capítulo 4 y 6) y 330 nm (capítulo 5), b) 8 lámparas con máximo de emisión en el UV-A (351 nm) y en el visible (420 nm), capítulo 4.

Caracterización de la estructura y morfología. Se utilizaron las siguientes técnicas (abreviadas por sus siglas en inglés): difracción de rayos X en polvo (PXRD), microscopía electrónica de transmisión de alta resolución (HRTEM), microscopía electrónica de barrido (SEM). Mediante la técnica de PXRD se determinó la estructura cristalina de las nanopartículas y las películas de perovskitas. La técnica de HRTEM se utilizó para determinar la forma y tamaño de las nanopartículas. La técnica de SEM se utilizó para estudiar la morfología y espesor de las películas sólidas de nanopartículas (capítulo 6 y 7).

Análisis de la composición. Se utilizaron las siguientes técnicas (abreviadas por sus siglas en inglés): espectroscopia de fluorescencia de rayos-X (XPS), análisis termogravimétrico (TGA), resonancia magnética nuclear (NMR) y espectroscopia infrarroja con transformada de Fourier-reflectancia total atenuada (FTIR-ATR).

Mediante XPS se determinó la relación entre los elementos que componen la perovskita, así como también la interacción de los ligandos con la superficie de las nanopartículas. Los estudios de TGA se llevaron a cabo registrando los termogramas de las nanopartículas y los precursores entre 25-800 °C (a 10 °C/min) en atmosfera de nitrógeno. Los espectros de ^1H NMR permitieron determinar la relación molar entre los componentes orgánicos de las nanopartículas de perovskita, es decir de metilamonio y de los ligandos orgánicos. Para ello, una vez sintetizadas las nanopartículas se centrifugaron y el sólido obtenido se re-disolvió en dimetilsulfóxido deuterado, disolvente en el cual las nanopartículas se transforman en sus correspondientes precursores. Finalmente, mediante la combinación de los resultados de TGA y de ^1H NMR se pudo determinar la relación molar entre los componentes orgánicos e inorgánicos (PbBr_2), así como el rendimiento de la reacción. El análisis por FTIR-ATR (capítulo 6) se llevó a cabo midiendo los espectros entre 400 y 4000 cm^{-1} (resolución 4 cm^{-1}) a temperatura ambiente. Las nanopartículas se depositaron a partir de dispersiones preparadas en hexano.

Preparación de películas sólidas de nanopartículas. Las películas de nanopartículas, descritas en los capítulos 4 y 5, se prepararon depositando una dispersión de nanopartículas en tolueno sobre el sustrato por *spin-coating* (1000 rpm durante 30 segundos). Por otra parte, las películas de nanopartículas descritas en los capítulos 6 y 7 se prepararon por el método de *centrifugal casting*. Este último método consiste en sedimentar la muestra mediante centrifugación sobre un determinado sustrato. Para ello, en el capítulo 6 se preparó una dispersión de nanopartículas en tolueno en un volumen final de 5 mL, después se adicionó en un tubo de centrifuga (50 mL) que contenía el sustrato de vidrio (1.5 cm^2) y se centrifugó a 6000 rpm durante 6 minutos. Finalmente, se eliminó el sobrenadante y la película depositada sobre el sustrato de vidrio se dejó secar en atmosfera de tolueno a temperatura ambiente. En el capítulo 7, se utilizó este procedimiento,

con la diferencia de que la preparación se llevó a cabo utilizando como disolvente acetato de etilo.

Preparación de los dispositivos electroluminiscentes. Los dispositivos descritos en la tesis fueron preparados y caracterizados por miembros del grupo de investigación dirigido por el Dr. Hendrik Jan Bolink del Instituto de Ciencia Molecular de la Universidad de Valencia. Los dispositivos descritos en el capítulo 4 se prepararon con la siguiente configuración:

- Dispositivo de control: ITO/Al₂O₃/CH₃NH₃PbBr₃-volumétrico /SPPO13/Ba/Ag. La película sólida de CH₃NH₃PbBr₃ volumétrico se preparó por el método de deposición a partir de una disolución de los precursores en disolución.
- Dispositivo con nanopartículas: ITO/PEDOT:PSS/pTPD/ nanopartículas de CH₃NH₃PbBr₃/Ba/Ag. La película de nanopartículas se preparó depositando una dispersión en tolueno (4 mg/ mL) por *spin-coating*.

El dispositivo descrito en capítulo 6 se preparó con la siguiente configuración:

- Dispositivo con nanopartículas: ITO/PEDOT:PSS/BmPyPhB/ nanopartículas de CH₃NH₃PbBr₃/Ba/Ag. La película de nanopartículas se preparó por el método de *centrifugal casting*.

Microscopía de fuerza Atómica (AFM). La técnica de AFM (por sus siglas en inglés) es una técnica de caracterización de superficies y se basa en la medida de las interacciones entre una punta y superficie de la muestra, lo que permite obtener imágenes o mapas de la topografía superficial. En el capítulo 5, se registraron imágenes de AFM de nanopartículas depositadas sobre sustratos de silicio a dos diferentes concentraciones (2 mg/mL y diluidas 50 veces). Por otra parte, la técnica de AFM conductivo permite determinar simultáneamente el mapa de conductividad y de topografía de la superficie de la muestra. En el capítulo 6 y 7 se estudió las propiedades conductoras de las películas sólidas de nanopartículas preparadas por el método de *centrifugal casting*. El registro de las imágenes se

realizó en un microscopio de fuerza atómica Park Systems NX20, usando puntas de Pt-Ir recubiertas con Si (CONTSCPT, 7 nm de diámetro).

Capítulo 4. Síntesis y caracterización de nanopartículas coloidales de perovskitas $\text{CH}_3\text{NH}_3\text{PbBr}_3$

El primer objetivo de esta tesis fue la síntesis de nanopartículas coloidales de $\text{CH}_3\text{NH}_3\text{PbBr}_3$ sin utilizar una plantilla. Para ello, se exploraron los métodos descritos para la síntesis de nanopartículas semiconductoras, tales como CdSe.^[63,64,84] Uno de los métodos generales para la síntesis de nanopartículas de CdSe consiste en la adición de los precursores inorgánicos a una mezcla de disolventes orgánicos de alta temperatura de ebullición (como octadeceno) y de ligandos orgánicos (como oleilamina). Los precursores se descomponen formando nuevas especies reactivas que producen la nucleación y crecimiento de las nanopartículas. Los ligandos orgánicos, controlan el crecimiento, previenen la aglomeración y dan estabilidad coloidal a las nanopartículas en disolventes orgánicos. Por tanto, nos propusimos realizar la síntesis de las nanopartículas de perovskita híbridas utilizando ligandos orgánicos en combinación con los precursores de la perovskita.

La síntesis se llevó a cabo por el método de inyección en caliente de los precursores de perovskita $\text{CH}_3\text{NH}_3\text{Br}$ y PbBr_2 a una mezcla de bromuro de alquilamonio y ácido oleico (OLA) en octadeceno (ODE) a 80 °C. Los mejores resultados se obtuvieron utilizando bromuro de octilamonio (OABr) como ligando. Se obtuvieron nanopartículas de $\text{CH}_3\text{NH}_3\text{PbBr}_3$ (P_{OA}) con tamaño promedio de 6 nm, dispersables en tolueno. El coloide presentó una banda de absorción y de emisión con máximos en 527 nm y 530 nm, respectivamente (figura 4.1 y 4.2), valores similares a los observados en las nanopartículas descritas dentro de material mesoporoso.^[5] Además, presentó un PLQY ca. 20 %. El desplazamiento del máximo de la banda de absorción hacia mayores energías con respecto a la observada en el material volumétrico de $\text{CH}_3\text{NH}_3\text{PbBr}_3$ (~540 nm), se atribuyó al efecto de confinamiento cuántico de las nanopartículas.

Los análisis de PXRD y HRTEM (figura 4.3) demostró la formación de nanopartículas con una estructura cristalina que coincide con la fase cúbica de $\text{CH}_3\text{NH}_3\text{PbBr}_3$ (grupo espacial $Pm3m$). Cabe destacar que este resultado fue el primer ejemplo de preparación de nanopartículas de $\text{CH}_3\text{NH}_3\text{PbBr}_3$ coloidales, con estructura 3D (*Journal of the American Chemical Society* **2014**, 136, 850-853). Además se demostró que, al contrario de las nanopartículas de CdSe, estas nanopartículas no necesitan un recubrimiento inorgánico para lograr una PLQY del 20 %.

Las características más importantes de las nanopartículas P_{OA} fueron: mayor intensidad de emisión comparadas con aquellas preparadas con sales de amonio de cadena más larga (figura 4.2), elevada dispersabilidad en disolventes orgánicos apróticos, estabilidad en estado sólido por más de tres meses y una notable estabilidad bajo continua irradiación en el UV (figura 4.4).

Para demostrar el ensamblaje de las nanopartículas en películas sólidas, en colaboración con el Dr. Hendrik Jan Bolink, se preparó una película de nanopartículas sobre vidrio, la cual presentó un máximo de la banda de emisión en 533 nm y un PLQY de 23 % (figura 4.5). Por lo tanto, se procedió a preparar un dispositivo electroluminiscente con las nanopartículas, el cual mostró una intensidad de electroluminiscencia (con máximo en 528 nm, figura 4.5) 10 veces mayor que la de un dispositivo preparado con una película de $\text{CH}_3\text{NH}_3\text{PbBr}_3$ volumétrico.

Teniendo en cuenta el éxito en la preparación de las nanopartículas coloidales de $\text{CH}_3\text{NH}_3\text{PbBr}_3$ y con el fin de mejorar sus propiedades, se estudió en detalle el efecto de la concentración de los precursores, de la longitud de la cadena de las sales alquílicas de amonio y de la adición de OLA sobre las propiedades ópticas de las nanopartículas coloidales (*Journal of Materials Chemistry A* **2015**, 3, 9187-9193). Los resultados revelaron que utilizando OABr como ligando en mayor concentración y sin la adición de OLA en la síntesis (tabla 4.1y figura 4.6), se obtienen nanopartículas de $\text{CH}_3\text{NH}_3\text{PbBr}_3$ ($\text{P}_{\text{OA}2}$), con un tamaño promedio de 5

nm, muy dispersables en tolueno (figura 4.7) y con un elevado PLQY (83 % para el coloide y 72 % para la película sólida), tabla 4.2. Además, las nanopartículas en disolución mostraron una alta estabilidad bajo irradiación continua con luz UV, observándose una disminución de solo 10 % después de irradiar a 350 nm durante 540 minutos (figura 4.8). En cuanto a la estructura, el análisis por PXRD y XPS confirmó que P_{OA2} mantienen la estructura cristalina de la perovskita $CH_3NH_3PbBr_3$ (figure 4.9, figura 4.10 y tabla 4.3). Además, mediante el análisis de la composición por las técnicas de TGA y 1H NMR (figura 4.11) se pudo determinar la relación molar entre los componentes orgánicos e inorgánicos (ver tabla 4.4).

En conclusión, se demostró por primera vez la síntesis de nanopartículas coloidales y luminiscentes (PLQY de 20%) de $CH_3NH_3PbBr_3$. Se utilizó una sal de alquilamonio para limitar el crecimiento de las nanopartículas y proveer estabilidad coloidal. Además, se prepararon películas sólidas luminiscentes y un dispositivo electroluminiscente a partir de dispersiones de nanopartículas. Interesantemente, las películas de nanopartículas conservaron las propiedades ópticas del coloide. Estos resultados pioneros abrieron la posibilidad de múltiples aplicaciones de las nanopartículas de perovskita luminiscentes para la preparación de dispositivos optoelectrónicos mediante el uso de técnicas de sencillas. Finalmente, se demostró la síntesis de nanopartículas de $CH_3NH_3PbBr_3$ con un PLQY de 83 %, mediante la optimización de las relaciones molares de los precursores y en ausencia de ácido oleico. Las nanopartículas mostraron una alta fotoestabilidad bajo irradiación continua en el UV de la dispersión y además conservaron sus propiedades luminiscentes en estado sólido.

Método experimental. Todos los reactivos utilizados se adquirieron en Sigma-Aldrich. Las nanopartículas de $CH_3NH_3PbBr_3$, P_{OA} , se sintetizaron mediante la adición de OABr (0.06 mmol) a una mezcla de OLA (0.3 mmol) y ODE (6.26 mmol) a 80 °C y en agitación. Posteriormente, se adicionó CH_3NH_3Br (0.04 mmol) y $PbBr_2$ (0.1 mmol). Las nanopartículas se precipitaron por adición de

acetona y se purificaron por centrifugación. De la misma forma, las nanopartículas P_{OA2} se prepararon siguiendo el mismo método, pero utilizando mayor concentración de OABr (0.16 mmol) y CH_3NH_3Br (0.24 mmol), en ausencia de ácido oleico.

Capítulo 5. Síntesis y propiedades ópticas de perovskitas con estructura bidimensional $(RNH_3)_2PbBr_4$

Las HOIP con una estructura inorgánica 2D, $(RNH_3)_2PbBr_4$, son materiales que han sido estudiados ampliamente como cristales y películas delgadas.^[23,46,59,94] En cuanto a perovskitas 2D en forma de nanopartículas, pocas estrategias se habían publicado antes del 2015 para su preparación. Los métodos utilizados eran nebulización, intercalación y precipitación.^[72-74] Después del éxito en la preparación de nanopartículas luminiscentes de perovskitas con estructura 3D descritas en la presente tesis, se exploró la extensión del método de inyección en caliente para la síntesis de nanopartículas de perovskita dispersables y con estructura 2D utilizando sales de alquilamonio para confinar el material a escala nanométrica. En este caso, la sal de alquilamonio jugaría un doble papel, el de formar parte de la estructura inorgánica 2D y el de actuar como ligando. Las sales de alquilamonio seleccionadas para llevar a cabo la síntesis fueron el bromuro de hexil-, octil- y octadecilamonio (HA, OA y ODA, respectivamente). Se estudió el efecto del tamaño de la cadena de dichas sales así como el de la adición de ácido oleico, sobre las propiedades ópticas y la procesabilidad de las nanopartículas. (*Journal of Materials Chemistry A* **2015**, 3, 14039-14045).

Brevemente, la síntesis se llevó a cabo mediante la inyección de $PbBr_2$ a una mezcla de bromuro de alquilamonio (RNH_3Br) y OLA en ODE a 80 °C. Posteriormente, se adicionó acetona para inducir la precipitación de las nanopartículas. Cabe destacar que utilizando ODA se obtuvieron nanopartículas luminiscentes (P_{ODA1}) y con una elevada dispersabilidad en tolueno, las cuales presentaron una banda de emisión estrecha en 397 nm y un PLQY del 21 % en disolución y 12 % en forma de película. Por el contrario, las perovskitas

preparadas con las sales de alquilamonio de cadena más corta fueron mucho menos emisivas (PLQY no medibles) y dispersables. El espectro de emisión de estas últimas presentó una banda ancha que se extiende hasta 600 nm aproximadamente. Llevando a cabo la síntesis en las mismas condiciones pero en ausencia de OLA, se observó que las perovskitas presentan una mejora en las propiedades (figura 5.2 y tabla 5.1), perovskitas P_{ODA2} , P_{OA2} , y P_{HA2} respectivamente. Por lo cual, la condición óptima seleccionada para la síntesis fue en ausencia de OLA.

En cuanto al efecto de la longitud de la cadena alquílica de la sal de amonio, se observó un desplazamiento de la banda de absorción a mayores energías con el incremento del tamaño de la cadena, desde 398 nm a 389 nm para P_{HA2} y P_{ODA2} , respectivamente (tabla 5.1). Este resultado concuerda con el efecto descrito en películas delgadas por otros autores.^[19,24,95] Con respecto a la fotoestabilidad en dispersión, las nanopartículas P_{ODA2} y P_{OA2} fueron las más fotoestables, con una disminución en la intensidad de emisión de solo 7 % después de 200 minutos de irradiación continua con luz UV (figura 5.3).

EL análisis por HRTEM mostró la formación de pequeñas nanopartículas que coexisten con material en forma las placas. El análisis por PXRD, realizados en colaboración con el Dr. Guillermo Mínguez Espallargas, demostró que la estructura de las perovskitas coincide con la estructura cristalina ortorrómbica (grupo espacial *Pbca*) de la perovskita $(RNH_3)_2PbBr_4$ (figura 5.4 y tabla 5.2).^[87,88,96] Además, los resultados de TGA y 1H NMR indicaron que las perovskitas están recubiertas con las sales de alquilamonio como ligando (figura 5.5).

Además, se demostró la estabilidad coloidal de las nanopartículas P_{ODA2} después de varios procesos de precipitación y redispersión (figura 5.6). También se demostró que P_{ODA2} se puede disolver en dimetilformamida para formar los precursores y luego volverse a formar ya sea por evaporación del disolvente o por re-precipitación en tolueno. Interesantemente, en este último proceso aumentó la formación de nanopartículas (P_{ODA2nm}) y el tamaño de las placas disminuyó (figura

5.7), aunque el PLQY fue más bajo (7%). Finalmente, se prepararon películas sólidas luminiscentes de nanopartículas de $P_{\text{ODA}2}$ las cuales mostraron propiedades ópticas similares a las nanopartículas en disolución (tabla 5.3).

En conclusión, se demostró la preparación de perovskitas cristalinas, luminiscentes, dispersables en tolueno y con una estructura 2D de $(\text{RNH}_3)_2\text{PbBr}_4$. La longitud de la cadena alquílica y la ausencia de ácido oleico juegan un papel en la formación y estabilidad coloidal de las perovskitas, siendo las perovskita 2D preparadas con el catión de cadena más larga la que presentó una mayor dispersabilidad, intensidad de luminiscencia (PLQY del 20 %) y estabilidad bajo irradiación UV. Estos materiales mostraron ser fácilmente procesables y por tanto de interés en aplicaciones optoelectrónicas.

Método Experimental. Para la síntesis de las perovskitas de $(\text{RNH}_3)_2\text{PbBr}_4$, $P_{\text{ODA}1}$, primero se adicionó bromuro de octadecilamonio (ODABr, 0.2 mmol) a una mezcla de OLA (0.3 mmol) y ODE (2 mL, 6.26 mmol) a 80 °C y en agitación. Luego, se adicionó el PbBr_2 (0.1 mmol) disuelto en dimetilformamida. Finalmente, las nanopartículas se precipitaron por adición de acetona y se purificaron por centrifugación. La síntesis de $P_{\text{OA}1}$, $P_{\text{HA}1}$ se llevó a cabo por el mismo procedimiento pero adicionando la sal de amonio correspondiente. De la misma manera se sintetizó $P_{\text{ODA}2}$, $P_{\text{OA}2}$ y $P_{\text{HA}2}$ pero en ausencia de OLA. Las películas de perovskita se prepararon por *spin-coating* (capítulo 3).

Capítulo 6. Química de superficie para obtener nanopartículas y películas sólidas de $\text{CH}_3\text{NH}_3\text{PbBr}_3$ muy luminiscentes

Como se demostró en el capítulo 4, las nanopartículas de $\text{CH}_3\text{NH}_3\text{PbBr}_3$ se pueden preparar con una alta dispersibilidad y luminiscencia (PLQY de hasta 83%) usando el método de inyección en caliente y ligandos de alquilamonio de cadena media.^[89,97] En 2015 Zhang et al.^[98] publicó otra interesante estrategia para la preparación de nanopartículas de $\text{CH}_3\text{NH}_3\text{PbBr}_3$ (PLQY de 70%) denominado método de re-precipitación asistida por ligando (LARP). El método consiste en la inyección de una disolución precursora en dimetilformamida, compuesta de una mezcla de $\text{CH}_3\text{NH}_3\text{X}$, PbX_2 y el ligando orgánico (octilamina y ácido oleico), en un solvente no polar (como tolueno) y a temperatura ambiente. Poco después, Huang et al.^[99] demostró el cambio de las propiedades ópticas de las nanopartículas de $\text{CH}_3\text{NH}_3\text{PbBr}_3$ con el tamaño siguiendo la misma estrategia, pero variando la temperatura del tolueno (0-60 °C) y usando oleilamina y OLA como ligandos (PLQY de hasta 93 %). Sin embargo, el rendimiento químico de la síntesis de las nanopartículas por el método LARP es limitado debido a la formación de material volumétrico.

Teniendo en cuenta estos resultados, el primer objetivo en este estudio fue alcanzar el máximo en las propiedades de emisión de las nanopartículas de $\text{CH}_3\text{NH}_3\text{PbBr}_3$, así como también prepararlas con un alto rendimiento químico. Para ello era necesario mejorar el recubrimiento orgánico y posiblemente la proporción de los componentes utilizados para la preparación de las nanopartículas. Además, nos enfocamos en explorar la preparación de películas sólidas de nanopartículas que conservaran las propiedades ópticas de las nanopartículas coloidales. El interés en la preparación de películas de nanopartículas está motivado por el hecho de que las películas de perovskita preparadas por los métodos a partir de disolución de los precursores son policristalinas y con una separación entre los granos que puede limitar la eficiencia en dispositivos optoelectrónicos.^[100-104] La preparación a partir de dispersiones

coloidales de nanopartículas podría mejorar la morfología de las películas. A este respecto, se planteó la hipótesis de que el ligando orgánico seleccionado, además de proporcionar una buena pasivación de la superficie de las nanopartículas, tendría que proporcionarles una baja tendencia a la agregación en disolución, permitir su ensamblaje en una película sólida compacta y ser compatible con el transporte de carga.

Estos objetivos se abordaron utilizando inicialmente el bromuro de 2-adamantilamonio (2ADBr) como único ligando y mediante el método de LARP. Además, considerando la afinidad con cucurbit[7]uril (CB) también se exploró la preparación de un sistema huésped-receptor en la superficie de las nanopartículas (figura 6.1).^[105,106] Sorprendentemente, las nanopartículas de $\text{CH}_3\text{NH}_3\text{PbBr}_3$ preparadas con 2ADBr como ligando, P_{AD} , presentaron una banda de emisión centrada en 520 nm (figura 6.1) y alcanzaron el máximo de eficiencia en la emisión con un PLQY $\approx 100\%$ (*Small* **2016**, *12*, 5245-5250). Por otra parte las nanopartículas preparadas en presencia de CB, $\text{P}_{\text{AD-CB}}$, presentaron un PLQY de 86 % y máximo de emisión en 519 nm (figura 6.1, tabla 6.1). Ambas nanopartículas mostraron una estructura cristalina cubica de $\text{CH}_3\text{NH}_3\text{PbBr}_3$, con un tamaño de 53 nm y 34 nm para P_{AD} y $\text{P}_{\text{AD-CB}}$ respectivamente (figura 6.2). El análisis por AFM reveló la formación de agregados de nanopartículas de P_{AD} con el incremento de la concentración (figura 6.3).

El análisis de la composición se llevó a cabo mediante TGA y ^1H RMN, los cuales revelaron que el rendimiento químico de la síntesis de las nanopartículas fue del 76 %. La interacción del CB con la superficie de las nanopartículas de $\text{P}_{\text{AD-CB}}$ se analizó registrando su espectro de ATR-FTIR y comparándolo con el de sus precursores (figura 6.4). En el espectro se observó que el máximo de la banda del CB en 1710 cm^{-1} , que corresponde a la vibración de estiramiento de los grupos carbonilos, se desplazó a 1734 cm^{-1} en el caso de $\text{P}_{\text{AD-CB}}$, indicando así la interacción de los carbonilos del CB con la superficie de las nanopartículas.

Los estudios de fotoestabilidad en disolución mostraron que la intensidad de emisión en función del tiempo de irradiación de P_{AD} disminuye un 25 % después de 180 minutos de irradiación continua con luz UV (figura 6.5), mientras que la de P_{AD-CB} permanece inalterada. Además, las disoluciones de P_{AD-CB} mostraron una mayor estabilidad en contacto con agua y bajo irradiación continua con luz UV (figura 6.6). Estos resultados indicaron que el CB como ligando reduce la descomposición de las nanopartículas por efecto de la humedad.

A pesar de las excepcionales propiedades ópticas de P_{AD} , el estudio de luminiscencia resuelta en el tiempo reveló tiempos de vida de emisión inusualmente largos en disolución (mayor a 200 ns, tabla 6.1). Tiempos de vida más cortos se obtuvieron después de un proceso de separación y dilución de las nanopartículas (figura 6.7), indicativo del efecto de la agregación de las nanopartículas en los tiempos de vida de luminiscencia.

Considerando las excelentes propiedades fotofísicas de las nanopartículas de $CH_3NH_3PbBr_3$ obtenidas con 2ADBr, posteriormente nos centramos en la optimización de la estabilidad coloidal de las nanopartículas, con el objetivo final de preparar películas sólidas de nanopartículas, para lo cual es importante usar nanopartículas que no se agreguen en disolución. Para ello, se exploró la combinación de ligandos, en particular 1 ó 2-adamantilamina y ácidos carboxílicos alquílicos (figura 6.8), para reducir la tendencia de agregación en la dispersión y a la vez preparar películas solidas de nanopartículas con óptimas propiedades de transporte (*Journal of Materials Chemistry C* **2018**, *6*, 6771-6777).

Utilizando este sistema binario de ligandos se prepararon con éxito nanopartículas coloidales de $CH_3NH_3PbBr_3$ (tabla 6.2 y tabla 6.3). Las nanopartículas de $CH_3NH_3PbBr_3$ con 2-adamantilamina (2ADA) mostraron las mejores propiedades fotofísicas, con bandas de emisión con máximos en 521 nm, PLQY cercanos al 100 % y tiempos de vida de luminiscencia menores a 50 ns (figura 6.9). Los altos rendimientos cuánticos, así como los tiempos de vida más cortos en comparación con los observados anteriormente, indicaron que el 2ADA permite un

recubrimiento eficiente de la superficie de la nanopartículas, mientras que el ácido carboxílico impide su agregación. Un análisis detallado por XPS de las nanopartículas de $\text{CH}_3\text{NH}_3\text{PbBr}_3$ con 2ADA y ácido propiónico, $\text{P}_{2\text{ADA-Propiónico}}$, demostró que la amina y el ácido carboxílico actúan como ligandos en la superficie de las nanopartículas (figura 6.10).

Posteriormente, se procedió a la preparación de películas de nanopartículas utilizando la técnica de *centrifugal casting*.^[83,125,126] Esta técnica nos permitió controlar el espesor y la homogeneidad de las películas por variación de la concentración de las nanopartículas de $\text{P}_{2\text{ADA-Propiónico}}$ en dispersión, obteniendo así películas sólidas de nanopartículas con un espesor de hasta 700 nm, aproximadamente (figura 6.13). La películas sólidas mantienen las propiedades ópticas del coloide, en particular un elevado PLQY de hasta 80 % (figura 6.14 y tabla 6.4).

Con la finalidad de evaluar las propiedades conductoras de las películas de nanopartículas, se preparó un dispositivo en colaboración con el Dr. Michele Sessolo. El dispositivo reveló buen transporte de carga y una moderada electroluminiscencia. Esta última se atribuyó a la falta de optimización en el dispositivo o de homogeneidad en la morfología y propiedades optoelectrónicas de la película. Para estudiar dichos efectos se realizó un análisis de la topografía y conductividad por AFM de una película solida de nanopartículas con un espesor de 291 nm (figura 6.15). La imagen de topografía de AFM mostró salientes y depresiones (rango ± 80 nm) en la morfología de la película, mientras que la imagen de AFM conductivo de la misma área reveló regiones con baja y alta conductividad, con máximos de corriente de 100 pA (figuras 6.16). Estos resultados indicaron que la heterogeneidad de la corriente observada en la película podría ser el limitante de la distribución de carga dentro de diodo, permitiendo un buen transporte de carga pero una electroluminiscencia ineficiente. No obstante, las áreas de alta conductividad en las imágenes de AFM conductivo indicaron la formación de regiones donde la interacción entre nanopartículas era muy eficiente,

debido a la fuerte interacción entre las moléculas de ADA, las cuales reducen la distancia entre las nanopartículas y permiten el ensamblaje en la película.

En conclusión, se demostró que la pasivación de las nanopartículas de $\text{CH}_3\text{NH}_3\text{PbBr}_3$ con bromuro de adamantilamonio como único ligando orgánico, permitió alcanzar el máximo de eficiencia en sus propiedades emisivas con un rendimiento cuántico de emisión de 100 %. Además, las nanopartículas coloidales se prepararon con alto rendimiento químico y estabilidad coloidal, manteniendo su estabilidad después de seis meses a temperatura ambiente. Las nanopartículas mostraron baja fotoestabilidad bajo irradiación continua con luz ultravioleta, sin embargo la capacidad del adamantilo para formar el sistema supramolecular con cucurbit[7]uril como ligando en la superficie mejoró la estabilidad bajo condiciones drásticas de irradiación y contacto con el agua.

Aunque el ligando de adamantilamonio mejoró las propiedades luminiscentes de las nanopartículas, se observó una agregación considerable en la dispersión y como consecuencia tiempo de vida de luminiscencia extraordinariamente largos. La combinación del sistema de ligandos 2-adamantilamina y ácidos carboxílico alquílicos permitió preparar nanopartículas coloidales con una alta dispersabilidad, luminiscencia y tiempos de vida cortos. Las nanopartículas coloidales de $\text{CH}_3\text{NH}_3\text{PbBr}_3$, en particular aquellas con ácido propiónico, permitió el ensamblaje eficaz de las nanopartículas en forma de películas solidas compactas con un espesor de varios cientos de nanómetros. Las películas mantuvieron las propiedades ópticas, en particular el rendimiento cuántico de emisión (de hasta 80 %) y además mostraron buenas propiedades de transporte de carga.

Método Experimental. La síntesis de las nanopartículas de $\text{CH}_3\text{NH}_3\text{PbBr}_3$ descritas en este capítulo se llevó a cabo por el método de LARP. Para la síntesis de P_{AD} se preparó una disolución precursora en dimetilformamida de $\text{CH}_3\text{NH}_3\text{Br}$, 2ADABr y PbBr_2 en una relación molar de 1.2:0.8:1.0. Seguidamente, la disolución precursora se inyectó en tolueno (5 mL) y se dejó en agitación a temperatura ambiente durante una hora. Posteriormente, las nanopartículas se

purificaron por centrifugación. La síntesis de P_{AD-CB} se llevó a cabo siguiendo el mismo procedimiento, pero adicionando además cucurbit[7]uril (CB) en una relación molar 2ADBr:CB de 12:1.

La síntesis de P_{2ADA-Propiónico}, se llevó a cabo por el mismo método, pero preparando una disolución precursora en dimetilformamida de CH₃NH₃Br, 2ADA, ácido propiónico y PbBr₂ en una relación molar de 1.0:1.1:0.8:9.5. Posteriormente, la disolución se inyectó en tolueno (5 mL) en agitación y a temperatura ambiente. Finalmente, las nanopartículas coloidales se purificaron por centrifugación. La síntesis de nanopartículas coloidales con diferentes ácidos carboxílicos y con 1-adamantilamina se llevó a cabo siguiendo el mismo procedimiento, pero sustituyendo la amina o el ácido correspondiente y manteniendo la misma relación molar entre los componentes. Las películas de nanopartículas se prepararon por el método de *centrifugal casting* (capítulo 3).

Capítulo 7. Síntesis de nanopartículas de $\text{CH}_3\text{NH}_3\text{PbBr}_3$ sin ligandos orgánicos y su preparación en forma de películas sólidas

Como se describió en el capítulo anterior, las películas de perovskita preparadas a partir de disoluciones de los precursores de la perovskita son películas policristalinas y su preparación con frecuencia es poco reproducible en cuanto a su morfología. Por lo tanto, existe un gran interés para la preparación de películas a partir de nanopartículas coloidales debido a su homogeneidad y propiedades optoelectrónicas. Teniendo en cuenta que la pasivación de las nanopartículas de perovskita con ligandos orgánicos puede interferir en las propiedades conductoras, el objetivo de este estudio fue la preparación de nanopartículas de perovskita sin ligandos orgánicos.

Existían pocos ejemplos de preparación de nanopartículas de $\text{CH}_3\text{NH}_3\text{PbBr}_3$ sin ligandos orgánicos, utilizando en particular los métodos de re-precipitación^[127-129] y de ablación laser.^[130,131] Por consiguiente, nos centramos en explorar la preparación de nanopartículas de $\text{CH}_3\text{NH}_3\text{PbBr}_3$ sin ligando orgánico, mediante el uso de un exceso de CH_3NH_3^+ y de la sal inorgánica de hexafluorofosfato de potasio (KPF_6), cuyo anión PF_6^- es más lipofílico y menos coordinante que el Br^- . Por lo cual, se planteó remplazar el exceso del catión CH_3NH_3^+ en la superficie de las nanopartículas por K^+ , teniendo en cuenta la mayor entalpia de formación de KBr que la de $\text{CH}_3\text{NH}_3\text{Br}$ (-394 kJ/mol vs -259 kJ/mol),^[132,133] con el objetivo final de formar nanopartículas coloidales estables. (*ACS Omega* **2018**, *3*, 1298-1303)

La síntesis se llevó a cabo mediante la inyección en acetato de etilo de una disolución precursora en dimetilformamida compuesta de $\text{CH}_3\text{NH}_3\text{Br}$, KPF_6 y PbBr_2 . Sorprendentemente, se obtuvieron nanopartículas estables en dispersión en acetato de etilo durante 3 horas. El espectro de absorción y emisión reveló una banda con máximos en 505 nm y 525 nm, respectivamente (figura 7.1). Además, no se observaron bandas de absorción adicionales que indicase la sustitución de

CH_3NH_3^+ por K^+ en la estructura cristalina de la perovskita.^[134] Las nanopartículas coloidales presentaron un PLQY de 17 % y un tiempo de vida media de 29 ns.

El análisis de la composición de las nanopartículas y de los sobrenadantes de la síntesis se llevó a cabo por ^1H NMR y ^{19}F NMR (figura 7.2). El espectro de ^{19}F NMR reveló que los aniones de PF_6^- permanecen en el sobrenadante y no en las nanopartículas. El espectro de PXRD demostró además que las nanopartículas tienen la estructura cristalina cúbica de $\text{CH}_3\text{NH}_3\text{PbBr}_3$ y un tamaño promedio de 62 nm (figura 7.3).^[52,135-137] Estos resultados indicaron que el catión K^+ no se incorporó en la estructura cristalina, por lo cual las nanopartículas de perovskita $\text{CH}_3\text{NH}_3\text{PbBr}$ están pasivadas con KBr y se denominaron MAP@K.

El efecto de K^+ se estudió además llevando a cabo la síntesis sin la adición de KPF_6 . El sólido naranja obtenido fue muy poco dispersable en acetato de etilo y el espectro de absorción presentó una banda poco intensa y una elevado *scattering*, lo cual se atribuyó a la formación de material $\text{CH}_3\text{NH}_3\text{PbBr}_3$ volumétrico de tamaño heterogéneo. Estos resultados confirmaron que el catión K^+ no solo pasiva la superficie sino que también permite la estabilidad coloidal de las nanopartículas de $\text{CH}_3\text{NH}_3\text{PbBr}_3$ en un disolvente medianamente polar y evitan el colapso de las nanopartículas.

Considerando la efectiva preparación de nanopartículas en forma de películas por el método de *centrifugal casting*,^[83] se preparó una película sólida de nanopartículas a partir de MAP@K en acetato de etilo. Sin embargo, ésta película presentó un recubrimiento incompleto del sustrato, figure 7.4. Por consiguiente, se realizó una optimización del método de deposición aumentando el volumen de la dispersión de nanopartículas (MAP@K_{F2}) y llevando a cabo la preparación a partir de una dispersión de MAP@K en una mezcla de acetato de etilo y tolueno (MAP@K_{F3}). Esta última condición permitió obtener películas homogéneas y luminiscentes con un máximo de emisión en 530 nm (PLQY de 7%).

Para el estudio de las propiedades conductoras de las películas de nanopartículas por AFM conductor, se preparó una película sólida sobre un sustrato conductor, MAP@K_{F4}, con un espesor promedio de 881 nm (figura 7.5). La imagen de la topografía por AFM mostró salientes y depresiones en un rango de ± 100 nm (figura 7.6). La imagen de conductividad mostró una distribución heterogénea de conductividad, con regiones de baja y alta magnitud de corriente. Las zonas de alta conductividad se atribuyeron a una alta densidad de nanopartículas con una conductividad eléctrica efectiva entre ellas. Las propiedades de transporte de carga fueron comparables con las observadas en una película policristalina de CH₃NH₃PbBr₃ preparada por *spin-coating* a partir de una disolución de los precursores en dimetilformamida.

En conclusión, en este estudio se demostró la preparación de nanopartículas de CH₃NH₃PbBr₃ libres de ligandos orgánicos, a partir de la adición de la sal de potasio en la disolución precursora y en exceso de metilamonio. Los cationes de potasio confinaron las nanopartículas a escala nanométrica, brindaron estabilidad coloidal en un disolvente moderadamente polar, y permitió el ensamble de las nanopartículas en forma de películas. El estudio de AFM conductor demostró la formación de regiones de alta conductividad distribuidas en diferentes regiones de la película. Se prevé que estos resultados promuevan el interés en nanopartículas híbridas desnudas debido a las nuevas oportunidades que ofrece este tipo de material.

Método Experimental. La síntesis de las nanopartículas de MAP@K se llevó a cabo por el método de LARP, utilizando acetato de etilo como disolvente. Para ello se preparó una disolución en dimetilformamida de CH₃NH₃Br, KPF₆ y PbBr₂ en una relación molar de 2:2:1. Seguidamente, la disolución precursora se inyectó en acetato de etilo (10 mL) en agitación y a temperatura ambiente. Posteriormente, las nanopartículas en disolución se centrifugaron y el sólido se dispersó en acetato de etilo. Por otra parte, la preparación de las películas se llevó a cabo por el método de *centrifugal casting*. La película MAP@K_{F1} se preparó añadiendo el coloide

MAP@K (10 ml) recién preparado a un tubo de centrifuga cónico (50 ml) que tenía el sustrato de vidrio en su parte inferior. La mezcla se centrifugó durante 7 minutos a 8000 rpm, y posteriormente, el sobrenadante se descartó. Finalmente, el sustrato de vidrio con la película sólida de nanopartículas depositadas se dejó secar en atmósfera de acetato de etilo a temperatura ambiente. MAP@K_{F2} se preparó siguiendo el método descrito para MAP@K_{F1} pero aumentando en volumen del colide a 20 ml, sin variar la concentración. MAP@K_{F3} se preparó siguiendo el método descrito para MAP@K_{F2} pero añadiendo tolueno (10 ml) al coloide en acetato de etilo antes de la etapa de centrifugación. Para el análisis por AFM la película MAP@K_{F4} se preparó siguiendo el método descrito para MAP@K_{F3} pero usando un sustrato de vidrio recubierto de ITO.

Capítulo 8. Conclusiones

Las conclusiones de esta tesis, enfocada en la síntesis de nanopartículas coloidales de perovskitas orgánicas-inorgánicas de bromuro de plomo, son:

- Se preparó por primera vez nanopartículas de perovskita $\text{CH}_3\text{NH}_3\text{PbBr}_3$ coloidales utilizando el método de inyección en caliente, un método sin plantilla. Las nanopartículas mostraron ser luminiscentes con rendimiento cuántico de emisión de 20 %. La sal de alquilamonio de longitud de cadena media junto con un surfactante, específicamente ácido oleico, controlaron el crecimiento y la dispersabilidad de las nanopartículas. Además, la dispersión de las nanopartículas en disolventes orgánicos permitió la preparación de una película sólida delgada con propiedades luminiscentes y de un dispositivo emisor de luz. La electroluminiscencia del dispositivo basado en la película de nanopartículas fue más alta que la observada en uno preparado con el mismo material volumétrico.
- Posteriormente, se prepararon nanopartículas coloidales de perovskita $\text{CH}_3\text{NH}_3\text{PbBr}_3$, con un rendimiento cuántico de emisión de hasta el 83 % siguiendo la misma estrategia. La longitud del catión de alquilamonio, la relación molar de los componentes de la perovskita y la eliminación del ácido oleico, fueron factores claves para las propiedades ópticas de las nanopartículas de perovskita $\text{CH}_3\text{NH}_3\text{PbBr}_3$. Además, las nanopartículas presentan buena fotoestabilidad bajo irradiación UV continua del coloide y conservan sus propiedades emisivas en estado sólido.
- Se preparó con éxito perovskitas luminiscentes y dispersables con estructura inorgánica 2D, $(\text{RNH}_3)_2\text{PbBr}_4$, por el método de inyección en caliente. El coloide obtenido con el bromuro de octadecilamonio presentó un rendimiento cuántico de emisión del 21% y una fácil procesabilidad.

- La pasivación de la superficie de las nanopartículas de $\text{CH}_3\text{NH}_3\text{PbBr}_3$ con bromuro de adamantilamonio como único ligando orgánico permitió obtener coloides con una excepcional luminiscencia (rendimiento del 100 %). Las nanopartículas coloidales se prepararon con alto rendimiento químico. Además, se mejoró la fotoestabilidad de las nanopartículas en disolución bajo irradiación continua y en contacto con agua a través de la formación del complejo adamantilamonio-cucurbit[7]uril en la superficie de las nanopartícula. Sin embargo, estos coloides mostraron una alta tendencia de agregación y, como consecuencia, tiempos de vida de emisión considerablemente largos.
- La síntesis nanopartículas de $\text{CH}_3\text{NH}_3\text{PbBr}_3$ usando la combinación de adamantilamina/ácido carboxílico alquílico como ligandos orgánicos disminuyó drásticamente la tendencia de agregación de las nanopartículas en disolución, y como consecuencia, el tiempo de vida de emisión de coloide, conservando a la vez su elevado rendimiento cuántico de emisión. Además, la sinergia de los ligandos orgánicos permitió el ensamblaje de las nanopartículas en una película sólida de nanopartículas con un espesor de varios cientos de nanómetros. Las películas sólidas de nanopartículas conservaron notablemente la morfología de las nanopartículas, así como también sus propiedades ópticas y presentaron además un buen transporte de carga.
- Finalmente, se preparó con éxito la síntesis de nanopartículas de $\text{CH}_3\text{NH}_3\text{PbBr}_3$ libres de ligandos orgánicos, mediante la adición de hexafluorofosfato de potasio y un exceso de bromuro de metilamonio a la disolución precursora. El catión de potasio en la superficie estabilizó las nanopartículas, el coloide en un disolvente moderadamente polar y permitió el ensamblaje de las nanopartículas en forma de películas sólidas. Además, las medidas de microscopia de fuerza atómica conductivo de la película de nanopartículas demostró la formación de regiones de alta conductividad la

cuales se pueden atribuir a la formación de regiones de nanopartículas con una efectiva conectividad eléctrica entre ellas. Las propiedades de transporte de carga de la película sólida de nanopartículas fueron comparables con las de una película delgada policristalina del material volumétrico.

References

- [1] Mitzi, D. B. In *Progress in Inorganic Chemistry*; John Wiley & Sons, Inc.: 1999; Vol. 48, p 1-121.
- [2] Burschka, J.; Pellet, N.; Moon, S.-J.; Humphry-Baker, R.; Gao, P.; Nazeeruddin, M. K.; Grätzel, M. *Nature* **2013**, *499*, 316-319.
- [3] Cai, B.; Xing, Y.; Yang, Z.; Zhang, W.-H.; Qiu, J. *Energy & Environmental Science* **2013**, *6*, 1480-1485.
- [4] Kim, H.-S.; Lee, C.-R.; Im, J.-H.; Lee, K.-B.; Moehl, T.; Marchioro, A.; Moon, S.-J.; Humphry-Baker, R.; Yum, J.-H.; Moser, J. E.; Grätzel, M.; Park, N.-G. *Scientific Reports* **2012**, *2*, 591.
- [5] Kojima, A.; Teshima, K.; Shirai, Y.; Miyasaka, T. *Journal of the American Chemical Society* **2009**, *131*, 6050-6051.
- [6] Liu, M.; Johnston, M. B.; Snaith, H. J. *Nature* **2013**, *501*, 395.
- [7] Kojima, A.; Ikegami, M.; Teshima, K.; Miyasaka, T. *Chemistry Letters* **2012**, *41*, 397-399.
- [8] Glazer, A. M. *Acta Crystallographica Section B* **1972**, *28*, 3384-3392.
- [9] Kieslich, G.; Sun, S.; Cheetham, A. K. *Chemical Science* **2014**, *5*, 4712-4715.
- [10] Weber, D. In *Zeitschrift für Naturforschung B* 1978; Vol. 33, p 1443.
- [11] Poglitsch, A.; Weber, D. *The Journal of Chemical Physics* **1987**, *87*, 6373-6378.
- [12] Wasylshen, R. E.; Knop, O.; Macdonald, J. B. *Solid State Communications* **1985**, *56*, 581-582.
- [13] Knop, O.; Wasylshen, R. E.; White, M. A.; Cameron, T. S.; Oort, M. J. M. V. *Canadian Journal of Chemistry* **1990**, *68*, 412-422.
- [14] Mitzi, D. B. *Journal of the Chemical Society, Dalton Transactions* **2001**, 1-12.
- [15] Mitzi, D. B. In *Progress in Inorganic Chemistry*; John Wiley & Sons, Inc.: 2007, p 1-121.
- [16] Saparov, B.; Mitzi, D. B. *Chemical Reviews* **2016**, *116*, 4558-4596.
- [17] Billing, D. G.; Lemmerer, A. *New Journal of Chemistry* **2008**, *32*, 1736-1746.
- [18] Gonzalez-Carrero, S.; Galian, R. E.; Pérez-Prieto, J. *Particle & Particle Systems Characterization* **2015**, *32*, 709-720.
- [19] Kitazawa, N.; Aono, M.; Watanabe, Y. *Thin Solid Films* **2010**, *518*, 3199-3203.
- [20] Kitazawa, N.; Aono, M.; Watanabe, Y. *Journal of Physics and Chemistry of Solids* **2011**, *72*, 1467-1471.
- [21] Naik, V. V.; Vasudevan, S. *The Journal of Physical Chemistry C* **2010**, *114*, 4536-4543.
- [22] Dohner, E. R.; Hoke, E. T.; Karunadasa, H. I. *Journal of the American Chemical Society* **2014**, *136*, 1718-1721.
- [23] Zhang, S.; Lanty, G.; Lauret, J.-S.; Deleporte, E.; Audebert, P.; Galmiche, L. *Acta Materialia* **2009**, *57*, 3301-3309.
- [24] Pradeesh, K.; Nageswara Rao, K.; Vijaya Prakash, G. *Journal of Applied Physics* **2013**, *113*, 083523.
- [25] Mitzi, D. B.; Wang, S.; Feild, C. A.; Chess, C. A.; Guloy, A. M. *Science* **1995**, *267*, 1473-1476.
- [26] Wang, S.; Mitzi, D. B.; Feild, C. A.; Guloy, A. *Journal of the American Chemical Society* **1995**, *117*, 5297-5302.

- [27] Li, Y. Y.; Lin, C. K.; Zheng, G. L.; Cheng, Z. Y.; You, H.; Wang, W. D.; Lin, J. *Chemistry of Materials* **2006**, *18*, 3463-3469.
- [28] Billing, D. G.; Lemmerer, A. *CrystEngComm* **2007**, *9*, 236-244.
- [29] Koutselas, I. B.; Ducasse, L.; Papavassiliou, G. C. *Journal of Physics: Condensed Matter* **1996**, *8*, 1217.
- [30] Takeoka, Y.; Asai, K.; Rikukawa, M.; Sanui, K. *Chemistry Letters* **2005**, *34*, 602-603.
- [31] Li, Y.; Zheng, G.; Lin, C.; Lin, J. *Solid State Sciences* **2007**, *9*, 855-861.
- [32] Tanaka, K.; Takahashi, T.; Ban, T.; Kondo, T.; Uchida, K.; Miura, N. *Solid State Communications* **2003**, *127*, 619-623.
- [33] Dvorak, M.; Wei, S.-H.; Wu, Z. *Physical Review Letters* **2013**, *110*, 016402.
- [34] Brandt, R. E.; Stevanović, V.; Ginley, D. S.; Buonassisi, T. *MRS Communications* **2015**, *5*, 265-275.
- [35] Manser, J. S.; Christians, J. A.; Kamat, P. V. *Chem Rev* **2016**, *116*, 12956-13008.
- [36] Ha, S. T.; Liu, X.; Zhang, Q.; Giovanni, D.; Sum, T. C.; Xiong, Q. *Advanced Optical Materials* **2014**, *2*, 838-844.
- [37] Kitazawa, N.; Watanabe, Y.; Nakamura, Y. *Journal of Materials Science* **2002**, *37*, 3585-3587.
- [38] Baikie, T.; Fang, Y.; Kadro, J. M.; Schreyer, M.; Wei, F.; Mhaisalkar, S. G.; Graetzel, M.; White, T. J. *Journal of Materials Chemistry A* **2013**, *1*, 5628.
- [39] Eperon, G. E.; Stranks, S. D.; Menelaou, C.; Johnston, M. B.; Herz, L. M.; Snaith, H. J. *Energy & Environmental Science* **2014**, *7*, 982.
- [40] Stoumpos, C. C.; Malliakas, C. D.; Kanatzidis, M. G. *Inorg Chem* **2013**, *52*, 9019-9038.
- [41] Knutson, J. L.; Martin, J. D.; Mitzi, D. B. *Inorganic Chemistry* **2005**, *44*, 4699-4705.
- [42] Tabuchi, Y.; Asai, K.; Rikukawa, M.; Sanui, K.; Ishigure, K. *Journal of Physics and Chemistry of Solids* **2000**, *61*, 837-845.
- [43] Suarez, B.; Gonzalez-Pedro, V.; Ripolles, T. S.; Sanchez, R. S.; Otero, L.; Mora-Sero, I. *The Journal of Physical Chemistry Letters* **2014**, *5*, 1628-1635.
- [44] Papavassiliou, G. C. *Progress in Solid State Chemistry* **1997**, *25*, 125-270.
- [45] Lanty, G.; Jemli, K.; Wei, Y.; Leymarie, J.; Even, J.; Lauret, J.-S.; Deleporte, E. *The Journal of Physical Chemistry Letters* **2014**, *5*, 3958-3963.
- [46] Cheng, Z.; Lin, J. *CrystEngComm* **2010**, *12*, 2646-2662.
- [47] Ahmad, S.; Baumberg, J. J.; Vijaya Prakash, G. *Journal of Applied Physics* **2013**, *114*, 233511.
- [48] Koutselas, I.; Bampoulis, P.; Maratou, E.; Evagelinou, T.; Pagona, G.; Papavassiliou, G. C. *The Journal of Physical Chemistry C* **2011**, *115*, 8475-8483.
- [49] Nobuaki, K. *Japanese Journal of Applied Physics* **1996**, *35*, 6202.
- [50] Abid, H.; Samet, A.; Dammak, T.; Mlayah, A.; Hlil, E. K.; Abid, Y. *Journal of Luminescence* **2011**, *131*, 1753-1757.
- [51] Ahmad, S.; Prakash, G. V.; SPIE: 2014; Vol. 8, p 13.
- [52] Baikie, T.; Barrow, N. S.; Fang, Y.; Keenan, P. J.; Slater, P. R.; Piltz, R. O.; Gutmann, M.; Mhaisalkar, S. G.; White, T. J. *Journal of Materials Chemistry A* **2015**, *3*, 9298-9307.
- [53] Mitzi, D. B. *Chemistry of Materials* **1996**, *8*, 791-800.
- [54] Saidaminov, M. I.; Abdelhady, A. L.; Murali, B.; Alarousu, E.; Burlakov, V. M.; Peng, W.; Dursun, I.; Wang, L.; He, Y.; Maculan, G.; Goriely, A.; Wu, T.; Mohammed, O. F.; Bakr, O. M. *Nat Commun* **2015**, *6*, 7586.

- [55] Maculan, G.; Sheikh, A. D.; Abdelhady, A. L.; Saidaminov, M. I.; Haque, M. A.; Murali, B.; Alarousu, E.; Mohammed, O. F.; Wu, T.; Bakr, O. M. *The Journal of Physical Chemistry Letters* **2015**, *6*, 3781-3786.
- [56] Mitzi, D. B. *Journal of Solid State Chemistry* **1999**, *145*, 694-704.
- [57] Mitzi, D. B. *Chemistry of Materials* **2001**, *13*, 3283-3298.
- [58] Yang, J.; Siempelkamp, B. D.; Liu, D.; Kelly, T. L. *ACS Nano* **2015**, *9*, 1955-1963.
- [59] Wei, Y.; Audebert, P.; Galmiche, L.; Lauret, J.-S.; Deleporte, E. *Materials* **2014**, *7*, 4789.
- [60] Mitzi, D. B.; Prikas, M. T.; Chondroudis, K. *Chemistry of Materials* **1999**, *11*, 542-544.
- [61] Chen, Q.; Zhou, H.; Hong, Z.; Luo, S.; Duan, H.-S.; Wang, H.-H.; Liu, Y.; Li, G.; Yang, Y. *Journal of the American Chemical Society* **2014**, *136*, 622-625.
- [62] Pérez-Prieto, J. *Photochemistry and Photobiology* **2013**, *89*, 1291-1298.
- [63] Talapin, D. V.; Rogach, A. L.; Kornowski, A.; Haase, M.; Weller, H. *Nano Letters* **2001**, *1*, 207-211.
- [64] Aguilera-Sigalat, J.; Rocton, S.; Sánchez-Royo, J. F.; Galian, R. E.; Pérez-Prieto, J. *RSC Advances* **2012**, *2*, 1632-1638.
- [65] Delgado-Pérez, T.; Bouchet Lydia, M.; de la Guardia, M.; Galian Raquel, E.; Pérez-Prieto, J. *Chemistry – A European Journal* **2013**, *19*, 11068-11076.
- [66] Agudelo-Morales, C. E.; Galian, R. E.; Pérez-Prieto, J. *Analytical Chemistry* **2012**, *84*, 8083-8087.
- [67] Gonzalez-Carrero, S.; de la Guardia, M.; Galian Raquel, E.; Pérez-Prieto, J. *ChemistryOpen* **2014**, *3*, 199-205.
- [68] Im, J.-H.; Lee, C.-R.; Lee, J.-W.; Park, S.-W.; Park, N.-G. *Nanoscale* **2011**, *3*, 4088-4093.
- [69] Im, J.-H.; Chung, J.; Kim, S.-J.; Park, N.-G. *Nanoscale Research Letters* **2012**, *7*, 353-353.
- [70] Kim, H.-S.; Lee, C.-R.; Im, J.-H.; Lee, K.-B.; Moehl, T.; Marchioro, A.; Moon, S.-J.; Humphry-Baker, R.; Yum, J.-H.; Moser, J. E.; Gratzel, M.; Park, N.-G. *Sci. Rep.* **2012**, *2*.
- [71] Lee, M. M.; Teuscher, J.; Miyasaka, T.; Murakami, T. N.; Snaith, H. J. *Science* **2012**, *338*, 643-647.
- [72] Audebert, P.; Clavier, G.; Alain-Rizzo, V.; Deleporte, E.; Zhang, S.; Lauret, J.-S.; Lanty, G.; Boissière, C. *Chemistry of Materials* **2009**, *21*, 210-214.
- [73] Saikumar, I.; Ahmad, S.; Baumberg, J. J.; Vijaya Prakash, G. *Scripta Materialia* **2012**, *67*, 834-837.
- [74] Papavassiliou, G. C.; Pagona, G.; Karousis, N.; Mousdis, G. A.; Koutselas, I.; Vassilakopoulou, A. *Journal of Materials Chemistry* **2012**, *22*, 8271-8280.
- [75] Papavassiliou, G. C.; Pagona, G.; Mousdis, G. A.; Karousis, N. *Chemical Physics Letters* **2013**, *570*, 80-84.
- [76] Kim, H.-S.; Im, S. H.; Park, N.-G. *The Journal of Physical Chemistry C* **2014**, *118*, 5615-5625.
- [77] Stranks, S. D.; Eperon, G. E.; Grancini, G.; Menelaou, C.; Alcocer, M. J. P.; Leijtens, T.; Herz, L. M.; Petrozza, A.; Snaith, H. J. *Science* **2013**, *342*, 341.
- [78] Snaith, H. J. *The Journal of Physical Chemistry Letters* **2013**, *4*, 3623-3630.
- [79] Era, M.; Morimoto, S.; Tsutsui, T.; Saito, S. *Applied Physics Letters* **1994**, *65*, 676-678.
- [80] Hattori, T.; Taira, T.; Era, M.; Tsutsui, T.; Saito, S. *Chemical Physics Letters* **1996**, *254*, 103-108.
- [81] Chondroudis, K.; Mitzi, D. B. *Chemistry of Materials* **1999**, *11*, 3028-3030.
- [82] Suzuki, K.; Kobayashi, A.; Kaneko, S.; Takehira, K.; Yoshihara, T.; Ishida, H.; Shiina, Y.; Oishi, S.; Tobita, S. *Physical Chemistry Chemical Physics* **2009**, *11*, 9850-9860.

- [83] Kim, J. Y.; Adinolfi, V.; Sutherland, B. R.; Voznyy, O.; Kwon, S. J.; Kim, T. W.; Kim, J.; Ihee, H.; Kemp, K.; Adachi, M.; Yuan, M.; Kramer, I.; Zhitomirsky, D.; Hoogland, S.; Sargent, E. H. *Nature Communications* **2015**, *6*, 7772.
- [84] Wadhavane, P. D.; Galian, R. E.; Izquierdo, M. A.; Aguilera-Sigalat, J.; Galindo, F.; Schmidt, L.; Burguete, M. I.; Pérez-Prieto, J.; Luis, S. V. *Journal of the American Chemical Society* **2012**, *134*, 20554-20563.
- [85] Audebert, P.; Clavier, G.; Alain-Rizzo, V. r.; Deleporte, E.; Zhang, S.; Lauret, J.-S. b.; Lanty, G. t.; Boissière, C. d. *Chemistry of Materials* **2009**, *21*, 210-214.
- [86] Vincent, B. R.; Robertson, K. N.; Cameron, T. S.; Knop, O. *Canadian Journal of Chemistry* **1987**, *65*, 1042-1046.
- [87] Pawley, G. *Journal of Applied Crystallography* **1981**, *14*, 357-361.
- [88] Coelho, A. A. In *TOPAS-Academic, 4.1 ed.*; TOPAS-Academic, 4.1 ed. Coelho Software: Brisbane, Australia, 2007.
- [89] Schmidt, L. C.; Pertegás, A.; Gonzalez-Carrero, S.; Malinkiewicz, O.; Agouram, S.; Mínguez Espallargas, G.; Bolink, H. J.; Galian, R. E.; Pérez-Prieto, J. *Journal of the American Chemical Society* **2014**, *136*, 850-853.
- [90] Muthu, C.; Nagamma, S. R.; Nair, V. C. *RSC Advances* **2014**, *4*, 55908-55911.
- [91] Aygüler, M. F.; Weber, M. D.; Puscher, B. M. D.; Medina, D. D.; Docampo, P.; Costa, R. D. *The Journal of Physical Chemistry C* **2015**, *119*, 12047-12054.
- [92] Noel, N. K.; Abate, A.; Stranks, S. D.; Parrott, E. S.; Burlakov, V. M.; Goriely, A.; Snaith, H. J. *ACS Nano* **2014**, *8*, 9815-9821.
- [93] Shkrob, I. A.; Marin, T. W. *The Journal of Physical Chemistry Letters* **2014**, *5*, 1066-1071.
- [94] Zhang, S.; Audebert, P.; Wei, Y.; Al Choueiry, A.; Lanty, G.; Bréhier, A.; Galmiche, L.; Clavier, G.; Boissière, C.; Lauret, J.-S.; Deleporte, E. *Materials* **2010**, *3*.
- [95] Takeoka, Y.; Asai, K.; Rikukawa, M.; Sanui, K. *Bulletin of the Chemical Society of Japan* **2006**, *79*, 1607-1613.
- [96] Kitazawa, N.; Aono, M.; Watanabe, Y. *Thin Solid Films* **2010**, *518*, 3199-3203.
- [97] Gonzalez-Carrero, S.; Galian, R. E.; Perez-Prieto, J. *Journal of Materials Chemistry A* **2015**, *3*, 9187-9193.
- [98] Zhang, F.; Zhong, H.; Chen, C.; Wu, X.-g.; Hu, X.; Huang, H.; Han, J.; Zou, B.; Dong, Y. *ACS Nano* **2015**, *9*, 4533-4542.
- [99] Huang, H.; Susha Andrei, S.; Kershaw Stephen, V.; Hung Tak, F.; Rogach Andrey, L. *Advanced Science* **2015**, *2*, 1500194.
- [100] Ono, L. K.; Qi, Y. *The Journal of Physical Chemistry Letters* **2016**, *7*, 4764-4794.
- [101] Long, R.; Liu, J.; Prezhdo, O. V. *Journal of the American Chemical Society* **2016**, *138*, 3884-3890.
- [102] Son, D.-Y.; Lee, J.-W.; Choi, Y. J.; Jang, I.-H.; Lee, S.; Yoo, P. J.; Shin, H.; Ahn, N.; Choi, M.; Kim, D.; Park, N.-G. *Nature Energy* **2016**, *1*, 16081.
- [103] Lee, B.; Lee, S.; Cho, D.; Kim, J.; Hwang, T.; Kim, K. H.; Hong, S.; Moon, T.; Park, B. *ACS Applied Materials & Interfaces* **2016**, *8*, 30985-30991.
- [104] Li, X.; Zhao, Y.-B.; Fan, F.; Levina, L.; Liu, M.; Quintero-Bermudez, R.; Gong, X.; Quan, L. N.; Fan, J.; Yang, Z.; Hoogland, S.; Voznyy, O.; Lu, Z.-H.; Sargent, E. H. *Nature Photonics* **2018**, *12*, 159-164.
- [105] Assaf, K. I.; Nau, W. M. *Chemical Society Reviews* **2015**, *44*, 394-418.
- [106] Liu, S.; Ruspic, C.; Mukhopadhyay, P.; Chakrabarti, S.; Zavalij, P. Y.; Isaacs, L. *Journal of the American Chemical Society* **2005**, *127*, 15959-15967.

- [107] Zhu, F.; Men, L.; Guo, Y.; Zhu, Q.; Bhattacharjee, U.; Goodwin, P. M.; Petrich, J. W.; Smith, E. A.; Vela, J. *ACS Nano* **2015**, *9*, 2948-2959.
- [108] Frances-Soriano, L.; Gonzalez-Bejar, M.; Perez-Prieto, J. *Nanoscale* **2015**, *7*, 5140-5146.
- [109] Gonzalez-Carrero, S.; Francés-Soriano, L.; González-Béjar, M.; Agouram, S.; Galian, R. E.; Pérez-Prieto, J. *Small* **2016**, *12*, 5245-5250.
- [110] Krajčovič, J.; Kovalenko, A.; Heinrichová, P.; Vala, M.; Weiter, M. *Journal of Luminescence* **2016**, *175*, 94-99.
- [111] Kovalenko, A.; Yumusak, C.; Heinrichova, P.; Stritesky, S.; Fekete, L.; Vala, M.; Weiter, M.; Sariciftci, N. S.; Krajcovic, J. *Journal of Materials Chemistry C* **2017**, *5*, 4716-4723.
- [112] Yan, H.; Hohman, J. N.; Li, F. H.; Jia, C.; Solis-Ibarra, D.; Wu, B.; Dahl, J. E. P.; Carlson, R. M. K.; Tkachenko, B. A.; Fokin, A. A.; Schreiner, P. R.; Vailionis, A.; Kim, T. R.; Devereaux, T. P.; Shen, Z.-X.; Melosh, N. A. *Nat Mater* **2017**, *16*, 349-355.
- [113] Shamsi, J.; Rastogi, P.; Caligiuri, V.; Abdelhady, A. L.; Spirito, D.; Manna, L.; Krahne, R. *ACS Nano* **2017**, *11*, 10206-10213.
- [114] Acik, M.; Park, I. K.; Koritala, R. E.; Lee, G.; Rosenberg, R. A. *Journal of Materials Chemistry A* **2018**, *6*, 1423-1442.
- [115] Huang, H.; Raith, J.; Kershaw, S. V.; Kalytchuk, S.; Tomanec, O.; Jing, L.; Susha, A. S.; Zboril, R.; Rogach, A. L. *Nature Communications* **2017**, *8*, 996.
- [116] Lashkor, M.; Rawson, F. J.; Preece, J. A.; Mendes, P. M. *Analyst* **2014**, *139*, 5400-5408.
- [117] Lashkor, M.; Rawson, F. J.; Preece, J. A.; Mendes, P. M. *The Analyst* **2014**, *139*, 5400-5408.
- [118] Huang, H.; Polavarapu, L.; Sichert, J. A.; Susha, A. S.; Urban, A. S.; Rogach, A. L. *NPG Asia Mater* **2016**, *8*, e328.
- [119] Gonzalez-Carrero, S.; Galian, R. E.; Pérez-Prieto, J. *Optics Express* **2016**, *24*, A285-A301.
- [120] Brandt, R. E.; Poindexter, J. R.; Gorai, P.; Kurchin, R. C.; Hoyer, R. L. Z.; Nienhaus, L.; Wilson, M. W. B.; Polizzotti, J. A.; Sereika, R.; Žaltauskas, R.; Lee, L. C.; MacManus-Driscoll, J. L.; Bawendi, M.; Stevanović, V.; Buonassisi, T. *Chemistry of Materials* **2017**, *29*, 4667-4674.
- [121] Gong, K.; Zeng, Y.; Kelley, D. F. *The Journal of Physical Chemistry C* **2013**, *117*, 20268-20279.
- [122] Chirvony, V. S.; Gonzalez-Carrero, S.; Suárez, I.; Galian, R. E.; Sessolo, M.; Bolink, H. J.; Martínez-Pastor, J. P.; Pérez-Prieto, J. *The Journal of Physical Chemistry C* **2017**, *13381-13390*.
- [123] Kagan, C. R.; Murray, C. B. *Nature Nanotechnology* **2015**, *10*, 1013-1026.
- [124] Lin, Q.; Yun, H. J.; Liu, W.; Song, H.-J.; Makarov, N. S.; Isaienko, O.; Nakotte, T.; Chen, G.; Luo, H.; Klimov, V. I.; Pietryga, J. M. *Journal of the American Chemical Society* **2017**, *139*, 6644-6653.
- [125] Kim, Y.; Yassitepe, E.; Voznyy, O.; Comin, R.; Walters, G.; Gong, X.; Kanjanaboos, P.; Nogueira, A. F.; Sargent, E. H. *ACS Applied Materials & Interfaces* **2015**, *7*, 25007-25013.
- [126] Qin, C.; Matsushima, T.; Sandanayaka, A. S. D.; Tsuchiya, Y.; Adachi, C. *The Journal of Physical Chemistry Letters* **2017**, *8*, 5415-5421.
- [127] Tachikawa, T.; Karimata, I.; Kobori, Y. *The Journal of Physical Chemistry Letters* **2015**, *6*, 3195-3201.
- [128] Umemoto, K.; Pu, Y.-J.; Yumusak, C.; Scharber, M. C.; White, M. S.; Sariciftci, N. S.; Yoshida, T.; Matsui, J.; Uji-i, H.; Masuhara, A. *Microsystem Technologies* **2018**, *24*, 619-623.

- [129] Li, Y.; Galisteo-Lopez, J. F.; Calvo, M. E.; Miguez, H. *ACS Appl Mater Interfaces* **2017**, *9*, 35505-35510.
- [130] Amendola, V.; Fortunati, I.; Marega, C.; Abdelhady, A. L.; Saidaminov, M. I.; Bakr, O. M. *Chemphyschem* **2017**, *18*, 1047-1054.
- [131] Lamberti, F.; Litti, L.; De Bastiani, M.; Sorrentino, R.; Gandini, M.; Meneghetti, M.; Petrozza, A. *Advanced Energy Materials* **2017**, *7*, 1601703.
- [132] Pedley, J. B. *Thermochemical data and structures of organic compounds I I*; Thermodynamics Research Center: College Station, Tex, 1994.
- [133] Lide, D. R. *CRC Handbook of Chemistry and Physics, 85th Edition*; Taylor & Francis, 2004.
- [134] Tarasova, A. Y.; Isaenko, L. I.; Kesler, V. G.; Pashkov, V. M.; Yelisseyev, A. P.; Denysyuk, N. M.; Khyzhun, O. Y. *Journal of Physics and Chemistry of Solids* **2012**, *73*, 674-682.
- [135] Chen, F.; Zhu, C.; Xu, C.; Fan, P.; Qin, F.; Gowri Manohari, A.; Lu, J.; Shi, Z.; Xu, Q.; Pan, A. *Journal of Materials Chemistry C* **2017**, *5*, 7739-7745.
- [136] Peng, W.; Wang, L.; Murali, B.; Ho, K.-T.; Bera, A.; Cho, N.; Kang, C.-F.; Burlakov, V. M.; Pan, J.; Sinatra, L.; Ma, C.; Xu, W.; Shi, D.; Alarousu, E.; Goriely, A.; He, J.-H.; Mohammed, O. F.; Wu, T.; Bakr, O. M. *Advanced Materials* **2016**, *28*, 3383-3390.
- [137] Zhang, Z.-Y.; Wang, H.-Y.; Zhang, Y.-X.; Li, K.-J.; Zhan, X.-P.; Gao, B.-R.; Chen, Q.-D.; Sun, H.-B. *Physical Chemistry Chemical Physics* **2017**, *19*, 2217-2224.
- [138] Moerman, D.; Eperon, G. E.; Pecht, J. T.; Ginger, D. S. *Chemistry of Materials* **2017**, *29*, 5484-5492.
- [139] Kutes, Y.; Zhou, Y.; Bosse, J. L.; Steffes, J.; Padture, N. P.; Huey, B. D. *Nano Letters* **2016**, *16*, 3434-3441.
- [140] Shi, D.; Adinolfi, V.; Comin, R.; Yuan, M.; Alarousu, E.; Buin, A.; Chen, Y.; Hoogland, S.; Rothenberger, A.; Katsiev, K.; Losovyj, Y.; Zhang, X.; Dowben, P. A.; Mohammed, O. F.; Sargent, E. H.; Bakr, O. M. *Science* **2015**, *347*, 519.
- [141] Yang, K.; Li, F.; Veeramalai, C. P.; Guo, T. *Applied Physics Letters* **2017**, *110*, 083102.

List of Publications

Published articles related with the thesis:

Chapter 4.

1. Schmidt, L. C.; Pertegás, A.; **Gonzalez-Carrero, S.**; Malinkiewicz, O.; Agouram, S.; Mínguez Espallargas, G.; Bolink, H. J.; Galian, R. E.; Pérez-Prieto, J., Nontemplate Synthesis of $\text{CH}_3\text{NH}_3\text{PbBr}_3$ Perovskite Nanoparticles. *Journal of the American Chemical Society* **2014**, *136* (3), 850-853.
Impact Factor (JCR): 12.113, Quartile: Q1, Cited by: 475
2. **Gonzalez-Carrero, S.**; Galian, R. E.; Pérez-Prieto, J., Maximizing the emissive properties of $\text{CH}_3\text{NH}_3\text{PbBr}_3$ perovskite nanoparticles. *Journal of Materials Chemistry A* **2015**, *3* (17), 9187-9193.
Invited contribution of special issue “perovskite solar cell”.
Impact Factor (JCR): 8.262, Quartile: Q1, Cited by: 160

Chapter 5.

3. **Gonzalez-Carrero, S.**; Espallargas, G. M.; Galian, R. E.; Pérez-Prieto, J., Blue-luminescent organic lead bromide perovskites: highly dispersible and photostable materials. *Journal of Materials Chemistry A* **2015**, *3* (26), 14039-14045.
Invited contribution of special issue “Perovskite Solar Cell”.
Impact Factor (JCR): 8.262, Quartile: Q1, Cited by: 46

Chapter 6.

4. **Gonzalez-Carrero, S.**; Francés-Soriano, L.; González-Béjar, M.; Agouram, S.; Galian, R. E.; Pérez-Prieto, J., The Luminescence of $\text{CH}_3\text{NH}_3\text{PbBr}_3$ Perovskite Nanoparticles Crests the Summit and Their Photostability under Wet Conditions is Enhanced. *Small* **2016**, *12* (38), 5245-5250.
Impact Factor (JCR): 8.643, Quartile: Q1, Cited by: 27
5. **Gonzalez-Carrero, S.**; Martínez-Sarti, L.; Sessolo, M.; Galian, R. E.; Pérez-Prieto, J., Highly photoluminescent, dense solid films from organic-capped $\text{CH}_3\text{NH}_3\text{PbBr}_3$ perovskite colloids. *Journal of Materials Chemistry C* **2018**, *6* (25), 6771-6777.
Impact Factor (JCR): 5.976, Quartile: Q1, Cited by: 1

Chapter 7.

6. **Gonzalez-Carrero, S.**; Schmidt, L. C.; Rosa-Pardo, I.; Martínez-Sarti, L.; Sessolo, M.; Galian, R. E.; Pérez-Prieto, J., Colloids of Naked $\text{CH}_3\text{NH}_3\text{PbBr}_3$ Perovskite Nanoparticles: Synthesis, Stability, and Thin Solid Film Deposition. *ACS Omega* **2018**, *3* (1), 1298-1303.
Invited contribution; Impact Factor (JCR): --, Quartile: --, Cited by: 1

Other publications generated from this thesis:

1. **Gonzalez-Carrero, S.**; de la Guardia, M.; Galian, R. E.; Pérez-Prieto, J., Pyrene-Capped CdSe@ZnS Nanoparticles as Sensitive Flexible Oxygen Sensors in Non-Aqueous Media. *ChemistryOpen* **2014**, 3 (5), 199-205.
Impact Factor (JCR): 3.250, Quartile: Q2, Cited by: 8
2. **Gonzalez-Carrero, S.**; Agudelo-Morales, C.; Guardia, M. d. l.; Galian, R. E.; Pérez-Prieto, J., Three independent channel nanohybrids as fluorescent probes. *RSC Advances* **2015**, 5 (109), 90065-90070.
Impact Factor (JCR): 3.250, Quartile: Q2, Cited by: 1
3. **Gonzalez-Carrero, S.**; Galian, R. E.; Pérez-Prieto, J., Organometal Halide Perovskites: Bulk Low-Dimension Materials and Nanoparticles. *Particle & Particle Systems Characterization* **2015**, 32 (7), 709-720.
Impact Factor (JCR): 4.367, Quartile: Q1, Cited by: 60
4. **Gonzalez-Carrero, S.**; Galian, R. E.; Pérez-Prieto, J., Organic-inorganic and all-inorganic lead halide nanoparticles [Invited]. *Optics Express* **2016**, 24 (2), A285-A301.
Invited contribution
Impact Factor (JCR): 3.307, Quartile: Q1, Cited by: 26
5. Francés-Soriano, L.; **Gonzalez-Carrero, S.**; Navarro-Raga, E.; Galian, R. E.; González-Béjar, M.; Pérez-Prieto, J., Efficient Cementing of CH₃NH₃PbBr₃ Nanoparticles to Upconversion Nanoparticles Visualized by Confocal Microscopy. *Advanced Functional Materials* **2016**, 26 (28), 5131-5138.
Impact Factor (JCR):12.124, Quartile: Q1, Cited by: 6
6. Chirvony, V. S.; **Gonzalez-Carrero, S.**; Suárez, I.; Galian, R. E.; Sessolo, M.; Bolink, H. J.; Martínez-Pastor, J. P.; Pérez-Prieto, J., Delayed Luminescence in Lead Halide Perovskite Nanocrystals. *The Journal of Physical Chemistry C* **2017**, 13381-13390.
Impact Factor (JCR):4.484, Quartile: Q2, Cited by: 19
7. Godin, R.; Ma, X.; **Gonzalez-Carrero, S.**; Du, T.; Li, X.; Lin, C.-T.; McLachlan, M. A.; Galian, R. E.; Pérez-Prieto, J.; Durrant, J. R., Tuning Charge Carrier Dynamics and Surface Passivation in Organolead Halide Perovskites with Capping Ligands and Metal Oxide Interfaces. *Advanced Optical Materials* **2018**, 6 (5), 1701203.
Impact Factor (JCR):7.430 Quartile: Q1, Cited by: 4

8. **Gonzalez-Carrero, S.;** Pérez-Prieto, J., Colloidal photoemissive nanoparticles. *ChemTexts* **2018**, 4 (3), 8.

Impact Factor (Journal Citation Reports)

Nontemplate Synthesis of $\text{CH}_3\text{NH}_3\text{PbBr}_3$ Perovskite Nanoparticles

Luciana C. Schmidt,^{†,§} Antonio Pertegás,[†] Soranyel González-Carrero,[†] Olga Malinkiewicz,[†] Said Agouram,[‡] Guillermo Mínguez Espallargas,[†] Henk J. Bolink,[†] Raquel E. Galian,^{*,†} and Julia Pérez-Prieto^{*,†}

[†]Instituto de Ciencia Molecular (ICMol), Universidad de Valencia, Catedrático José Beltrán 2, 46980 Paterna, Valencia, Spain

[‡]Department of Applied Physics and Electromagnetism, University of Valencia, Edif. Investigación, c/Dr. Moliner 50, 46100 Burjassot, Spain

Supporting Information

ABSTRACT: To date, there is no example in the literature of free, nanometer-sized, organolead halide $\text{CH}_3\text{NH}_3\text{PbBr}_3$ perovskites. We report here the preparation of 6 nm-sized nanoparticles of this type by a simple and fast method based on the use of an ammonium bromide with a medium-sized chain that keeps the nanoparticles dispersed in a wide range of organic solvents. These nanoparticles can be maintained stable in the solid state as well as in concentrated solutions for more than three months, without requiring a mesoporous material. This makes it possible to prepare homogeneous thin films of these nanoparticles by spin-coating on a quartz substrate. Both the colloidal solution and the thin film emit light within a narrow bandwidth of the visible spectrum and with a high quantum yield (ca. 20%); this could be advantageous in the design of optoelectronic devices.

Organic–inorganic hybrid materials combine useful properties of both organic and inorganic materials, such as plastic mechanical properties (organic material) and good electronic mobility (inorganic material).¹ Among this type of materials, there is presently a great interest in organolead halide perovskites of general APbX_3 (A = organic ammonium cation, X = halide anion) stoichiometry. In these compounds, the lead cations are in a 6-fold coordination and are surrounded by an octahedron of halide anions together with the ammonium cations in a 12-fold cuboctahedral coordination.^{1,2} These perovskites are versatile materials prepared from abundant and low cost starting compounds and exhibit very interesting features, such as unique optical³ and excitonic properties,⁴ as well as electrical conductivity.⁵

Specifically, the iodide and bromide versions of $\text{CH}_3\text{NH}_3\text{PbX}_3$ have led to a breakthrough performance in thin film solar cells.^{3,5–7}

First reports of the use of these perovskites in photovoltaic applications were obtained with solar cells employing mesoporous metal oxides, such as titania^{3–5,7,8} and alumina,^{6,8–10} whose porosity permits the formation of $\text{CH}_3\text{NH}_3\text{PbX}_3$ perovskite nanoparticulate material, i.e., the confinement of the array extending in three dimensions to the nanometer scale to build zero-dimensional material. Optimization of the device, specifically filling the pores with the

perovskites, has led to very highly efficient devices as was recently reported by the Grätzel group.³ It has also been demonstrated that a thin film of bulk $\text{CH}_3\text{NH}_3\text{PbX}_3$ deposited on top of an n-type metal oxide leads to solar cells with efficiencies around 10.9%.¹⁰ This is particularly interesting as it indicates that the perovskite layer (the thickness was around 300 nm) not only functions as the principal light absorber¹¹ but also as the transporter of electrons and/or holes.¹² Hence, $\text{CH}_3\text{NH}_3\text{PbX}_3$ perovskites, both as confined nanomaterials in nanoporous materials,^{3–12} and as “bulk” thin films, have led to efficient solar cells. Thin films prepared with APbX_3 perovskite nanoparticles could outperform the above-mentioned architectures, but no suitable synthetic procedure to obtain particles with sizes as small as several nanometers has yet been reported.

The availability of stable colloidal solutions of $\text{CH}_3\text{NH}_3\text{PbX}_3$ nanoparticles and mainly those with sizes below 10 nm would enable the preparation of new device architectures that could further enhance solar cell performance and elucidate perovskite operational mechanisms. Such colloidal solutions of nanometer-sized APbX_3 perovskites have, to our knowledge, not been reported. We presumed that by following the strategies described for the synthesis of quantum dots (zero-dimensional materials), a good organic capping agent, such as long alkyl chain amines, would favor the formation of $\text{CH}_3\text{NH}_3\text{PbX}_3$ nanoparticles, which would eventually be dispersible in aprotic solvents.^{13–15}

In this report, we demonstrate the preparation of highly crystalline 6 nm-sized $\text{CH}_3\text{NH}_3\text{PbX}_3$ nanoparticles as stable colloidal solutions. Highly fluorescent thin films and first electroluminescent devices were prepared using the colloidal solution of these nanoparticles.

The perovskite nanoparticles were prepared using bromide, rather than iodide, due to the higher stability of the former,¹⁶ and due to the most interesting luminescent properties. The nanoparticles were synthesized using a simple and reliable preparation method in which a mixture of $\text{CH}_3\text{NH}_3\text{Br}$ and a medium or long chain alkyl ammonium bromide was reacted with PbBr_2 in the presence of oleic acid and octadecene. We propose that while the methyl ammonium cations are embedded in the voids of a set of corner-sharing PbX_6 octahedra (Figure 1), the longer alkyl chain cations only fit the periphery of the octahedra set with their chains dangling

Received: October 31, 2013

Published: January 3, 2014

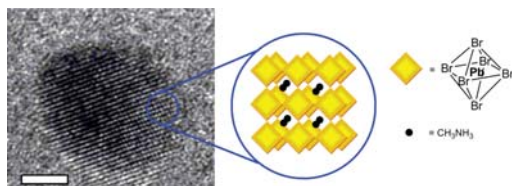


Figure 1. HRTEM image of an isolated perovskite nanoparticle (scale bar 2 nm) and schematic representation of an array of corner sharing MX_6 octahedra confined in the three dimensions due to the organic capping.

outside it. Thus, these ammonium ions would act as the capping ligands of the nanoparticle, limiting the growth of the array extending in three dimensions. This strategy produces intrinsic perovskite nanoparticles stabilized by the alkyl chains.

To prove the preparation of the $\text{CH}_3\text{NH}_3\text{PbX}_3$ perovskite nanoparticles was achievable, besides adding methylammonium bromide ($\text{CH}_3\text{NH}_3\text{Br}$), the long alkyl chain ammonium cation octylammonium bromide or octadecylammonium bromide was used in the preparation of the material. This longer chain alkyl ammonium cation might act as a better capping ligand to isolate the nanoparticle core, while nanoparticles with the methylammonium cation might be advantageous in the application of the nanoparticles in solar cells.¹⁷

In all the cases, the addition of the long chain ammonium bromide to a warm (80 °C) solution of oleic acid in octadecene (a noncoordinating solvent), was followed by the consecutive addition of methylammonium bromide and PbBr_2 , and right after, addition of acetone induced the precipitation of a yellow solid from the solution. The methylammonium salt and the lead bromide had previously been dissolved in a small amount of dimethylformamide (DMF) to improve their solubility in the media. The total ammonium salt concentration was kept at 0.045 M and a PbBr_2 equimolar concentration was used. Remarkably, the solid proved to be dispersible in toluene, thus suggesting the formation of perovskite nano-hybrids. For comparison's sake, the reaction between the $\text{CH}_3\text{NH}_3\text{Br}$ and the lead bromide under the same conditions led to an orange solid that could hardly be dispersed in toluene.

To determine the best molar ratio between the ammonium salts, preliminary assays were carried out using octadecylammonium bromide. The $\text{CH}_3(\text{CH}_2)_{17}\text{NH}_3\text{Br}/\text{CH}_3\text{NH}_3\text{Br}$ molar ratios used were 0.5:0.5, 0.6:0.4, and 0.7:0.3 and the samples were labeled as $\text{P}_{\text{ODA}1}$, $\text{P}_{\text{ODA}2}$, and $\text{P}_{\text{ODA}3}$, respectively, in which P refers to perovskite, ODA refers to octadecylammonium cation, and 1,2,3 indicates an increasing molar ratio.

The UV-visible absorption spectra of the colloidal solutions exhibit a peak at ca. 525 nm, 16 nm blue-shifted compared to that of $\text{CH}_3\text{NH}_3\text{PbBr}_3$ bulk that can be attributed mainly to the particle-size quantum confinement effect in the APbBr_3 nanoparticles (Figures S1A, S2A, and S3A for $\text{P}_{\text{ODA}1}$, $\text{P}_{\text{ODA}2}$, and $\text{P}_{\text{ODA}3}$, respectively); a similar absorption has been reported for $\text{CH}_3\text{NH}_3\text{PbBr}_3$ within mesoporous titania and alumina.⁶ Consequently, the long chain ammonium salt played a key role in the formation of the hybrid perovskite nanoparticles and in their capacity to give rise to colloidal solutions.

However, in addition to the peak at ca. 525 nm, the spectra of the P_{ODA} samples presented others at lower wavelengths, suggesting that the formation of the APbBr_3 perovskite structure was accompanied by the formation of perovskites

with other stoichiometries.^{18–21} Transmission electron microscopy (TEM) images showed that the $\text{CH}_3(\text{CH}_2)_{17}\text{NH}_3\text{Br}/\text{CH}_3\text{NH}_3\text{Br}$ 0.6:0.4 molar ratio used in $\text{P}_{\text{ODA}2}$ proved to be the most effective in the formation of nanoparticles (see Figures S4, S5, and S6 for $\text{P}_{\text{ODA}1}$, $\text{P}_{\text{ODA}2}$, $\text{P}_{\text{ODA}3}$, respectively). Interestingly, the fluorescence spectra of the P_{ODA} samples mainly showed the near band edge emission attributable to the APbBr_3 nanoparticles with a narrow full width at the half-maximum (fwhm). The emission wavelength maximum and fwhm values were at 529 (fwhm = 26 nm), at 526 (fwhm = 24 nm), and at 524 nm (fwhm = 23 nm) for $\text{P}_{\text{ODA}1}$, $\text{P}_{\text{ODA}2}$, and $\text{P}_{\text{ODA}3}$, respectively. However, while this emission band was highly symmetrical in the case of $\text{P}_{\text{ODA}2}$ and $\text{P}_{\text{ODA}3}$, this was not the case for $\text{P}_{\text{ODA}1}$, which showed a shape similar to that of $\text{CH}_3\text{NH}_3\text{PbBr}_3$ bulk (Figures S1B, S2B, and S3B).

The rather long chain of ODA might make the formation of perovskites with other stoichiometries competitive with the formation of the $\text{CH}_3\text{NH}_3\text{PbX}_3$ nanoparticles. Therefore, assays were performed using the shorter octylammonium bromide ($\text{CH}_3(\text{CH}_2)_7\text{NH}_3\text{Br}$) in the synthesis of the nanoparticles. In addition, as mentioned above, the use of shorter alkyl ammonium cations could be advantageous for future applications of these nanoparticles. The $\text{CH}_3(\text{CH}_2)_7\text{NH}_3\text{Br}/\text{CH}_3\text{NH}_3\text{Br}$ 0.6:0.4 molar ratio was used since it seemed to be the best ratio for the preparation of the $\text{CH}_3\text{NH}_3\text{PbX}_3$ nanoparticles, taking into account the full set of data (resulting from TEM, absorption, and emission measurements) for P_{ODA} .

Remarkably, $\text{P}_{\text{OA}2}$ (OA refers to octylammonium cation) also proved to be dispersible in toluene and its absorption spectrum exhibited a peak at λ_{max} 527 nm (Figure 2a).

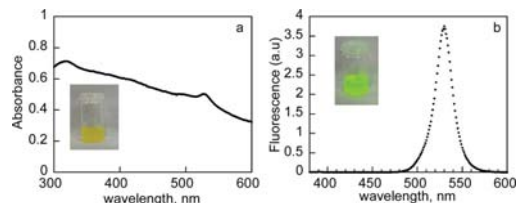


Figure 2. UV-visible absorption (a) and room-temperature fluorescence (b) spectra of $\text{P}_{\text{OA}2}$ in toluene. Inset: photographs of the emitter illuminated with ambient light (a) and UV light-lamp centered at 365 nm (b).

Even more remarkably, its emission spectrum only exhibited a highly symmetric band centered at $\lambda_{\text{max}} = 530$ nm, which was narrower (fwhm = 21 nm) than that of the P_{ODA} samples (Figure 2b). The very small Stokes shift indicates that the structure does not undergo changes when it is in the excited state and that it is a rigid structure. Hence, considerable autoabsorption occurs which hinders the determination of the exact photoluminescence quantum yield (Φ_f) and a value of 17% was registered when using considerably diluted solutions and the excitation wavelength was as far away as possible from the absorption maximum. It has been reported that excitons in the bulk $\text{CH}_3\text{NH}_3\text{PbBr}_3$ are of the Wannier type, producing a strong delocalization due to the weak exciton binding energy of 0.076 eV.²² Therefore, the high Φ_f for the colloidal dispersions indicates that the exciton binding energy is significantly increased, preventing dissociation of the exciton prior to its radiative decay.

All these data suggested that the preparation of APbBr₃ perovskite nanoparticles had been successful when using OA as the capping ligand and a 0.6:0.4 CH₃(CH₂)₇NH₃Br/CH₃NH₃Br molar ratio. It is worth mentioning that the fluorescence of the P_{OA}2 was higher than the P_{ODA}2 (Figure S7). In addition, these results indicated that the length of the alkyl chain of the ammonium cation exerted a considerable effect; thus, the composition homogeneity in APbBr₃ nanoparticles was greater for P_{OA}2 samples, with an alkyl chain of eight carbon atoms, than that of P_{ODA}2 with 18 carbon atoms.

Remarkably, P_{OA}2 samples showed an extraordinary stability under light illumination (see Figure S8, irradiation under two different conditions).

To probe the dispersibility of P_{OA}2 (2 mg/mL), the following organic solvents were used: toluene, hexane, tetrahydrofuran, chloroform, dioxane, dimethylsulfoxide, anisole, ethyl acetate, isopropanol, and methanol. P_{OA}2 formed stable colloidal solution in all the solvents except in DMSO and isopropanol, where the solution became immediately colorless. This suggested that the nanoparticles reverted back to their precursors in the highly polar aprotic solvent as well as in the protic solvents (Figure S9).

The X-ray powder diffraction (XRPD) pattern of the solid sample of P_{OA}2 was measured to further confirm the phase purity of P_{OA}2 as well as the crystallinity of the sample (Figure S10). The XRPD pattern of the sample showed that it was highly crystalline. Pawley refinement^{23,24} performed by using the TOPAS computer program, demonstrated that P_{OA}2 presented an excellent fit to a single-phase model corresponding to the cubic phase of the hybrid organic–inorganic CH₃NH₃PbBr₃ perovskite ($a = 5.9334$ (5) Å, space group = $Pm\bar{3}m$).^{25,26} The list of peak positions of the XRPD pattern is shown in Table S1. Energy-dispersive X-ray spectroscopy (EDS) analysis in nanoprobe mode showed that P_{OA}2 presented a Br/Pb ratio of 77/23 in good agreement with a PbBr₃ stoichiometry. In addition, TEM images of P_{OA}2 sample proved it mainly consisted of spherical nanoparticles with an average size of 6.2 ± 1.1 nm (Figure S11).

Figure 3 shows representative high resolution TEM (HRTEM) images of one nanoparticle and their corresponding fast Fourier transform (FFT) patterns, indicating that the nanoparticles possess crystalline surfaces with no sign of an amorphous layer. The HRTEM images show well-defined lattice spacing and FFT patterns and well-defined spots which are in accordance with the crystallographic parameters for the CH₃NH₃PbBr₃ bulk, thus demonstrating not only that the nanoparticles were highly crystalline but also that they possessed the same stoichiometry as the bulk. The images in Figure 3 show an interplanar distance from fringes of about 2.98 Å, which is characteristic of (002) planes of cubic phase structure of CH₃NH₃PbBr₃ with $Pm\bar{3}m$ space group, two interplanar spacing measurements at about 2.103 and 1.87 Å, which can be attributed to (022) and (031) family planes, respectively, and are in good agreement with the data for a cubic structure with lattice parameter of about 5.93 Å. The mean value of a -lattice parameter determined from d -spacing of 5.95 ± 0.03 Å was in good agreement with the XRPD value of 5.9334 (5) Å measured in the bulk perovskite.

The crystalline P_{OA}2 nanoparticles kept in the solid state for more than three months proved to be dispersible in toluene. The colloidal solutions were stable for up to 24 h. Consequently, in a first attempt to make use of the colloidal dispersion of P_{OA}2 as a starting material for optoelectronic

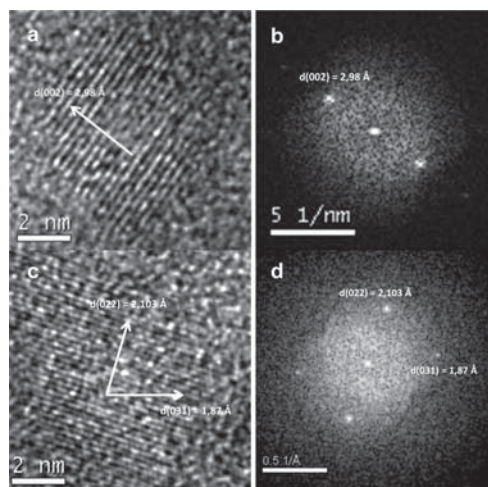


Figure 3. HRTEM images of individual nanoparticles from P_{OA}2 (a and c) and their corresponding FFT analyses (b and d).

devices, such solutions were used to prepare a homogeneous and fluorescent thin film on a quartz substrate. Thin films were prepared simply by spin-coating the colloidal solution on a thoroughly cleaned substrate. To facilitate good adhesion of the nanoparticles a short O₂ plasma treatment was employed to ensure a polar top surface of the substrates.

The emission spectrum of P_{OA}2 film also showed a narrow emission band (fwhm = 22 nm) whose maximum was at 533 nm, i.e., only 3 nm red-shifted compared to that of P_{OA}2 colloidal solution in toluene (Figure 4). The Φ_f of the film,

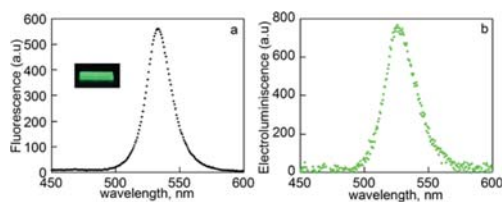


Figure 4. (a) Room-temperature fluorescence spectrum ($\lambda_{exc} = 350$ nm) of a thin film prepared using colloidal P_{OA}2. (b) Room-temperature electroluminescent spectrum of the device ITO/PEDOT:PSS/pTPD/P_{OA}2/Ba/Ag at 6 V.

measured with an integration sphere, was ca. 23%. As mentioned previously, there is a considerable amount of autoabsorption due to the very small Stokes shift in the nanoparticles. Therefore, for these films, in which the nanoparticles are present at high concentration, the Φ_f is less accurate and the registered value is most likely to be at a higher level as part of the emitted light is reabsorbed by the particles, thus leading to radiative losses.

A thin film light-emitting device based on P_{OA}2 nanoparticles was also prepared and its performance was compared with that of a reference device based on a bulk film of the same material (Figure S12). A very strong improvement in the electroluminescence is observed when the nanoparticles are used. This

clearly demonstrates the benefit of nanoparticles over bulk films in already one application.

We also succeeded to prepare APbI₃ nanoparticles by performing small variations on the here reported strategy; the preliminary results are promising (Figure S13), but a better homogeneity of the samples is expected by further fine-tuning of the preparation method for these systems.

In summary, our results show that hybrid organic–inorganic APbBr₃ (A: alkyl ammonium ion) perovskite nanoparticles can be easily and efficiently prepared. The method makes use of the capacity of medium alkyl chain organic ammonium cations to stabilize small sized (ca. 6 nm) crystalline nanoparticles. These nanoparticles can be kept stable in a solid state and maintained dispersed in aprotic, moderate polarity, organic solvents for more than three months. This made the preparation of a homogeneous thin film by spin-coating on a quartz substrate at room temperature possible. This fact is promising, since perovskite films could be compatible with flexible substrates. Both the colloidal solution and the film exhibit a high Φ_f and a narrow emission band, whose λ_{max} only changed slightly from the colloidal solution to the film, although considerably blue-shifted compared to that of the CH₃NH₃PbBr₃ bulk perovskite. Studies on the suitability of other combinations of short/long chain ammonium salts for preparing stable hybrid PbBr₃ colloidal solutions (for their application in optical devices) is worth studying and will be performed in due course.

■ ASSOCIATED CONTENT

Supporting Information

Spectroscopy data and TEM images of the perovskite nanoparticles. This material is available free of charge via the Internet at <http://pubs.acs.org>.

■ AUTHOR INFORMATION

Corresponding Authors

raquel.galian@uv.es

julia.perez@uv.es

Present Address

[§]L.C.S.: CONICET-INFIQC, Dpto. Qca. Org., UNC, Haya de la Torre y Medina Allende, Ciudad Univ., 5000-Córdoba, Argentina

Notes

The authors declare no competing financial interest.

■ ACKNOWLEDGMENTS

We thank the Spanish Ministry of Economy and Competitiveness (MINECO Project CTQ2011-27758, MAT2011-24594 and FPI grant to A.P.), European Community (Seventh Framework Programme, ORION, Grant 229036), Generalitat Valenciana (Prometeo/2012/053, ACOMP/2013/008, and FGVU (H.J.B. and R.E.G.)). The authors are grateful to SCSIE, University of Valencia for providing HRTEM facility. This article is dedicated to Professor Gregorio Asensio on the occasion of his 65th birthday.

■ REFERENCES

- (1) Mitzi, D. B. In *Progress in Inorganic Chemistry*; John Wiley & Sons, Inc.: New York, 1999; Vol. 48, p 1.
- (2) Mitzi, D. B. *J. Chem. Soc., Dalton Trans.* **2001**, 1.
- (3) Burschka, J.; Pellet, N.; Moon, S.-J.; Humphry-Baker, R.; Gao, P.; Nazeeruddin, M. K.; Grätzel, M. *Nature* **2013**, *499*, 316.
- (4) Cai, B.; Xing, Y.; Yang, Z.; Zhang, W.-H.; Qiu, J. *Energy Environ. Sci.* **2013**, *6*, 1480.

- (5) Kim, H.-S.; Lee, C.-R.; Im, J.-H.; Lee, K.-B.; Moehl, T.; Marchioro, A.; Moon, S.-J.; Humphry-Baker, R.; Yum, J.-H.; Moser, J. E.; Grätzel, M.; Park, N.-G. *Sci. Rep.* **2012**, *2*, 591.

- (6) Kojima, A.; Ikegami, M.; Teshima, K.; Miyasaka, T. *Chem. Lett.* **2012**, *41*, 397.

- (7) Kojima, A.; Teshima, K.; Shirai, Y.; Miyasaka, T. *J. Am. Chem. Soc.* **2009**, *131*, 6050.

- (8) Noh, J. H.; Im, S. H.; Heo, J. H.; Mandal, T. N.; Seok, S. I. *Nano Lett.* **2013**, *13*, 1764.

- (9) Carnie, M. J.; Charbonneau, C.; Davies, M. L.; Troughton, J.; Watson, T. M.; Wojciechowski, K.; Snaith, H.; Worsley, D. A. *Chem. Commun.* **2013**, *49*, 7893.

- (10) Lee, M. M.; Teuscher, J.; Miyasaka, T.; Murakami, T. N.; Snaith, H. J. *Science* **2012**, *338*, 643.

- (11) Ball, J. M.; Lee, M. M.; Hey, A.; Snaith, H. J. *Energy Environ. Sci.* **2013**, *6*, 1739.

- (12) Etgar, L.; Gao, P.; Xue, Z.; Peng, Q.; Chandiran, A. K.; Liu, B.; Nazeeruddin, M. K.; Grätzel, M. *J. Am. Chem. Soc.* **2012**, *134*, 17396.

- (13) Talapin, D. V.; Rogach, A. L.; Kornowski, A.; Haase, M.; Weller, H. *Nano Lett.* **2001**, *1*, 207.

- (14) Wadhavane, P. D.; Galian, R. E.; Izquierdo, M. A.; Aguilera-Sigalat, J.; Galindo, F.; Schmidt, L.; Burguete, M. I.; Pérez-Prieto, J.; Luis, S. V. *J. Am. Chem. Soc.* **2012**, *134*, 20554.

- (15) Aguilera-Sigalat, J.; Rocton, S.; Sanchez-Royo, J. F.; Galian, R. E.; Perez-Prieto, J. *RSC Adv.* **2012**, *2*, 1632.

- (16) Baikie, T.; Fang, Y.; Kadro, J. M.; Schreyer, M.; Wei, F.; Mhaisalkar, S. G.; Grätzel, M.; White, T. J. *J. Mater. Chem. A* **2013**, *1*, 5628.

- (17) Sun, L.; Choi, J. J.; Stachnik, D.; Bartnik, A. C.; Hyun, B.-R.; Malliaras, G. G.; Hanrath, T.; Wise, F. W. *Nanotechnol.* **2012**, *7*, 369.

- (18) Tabuchi, Y.; Asai, K.; Rikukawa, M.; Sanui, K.; Ishigure, K. *J. Phys. Chem. Solids* **2000**, *61*, 837.

- (19) Takeoka, Y.; Fukasawa, M.; Matsui, T.; Kikuchi, K.; Rikukawa, M.; Sanui, K. *Chem. Commun.* **2005**, 378.

- (20) Audebert, P.; Clavier, G.; Alain-Rizzo, V. R.; Deleporte, E.; Zhang, S.; Lauret, J.-S. B.; Lanty, G. T.; Boissière, C. D. *Chem. Mater.* **2009**, *21*, 210.

- (21) Vincent, B. R.; Robertson, K. N.; Cameron, T. S.; Knop, O. *Can. J. Chem.* **1987**, *65*, 1042.

- (22) Tanaka, K.; Takahashi, T.; Ban, T.; Kondo, T.; Uchida, K.; Miura, N. *Solid State Commun.* **2003**, *127*, 619.

- (23) Pawley, G. J. *Appl. Crystallogr.* **1981**, *14*, 357.

- (24) Coelho, A. A.; *TOPAS-Academic*, 4.1 ed.; Coelho Software: Brisbane, Australia, 2007.

- (25) Knop, O.; Wasylishen, R. E.; White, M. A.; Cameron, T. S.; Oort, M. J. M. V. *Can. J. Chem.* **1990**, *68*, 412.

- (26) Poglitsch, A.; Weber, D. J. *Chem. Phys.* **1987**, *87*, 6373.

Non-template Synthesis of CH₃NH₃PbBr₃ Perovskite Nanoparticles

Luciana C. Schmidt,^{a†} Antonio Pertegás,^a Soranyel González-Carrero,^a Olga Malinkiewicz,^a Said Agouram,^b Guillermo Mínguez Espallargas,^a Henk J. Bolink,^a Raquel E. Galian,^{a*} and Julia Pérez-Prieto^{a*}

^a Instituto de Ciencia Molecular (ICmol), Universidad de Valencia, Catedrático José Beltrán 2, 46980, Paterna, Valencia, Spain. Fax: 34 963543576; Tel:34 963543050; E-mail: raquel.galian@uv.es, julia.perez@uv.es

^b Department of Applied Physics and Electromagnetism, University of Valencia, Edif. Investigación, c/ Dr. Moliner 50, 46100, Burjassot, Spain.

Supplementary Information

Material and methods	S2-S4
Figure S1: Absorption and emission spectra of P _{ODA1}	S5
Figure S2 : Absorption and emission spectra of P _{ODA2}	S6
Figure S3: Absorption and emission spectra of P _{ODA3}	S7
Figure S4: TEM images of P _{ODA1}	S8
Figure S5: TEM images of P _{ODA2}	S9
Figure S6: TEM images of P _{ODA3}	S10
Figure S7: Photographs of P _{OA2} and P _{OAD2} in toluene under ambient light and UV-light.	S11
Figure S8. Room-temperature fluorescence intensity of P _{OA2} in toluene as a function of the illumination time and sample irradiation by using a fluorimeter excitation.	S12
Figure S9: Photographs of the solutions obtained after solid P _{OA2} (2 mg) was dispersed in different organic solvents (1 mL)	S13
Figure S10. Observed (<i>blue</i>) and calculated (<i>red</i>) profiles and difference plot [(I _{obs} – I _{calcd})] (<i>green</i>) of the X-ray powder diffraction Pawley refinement for P _{OA2} .	S14
Table S1: XRD parameters of P _{OA2}	S14
Figure S11. TEM images of P _{OA2} . Inset in c: zoom of two NPs.	S15
Figure S12. Current density and room-temperature luminance versus applied voltage for device type I (ITO/Al ₂ O ₃ /n-Perovskite/SPPO13/Ba/Ag) and type II (ITO/PEDOT:PSS/pTPD/P _{OA2} /Ba/Ag).	S16
Figure S11. TEM images of ODA-capped CH ₃ NH ₃ PbI ₃ nanoparticles.	S17

MATERIAL AND METHODS

Materials

All commercial materials were used as received: aqueous dispersion of poly(3,4-ethylenedioxythiophene):poly(styrenesulfonate) (PEDOT:PSS, CLEVIOS™ P VP Al 4083 (Heraeus); Aluminum oxide nanoparticles, <50 nm particle size (DLS), 20 wt. % in isopropanol (Aldrich); SPPO13 (2,7-bis(diphenylphosphoryl)-9,9'-spirobi[fluorene], Luminescence Technology Corp.) and pTPD (Poly[*N,N'*-bis(4-butylphenyl)-*N,N'*-bis(phenyl)-benzidine], American Dye Source Inc.). All the reagents used in the synthesis of the perovskites and the alkyl ammonium bromides were purchased from Aldrich and used as received. The organic solvents were of spectroscopic grade (Scharlab).

The precursors, methylammonium bromide ($\text{CH}_3\text{NH}_3\text{Br}$) and octylammonium bromide ($\text{CH}_3(\text{CH}_2)_7\text{NH}_3\text{Br}$), were synthesized by reaction of the corresponding amine in water/HBr, accordingly to the previously reported procedure.¹ In the case of octadecylammonium bromide ($\text{CH}_3(\text{CH}_2)_{17}\text{NH}_3\text{Br}$), it was prepared by using a similar methodology but the amine was previously dissolved in acetonitrile at 60°C and then HBr was added. In all cases, the precipitate was washed several times with diethyl ether, dried under vacuum and used without further purification.

Synthesis of P_{ODA1} . A solution of oleic acid (85 mg, 0.3 mmol) in 2 ml of octadecene was stirred and heated at 80 °C and then, octadecylammonium bromide (17.5 mg, 0.05 mmol) was added. Subsequent addition of methylammonium bromide (5.5 mg, 0.05 mmol dissolved in 100 μl of DMF) and lead(II) bromide (36.7 mg, 0.1 mmol dissolved in 100 μl of DMF) produced a yellow dispersion from which the nanoparticles were immediately precipitated by addition of acetone followed by centrifugation (7000 rpm, 10 min). Finally, the nanoparticles were dispersed in toluene.

Synthesis of P_{ODA2} . The same procedure than for P_{ODA1} was followed, except that the quantity of octadecylammonium bromide and methylammonium bromide was 21 mg (0.06 mmol) and 4.4 mg (0.04 mmol), respectively.

Synthesis of P_{ODA3} . The same procedure than for P_{ODA1} was followed, except that the quantity of octadecylammonium bromide and methylammonium bromide was 24.5 mg (0.07 mmol) and 3.3 mg (0.03 mmol), respectively.

Synthesis of P_{OA2} . A solution of oleic acid (85 mg, 0.3 mmol) in 2 ml of octadecene was stirred and heated at 80 °C and then, octylammonium bromide (12.6 mg, 0.06 mmol) was added. Subsequent addition of methylammonium bromide (4.4 mg, 0.04 mmol dissolved in 100 μl of DMF) and lead(II) bromide (36.7 mg, 0.1 mmol dissolved in 100 μl of DMF) produced a yellow dispersion from which the nanoparticles were immediately precipitated by addition of acetone followed by centrifugation (7000 rpm, 10 min). Finally, the nanoparticles were dispersed in

toluene.

Film preparation. Quartz substrates were extensively cleaned using detergent, de-mineralized water, and isopropyl alcohol, respectively, followed by 90 min UV-ozone treatment and 10 min of oxygen plasma cleaning in order to enhance good thin film formation. A colloidal solution of POA_2 perovskite in toluene was spin-coated on top of the quartz substrates with 1000 rpm during 30 sec resulting in film thickness of ca. 20-30 nm.

Characterization Methods

UV-visible spectra of the samples were recorded using a quartz cuvettes spectrometer in a UV-visible spectrophotometer Agilent 8453E.

Steady-state fluorescence spectra were measured on a Amnico Browman series 2 Luminescence spectrometer, equipped with a lamp power supply and working at room temperature. The AB2 software (v. 5.5) was used to register the data. All the data were acquired using 1cm×1cm path length quartz cuvettes, using an excitation wavelength of 350 nm.

Transmission electron microscopy TEM, high resolution TEM (HRTEM), selected area electron diffraction, and energy dispersive X-ray spectroscopy EDS in nanoprobe mode was carried out by using a Field Emission Gun (FEG) TECNAI G² F20 microscope operated at 200 kV. TEM samples were prepared from a toluene dispersion of the NPs, and a few drops of the resulting suspension were deposited onto a carbon film supported on a copper grid, which was subsequently dried.

The electroluminescent devices were made as follows. Indium tin oxide ITO-coated glass plates were patterned by conventional photolithography (Naranjo Substrates). The substrates were cleaned ultrasonically in water-soap, water and 2-propanol baths. After drying, the substrates were placed in a UV-ozone cleaner (Jelight 42-220) for 20 min. Next layers were prepared as follows:

Type 1: A layer of Al_2O_3 nanoparticles was coated by spin-coating on ITO at 2000 rpm from a dispersion of 1:2 isopropanol:ethanol v/v. After that, the sample was sintered at 300°C during 2 hours. The perovskite layer was coated using a two-step process: a) A solution of 50 mg/mL in DMF of PbBr_2 was spin-coated at 1500 rpm on the Al_2O_3 nanoparticle layer b) the substrate was dipped in a methyl ammonium bromide solution (10 mg/mL in 2-propanol). The SPPO13 layer was prepared from a solution of 10 mg/mL in anisole at 1000 rpm for 60s.

Type 2: An 80 nm layer of PEDOT:PSS was spin-coated on the ITO-glass substrate. After that, a chlorobenzene solution of 7 mg/mL was used to coat the pTPD layer at 2000 rpm during 30 s. The layer was annealed at 180°C for 30 minutes and after that, the samples were washed 3 times with chlorobenzene at 2000 rpm. The perovskite layer was prepared from POA2 nanoparticles in toluene (4 mg/mL).

Finally, all the devices were transferred into an inert atmosphere glove-box, where the barium/silver electrode was thermally evaporated using a shadow mask. The size of the device was 6.5 mm².

The thickness of the films was determined with an Ambios XP-1 profilometer. Thin film photoluminescence spectra and quantum yields were measured with a Hamamatsu C9920-02 Absolute PL Quantum Yield Measurement System. It consists of an excitation light source (a xenon lamp linked to a monochromator), an integration sphere and a multi-channel spectrometer. Current density and luminance versus voltage sweeps were measured by using a Keithley 2400 source meter and a photodiode coupled to the Keithley 6485 pico-ammeter calibrated using a Minolta LS100 luminance meter. Electroluminescence spectra were recorded with an Avantes fiber-optics photo-spectrometer. The devices were not encapsulated and were characterized inside the glovebox.

Stability tests of toluene colloidal solutions of P_{OA}2 under light illumination

Test 1. A toluene colloidal solution of P_{OA}2 was irradiated for up to 60 min, using 10 x 10 mm quartz cuvette placed in a Luzchem photoreactor equipped with eight UV-A lamps (316-400 nm, maximum at 351 nm). The room-temperature fluorescence of the sample ($\lambda_{\text{exc}} = 350$ nm, $\lambda_{\text{em}} = 528$ nm) was recorded every 3 min.

Test 2. A toluene colloidal solution of P_{OA}2 was illuminated for up to 160 min, using 10 x 10 mm quartz cuvette placed in the sample-holder of a PTI- LPS-220B spectrometer equipped with a Xenon lamp (75 W). The Felix 32 analysis software was used to register the data.

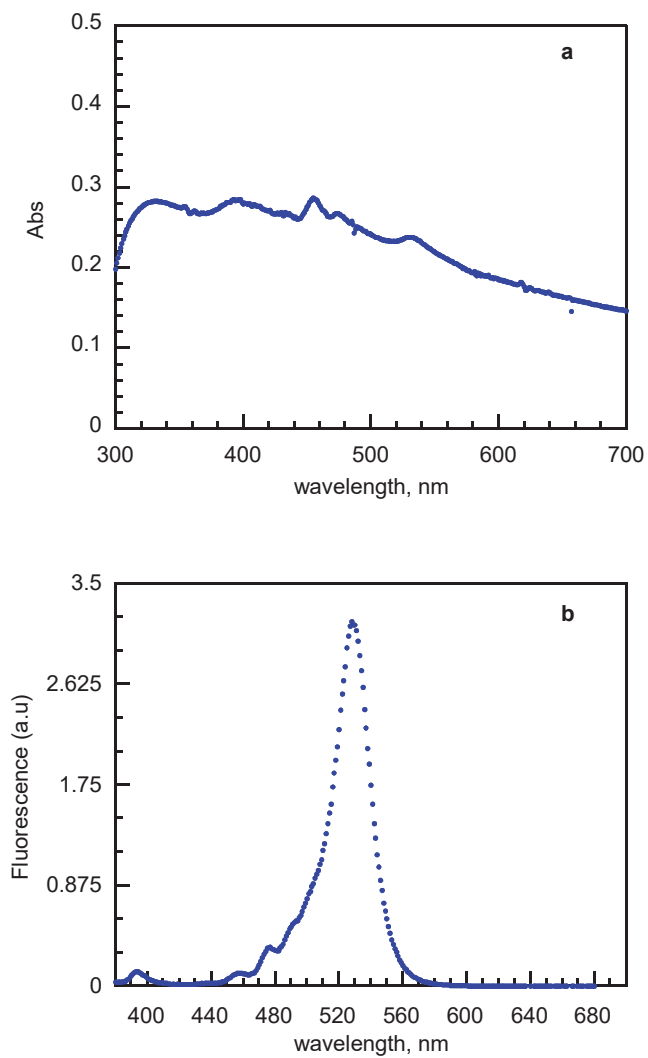


Figure S1. Absorption (a) and room-temperature emission (b) spectra of **P_{ODA1}** in toluene ($\lambda_{\text{exc}} = 350 \text{ nm}$; $\lambda_{\text{em}} = 393, 457 \text{ nm}, 475 \text{ nm}, 529 \text{ nm}$; FWHM = 26 nm)

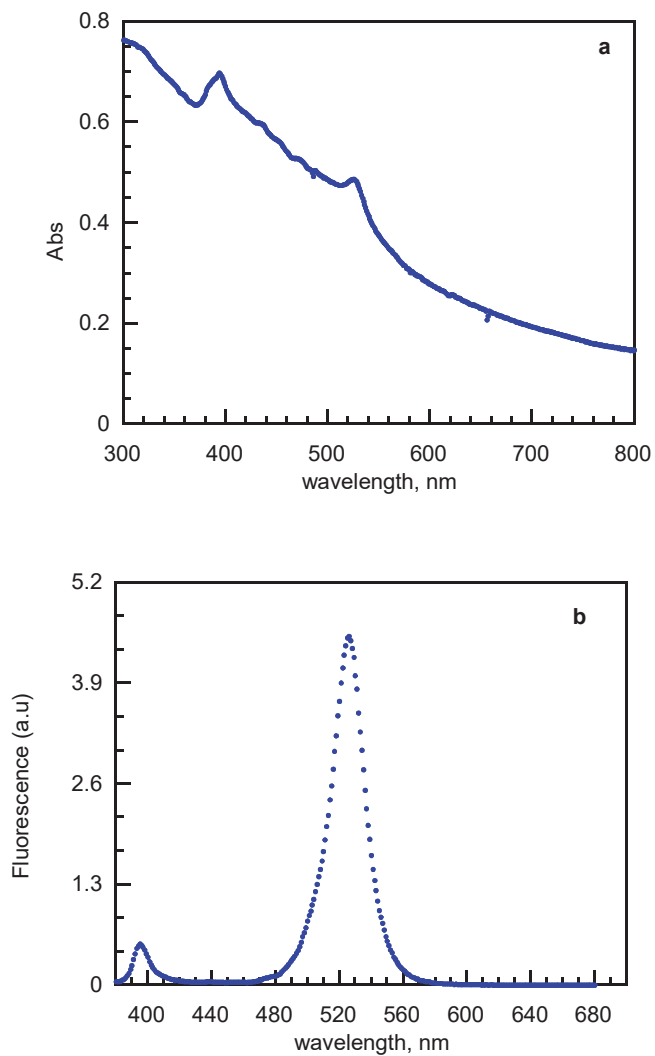


Figure S2. Absorption (a) and room-temperature emission spectra (b) of P_{ODA2} in toluene ($\lambda_{\text{exc}} = 350$ nm; $\lambda_{\text{em}} = 395$ and 526 nm; FWHM = 24 nm)

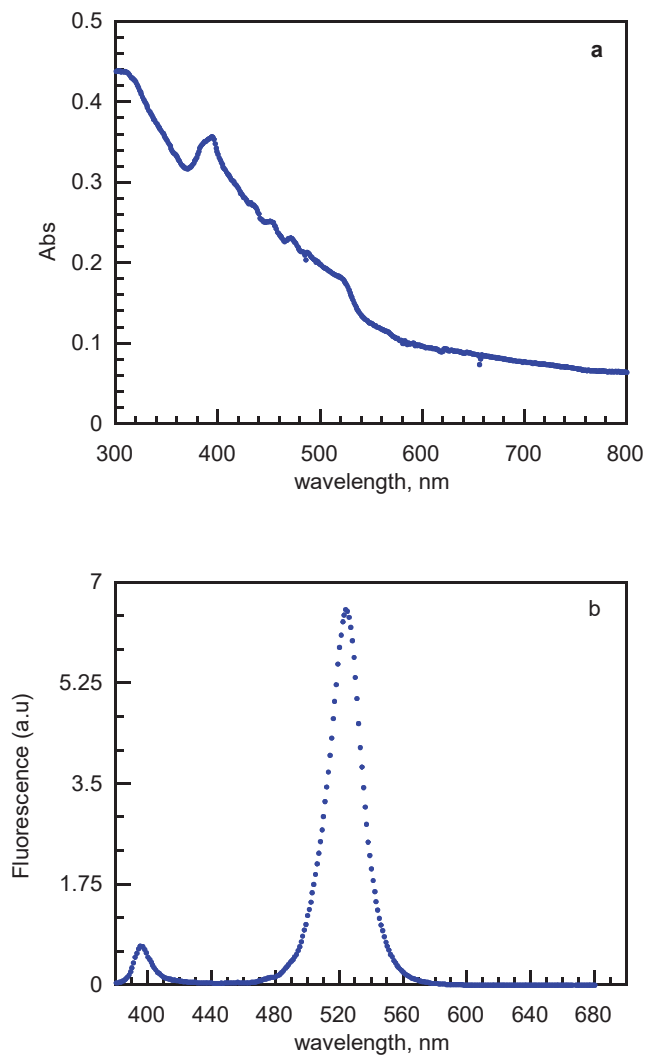


Figure S3. Absorption (a) and room-temperature emission (b) spectra of P_{ODA3} in toluene ($\lambda_{\text{exc}} = 350$ nm; $\lambda_{\text{em}} = 395$ and 524 nm; FWHM = 23 nm)

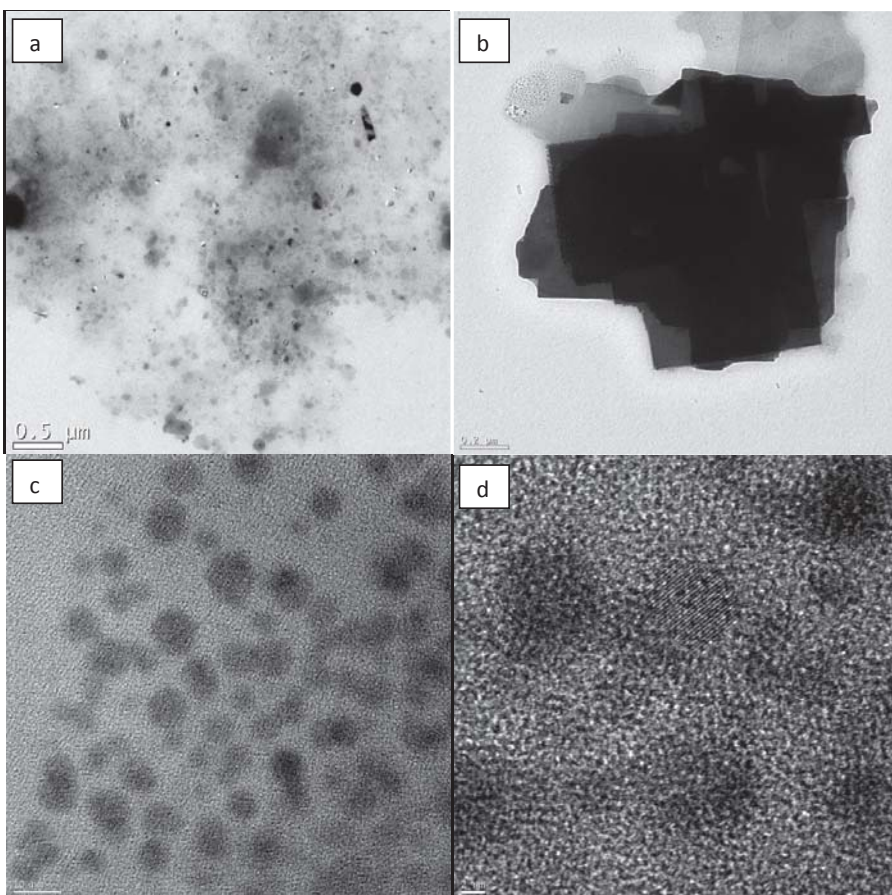


Figure S4. TEM images of P_{ODA1}, scale bar: 0.5 μm (a), 0.2 μm (b), 10 nm (c) and 2 nm (d).

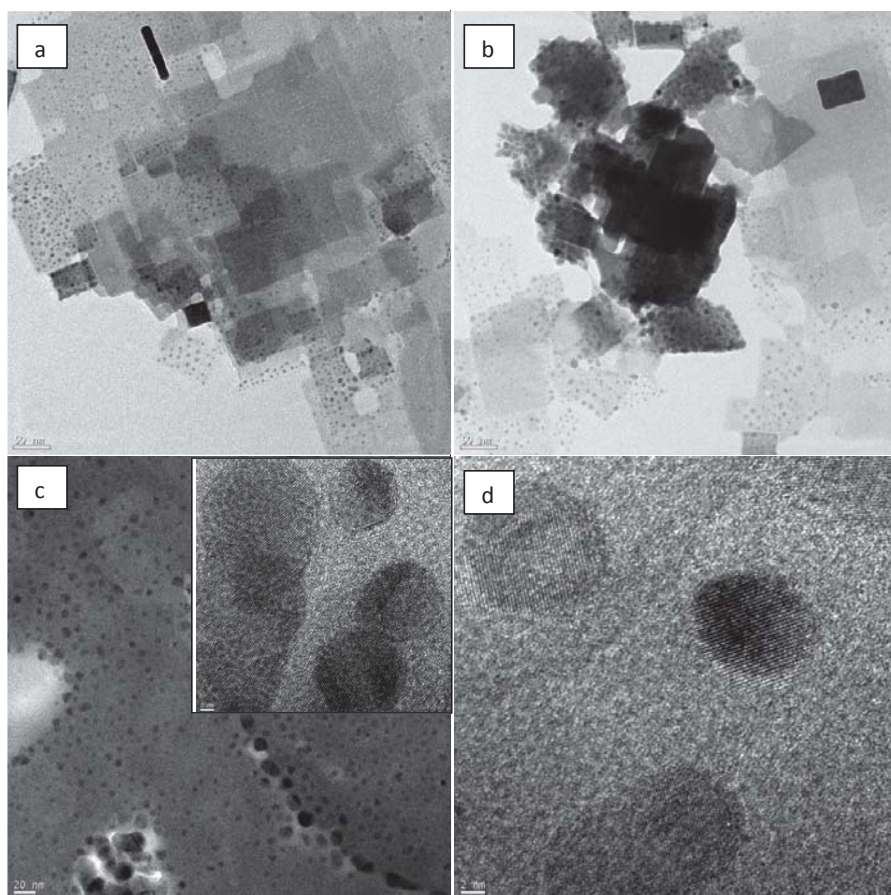


Figure S5. TEM images of $P_{\text{ODA}2}$, scale bar: 50 nm (a), 50 nm (b), 20 nm (c) and 2 nm (d).

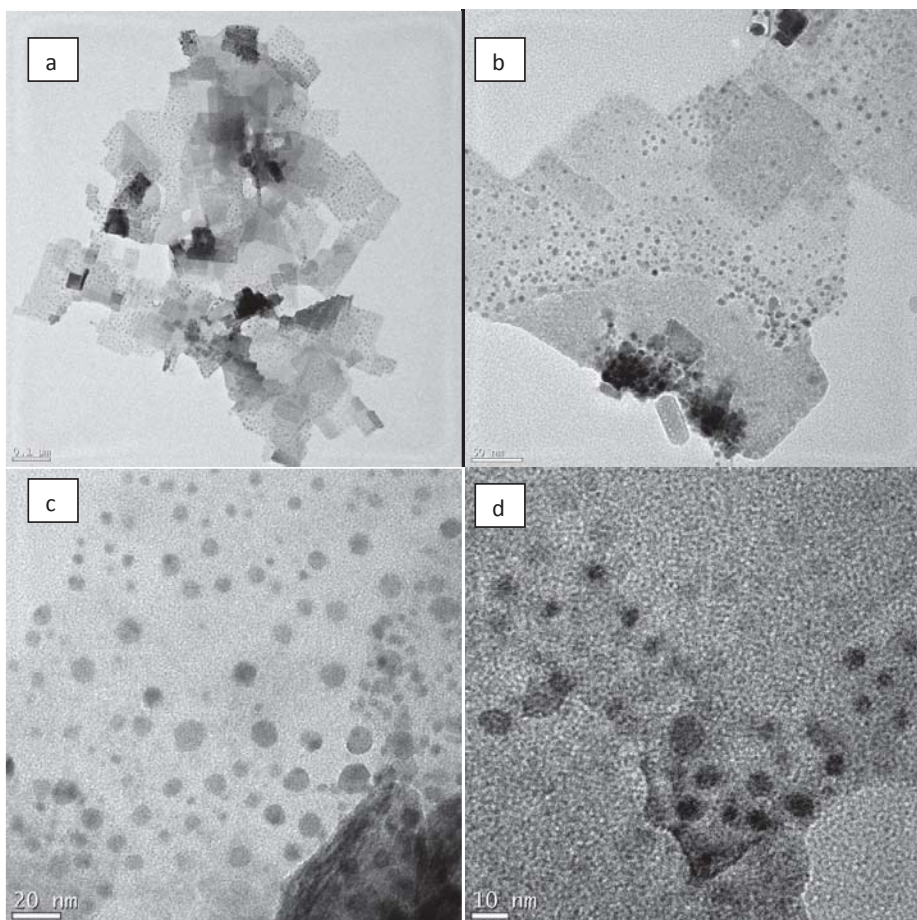


Figure S6. TEM images of P_{ODA3} , scale bar: 0.1 μm (a), 50nm (b), 20 nm (c) and 10 nm (d).

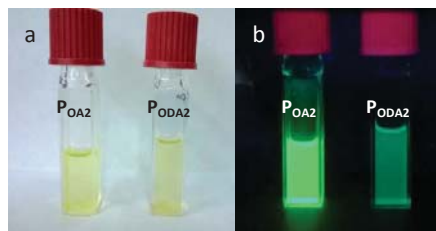


Figure S7. Photographs of P_{OA2} and P_{ODA2} in toluene under lab light (a) and UV-light (b).

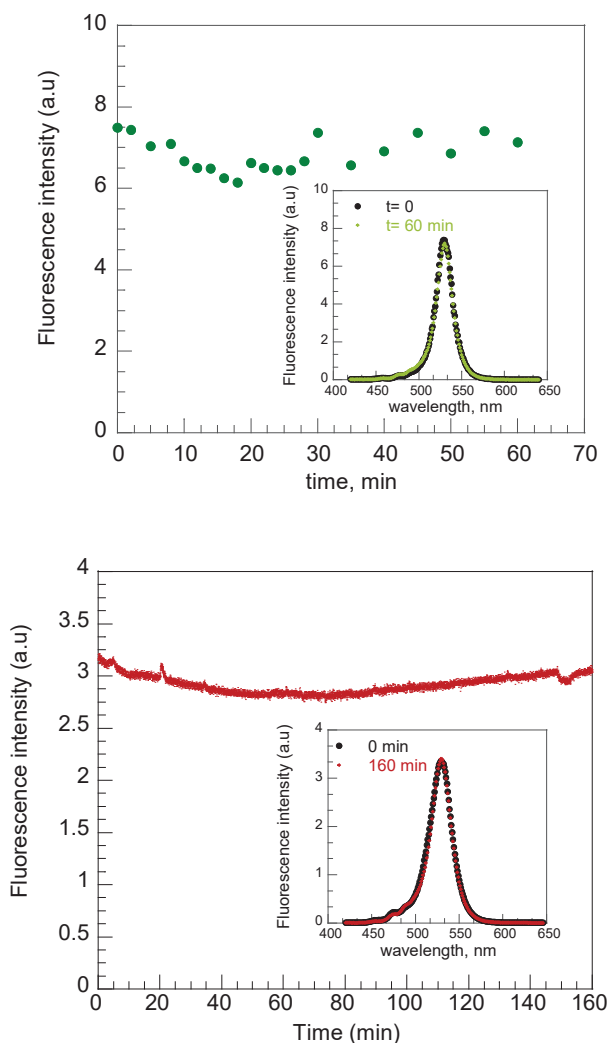


Figure S8. Room-temperature fluorescence intensity of P_{OA2} in toluene ($\lambda_{em}=528$ nm) as a function of the illumination time. Top: the sample was irradiated by using eight UVA lamps (intensity $5.3 \text{ mW}\cdot\text{cm}^{-2}$); inset: fluorescence spectra of the sample ($\lambda_{exc}=350$ nm; $\lambda_{em}=528$ nm) before and after 60 minutes irradiation. Bottom: the sample was continuously irradiated by using a fluorimeter excitation lamp ($\lambda_{exc}=350$ nm); inset: fluorescence spectra of the sample ($\lambda_{exc}=350$ nm; $\lambda_{em}=528$ nm) before and after 160 minutes of illumination.

Dispersibility of P_{OA2} in organic solvents

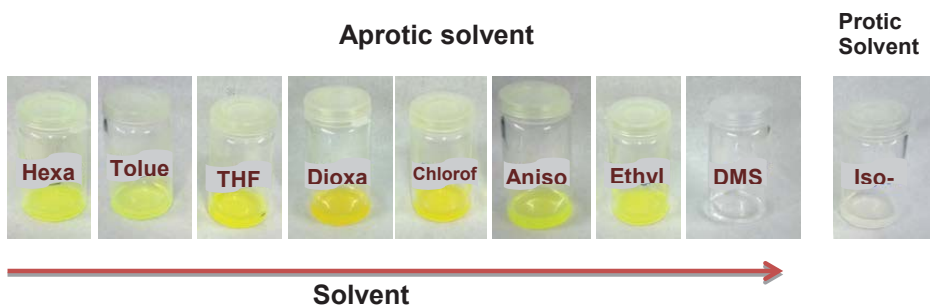


Figure S9. Photographs of the solutions obtained after solid P_{OA2} (2 mg) was dispersed in different organic solvents (1 mL); methanol led to the same result to isopropanol (this photograph has not been included).

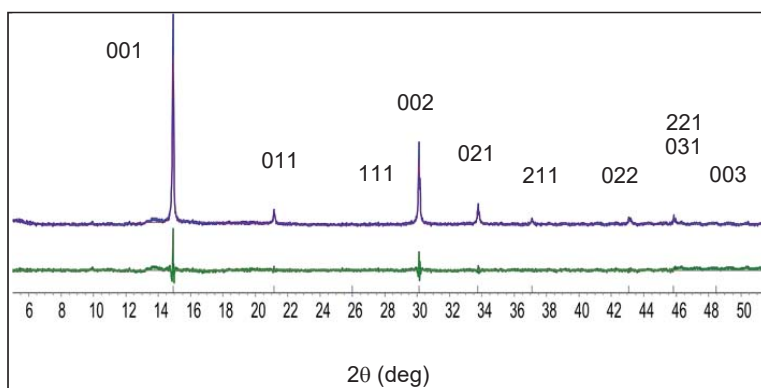


Figure S10. Observed (*blue*) and calculated (*red*) profiles and difference plot [$I_{\text{obs}} - I_{\text{calcd}}$] (*green*) of the X-ray powder diffraction Pawley refinement for $P_{\text{OA}2}$ ($\lambda = \text{Cu } K_{\alpha}$, 2θ range 5.0–50.0 °); tick marks indicate peak positions for $P_{\text{OA}2}$ (see Table S1).

Table S1: XRD parameters of $P_{\text{OA}2}$ ($\lambda = \text{Cu } K_{\alpha}$)

hkl	d (Å)	2-theta (°)
001	5.93482	14.91526
011	4.19655	21.15379
111	3.42647	25.98318
002	2.96741	30.09099
021	2.65413	33.74296
211	2.42288	37.07516
022	2.09828	43.07498
221	1.97827	45.83172
003	1.97827	45.83172
031	1.87676	48.46513

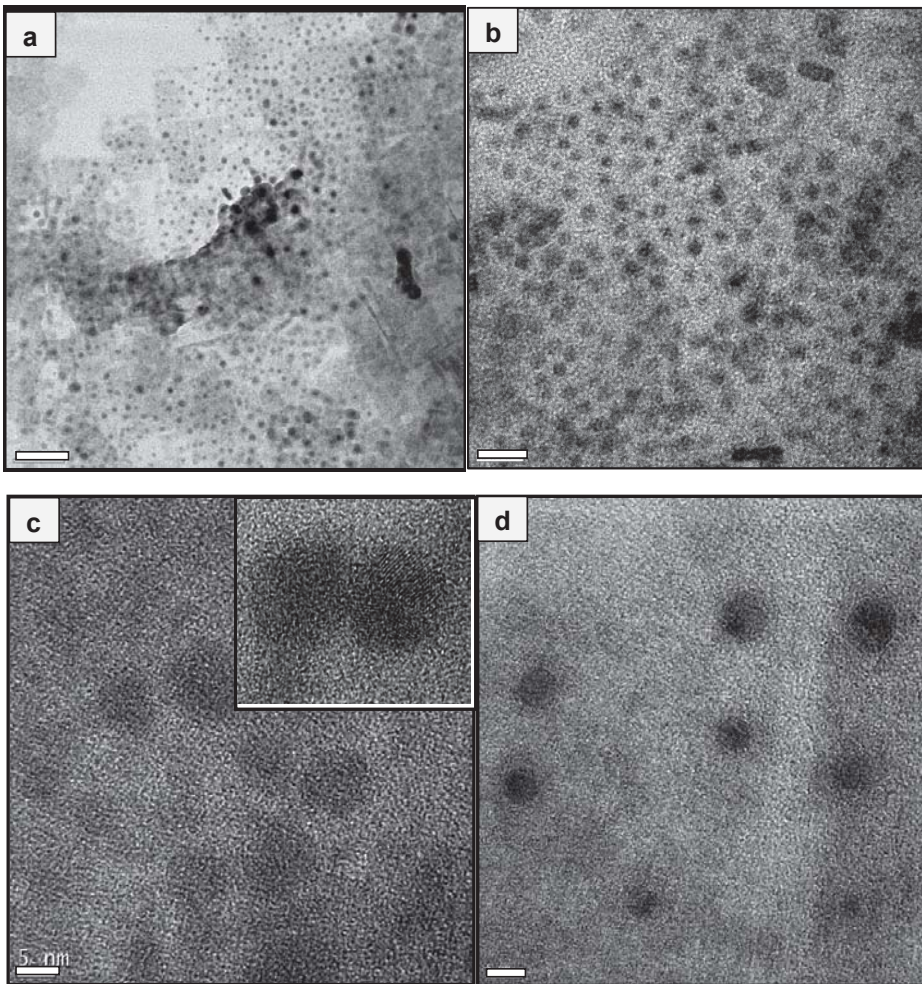


Figure S11. TEM images of P_{OA2} ; scale bar: 50 nm (a), 20 nm (b) and 5 nm (c, d). Inset in c: zoom of two NPs.

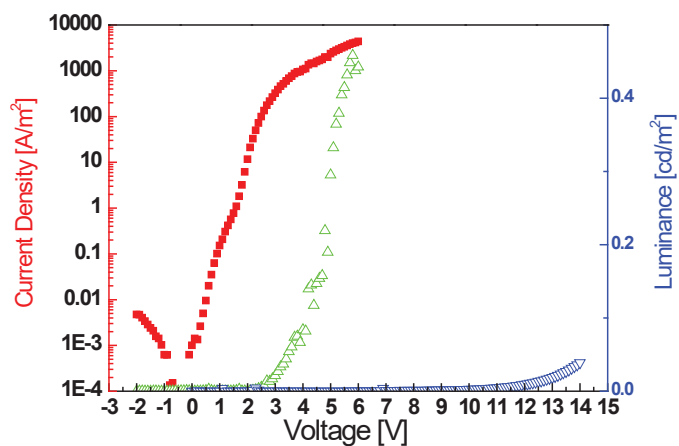


Figure S12. Current density (red solid squares) and room-temperature luminance (open symbols) versus applied voltage for device type I (ITO/ Al_2O_3 /n-Perovskite/SPPO13/Ba/Ag; blue down triangles) and type II (ITO/PEDOT:PSS/pTPD/ $\text{P}_{\text{O}A2}$ /Ba/Ag; green up triangles).

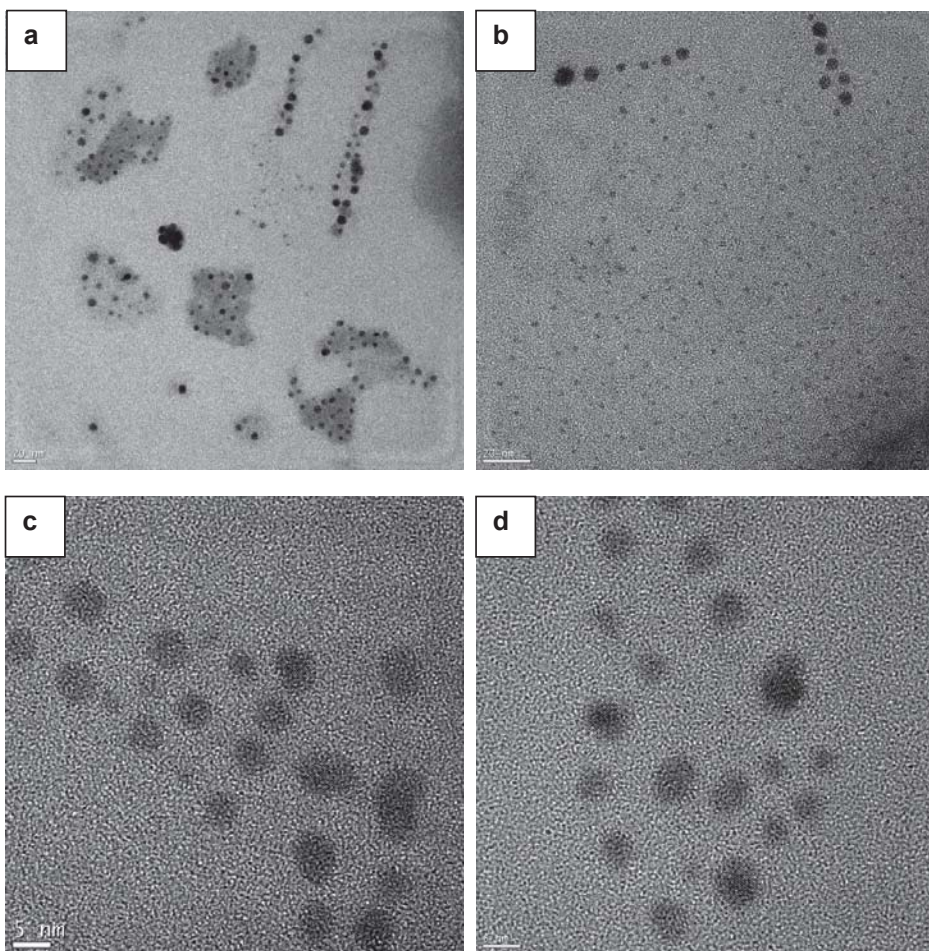


Figure S13. TEM images of ODA-capped $\text{CH}_3\text{NH}_3\text{PbI}_3$ nanoparticles synthesized by performing small variations on the strategy reported in the manuscript, scale bar: 20 nm (a, b) and 5 nm (c, d).

(1) Papavassiliou, G. C.; Pagona, G.; Karousis, N.; Mousdis, G. A.; Koutselas, I.; Vassilakopoulou, A. *Journal of Materials Chemistry* **2012**, *22*, 8271.



Cite this: *J. Mater. Chem. A*, 2015, **3**, 9187

Received 31st October 2014
Accepted 1st December 2014

DOI: 10.1039/c4ta05878j

www.rsc.org/MaterialsA

Maximizing the emissive properties of $\text{CH}_3\text{NH}_3\text{PbBr}_3$ perovskite nanoparticles†

Soranyel Gonzalez-Carrero, Raquel E. Galian* and Julia Pérez-Prieto*

Highly luminescent and photostable $\text{CH}_3\text{NH}_3\text{PbBr}_3$ nanoparticles have been prepared by fine-tuning the molar ratio between $\text{CH}_3\text{NH}_3\text{Br}$, PbBr_2 , a medium-size alkyl-chain ammonium salt, and 1-octadecene. The nanoparticles exhibit an excellent photoluminescence quantum yield (ca. 83%) and average recombination lifetime (ca. 600 ns) in toluene dispersion.

1. Introduction

Currently, scientists have shown great interest in organolead halide perovskites with the general formula of APbX_3 (A = organic ammonium cation and X = halide anion). These compounds present a three-dimensional (3D) inorganic framework consisting of corner-sharing PbX_6 octahedra and small-sized organic cations in the voids between the octahedra.

Organometal halide perovskites combine the favourable properties of the inorganic semiconductor, namely its excellent charge carrier mobility, with the flexibility and low-temperature processability of the organic material.¹ In particular, methylammonium (MA) lead trihalide perovskite materials allow low-cost solution processing, and they absorb broadly across the solar spectrum. Easy and rapid generation of charge carriers, transport of both electrons and holes, and high photoluminescence (PL) efficiency are desirable properties for optoelectronic devices.^{2–5}

The revolution in the use of hybrid perovskites as novel materials for solid state solar cells started in 2012, when Grätzel and Snaith reported, practically at the same time, photovoltaic power conversion efficiencies of 9.7% and 10.9%, respectively.^{6–8} In this regard, thin films of organometal halide perovskites have been recently prepared by vapour deposition; however, the functional perovskites have mostly been prepared as nanoparticulate materials using a template method, specifically by using the pores of mesoporous TiO_2 and Al_2O_3 ,⁹ which in the case of TiO_2 also act as electron transporters. It is likely that these mesoporous materials also improve the uniformity of the perovskite coating.

Instituto de Ciencia Molecular (ICMol), Universidad de Valencia, Catedrático José Beltrán 2, 46980, Paterna, Valencia, Spain. E-mail: Raquel.galian@uv.es; julia.perez@uv.es; Fax: +34 963543273; Tel: +34 963544307

† Electronic supplementary information (ESI) available: Additional absorption, emission, TGA, XPS, NMR spectra for perovskite and precursors, as well as tables with photophysical properties and nanoparticle composition data. See DOI: 10.1039/c4ta05878j

Remarkably, thin films of $\text{MAPbI}_{3-x}\text{Cl}_x$ mixed halide perovskites capped by poly(methyl methacrylate), PMMA, have shown high charge mobility and low bimolecular non-radiative recombination (PL decay of ca. 273 ns), thus making it possible to generate carrier diffusion lengths exceeding 1 micron; comparatively, the PL decay of MAPbI_3 was ca. 96.6 ns, and the carrier diffusion length was ca. 100 nm.¹⁰

Recently, studies on the photophysical properties of simple solution-processed crystalline films of these organic-metallic mixed halides, prepared by spin coating followed by annealing at 100 °C and subsequent capping with a thin layer of PMMA, showed that, at room temperature, they exhibited moderate to high PL quantum efficiencies depending on the excitation density (from 35% at 25 $\mu\text{J cm}^{-2}$ to 70% at 1 mJ cm^{-2}).⁴ The decreased PL efficiency at low excitation density was attributed to the presence of defects that caused non-radiative decay, and it was suggested that at high excitation density, the defects were filled and radiative recombination became dominant. Photoexcitation in the pristine perovskite caused the formation of free charge carriers within 1 picosecond; the carriers underwent bimolecular recombination on the time scale of tens of nanoseconds at higher excitation densities. The long carrier lifetimes, together with the exceptionally high luminescence yield of the films, were unique to these simply prepared inorganic semiconductors. The high PL efficiency evidenced the small contribution of non-radiative pathways to the PL decay of these materials; this is highly relevant and contrasts with the relatively low emission of other semiconductors, which are not capped with a high energy gap inorganic shell (such as CdSe nanoparticles).¹¹

The improved performance of $\text{MAPbI}_{3-x}\text{Cl}_x$ mixed halide perovskite compared with that of MAPbI_3 in meso-structured solar cells has been attributed to lower charge recombination rates rather than to better charge mobility.¹²

A critical issue of organolead iodide perovskite materials is their stability. MAPbI_3 perovskite reverts to its precursors; this is attributed to the hydroscopic amine salts.¹³ However, the bromide-based perovskites have been proved to be less moisture-sensitive.¹⁴

Bromide MAPbBr₃ perovskites can be applied as light absorbers for high energy photons, and they can serve as the front cell in tandem cells. This perovskite can provide a higher open-circuit voltage in perovskite solar cells than the iodide analogue.^{15,16} However, the optical performance of MAPbBr₃ perovskite is considerably lower than that of the mixed Br/Cl perovskites.

Thin films of MAPbBr_{3-x}Cl_x perovskites have been prepared by spin-coating the mixtures of the perovskite precursors on top of an Al₂O₃ mesoporous layer, followed by heating at 100 °C. In particular, MAPbBr_{2.4}Cl_{0.6} (λ_{max} at 525 nm, average recombination lifetime, τ_{av} , 446 ns) exhibited the strongest PL emission among the mixed bromide/chloride perovskites. The τ_{av} of CH₃NH₃PbBr_{3-x}Cl_x perovskites was considerably longer than that of MAPbI_{3-x}Cl_x; this suggests that the former compounds have superior charge diffusion properties. Under the same conditions, MAPbBr₃ perovskite showed a much shorter lifetime (τ_{av} of 100 ns; λ_{max} at 530 nm).¹⁴

We recently reported that six-nm sized MAPbBr₃ perovskite nanoparticles can exhibit a considerable PL quantum yield (ca. 20% as a colloidal solution and film; λ_{max} at 530 nm) at low excitation densities.¹⁷ These nanoparticles were prepared by simply confining the 3D inorganic framework with octylammonium bromide (OABr). The method involved the use of a 1 : 1 molar ratio of the total ammonium salt and PbBr₂ concentrations, an OABr/MABr molar ratio of 0.6 : 0.4, in the presence of oleic acid (OLA), and 1-octadecene (ODE). The role of the latter two compounds in the emissive properties of the nanoparticles, if any, was not studied. The electroluminescence measurements of the film prepared from the colloidal solution exhibited a response ten times greater than that of the bulk material.

Encouraged by our preliminary results and those mentioned above, we focused on improving the organic capping of the bromide nanoparticles, taking into account the fact that surface states would be highly accessible for passivation treatment.^{18,19} We envisaged that some methyl ammonium salt could be lost during the nanoparticle preparation, and that MABr/PbBr₂ molar ratios greater than one could be advantageous.

We report here the preparation of highly dispersible MAPbBr₃ nanoparticles (Fig. 1), which exhibit an extraordinarily high photoluminescence quantum yield and lifetime, in toluene solution and film, as well as high stability and

photostability. These nanoparticles have been prepared by a non-template strategy, adjusting the molar ratio between the total ammonium salts and PbBr₂, as well as the OABr/MABr/ODE molar ratio, and by eliminating the use of oleic acid.

2. Experimental section

2.1 Materials and methods

All the chemicals were of analytical grade and used as received without further purification. Toluene was of HPLC quality for spectroscopic measurements.

UV-visible measurements. UV-vis spectra were recorded at room temperature using a quartz spectrometer cuvette in a UV-visible spectrophotometer Agilent 8453E.

Photoluminescence steady state studies. Steady-state photoluminescence spectra (LPS-220B, motor driver (MD-5020), Brytebox PTI) were obtained at room temperature on a spectrofluorometer PTI equipped with a lamp power supply. Felix 32 analysis software was used to register the data. All the data were acquired using 1 × 1 cm² path length quartz cuvettes.

The emission spectra (λ_{exc} = 350 nm) of the perovskites dispersed in toluene were measured under air atmosphere (unless otherwise indicated).

The photoluminescence spectra and quantum yields of the films were measured with a Hamamatsu C9920-02 absolute PL quantum yield measurement system (λ_{exc} = 350 nm).

Time resolved photoluminescence. Experiments were carried out using a Compact fluorescence lifetime spectrometer C11367, Quantaaurus-Tau with a LED pulse light source of 340, 405, and 470 nm. The average lifetime was obtained from the tri-exponential decays.

Microscopy images. Structural and morphological characterization were performed using bright field transmission electron microscopy (TEM), dark field TEM, selected area electron diffraction (SAED) and high resolution TEM (HRTEM). All these characterization techniques were carried out using a field emission gun (FEG) TECNAI G2 F20 microscope, operated at 200 kV. TEM samples were prepared by depositing a few drops of the perovskite solution on a carbon film supported on a copper grid (200 mesh); the samples were subsequently dried overnight.

X-ray power diffraction (XRPD). The XRPD analysis was performed on a Bruker D8 Advance A25 diffractometer using Cu K α (λ = 1.54060 Å) radiation at a voltage of 40 kV and 30 mA, and LynxEye detector. The powder diffraction pattern was scanned over the angular range of 2-80° (2 θ) with a step size of 0.020°, at room temperature.

Nuclear magnetic resonance (¹H-NMR). The spectra were acquired at room temperature using a Bruker DPX300 spectrometer with a 300 MHz Bruker magnet (7 T). The chemical shifts (δ) are reported in ppm relative to tetramethylsilane (TMS).

Thermogravimetry analysis (TGA). TGA was carried out using a Mettler Toledo TGA/SDTA 851e system with an operative temperature range of 25–1100 °C and 0.1 microgram sensitivity. The samples were heated from 25 to 800 °C with at a rate of 10 °C min⁻¹, under a nitrogen flux of 40 mL min⁻¹.



Fig. 1 Image of the toluene dispersion of CH₃NH₃PbBr₃ nanoparticles under (a) lab light and (b) UV-laser pointer excitation.

X-ray photoelectron spectroscopy (XPS). XPS data were acquired with Specs using a Phoibos 150-9MCD X-ray photoelectron spectrometer. The incident radiation was 50 W. The C 1s peak at 285 eV was set as a reference for all XPS peak positions.

2.2 Synthesis of nanoparticles

Synthesis of P_{OA1} . A solution of oleic acid (OLA, 0.30 mmol, 85 mg) in 1-octadecene (ODE, 6.26 mmol, 2.0 mL) was stirred and heated to 80 °C, and then octylammonium bromide (OABr, 0.16 mmol, 33.5 mg) was added. Subsequently, methylammonium bromide (MABr, 0.24 mmol, 26.4 mg, dissolved in 100 μ L of DMF) and lead(II) bromide (0.10 mmol, 36.7 mg, dissolved in 200 μ L of DMF) were added. No color change was observed after the addition of lead(II) bromide. The solution was cooled to 60 °C and immediately after the addition of acetone (5 mL), the precipitation of a yellow precipitate was induced. The unreactive material was separated by centrifugation (7000 rpm, 10 min, 20 °C).

Samples P_{OA2} and P_{OA3} were prepared following the same procedure but in the absence of OLA and ODE, respectively (see Table S1† for details).

Film preparation. The quartz substrates were extensively cleaned using detergent, de-mineralized water, and isopropyl alcohol, successively, followed by 20 min of UV-ozone treatment to facilitate good thin film formation. A solution of perovskite in toluene was spin-coated on top of the quartz substrates at 1500 rpm over 60 s, resulting in the formation of the film.

Photostability assays. The photostabilities of P_{OA1} and P_{OA2} samples were analysed using two different irradiation sources. Thus, toluene colloidal solutions in 10 \times 10 mm² quartz cuvettes were irradiated in a Luzchem photoreactor equipped with eight visible lamps (380–490 nm, maximum at 419 nm with a dose of 70.02 Wm⁻² in 401–700 nm range). The room temperature photoluminescence of the samples ($\lambda_{exc} = 350$ nm, $\lambda_{em} = 521$ nm) was recorded every 5 min.

In addition, 10 \times 10 mm² quartz cuvettes containing the colloidal solutions were placed in the sample-holder of a PTI-LPS-220B spectrometer equipped with a xenon lamp (75 W), and the samples were illuminated with UV light ($\lambda_{exc} = 350$ nm). The Felix 32 analysis software was used to register the data.

3. Results and discussion

3.1 Synthesis of $CH_3NH_3PbBr_3$ nanoparticles

The preparation of the nanoparticles was attempted by following our previously reported non-template strategy,¹⁷ but using a larger molar ratio of the total ammonium (OABr plus MABr) and $PbBr_2$ salts (specifically, 4 : 1) and varying the relative molar ratio between the ammonium salts (from 0.8 : 3.2 to 2.4 : 1.6). The amount of oleic acid (OLA) was maintained (3 : 1 OLA/ $PbBr_2$ molar ratio), while the ODE/ $PbBr_2$ molar ratio was fixed at 62.6 : 1.0. A control sample (P_c) lacking OABr was also prepared using the same reaction conditions and quantities of all the other compounds. As expected, the solid P_c obtained after precipitation/centrifugation from the control experiment

was minimally dispersible in toluene, and it exhibited an emission maximum at $\lambda_{max} = 538$ nm, *i.e.*, at a wavelength close to that of the bulk $MAPbBr_3$ perovskite. In contrast, we obtained a more dispersible and emissive perovskite (P_{OA1}) by adding OABr and using an OA/MA/ $PbBr_2$ molar ratio of 1.6 : 2.4 : 1. The change of the OA/MA/ $PbBr_2$ molar ratio to 2.4 : 1.6 : 1 led to a colloid solution whose emission spectrum showed several peaks, which evidenced the formation of a mixture of perovskites with different stoichiometry (spectrum not shown).

Fig. S1 in the ESI† shows the comparison between the absorption and emission ($\lambda_{ex} = 350$ nm) spectra of the toluene dispersion of P_c sample and that of P_{OA1} . The toluene dispersion of P_{OA1} exhibited a peak emission that was considerably blue-shifted compared with that of P_c (513 nm *vs.* 538 nm). In addition, the emission spectrum of the film prepared from the toluene dispersion of P_{OA1} exhibited a red-shifted peak at $\lambda_{max} = 526$ nm, a slightly broader peak (full width at half maximum, fwhm, 36 nm *vs.* 31 nm), and a smaller emission quantum yield (34% *vs.* 67%) than that of the toluene dispersion.

We then evaluated the role of OLA in the optical properties of the nanoparticles. The preparation of the nanoparticles was carried out under the same reaction conditions, using the OA/MA/ $PbBr_2$ molar ratio of 1.6 : 2.4 : 1 and maintaining the amount of ODE, but in the absence of OLA (Table S1†). After precipitation and centrifugation, the solid P_{OA2} was dispersed in toluene.

Interestingly, P_{OA2} showed an improvement in the optical properties of both the colloidal perovskite solution and the film prepared from it (Fig. 2). Thus, (i) the absorption spectrum of the colloidal solution showed less scattering than that of the nanoparticles prepared in the presence of OLA, (ii) the

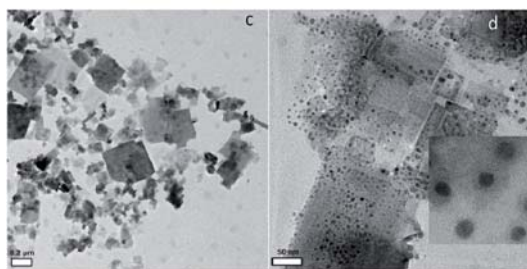
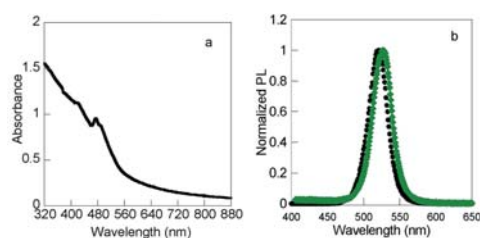


Fig. 2 (a) Absorption spectrum of P_{OA2} in toluene solution and (b) normalized emission ($\lambda_{exc} = 350$ nm) spectra of P_{OA2} in toluene solution (●) and film (○); (c and d) HRTEM images of P_{OA2} , scale bar 0.2 μ m (c) and 50 nm (d); inset: HRTEM image of P_{OA2} , scale bar 5 nm.

nanoparticles exhibited an enhanced emission (ca. 83% yield for the colloid and 72% for the film), and (iii) the emission band of the film was even narrower (fwhm of 30 nm vs. 32 nm for the colloidal dispersion).

The role of ODE in the eventual optical performance of the nanoparticles was also analysed by preparing the nanoparticles under the same reaction conditions as for sample P_{OA1} (OA/MA/PbBr₂ molar ratio of 1.6 : 2.4 : 1, oleic acid/PbBr₂ molar ratio of 3 : 1), but in the absence of ODE (Table S1†). This sample (P_{OA3}) exhibited an emission quantum yield ca. 52% in toluene dispersion and ca. 41% in the film (see spectra in Fig. S2†).

The influence of the alkyl-chain length of the longer ammonium salt on the emissive properties of the nanomaterial was also analysed (Table S2†). The reaction was carried out using ethylammonium bromide (EABr), hexylammonium bromide (HABr), and octadecylammonium bromide (ODABr) instead of OABr, and under all the same conditions as those used for the preparation of P_{OA2} . A non-dispersible perovskite was obtained in the case of EABr, while ODABr led to a perovskite with a lower-dimension framework (spectra not shown). However, HABr led to a perovskite (P_{HXA}) dispersible in toluene, which exhibited a narrow emission at λ_{max} 526 nm, i.e., 5 nm red-shifted compared to that of P_{OA2} (Fig. S3†). The PL quantum yield was lower than that of P_{OA1} and P_{OA2} (specifically, 58% for the colloidal dispersion and 38% for the film).

Regarding the size of the particles, high resolution transmission electron microscopy (HRTEM) analyses of the emissive samples showed that smaller nanoparticles were obtained in the absence of OLA and ODE. Thus, P_{OA2} and P_{OA3} consisted of spherical nanoparticles with average sizes of 5.5 ± 1.5 nm and 5.9 ± 1.8 nm, respectively (see Fig. 2 for P_{OA2} and Fig. S2† for P_{OA3}), whereas P_{OA1} comprised spherical nanoparticles with an average size of 7.0 ± 1.5 nm. In all the cases, most of the nanoparticles were embedded in an amorphous material forming plaques, which were smaller in the case of P_{OA2} (mostly 60×50 nm²).

The fast Fourier transform (FFT) patterns of P_{OA1} and P_{OA2} nanoparticles showed that they possessed crystalline surfaces. The lattice spacing in the HRTEM images and FFT patterns were in agreement with the crystallographic parameters for the CH₃NH₃PbBr₃ bulk material. The interplanar spacings determined from the FFT patterns were 5.91, 4.11, 3.48 and 2.94 Å, which can be attributed to the 001, 011, 111 and 002 family planes of the cubic phase structure of CH₃NH₃PbBr₃ with $Pm\bar{3}m$ space group.

In addition, the X-ray powder diffraction (XRPD) analysis of solid P_{OA1} and P_{OA2} confirmed the phase purity of the perovskites as well as the crystallinity of the samples (Fig. 3).

The XRPD pattern of the samples demonstrated that they presented an excellent fit to a single-phase model corresponding to the cubic phase of the hybrid organic–inorganic MAPbBr₃ perovskite ($a = 5.9334$ (5) Å, space group = $Pm\bar{3}m$).^{20,21} The XRPD peaks of the samples were very broad. This is consistent with the formation of MAPbBr₃, mostly as nanoparticles, particularly in the case of P_{OA2} .

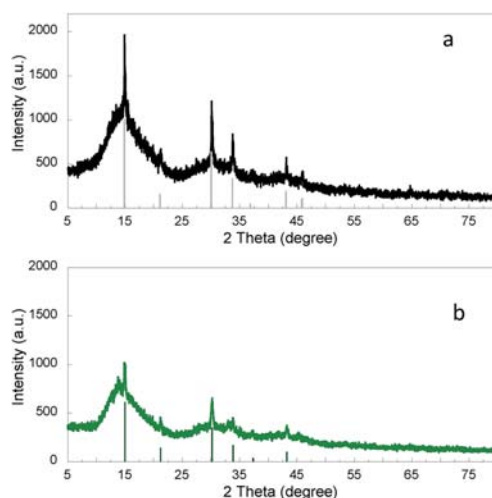


Fig. 3 X-ray diffraction patterns of P_{OA1} (a) and P_{OA2} (b). The vertical bars correspond to the peaks of CH₃NH₃PbBr₃ cubic phase.

The X-ray photoelectron microscopy (XPS) spectra of P_{OA1} and P_{OA2} were analysed, using a C peak at 285.0 eV as reference. Remarkably, in general, all the peaks of P_{OA2} were slightly shifted to a higher binding energy compared to those of P_{OA1} (see Fig. S4–S8†). In both the samples, the XPS spectrum of Pb 4f showed two symmetric peaks attributed to Pb 4f_{7/2} and Pb 4f_{5/2} levels at binding energies (BE) of ca. 138.7 eV and 143.6, respectively. The spin orbit split between the Pb 4f_{7/2} and Pb 4f_{5/2} levels was 4.9 eV, which agrees with the value reported in the literature (4.8 eV).²² The very small peak at a lower binding energy (ca. 136.8 eV) could be attributed to the presence of metallic lead, and has also been detected in the XPS spectra of CH₃NH₃PbI₃/TiO₂ system.²³

The Br 3d XPS BE of the perovskite was at ca. 69.1 eV. The N 1s XPS spectra showed the presence of one peak at 402.6 eV, corresponding to the –N– of the ammonium salts.²⁴ In addition, a very small peak at ca. 400.0 eV was also detected in the case of P_{OA1} ; this could be assigned to a small amount of free amines.²⁵

The deconvolution of the C 1s XPS spectra presented two peaks at ca. 285.7 and 285.0 eV. The peak at the lower energy value can be attributed to C–C/C–H bond, as well as to the C=C bond of OLA and ODE; the peak at 285.7 eV can be assigned to the C–N⁺ bond of the ammonium salts.²⁶ The spectra showed the larger contribution of the peak at a BE of ca. 285.7 eV for P_{OA2} compared to P_{OA1} ; this is consistent with the results found for the analysis of the composition of the nanoparticles by ¹H-NMR and TGA (see below).

Finally, in the case of P_{OA1} , the O 1s XPS band at 532.9 eV was accompanied by a small band at 528.8 eV, which was consistent with the presence of small amounts of PbO.²⁷ The formation of PbO could be tentatively attributed to the presence of oleic acid in the preparation of the nanoparticles.²⁸

The quantification of lead and bromine by XPS led to a 73 : 28 molar ratio for P_{OA2} , while the ratio was 68 : 32 for P_{OA1} .

3.2 Analysis of the composition of $\text{CH}_3\text{NH}_3\text{PbBr}_3$ nanoparticle samples

The composition of P_{OA1} and P_{OA2} , obtained after their precipitation/centrifugation steps, as well as the composition of the resulting supernatants, were studied using thermogravimetric analysis (TGA) and $^1\text{H-NMR}$. Solvent removal from the supernatant, followed by the addition of ethyl ether, caused the precipitation of a solid (Ss). In addition, the ether solution was distilled, thus recovering ODE accompanied by OABr (plus OLA in the case of the synthesis of P_{OA1}).

The TGA of P_{OA1} and P_{OA2} samples was compared with that of the individual precursors (MABr, OABr, ODE, OLA, lead bromide), as well as with that of methylamine and octylamine (see TGA of all the precursors in Fig. S9–S11†). The peak of the first derivative indicates the point at which the greatest rate change on the weight loss curve occurred. The TGA of P_{OA1} (Fig. 4) showed that it lost ca. 16.0% of its weight before reaching 200 °C, followed by a weight loss of ca. 24.0% before reaching 360 °C (corresponding to at least two different components), and then a weight loss of 56.6% before reaching 600 °C. The spectrum showed that 2.6% of the mass did not decompose or sublimate at temperatures above 800 °C. The remaining residue may consist of impurities present in the material or decomposition products. The peaks of the first derivative were at 178, 345, and 580 °C.

The trend in the P_{OA2} sample (Fig. 4) was considerably similar; however, the temperature of the first derivative peaks shifted to higher values (183, 358, and 616 °C), suggesting a higher stability of the components that were used to build the nanoparticles in the absence of oleic acid. Sample P_{OA2} lost 17.63% weight before reaching 210 °C, followed by a weight loss of ca. 24.15% before reaching 380 °C (corresponding to at least two different components), and then a weight loss of 58.05% before reaching 650 °C. In addition, the sample completely sublimated at temperatures below 700 °C.

The first loss of weight in sample P_{OA1} and sample P_{OA2} could be attributed to the loss of octylamine; however, there was no match between the temperatures of the first derivative peaks of these peaks and those of the amines (Fig. S11†). In addition, MABr and OABr ammonium salts underwent weight loss at a temperature above 200 °C, and 100% weight loss occurred in

one step, suggesting the sublimation of these materials (Fig. S9†).^{29–31} It has been previously suggested that the ammonium salts, such as MABr, are incorporated in the crystal lattice of the perovskite in the form of MA^+Br^- , and as a consequence they can be released at a lower temperature than that required for the ammonium salt.³² The second step of the weight loss could be ascribed to the loss of ODE and the remaining ammonium salts (plus OLA in the case of P_{OA1}), while the third step is consistent with the loss of lead bromide from the perovskite. Interestingly, the sublimation temperature of the lead bromide in P_{OA2} is closer to that of PbBr_2 than to that of P_{OA1} .

In addition, the solids obtained after the precipitation/centrifugation of P_{OA1} and P_{OA2} (Ss_1 and Ss_2 , respectively) were also studied by TGA. The spectra (Fig. S12 and S13†) showed the presence of ca. 13% lead bromide. This could be ascribed to the incomplete precipitation of the nanoparticles during the centrifugation step.

Further data on the composition of P_{OA1} and P_{OA2} samples were extracted from their $^1\text{H-NMR}$ spectra, which provided information on the molar ratio of the organic components, combined with their TGA spectra, which provided information on the PbBr_2 weight percentage in the isolated mass. Fig. S14–S17† show the $^1\text{H-NMR}$ spectra of the pure precursors used in the quantification.

The $^1\text{H-NMR}$ spectra of the supernatants were also analysed (spectra not included); the data obtained from these, combined with those of the corresponding samples (P_{OA1} and P_{OA2} spectra in Fig. S14† and 5, respectively; spectra of the precursors are included in Fig. S15–S18†), were consistent with the amount of material used in the preparation of the nanoparticles. The molar composition of P_{OA1} and P_{OA2} as well as the yield of isolated perovskite are shown in Tables S3 and S4.† These data indicated that the perovskite nanoparticles capped by the ammonium salts and ODE, which was incorporated into the organic capping *via* chain interdigitation between the alkyl chains, cooperated in their stability/dispersability.

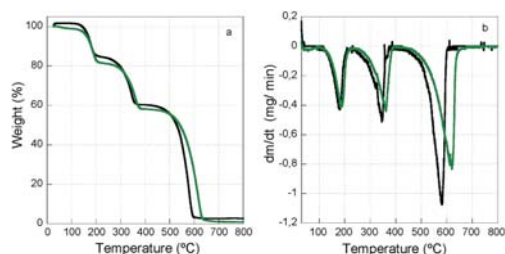


Fig. 4 TGA heating curves of P_{OA1} (black) and P_{OA2} (green) nanoparticles expressed as weight% as a function of applied temperature (a) and the corresponding 1^{st} derivative (b).

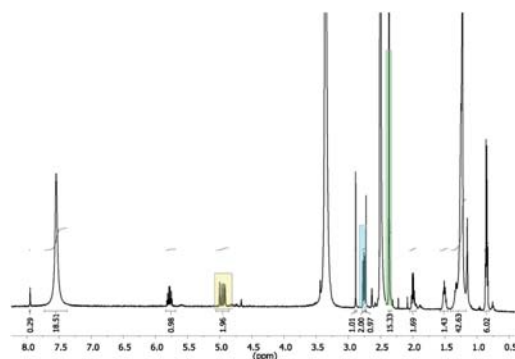


Fig. 5 $^1\text{H-NMR}$ spectrum of P_{OA2} in deuterated DMSO; the signals of MABr, OABr, and ODE used for the quantification are marked in green, cyan, and yellow, respectively.

It has been suggested that iodopentafluorobenzene passivates the excess of iodide ions on the surface of mixed halide (I, Cl) lead perovskites.³³ Therefore, we propose that the ammonium moiety of OA binds to the under-coordinated bromide ions of the perovskite nanoparticles.

In addition, ODE may bind to under-coordinated lead ions on the perovskite crystal surface *via* its double bond, thus passivating these defect sites and decreasing the rate of non-radiative recombination in the perovskite. It has recently been reported that weak Lewis bases can play a relevant role in the emissive properties of perovskites. Moreover, Snaith *et al.* recently suggested that thiophene and pyridine can bind to the under-coordinated Pb atoms of mixed halide (Cl, I) lead perovskite films, thus enhancing their photoluminescence and solar cell performance (up to 16.5%).^{34,35}

3.3 Time resolved photoluminescence analysis

Time-resolved photoluminescence spectroscopy was used to study the recombination lifetimes of **P_{OA1}** and **P_{OA2}** perovskites (in both the colloidal solution and the film). The PL decays were registered at λ_{em} *ca.* 520 nm, under both nitrogen and air atmosphere, and fitted with a triexponential function of time (t),

$$I(t) = \sum_i \alpha_i \left(-\frac{t}{\tau_i} \right) \quad (1)$$

where τ_i represents the decay time and α_i represents the amplitude of the component. The emission lifetimes and their corresponding contributions to the total signal are shown in Tables S5–S6.† The average recombination lifetimes (τ_{av}) were estimated with the τ_i and α_i values from the fitted curve data according to eqn (2).

$$\tau_{\text{av}} = \frac{\sum_i \alpha_i \tau_i^2}{\sum_i \alpha_i \tau_i} \quad (2)$$

The τ_{av} values for **P_{OA1}** and **P_{OA2}** showed a slight dependence on the excitation wavelength (340, 405, 470 nm) and on the presence of oxygen (Table 1). The toluene colloidal solutions of **P_{OA2}** exhibited a considerably longer τ_{av} than **P_{OA1}**, reaching values close to 600 ns in solution and *ca.* 410 ns in film. The latter value is close to that recently reported for a MAPbBr_{3-x}Cl_x film. The radiative rate constant (k_r) and non-radiative rate constant (k_{nr}) were estimated using eqn (3) and (4), where Φ_{PL} is the photoluminescence quantum yield.

Average lifetime (τ_{av}), quantum yield (Φ_{PL}), radiative (k_r) and non-radiative (k_{nr}) constants; $\lambda_{\text{exc}} = 340$ nm.

$$\Phi_{\text{PL}} = k_r \tau_{\text{av}} \quad (3)$$

$$\tau_{\text{av}} = \frac{1}{(k_r + k_{\text{nr}})} \quad (4)$$

These data revealed the remarkably low value of k_{nr} , which was not only of the same order of magnitude as k_r but was even five times lower, except for the **P_{OA1}** film. This evidenced the considerable reduction of surface defects that otherwise would

Table 1 Photoluminescence data of **P_{OA1}** and **P_{OA2}**^a

Sample	τ_{av} (ns)	Φ_{PL}	k_r (s ⁻¹)	k_{nr} (s ⁻¹)
P_{OA1} (air)	415.09	0.673	1.61×10^6	0.79×10^6
P_{OA1} (N ₂)	411.17	0.673	1.64×10^6	0.80×10^6
P_{OA1} film	344.38	0.342	0.99×10^6	1.91×10^6
P_{OA2} (air)	594.45	0.831	1.39×10^6	0.29×10^6
P_{OA2} (N ₂)	552.56	0.802	1.45×10^6	0.36×10^6
P_{OA2} film	412.09	0.723	1.75×10^6	0.67×10^6

^a Excitation at 340 nm.

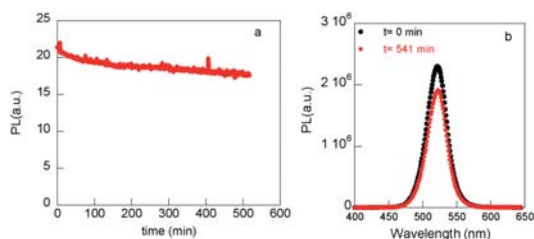


Fig. 6 (a) Photoluminescence of **P_{OA2}** dispersed in toluene as a function of irradiation time; $\lambda_{\text{exc}} = 350$ nm, PL registered at 520 nm under air atmosphere. (b) Photoluminescence spectra before and after 541 minutes of irradiation.

trap excited electrons and decrease the emissive properties of the perovskites.

3.4 Stability and photostability of **P_{OA1}** and **P_{OA2}** samples

P_{OA2} stored as a solid in the dark and under air atmosphere preserved its emissive properties for more than five months, whereas **P_{OA1}** was considerably less stable.

The photostability of **P_{OA1}** and **P_{OA2}** colloidal solutions under light irradiation in the presence and in the absence of air was studied under two different light sources: fluorimeter lamps (λ_{ex} at 350 nm) and visible lamps (8 lamps, 400–700 nm, maximum centred at 420 nm). The UV irradiation of **P_{OA2}** under air atmosphere led to a loss of 7% emission intensity in the first 30 min and an additional loss of 10% after the following 481 min (Fig. 6). Moreover, **P_{OA1}** presented high photostability, with a decrease of luminescence of <10% after 183 min of excitation at 350 nm (figure not shown). Finally, the photoluminescence of **P_{OA2}** decreased by only 6% after visible-light irradiation for 75 min under air atmosphere (Fig. S19†).

Conclusions

We have demonstrated here that highly luminescent and photostable CH₃NH₃PbBr₃ nanoparticles can be prepared by following the strategies described for the synthesis of other materials confined in the three dimensions (*i.e.*, zero-dimension materials). The completion of the coordination sphere of the ions at the nanoparticle surface may be the origin for the low non-radiative recombination rate constant of these

nanoparticles. The ammonium cation may bind to the under-coordinated bromide anions, whereas a weak Lewis base, such as 1-octadecene, may bind to the under-coordinated Pb cations. The fine-tuning of the molar ratios of all the components eventually results in the formation of nanoparticles with a high photoluminescence recombination lifetime (>420 ns) and photostability under UV light (<18% emission loss after 8.5 h). This perovskite preserves its emissive properties in the solid state, which makes it promising for use in light emitting devices and photovoltaic applications.

Acknowledgements

We thank MINECO (Project CTQ2011-27758, contract granted to S.G.-C), GVA (ACOMP/2013/008) and FGVU (R.E.G contract).

Notes and references

- 1 D. B. Mitzi, in *Progress in Inorganic Chemistry*, John Wiley & Sons, Inc., 2007, pp. 1–121.
- 2 C. S. Ponseca, T. J. Savenije, M. Abdellah, K. Zheng, A. Yartsev, T. Pascher, T. Harlang, P. Chabera, T. Pullerits, A. Stepanov, J.-P. Wolf and V. Sundström, *J. Am. Chem. Soc.*, 2014, **136**, 5189–5192.
- 3 O. D. Miller, E. Yablonovitch and S. R. Kurtz, *IEEE J. Photovoltaics*, 2012, **2**, 303–311.
- 4 F. Deschler, M. Price, S. Pathak, L. E. Klintberg, D.-D. Jarausch, R. Higler, S. Hüttner, T. Leijtens, S. D. Stranks, H. J. Snaith, M. Atatüre, R. T. Phillips and R. H. Friend, *J. Phys. Chem. Lett.*, 2014, **5**, 1421–1426.
- 5 N.-G. Park, *Mater. Today*, 2014, DOI: 10.1016/j.mattod.2014.07.007.
- 6 L. Etgar, P. Gao, Z. Xue, Q. Peng, A. K. Chandiran, B. Liu, M. K. Nazeeruddin and M. Grätzel, *J. Am. Chem. Soc.*, 2012, **134**, 17396–17399.
- 7 M. M. Lee, J. Teuscher, T. Miyasaka, T. N. Murakami and H. J. Snaith, *Science*, 2012, **338**, 643–647.
- 8 H.-S. Kim, C.-R. Lee, J.-H. Im, K.-B. Lee, T. Moehl, A. Marchioro, S.-J. Moon, R. Humphry-Baker, J.-H. Yum, J. E. Moser, M. Grätzel and N.-G. Park, *Sci. Rep.*, 2012, **2**, 591.
- 9 A. Kojima, M. Ikegami, K. Teshima and T. Miyasaka, *Chem. Lett.*, 2012, **41**, 397–399.
- 10 S. D. Stranks, G. E. Eperon, G. Grancini, C. Menelaou, M. J. P. Alcocer, T. Leijtens, L. M. Herz, A. Petrozza and H. J. Snaith, *Science*, 2013, **342**, 341–344.
- 11 D. V. Talapin, A. L. Rogach, E. V. Shevchenko, A. Kornowski, M. Haase and H. Weller, *J. Am. Chem. Soc.*, 2002, **124**, 5782–5790.
- 12 C. Wehrenfennig, G. E. Eperon, M. B. Johnston, H. J. Snaith and L. M. Herz, *Adv. Mater.*, 2014, **26**, 1584–1589.
- 13 J. H. Noh, S. H. Im, J. H. Heo, T. N. Mandal and S. I. Seok, *Nano Lett.*, 2013, **13**, 1764–1769.
- 14 M. Zhang, H. Yu, M. Lyu, Q. Wang, J.-H. Yun and L. Wang, *Chem. Commun.*, 2014, **50**, 11727–11730.
- 15 S. Ryu, J. H. Noh, N. J. Jeon, Y. Chan Kim, W. S. Yang, J. Seo and S. I. Seok, *Energy Environ. Sci.*, 2014, **7**, 2614–2618.
- 16 E. Edri, S. Kirmayer, M. Kulbak, G. Hodes and D. Cahen, *J. Phys. Chem. Lett.*, 2014, **5**, 429–433.
- 17 L. C. Schmidt, A. Pertegás, S. González-Carrero, O. Malinkiewicz, S. Agouram, G. Mínguez Espallargas, H. J. Bolink, R. E. Galian and J. Pérez-Prieto, *J. Am. Chem. Soc.*, 2014, **136**, 850–853.
- 18 J. Aguilera-Sigalat, S. Rocton, J. F. Sanchez-Royo, R. E. Galian and J. Perez-Prieto, *RSC Adv.*, 2012, **2**, 1632–1638.
- 19 J. Pérez-Prieto, *Photochem. Photobiol.*, 2013, **89**, 1291–1298.
- 20 O. Knop, R. E. Wasylshen, M. A. White, T. S. Cameron and M. J. M. V. Oort, *Can. J. Chem.*, 1990, **68**, 412–422.
- 21 A. Poglitsch and D. Weber, *J. Chem. Phys.*, 1987, **87**, 6373–6378.
- 22 W. E. Morgan and J. R. Van Wazer, *J. Phys. Chem.*, 1973, **77**, 964–969.
- 23 R. Lindblad, D. Bi, B.-w. Park, J. Oscarsson, M. Gorgoi, H. Siegbahn, M. Odelius, E. M. J. Johansson and H. Rensmo, *J. Phys. Chem. Lett.*, 2014, **5**, 648–653.
- 24 S. Chen, T. W. Goh, D. Sabba, J. Chua, N. Mathews, C. H. A. Huan and T. C. Sum, *APL Mater.*, 2014, **2**, 081512–081517.
- 25 R. E. Galian, M. de la Guardia and J. Pérez-Prieto, *Langmuir*, 2011, **27**, 1942–1945.
- 26 A. Adenier, M. M. Chehimi, I. Gallardo, J. Pinson and N. Vilà, *Langmuir*, 2004, **20**, 8243–8253.
- 27 H. Kanai, M. Yoshiki, M. Hayashi, R. Kuwae and Y. Yamashita, *J. Am. Ceram. Soc.*, 1994, **77**, 2229–2231.
- 28 C. A. Cattley, A. Stavrinadis, R. Beal, J. Moghal, A. G. Cook, P. S. Grant, J. M. Smith, H. Assender and A. A. R. Watt, *Chem. Commun.*, 2010, **46**, 2802–2804.
- 29 These results contrast with the theoretical prediction that primary ammonium bromides decompose to the corresponding amine plus HBr, ref. 30.
- 30 A. Dualeh, P. Gao, S. I. Seok, M. K. Nazeeruddin and M. Grätzel, *Chem. Mater.*, 2014, 6160–6164.
- 31 M. Sawicka, P. Storoniak, P. Skurski, J. Błażejowski and J. Rak, *Chem. Phys.*, 2006, **324**, 425–437.
- 32 Y. Zhao and K. Zhu, *J. Am. Chem. Soc.*, 2014, **136**, 12241–12244.
- 33 A. Abate, M. Saliba, D. J. Hollman, S. D. Stranks, K. Wojciechowski, R. Avolio, G. Grancini, A. Petrozza and H. J. Snaith, *Nano Lett.*, 2014, **14**, 3247–3254.
- 34 N. K. Noel, A. Abate, S. D. Stranks, E. S. Parrott, V. M. Burlakov, A. Goriely and H. J. Snaith, *ACS Nano*, 2014, **8**, 9815–9821.
- 35 I. A. Shkrob and T. W. Marin, *J. Phys. Chem. Lett.*, 2014, **5**, 1066–1071.

Electronic Supplementary Information

Approaching the top of the emissive properties of CH_3PbBr_3 perovskite nanoparticles

Soranyel Gonzalez-Carrero, Raquel E. Galian* and Julia Pérez-Prieto*

Electronic Supplementary Information

Figure S1: Absorption spectra of Pc and P_{OA1} in toluene. Emission spectra of Pc and P_{OA1} in toluene; and P_{OA1} film.	S2
Table S1: Synthesis of P_{OA} perovskites in the presence and in the absence of ODE and OLA	S3
Table S2: Study of the influence of the alkyl-chain length of the longer ammonium salt on the emissive properties of the perovskites in the absence of OLA	
Figure S2: Absorption and emission spectra of P_{OA3} in toluene; emission recorded at $\lambda_{\text{exc}}=350$ nm.	S4
Figure S3: Absorption and emission spectra of P_{HXA} in toluene and HRTEM images.	S5
Figure S4: XPS spectra of C_{1s} for P_{OA1} and P_{OA2}	S6
Figure S5: XPS spectra of N_{1s} for P_{OA1} and P_{OA2}	S7
Figure S6: XPS spectra of O_{1s} for P_{OA1} and P_{OA2}	S8
Figure S7: XPS spectra of Pb_{4f} for P_{OA1} and P_{OA2}	S9
Figure S8: XPS spectra of Br_{3d} for P_{OA1} and P_{OA2}	S10
Figure S9: TGA heating curve and its 1 st derivative peaks of MABr, OABr, and lead bromide.	S11
Figure S10: TGA heating curve and its 1 st derivative peaks of OLA and ODE.	S12
Figure S11: TGA heating curve and its 1 st derivative peaks of MA and OA.	S13
Figure S12: TGA heating curve of Ss1 and its 1 st derivative peaks	S14
Figure S13: TGA heating curve of Ss2 and its 1 st derivative peaks	
Figure S14: ¹ H NMR (300 MHz) spectrum of P_{OA1} in deuterated DMSO	S15
Figures S14-S18. ¹ H-NMR of the precursors	S16-S19
Table S3. Quantification of the component molar ratio in P_{OA1} by using TGA and ¹ H-RMN data	S20
Table S4. Quantification of the component molar ratio in P_{OA2} by using TGA and ¹ H-RMN data	
Table S5. Decay photoluminescence lifetimes (τ) of toluene solutions of P_{OA1} at different excitation wavelengths (λ_{exc})	S21
Table S6. Decay photoluminescence lifetimes (τ) of toluene solutions of P_{OA2} at different excitation wavelengths (λ_{exc})	
Figure S18. Left: Room-temperature photoluminescence of P_{OA2} in toluene ($\lambda_{\text{em}}=521$ nm) as a function of the illumination time. Right: fluorescence spectra of the sample ($\lambda_{\text{exc}}=350$ nm; $\lambda_{\text{em}}=521$ nm) before and after 75 minutes irradiation.	S22

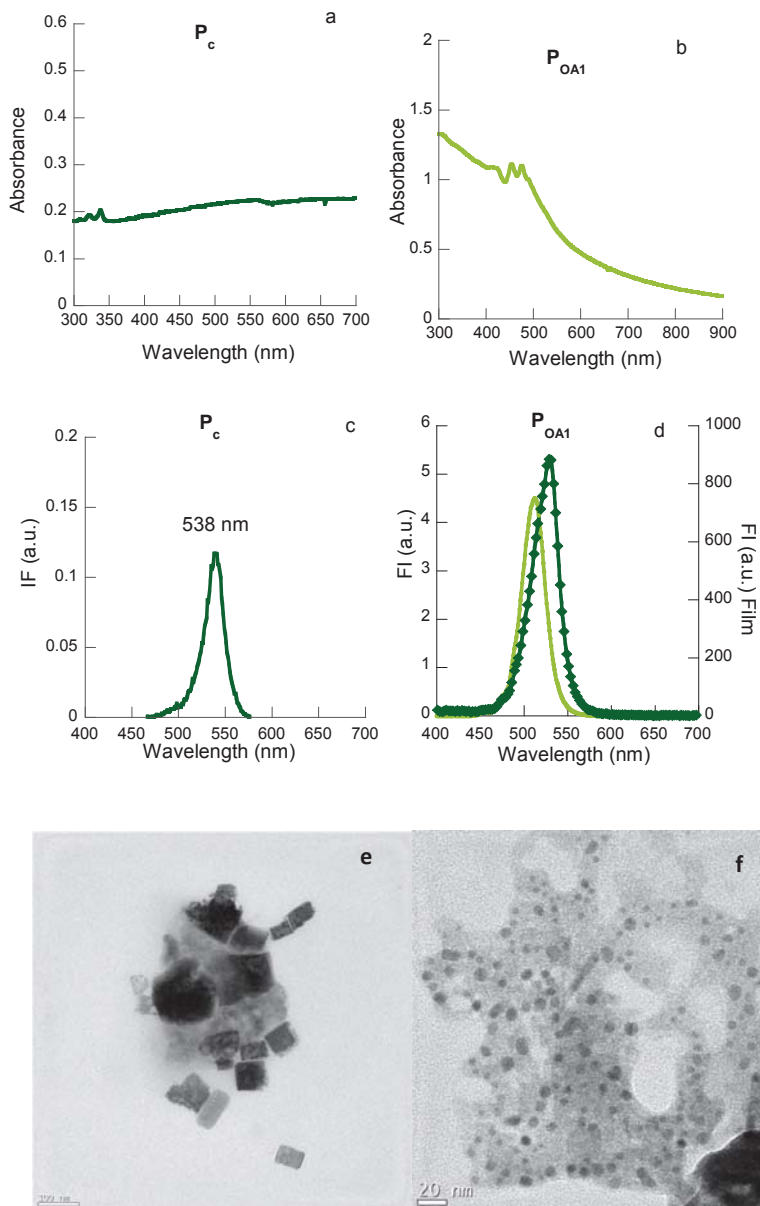


Figure S1: Absorption spectra of **Pc** (a) and **P_{OA1}** (b) in toluene. Emission spectra of **Pc** (c) and **P_{OA1}** in toluene (light green) (d); and **P_{OA1}** film (dark green) (d). Emission recorded at $\lambda_{exc}=350$ nm. (d) HRTEM images (scale bar 20 nm) of **Pc** (e) and **P_{OA1}** (f).

Table S1: Synthesis of P_{OA} perovskites in the presence and in the absence of ODE and OLA

Name	OABr (mmol)	MABr (mmol)	PbBr ₂ (mmol)	ODE (mmol)	OLA (mmol)	Emission properties (λ , nm)	ϕ_F
P_{OA1}	0.16	0.24	0.1	6.26	0.3	513	0.67
P_{OA2}	0.16	0.24	0.1	6.26	-	526	0.83
P_{OA3}	0.16	0.24	0.1	-	0.3	525	0.52

Table S2: Study of the influence of the alkyl-chain length of the longer ammonium salt on the emissive properties of the perovskites in the absence of OLA

Name	Ammonium salt	Ammonium salt (mmol)	MABr (mmol)	PbBr ₂ (mmol)	ODE (mmol)	Emission maximum (λ , nm)	ϕ_F
P_{EA}	EABr	0.16	0.24	0.1	6.26	^a	-
P_{HA}	HABr	0.16	0.24	0.1	6.26	526	0.58

^a An orange solid not dispersible in toluene was obtained.

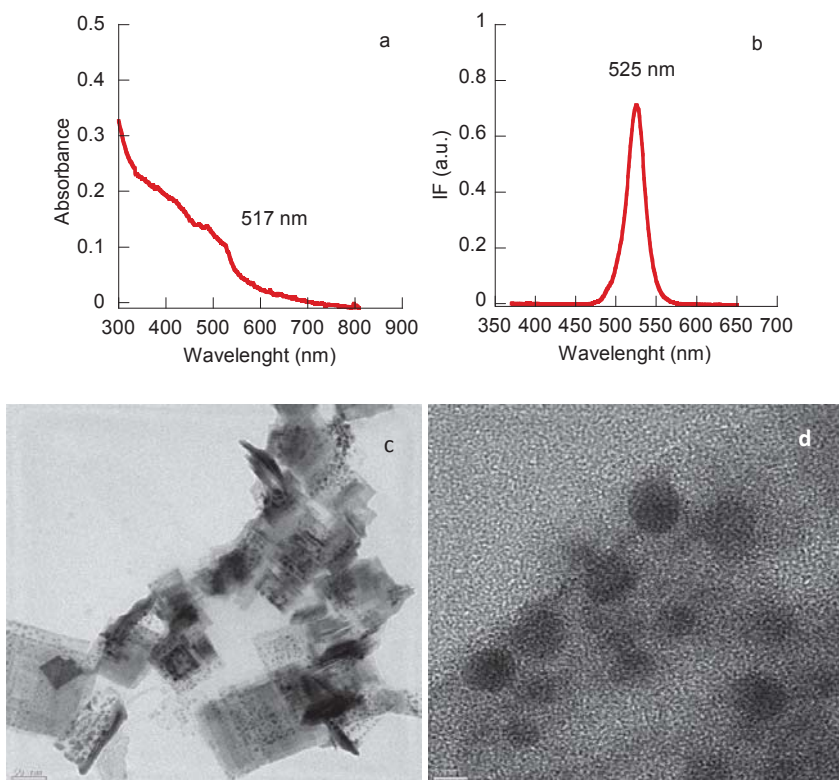


Figure S2: Absorption (a) and emission (b) spectra of P_{OA3} in toluene; emission recorded at $\lambda_{exc}= 350$ nm. (c) and (d) HRTEM images at 50 and 5 nm scale, respectively. Nanoparticle size 5.92 ± 1.79 nm.

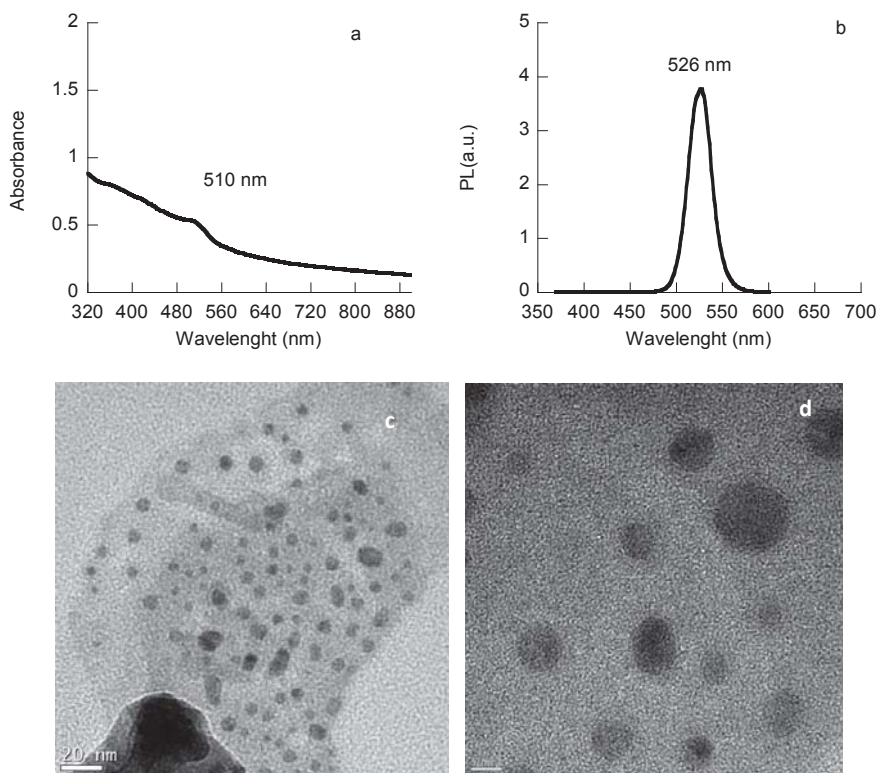


Figure S3: Absorption and emission spectra of P_{HA} (a, b) in toluene; emission recorded at $\lambda_{\text{exc}} = 350$ nm, and HRTEM images with a scale bar of 20 (c) and 5 nm (d). Size 5.92 ± 2.05 nm

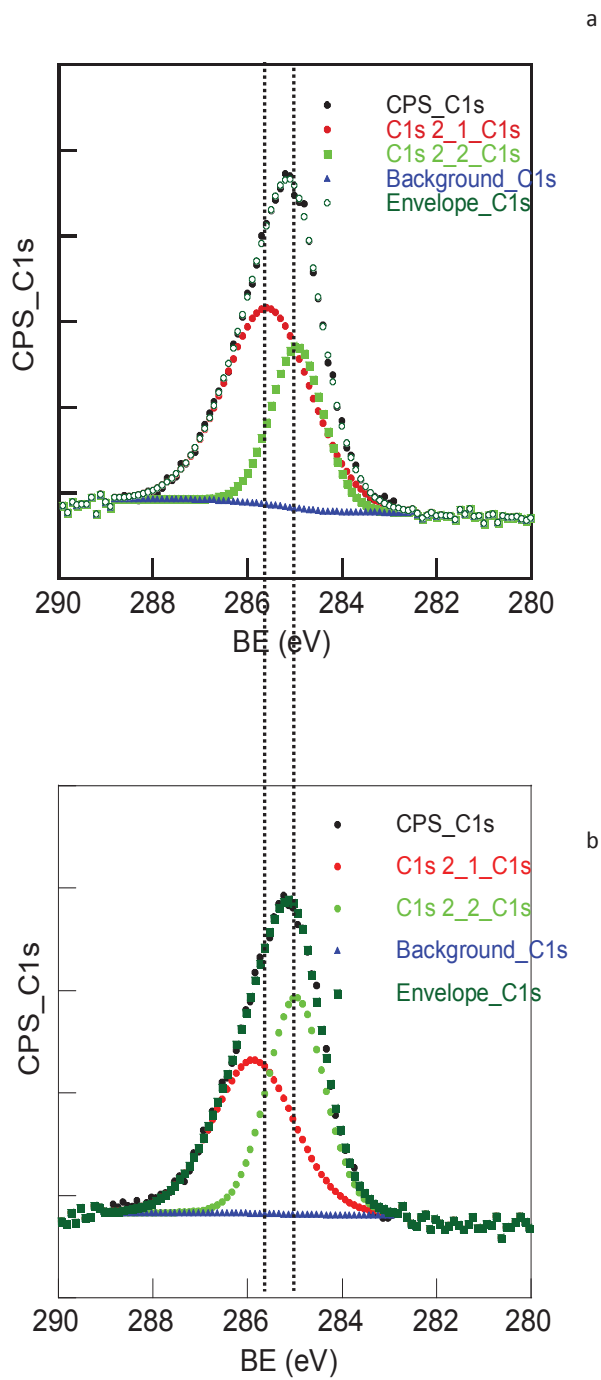


Figure S4: XPS spectra of C1s for P_{OA1} (a) and P_{OA2} (b)

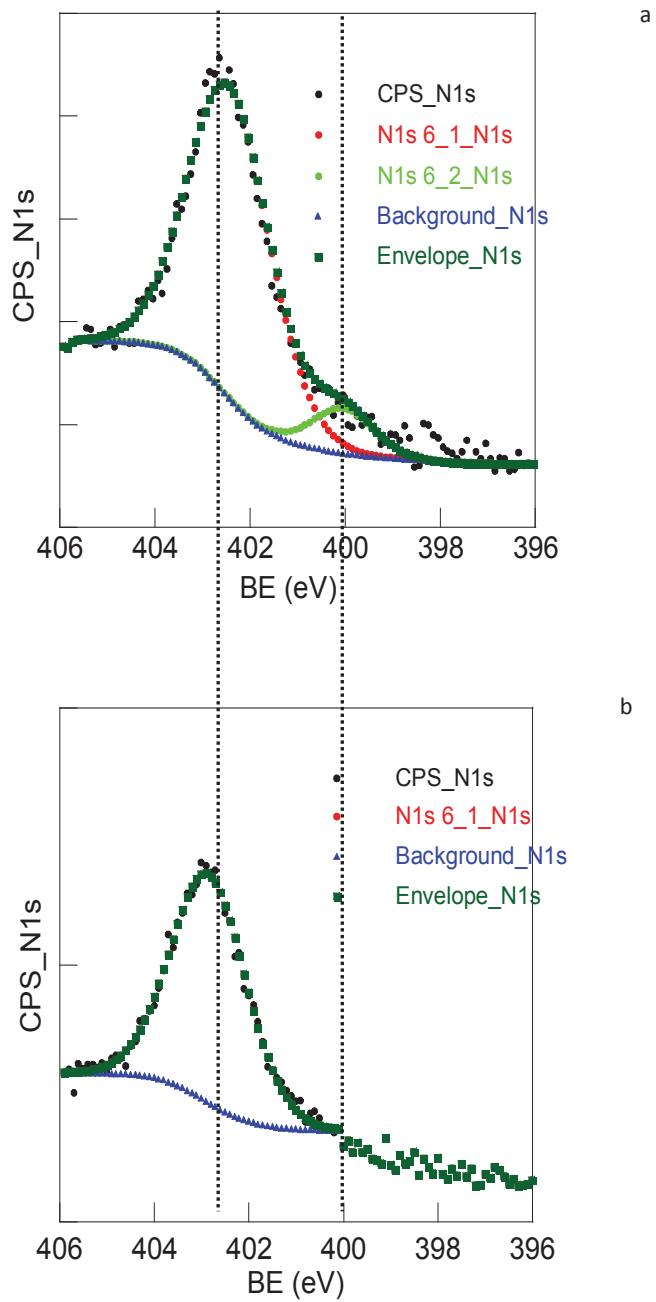


Figure S5: XPS spectra of N1s for P_{OA1} (a) and P_{OA2} (b)

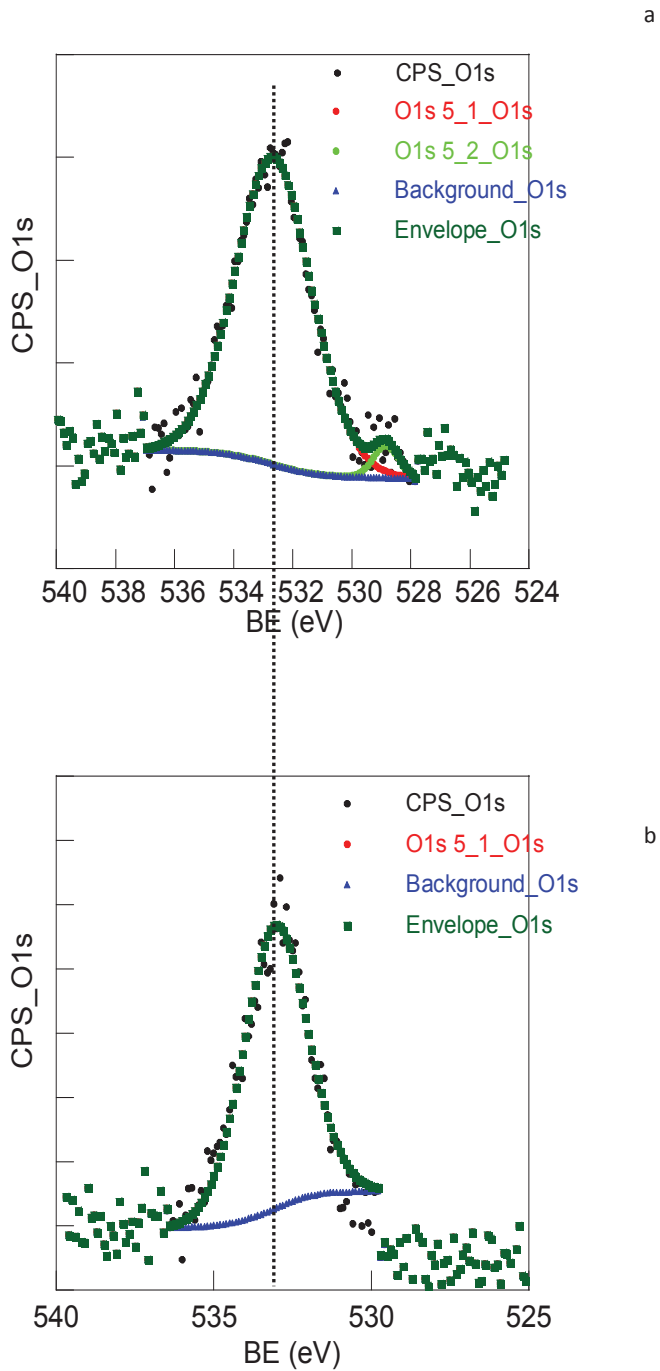
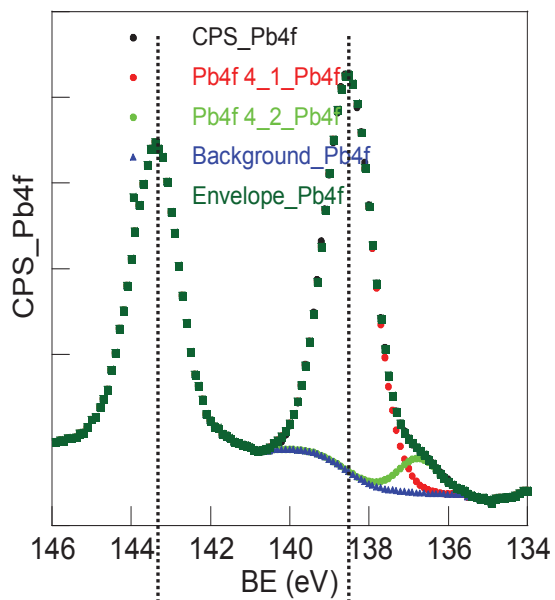


Figure S6: XPS spectra of O1s for $P_{O_{A1}}$ (a) and $P_{O_{A2}}$ (b)

a



b

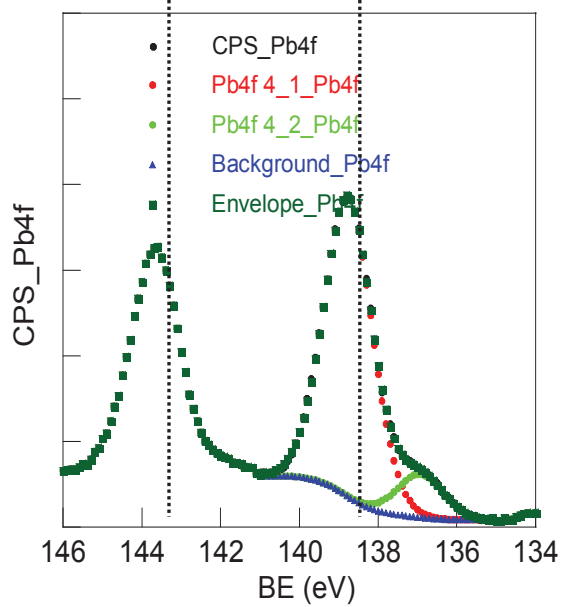


Figure S7: XPS spectra of Pb4f for P_{OA1} (a) and P_{OA2} (b)

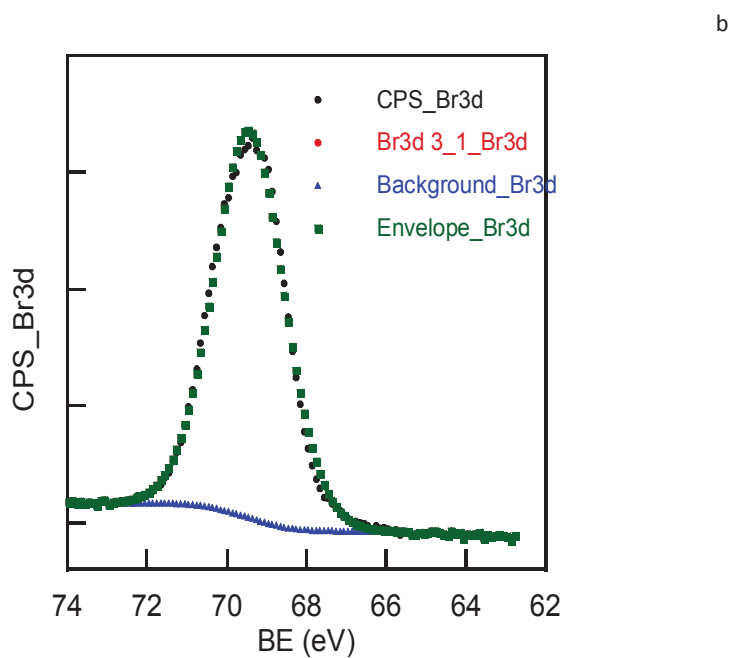
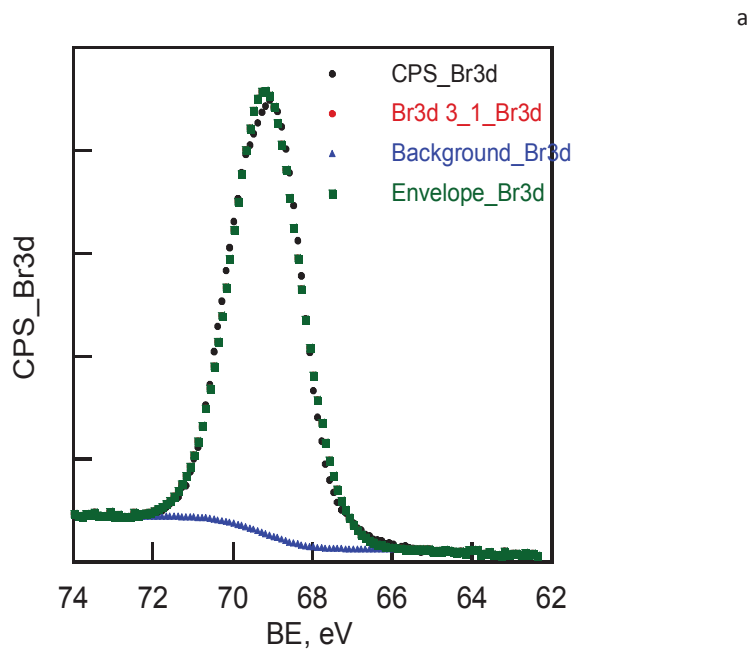


Figure S8: XPS spectra of Br 3d for P_{OA1} (a) and P_{OA2} (b)

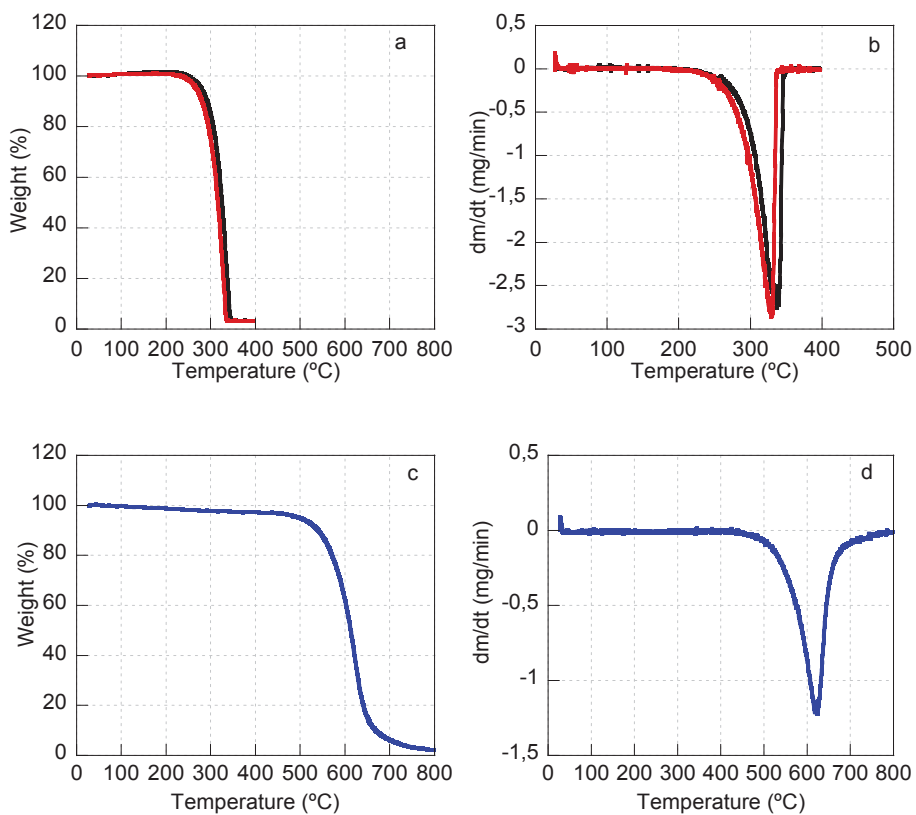


Figure S9: TGA heating curve of MABr and OABr (a, black and red, respectively) and of PbBr₂ (c); 1st derivative peaks of MABr and OABr (b, black and red, respectively) and of PbBr₂ (d).

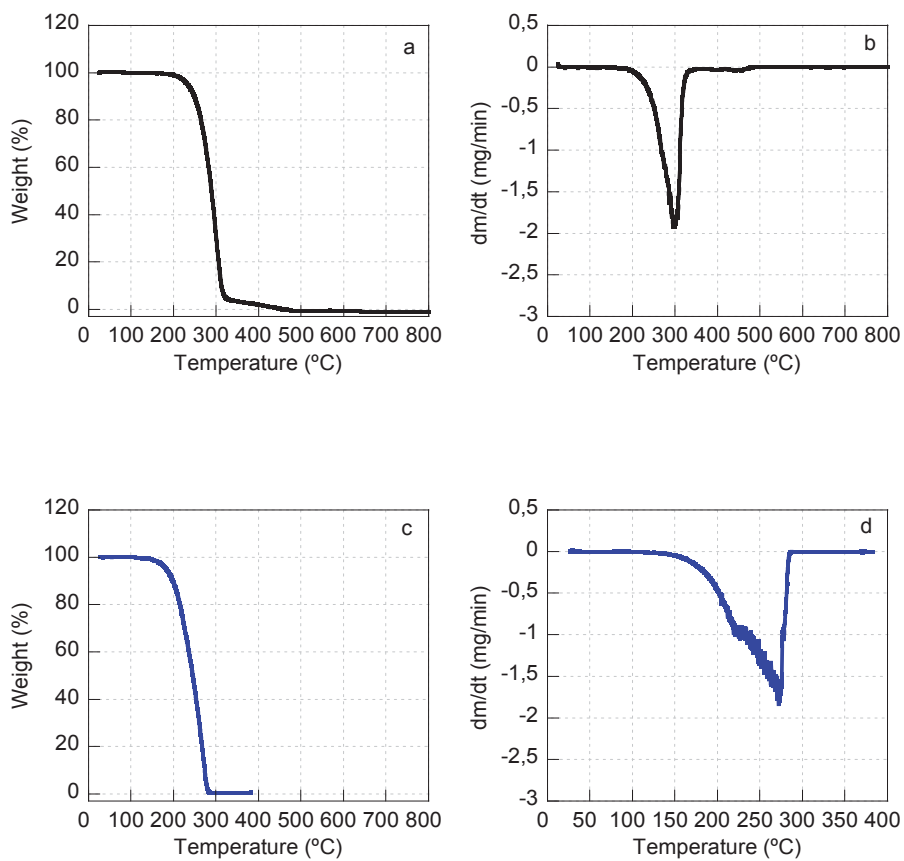


Figure S10: TGA heating curve of OLA and ODE (a and c, in black and blue, respectively) and its 1st derivative peaks (b and d).

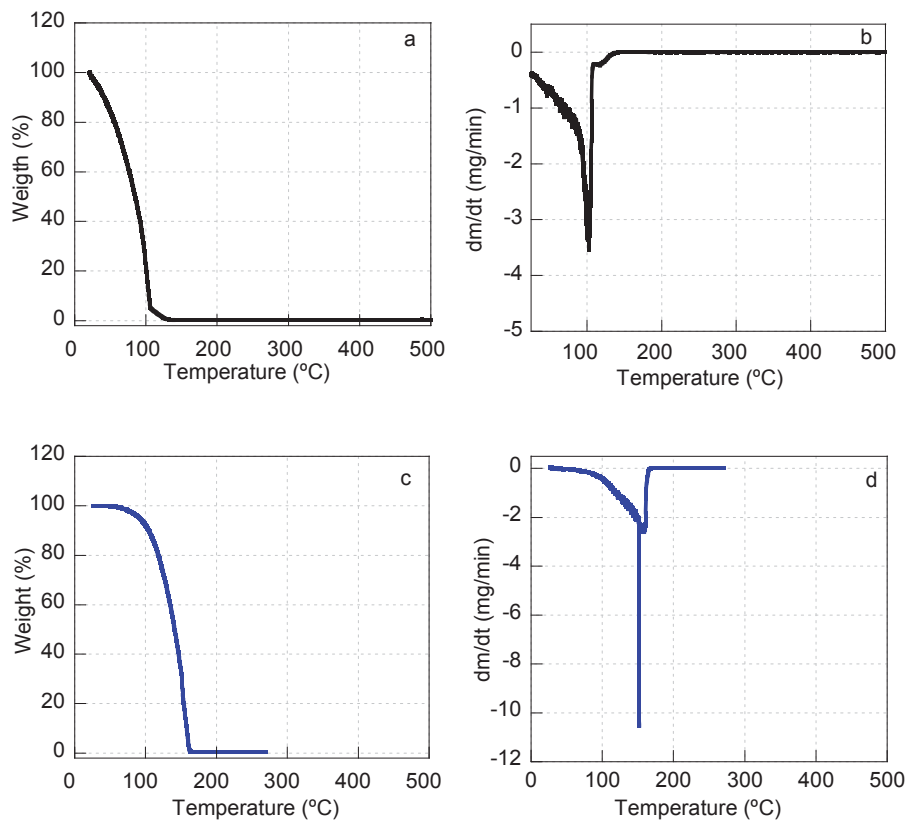


Figure S11: TGA heating curve of MA and OA (a and c, in black and blue, respectively) and its 1st derivative peaks (b and d).

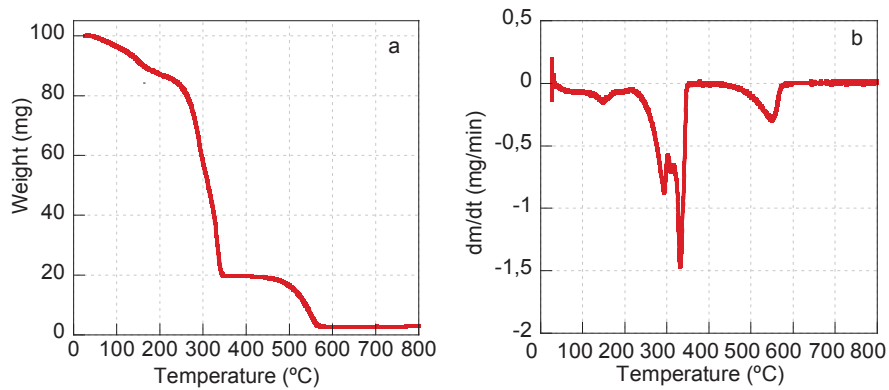


Figure S12: TGA heating curve of **Ss1** (a) and its 1st derivative peaks (b).

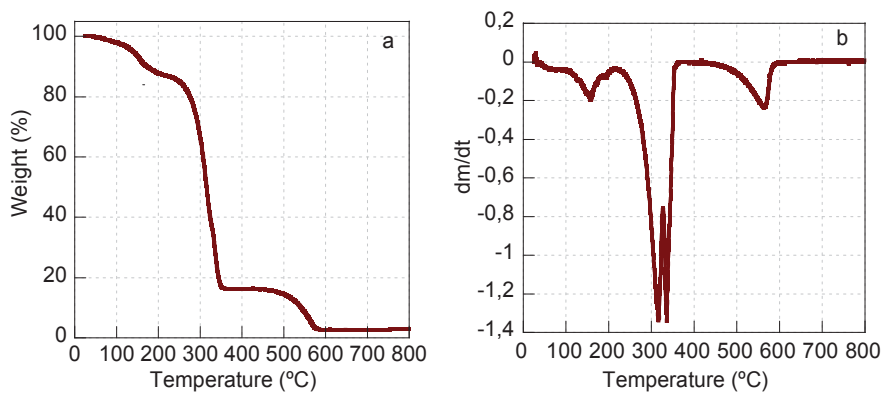


Figure S13: TGA heating curve of **Ss2** (a) and its 1st derivative peaks (b).

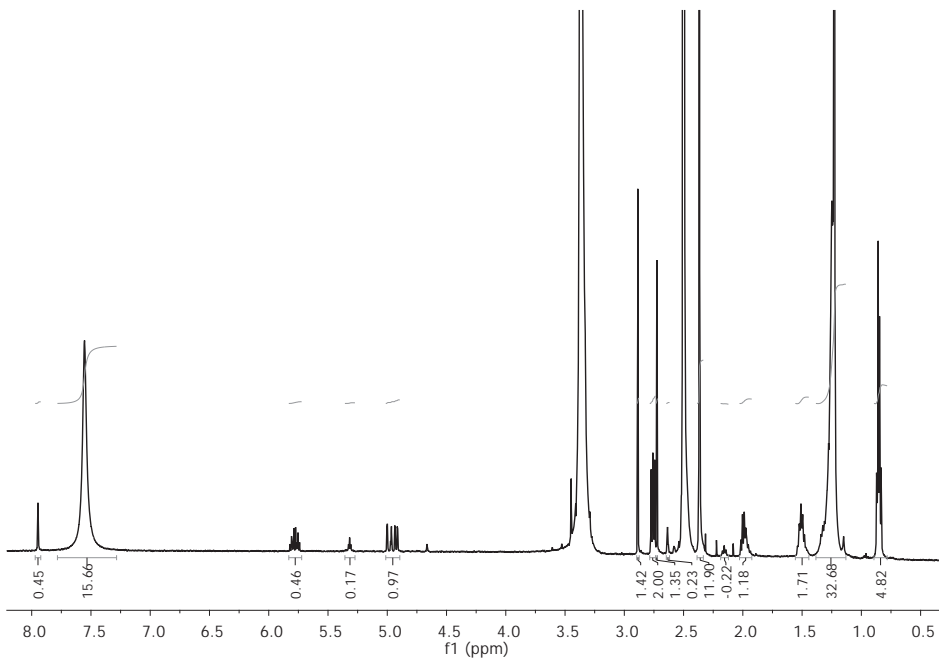


Figure S14: ¹H NMR (300 MHz) spectrum of P_{OA1} in deuterated DMSO

¹H-NMR of the precursors

Methylammonium bromide

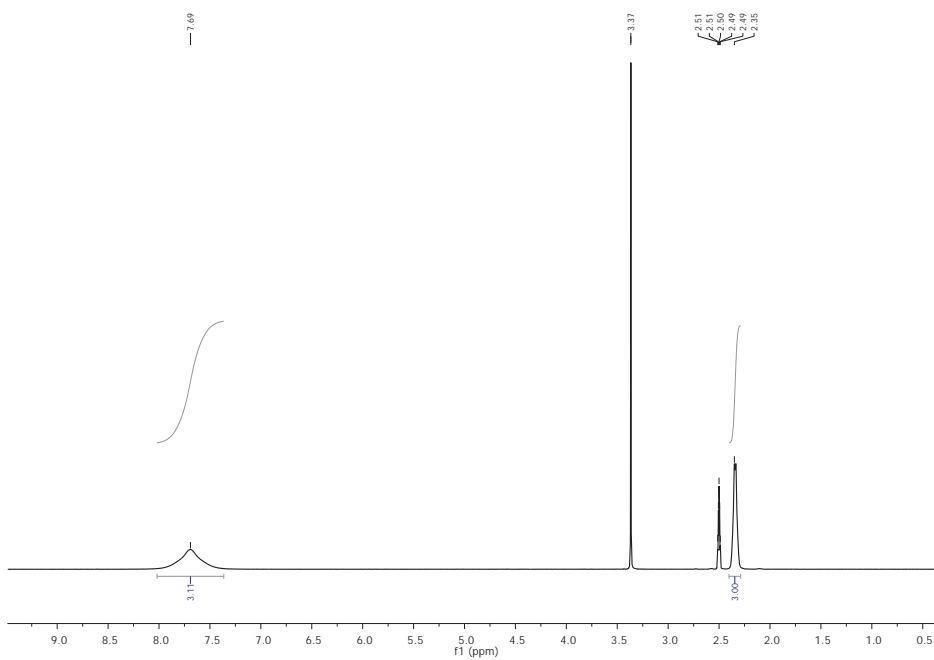


Figure S15. ¹H NMR (300 MHz) spectrum of methylammonium bromide in deuterated DMSO.

¹H NMR (300 MHz, d-DMSO) δ 7.69 (s, 3H), 2.34 (s, 3H).

Octylammonium bromide

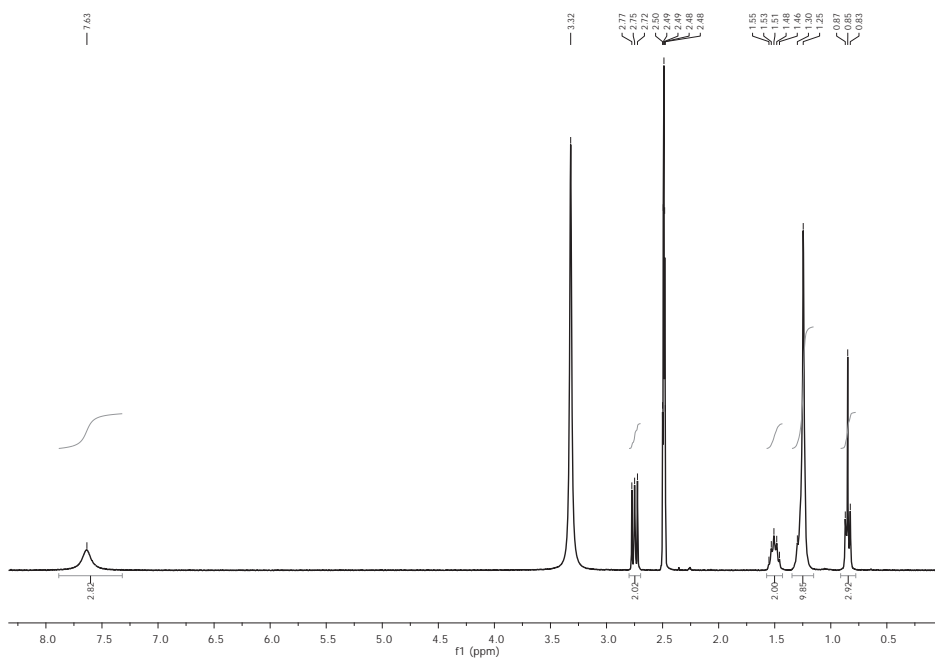


Figure S16. ^1H NMR (300 MHz) spectrum of octylammonium bromide in deuterated DMSO.

^1H NMR (300 MHz, d-DMSO) δ 7.63 (s, 3H), 2.75 (t, J = 7.5 Hz, 2H), 1.59 – 1.41 (m, 2H), 1.27 (s, 10H), 0.85 (t, J = 7.0 Hz, 3H).

Oleic acid

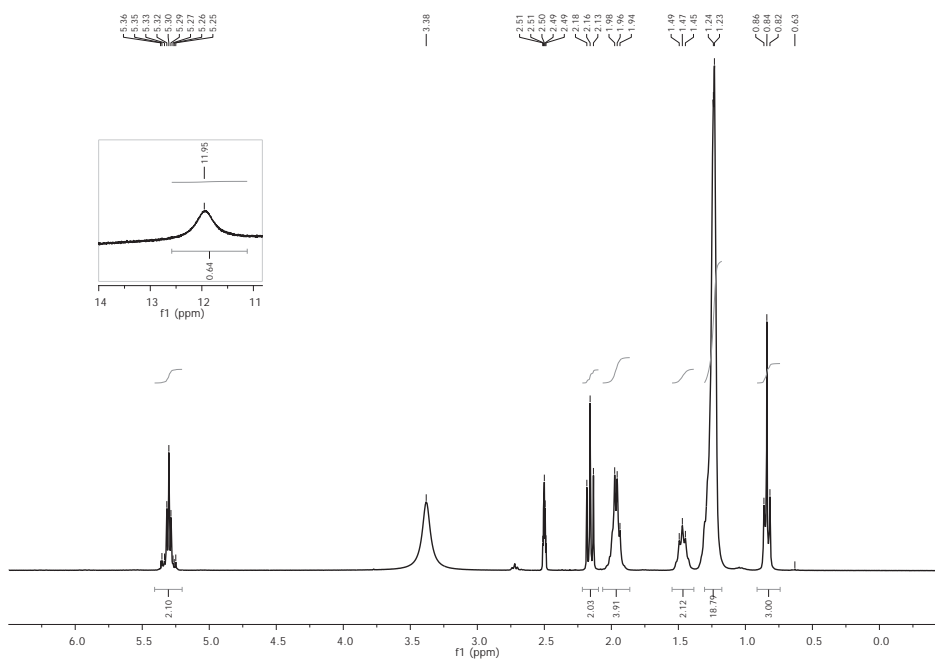


Figure S17. ¹H NMR (300 MHz) spectrum of oleic acid in deuterated DMSO.

¹H NMR (300 MHz, d-DMSO) δ 11.95 (s, 1H), 5.41 – 5.20 (m, 2H), 2.16 (t, J = 7.4 Hz, 2H), 2.06 – 1.86 (m, 4H), 1.55 – 1.38 (m, 2H), 1.23 (d, J = 2.3 Hz, 19H), 0.91 – 0.74 (m, 3H).

Octadecene

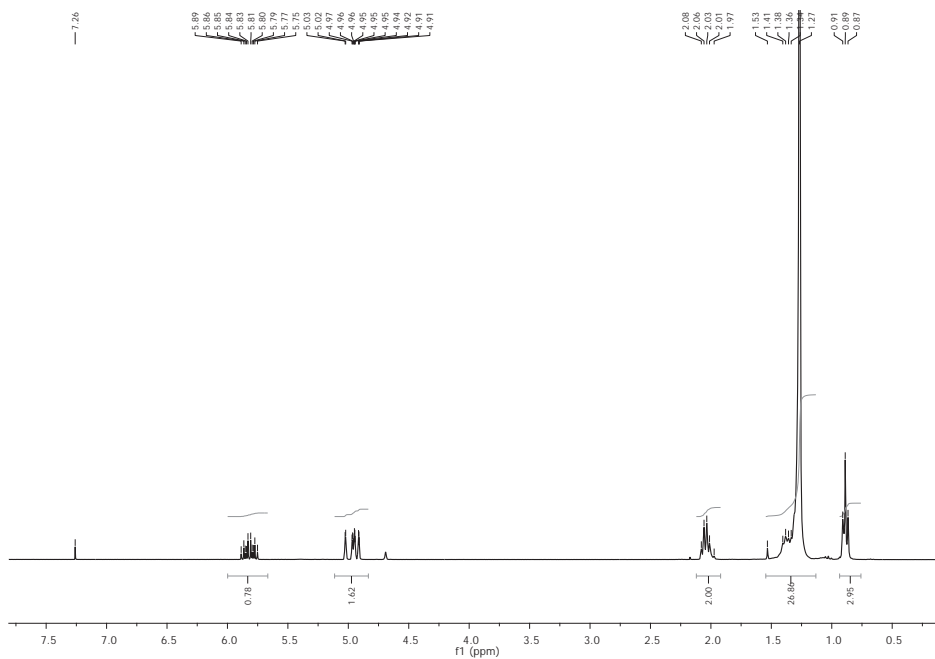


Figure S18. ¹H NMR (300 MHz) spectrum of 1-octadecene in deuterated DMSO.

¹H NMR (300 MHz, CDCl₃) δ 5.82 (ddt, *J* = 16.9, 10.2, 6.7 Hz, 1H), 5.12 – 4.76 (m, 2H), 2.12 – 1.92 (m, 2H), 1.60 – 0.97 (m, 27H), 0.89 (t, *J* = 6.6 Hz, 3H).

Table S3. Quantification of the component molar ratio in P_{OA1} by using TGA and 1H -RMN data

Reagents	Reagents mmol	P_{OA1}	
		Component mmol	Component/ $PbBr_2^*$ Molar ratio
OABr	0.24	0.031	0.35
MABr	0.16	0.122	1.39
ODE	6.17	0.015	0.17
OLA	0.29	0.003	0.03
PbBr₂	0.10	0.088	1.00

*Moles of $PbBr_2$ calculated by TGA.

Table S4. Quantification of the component molar ratio in P_{OA2} by using TGA and 1H -RMN data

Reagents	Reagents mmol	P_{OA2}	
		Component mmol	Component/ $PbBr_2^*$ Molar ratio
OABr	0.24	0.011	0.11
MABr	0.16	0.131	1.37
ODE	6.17	0.025	0.26
PbBr₂	0.10	0.088	1.00

*Moles of $PbBr_2$ calculated by TGA.

Table S5. Decay photoluminescence lifetimes (τ) of toluene solutions of P_{OA1} at different excitation wavelengths (λ_{exc})

λ_{exc}	τ_{av} (ns)	τ_1 (A ₁ %) (ns)	τ_2 (A ₂ %) (ns)	τ_3 (A ₃ %) (ns)
340 nm	411.17	18.68 (54.62)	123.53 (34.52)	643.80 (10.86)
405 nm	415.92	13.22 (61.36)	115.20 (30.20)	661.60 (8.45)
470 nm	403.78	18.36 (61.11)	132.29 (29.87)	657.56 (9.02)

Table S6. Decay photoluminescence lifetimes (τ) of toluene solutions of P_{OA2} at different excitation wavelengths (λ_{exc})

λ_{exc}	τ_{av} (ns)	τ_1 (A ₁ %) (ns)	τ_2 (A ₂ %) (ns)	τ_3 (A ₃ %) (ns)
340 nm	594.45	19.65 (57.99)	148.88 (32.31)	910.85 (9.71)
405 nm	611.43	15.08 (58.27)	138.03 (32.20)	913.33 (9.53)
470 nm	621.80	20.10 (55.93)	149.14 (33.55)	931.83 (10.53)

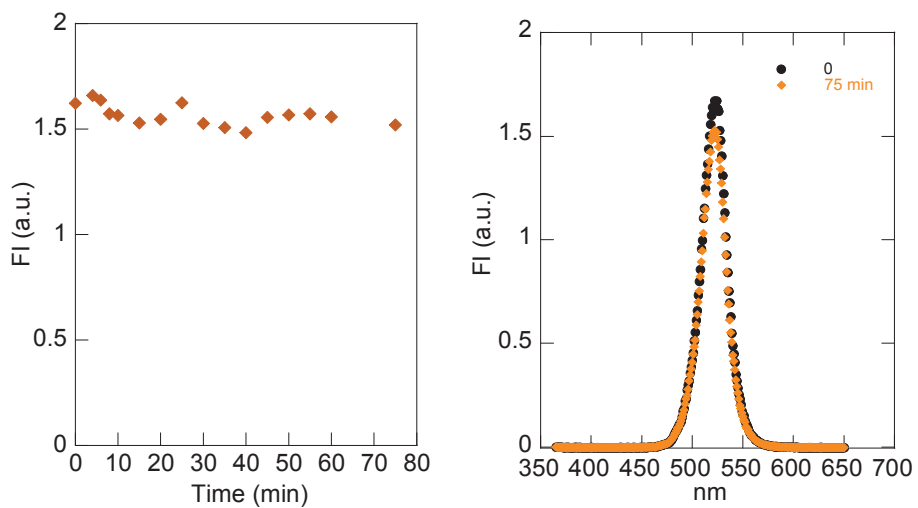


Figure S19. Left: Room-temperature photoluminescence of $\text{P}_{\text{OA}2}$ in toluene ($\lambda_{\text{em}} = 521$ nm) as a function of the illumination time. Right: fluorescence spectra of the sample ($\lambda_{\text{exc}} = 350$ nm; $\lambda_{\text{em}} = 521$ nm) before and after 75 minutes irradiation.



Cite this: *J. Mater. Chem. A*, 2015, **3**, 14039

Blue-luminescent organic lead bromide perovskites: highly dispersible and photostable materials†

Soranyel Gonzalez-Carrero, Guillermo Mínguez Espallargas, Raquel E. Galian* and Julia Pérez-Prieto*

The preparation of a blue-luminescent and photostable organic–inorganic hybrid perovskite with an X-ray powder diffraction spectrum consistent with a two-dimensional inorganic framework is reported. This perovskite can be produced with a high reaction yield and valuable optical properties, such as luminescence quantum yield over 20%, radiative rate constant of up to $80 \times 10^6 \text{ s}^{-1}$, and high photostability under UV light. This material remains stable as a solid, is toluene-dispersible, and can be reverted reversibly into its precursors by using dimethylformamide (DMF). Moreover, the DMF dispersion can be injected into toluene to produce a nanomaterial or be used to prepare films by spin-coating on a substrate; both, the nanomaterial and the film exhibit practically the same optical features as the initial perovskite.

Received 9th March 2015
Accepted 19th May 2015

DOI: 10.1039/c5ta01765c

www.rsc.org/MaterialsA

1. Introduction

The processability of a material *i.e.*, its ability to be worked and shaped, is a relevant property for its application in devices. In addition, there is great interest in the preparation of stable and dispersible materials with high photoluminescence (PL) quantum yield, narrow emission spectrum, and high photostability.

Organometal halide perovskites combine the favourable properties of the inorganic material, namely its structural rigidity and stability, as well as electronic, optical, and transport properties with the flexibility and low-temperature processability of the organic material.¹ Organolead halide perovskites with the general formula of APbX_3 (A = alkyl ammonium cation, X = halide anion)^{2,3} present a three-dimensional (3D) inorganic framework consisting of corner-sharing PbX_6 octahedra, and small-sized organic cations in the voids between the octahedra. In these perovskites, the organic cation should be of a relatively small size to fit into the octahedra. If the cation is too large, the 3D perovskite structure becomes unsuitable, consequently the dimension of the inorganic framework is reduced and, concomitantly, the exciton band of the perovskite shifts to higher energies.^{1,4} Stable excitons with large binding energy are

formed even at room-temperature due to the low dimensionality of the inorganic framework and the dielectric confinement (dielectric constant mismatch between the inorganic and organic constituents: 2.4 vs. 6.1 for the organic layer and the metal halide layer, respectively).^{5,6}

Perovskites with a 2D inorganic framework are built from the monolayers of corner-sharing PbX_6 octahedra sandwiched between organic molecular layers.¹ The radiative decay rate of the excitons increases in low-dimensional frameworks. The unique properties of confined excitons are of great interest for optical devices.⁷

The most simple hybrid lead halide perovskites with a 2D-layered framework present a general A_2PbX_4 formula;^{8–12} they have been widely studied (mostly as thin films) and exhibit low photostability. In addition, it has been reported that those with the formula $(\text{C}_n\text{H}_{2n+1}\text{NH}_3)_2\text{PbX}_4$ ($n > 10$; X = I and Br) tend to show phase transitions (which are eventually reflected in optical features) with temperature and other parameters.^{13,14}

We report here the easy and efficient preparation of a highly dispersible, blue-luminescent lead perovskite with octadecylammonium bromide as the organic component (P_{ODA}).

This material exhibits considerable emission (quantum yield, Φ_{PL} , over 20%) and its X-ray powder diffraction (PXRD) spectrum was compatible with that of 2D-layered A_2PbBr_4 perovskites. Promising features of these P_{ODA} perovskites for device applications are that it is easy to prepare them with a high yield, they are stable in both colloidal solutions and in solids, and they exhibit an extraordinary photostability. Remarkably, they can be reverted back into their precursors by using a polar solvent; then, the resulting dispersion can be used to prepare films or to produce nanoparticles by injecting it into

Instituto de Ciencia Molecular (ICMol), Universidad de Valencia, Catedrático José Beltrán 2, 46980, Paterna, Valencia, Spain. E-mail: Raquel.galian@uv.es; julia.perez@uv.es; Fax: +34 963543273; Tel: +34 963544307

† Electronic supplementary information (ESI) available: Additional absorption, emission, TGA, XPS, NMR spectra of perovskite and precursors, as well as tables with photophysical and nanoparticle composition data. See DOI: 10.1039/c5ta01765c

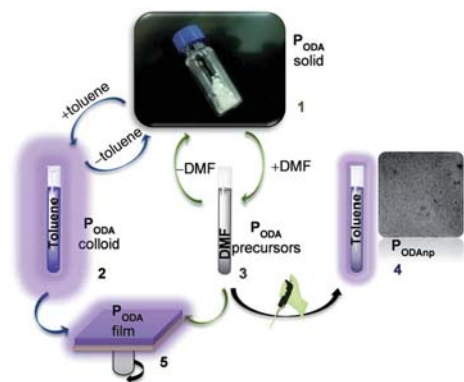


Fig. 1 Picture showing the processability of the P_{ODA} perovskite and its reversible assembling–disassembling.

toluene (Fig. 1). All these materials exhibit practically the same absorption/emission spectra and similar XRD spectra.

2. Experimental section

2.1 Materials and methods

All chemicals were of analytical grade and used as received without further purification. Toluene was of HPLC quality for spectroscopic measurements.

UV-vis spectra were recorded at room temperature using quartz cuvettes in an Agilent 8453E UV-visible spectrophotometer. Fluorescence spectra were measured on an Amnco Browman series 2 Luminescence spectrometer, equipped with a lamp power supply working at room temperature. The AB2 software (v. 5.5) was used to register the data. All the data were acquired using $1\text{ cm} \times 1\text{ cm}$ path length quartz cuvettes. The emission spectra of the perovskites dispersed in toluene were measured under an air atmosphere (unless otherwise indicated).

The photoluminescence spectra and quantum yields of the films were measured with a Hamamatsu C9920-02 absolute PL Quantum Yield Measurement System.

Lifetime measurements were performed using a Quantaurus-Tau C11367 Compact fluorescence lifetime spectrometer. The average lifetime was calculated by fitting multiexponential decay curves.

Structural and morphological characterisations were performed using bright field transmission electron microscopy (TEM) and high resolution TEM (HRTEM). A field emission gun (FEG) TECNAI G2 F20 microscope, operating at 200 kV, was used. TEM samples were prepared by depositing a few drops of the perovskite solution on the carbon film supported on a copper grid (200 mesh); the samples were subsequently dried overnight.

The PXRD analysis was performed on a Bruker D8 Advance A25 diffractometer using $\text{CuK}\alpha$ ($\lambda = 1.54060\text{ \AA}$) radiation at a voltage of 40 kV and 30 mA, and a LynxEye detector.

The $^1\text{H-NMR}$ spectra were registered at room temperature using a Bruker DPX300 spectrometer, with a 300 MHz Bruker magnet. The chemical shifts (δ) are reported in ppm using tetramethylsilane (TMS) as a reference.

The thermogravimetric analysis was carried out using a Mettler Toledo TGA/SDTA 851e system with an operative temperature range of 25–1100 °C and 0.1 microgram sensitivity.

The photostability of the colloidal solutions was analysed using $10 \times 10\text{ mm}$ quartz cuvettes placed in the sample-holder of a PTI-LPS-220B spectrometer equipped with a Xenon lamp and the samples illuminated with UV-light Felix 32 analysis software were used to register the data.

The XPS data were acquired with a Specs using a Phoibos 150-9MCD X-ray photoelectron spectrometer. The incident radiation was 50 W. The C_{1s} peak at 285 eV was set as a reference for all XPS peak positions.

2.2 Synthesis of the perovskites

Hexyl- and octyl-ammonium bromide were synthesised by the reaction of the corresponding amine in water/HBr, in accordance with the previously reported procedure.¹⁵ In the case of octadecylammonium bromide, it was prepared by using a similar methodology but the amine was previously dissolved in acetonitrile at 60 °C and then HBr was added. In all cases, the precipitate was washed several times with diethyl ether, dried under vacuum, and used without further purification.

For the synthesis of $P_{\text{HXA}1}$, a solution of oleic acid (OLA, 0.30 mmol, 85 mg) in 1-octadecene (ODE, 6.26 mmol, 2.0 mL) was stirred and heated at 80 °C and then hexylammonium bromide (HXABr , 0.2 mmol, 36.42 mg) was added. Subsequently, lead(II) bromide (0.10 mmol, 36.7 mg, dissolved in 200 μL of DMF) was added. No colour change was observed after the addition of lead(II) bromide. The addition of acetone (5 mL) induced the precipitation of a white solid ($P_{\text{HXA}1}$). The remaining material was separated by centrifugation (7000 rpm, 10 min, 20 °C), washed with acetone, and dried at room temperature. Samples $P_{\text{OCA}1}$ and $P_{\text{ODA}1}$ were prepared following the same procedure.

Samples $P_{\text{HXA}2}$, $P_{\text{OCA}2}$, and $P_{\text{ODA}2}$ were prepared following the same procedure as that for $P_{\text{HXA}1}$ but in the absence of OLA. Samples $P_{\text{ODA}3}$ and $P_{\text{ODA}4}$ were prepared following the same procedure as that for $P_{\text{ODA}1}$ but either in the absence of 1-octadecene ($P_{\text{ODA}3}$) or halving the amount of ODE and OLA ($P_{\text{ODA}4}$). For the synthesis of $P_{\text{ODA}2\text{nm}}$, $P_{\text{ODA}2}$ was added to DMF (4 mg mL^{-1}) and then 100 μL of the DMF solution was injected into toluene (4 mL).

Films were prepared by using quartz substrates cleaned thoroughly by using detergent, de-mineralised water and isopropyl alcohol, followed by a 20 min UV-ozone treatment. A solution of perovskite in toluene (3 mg/1 mL) was spin-coated on top of the quartz substrate (1500 rpm for 60 s).

3. Results and discussion

3.1 Synthesis of the perovskites

The preparation of the perovskites was carried out by following our previously reported non-template strategy for the

$\text{CH}_3\text{NH}_3\text{PbBr}_3$ nanoparticles,¹⁶ but using a 2 : 1 molar ratio between the ammonium salt (hexyl-, octyl-, or octadecylammonium bromide, HXABr, OCABr, and ODABr, respectively) and PbBr_2 . The ODE/ PbBr_2 molar ratio was fixed at 62.6 : 1.0. In the assays in which oleic acid (OLA) was also added, the OLA/ PbBr_2 molar ratio was 3 : 1. The addition of acetone induced the precipitation of the perovskites as a white solid. The unreactive material was separated from the solid after centrifugation (7000 rpm, 10 min, 20 °C), washed with acetone, and dried at room temperature.

The perovskite with the longest ammonium alkyl chain, $\text{P}_{\text{ODA}1}$, was particularly dispersible in toluene, exhibited a sharp and intense exciton absorption peak at 389 nm, had a narrow emission peak (full width at half maximum, FWHM, ~13 nm) at λ_{max} ca. 397 nm, and presented an emission quantum yield of ~21% (Fig. S1† and Table 1).

In addition, the emission spectrum of the film prepared from the toluene dispersion of $\text{P}_{\text{ODA}1}$ exhibited a peak at $\lambda_{\text{max}} = 398$ nm, an FWHM of ~21 nm, and a smaller emission quantum yield than that of the toluene dispersion (~12% vs. 21%, Table 1). The absorption and emission wavelength maxima of these perovskites were similar to those for spin-coated films of $(\text{C}_n\text{H}_{2n+1}\text{NH}_3)_2\text{PbBr}_4$ perovskites with long ammonium alkyl chains, such as those with $n = 12$.^{17,18}

By contrast, the other two perovskites ($\text{P}_{\text{HXA}1}$ and $\text{P}_{\text{OCA}1}$) proved to be less dispersible, they exhibited a much broader absorption peak, their absorption and emission peaks red-shifted to ca. 400 nm and 410 nm, respectively, and they presented a wider emission band with a considerable tail extending to a wavelength of up to ca. 600 nm, and their emission quantum yield was unmeasurable (Fig. S1†). The wavelength of the absorption and emission peaks of these perovskites matched those reported for their spin-coated films.¹⁷ Moreover, (cyclohexylmethylammonium)₂ PbBr_4 based nanoparticles exhibit emission peaks at 411 nm, only slightly shifted with respect to the spin-coated films.¹⁹

To evaluate the effect of OLA on the optical properties of these perovskites, they were prepared under the same reaction conditions, but without OLA. After precipitation and

centrifugation the solids (samples $\text{P}_{\text{HXA}2}$, $\text{P}_{\text{OCA}2}$, and $\text{P}_{\text{ODA}2}$) were dispersed in toluene. Interestingly, there was a slight improvement in the optical properties of the colloidal perovskites, in particular, the quantum yields of $\text{P}_{\text{HXA}2}$ and $\text{P}_{\text{OCA}2}$ were measurable (see Fig. 2 and Table 1).

Additionally, the preparation of P_{ODA} perovskites was carried out under the same conditions as those of $\text{P}_{\text{ODA}1}$ but (i) in the absence of ODE (sample $\text{P}_{\text{ODA}3}$), and (ii) halving the amount of ODE and OLA (sample $\text{P}_{\text{ODA}4}$). Both samples proved to be less emissive than $\text{P}_{\text{ODA}2}$ (ca. 11% and 14% vs. 21%), thus showing the importance of ODE for the emissive properties of the P_{ODA} perovskites (spectrum not shown).

3.2 Time-resolved photoluminescence studies

Time-resolved photoluminescence (PL) spectroscopy was used to study the recombination lifetime of the perovskites. The toluene samples were excited at 337 nm and the PL decays were registered at the λ_{em} maximum, under both nitrogen and air atmospheres, and they were fitted with a biexponential function of time (t),

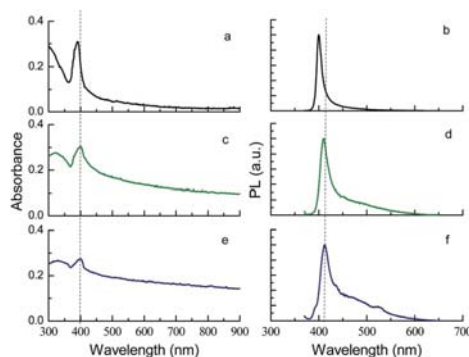


Fig. 2 Absorption and emission ($\lambda_{\text{exc}} = 330$ nm) of colloidal solutions (0.2 mg mL^{-1}) of $\text{P}_{\text{ODA}2}$ (a and b), $\text{P}_{\text{OCA}2}$ (c and d) and $\text{P}_{\text{HXA}2}$ (e and f) in toluene.

Table 1 Absorption and emission data of the perovskites

	OA nm	PL ^a (nm)	FWHM (nm)	τ_1 (ns)	ϕ (%)	k_r (10^6 s^{-1})	k_{nr} (10^8 s^{-1})
$\text{P}_{\text{ODA}1}/\text{air}$	389	397	13	3.154	22.9	72.61	2.44
$\text{P}_{\text{ODA}1}/\text{N}_2$	389	397	14	3.120	20.1	64.42	2.56
Film ^b	389	398	21	1.810 ^c	11.9	65.49	7.77
$\text{P}_{\text{ODA}2}/\text{air}$	390	397	11	2.773	19.8	71.40	2.88
$\text{P}_{\text{ODA}2}/\text{N}_2$	390	397	16	2.650	21.4	80.75	2.97
Film ^b	389	398	19	2.180 ^c	5.8	26.58	4.32
$\text{P}_{\text{ODA}2}/\text{nm}$	390	396	10	1.642 ^c	7.0	42.68	5.67
Film ^b	390	403	22	2.217 ^c	6.3	28.51	4.24
$\text{P}_{\text{HXA}2}/\text{air}$	398	408	28	2.618	0.5	1.91	3.80
$\text{P}_{\text{HXA}2}/\text{N}_2$	398	408	26	2.413	0.5	2.07	4.12
$\text{P}_{\text{OCA}2}/\text{air}$	396	409	24	2.615	0.5	1.91	3.80
$\text{P}_{\text{OCA}2}/\text{N}_2$	396	409	26	2.670	0.7	2.62	3.72

^a Wavelength of the maximum emission (λ_{ex} at 340 nm). ^b Film prepared by spin-coating of toluene dispersion of the perovskite on quartz. ^c Average lifetime (τ_{av}).

$$I(t) = \sum_i \alpha_i \left(-\frac{t}{\tau_i} \right) \quad (1)$$

where τ_i is the decay time and α_i represents the amplitudes of the components. The emission lifetimes and their corresponding contributions to the total signal are shown in Table S1.† In the case of the films, their average recombination lifetimes (τ_{av}) were estimated with the τ_i and α_i values from the fitted curve data according to eqn (2).

$$(\tau_{av}) = \frac{\sum \alpha_i \tau_i^2}{\sum \alpha_i \tau_i} \quad (2)$$

However, in the colloidal systems there was a main contribution (>97%) and therefore the decay lifetime (τ_1) of this contribution was used for the subsequent estimation of the kinetic rate constants for the perovskites.

The τ_1 for the perovskites was quite similar (between 1.8 and 3.1 ns) and showed a negligible dependence on the presence of oxygen (Table 1). The large difference between the emission quantum yields of P_{ODA} and the other perovskites with a shorter alkyl chain suggested drastic differences between their radiative decay rates. The radiative rate constant (k_r) and the non-radiative rate constant (k_{nr}) were estimated by using eqn (3) and (4); where Φ_{PL} is the photoluminescence quantum yield.

$$\Phi_{PL} = k_r \times \tau_1 \quad (3)$$

$$\tau_1 = \frac{1}{(k_r + k_{nr})} \quad (4)$$

These data revealed the remarkably (up to forty times) faster radiative decay for P_{ODA} perovskites, while the variation of the k_{nr} value was relatively small among the perovskites. Therefore, the emission efficiency of the perovskites appeared to be governed by the excitonic properties of the perovskite inorganic framework and not by the concentration of surface defects.

In this respect, drastic effects on the optical properties of 2D-layered A_2PbBr_4 perovskite single crystals (A = butyl, phenylmethyl, and 2-phenylethyl-ammonium) have previously been reported and they were attributed to variations in the network arrangement and structural distortion caused by the different alkylammonium salts.²⁰ Also in this case the relative quantum efficiencies matched the relative radiative decay.

3.3 Analysis of the composition of the perovskite samples

The optical features of P_{ODA} perovskites were considerably different from those of P_{OCA} and P_{HXA} perovskites. It has been reported that (methylbenzylammonium)₂PbBr₄ crystallizes in two different phases with absorption excitonic peaks at 404 and 386 nm and emission peaks at 409 and 394 nm, respectively.²¹ Moreover, the exciton absorption and PL peaks of (dodecylammonium)₂PbI₄ thin films and single crystals changed when heated on account of the presence of two structural orthorhombic and monoclinic (metastable) phases; the emission peak of the stable phase appears at a shorter

wavelength.²² Therefore, the differences between P_{ODA} perovskites and P_{OCA} and P_{HXA} could be related to different structural phases.

TGA analysis of the P_{HXA1} , P_{OCA1} , P_{ODA1} , P_{HXA2} , P_{OCA2} , and P_{ODA2} perovskites obtained after the precipitation and purification step can give valuable information on the composition of these perovskites. The TGA heating curves of the perovskites was registered (see Fig. 3, S2 and S3†). The peak of the first derivative indicates the point of greatest rate of change on the weight loss curve.

The TGA of P_{ODA2} shows that it lost ca. 41% of its weight before reaching ~250 °C, followed by another weight loss of ca. 35% before reaching ~400 °C, and then a weight loss of 20% before reaching 580 °C. Only 5% of the mass did not decompose or sublimate at temperatures of up to 800 °C; this residue may be made up of impurities present in the material or decomposition products. The peaks of the first derivative were at 200, 353, and 560 °C. The TGA of P_{ODA2} showed sharper peaks slightly shifted to higher values than those of P_{ODA1} (Fig. S3†), suggesting a higher stability of the components that build the perovskite in the absence of oleic acid.

The first loss of weight in sample P_{ODA1} and sample P_{ODA2} could be attributed to the loss of the organic capping of the nanoparticles. The second step of the weight loss could be ascribed to the loss of the ODABr in the perovskite framework, while the third step is consistent with the loss of the perovskite lead bromide.

The weight percentage of the three sublimation steps in the TGA of P_{HXA} and P_{OCA} perovskites was consistent with the molecular weight of the corresponding alkyl ammonium salt (Fig. 3 compares the TGA of P_{ODA2} and P_{OCA2}).

TGA and ¹H-NMR analysis of the P_{HXA1} , P_{OCA1} , P_{ODA1} , P_{HXA2} , P_{OCA2} , and P_{ODA2} perovskites obtained after the precipitation and purification steps, combined with those of the resulting supernatants, confirmed that these perovskites were obtained with a chemical yield higher than 44% (Fig. S2–S10 and Table S2–S4; the detailed analysis is included in the ESI†). In addition, these data indicated that the perovskite nanoparticles were capped by the ammonium salt and ODE.

The X-ray photoelectron microscopy (XPS) spectra of P_{HXA2} , P_{OCA2} , and P_{ODA2} were analysed using the C peak at 285.0 eV as

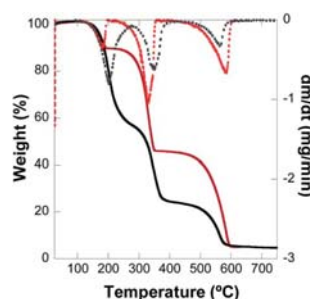


Fig. 3 TGA heating curves of P_{ODA2} (black) and P_{OCA2} (red) expressed as weight% as a function of temperature (—) and the corresponding 1st derivatives (---).

the reference (Fig. S11–S15†). The O_{1s} spectrum showed a peak centred at 532.4 eV. The deconvolution of the C_{1s} XPS spectra was fitted to two peaks at *ca.* 285.7 and 285.0 eV, corresponding to the C–C/C–H and C–N bonds, respectively.²³ The differences in the relative contribution of the peaks among the perovskites were consistent with the ammonium salt/ODE molar ratio estimated for them (see Tables S2–S4†).

The Pb_{4f} spectrum showed two symmetric peaks attributed to $Pb\ 4f_{7/2}$ and $Pb\ 4f_{5/2}$ levels at binding energies (BE) of *ca.* 138.7 eV and 143.5 eV, respectively. The spin–orbit split between them was 4.9 eV, which agrees with the value reported in the literature (4.8 eV).²⁴ The N_{1s} spectrum showed the presence of a peak at 402.0 eV relative to the –N– of the ammonium salts.²⁵ Finally, the Br_{3d} peak was observed at *ca.* 68.8 eV with the FWHM of 2.31, 2.06, and 2.12 eV for P_{HXA2} , P_{OCA2} and P_{ODA2} , respectively. The P_{ODA2} spectrum showed that the peak was at a slightly higher energy (0.2 eV) than those of the other perovskites.

3.4 TEM and PXRD analysis of the perovskite samples

High resolution transmission electron microscopy (HRTEM) analyses of P_{HXA2} , P_{OCA2} and P_{ODA2} samples showed that they consisted of nanoparticles coexisting with material forming plaques²⁶ (Fig. S16 and S17†). Therefore, we observe the formation of some 0D materials.

X-ray powder diffraction was used to examine the phase purity and crystallinity of P_{HXA2} , P_{OCA2} and P_{ODA2} . Fig. 4 shows the diffraction patterns of the three compounds, revealing intense diffraction peaks that correspond to the (0 0 2*l*) reflections, which appear at lower 2θ values as the alkyl chain increases. Pawley refinements,²⁷ performed by using the TOPAS computer program,²⁸ demonstrated that the three compounds present an excellent fit to a single-phase model corresponding

to the orthorhombic phases of the hybrid organic–inorganic $(R-NH_3)_2PbBr_4$ perovskite, where the unit cell dimension perpendicular to the inorganic layer is largely influenced by the length of the organic cation, as it has been previously observed (Fig. S18†).¹⁷ The unit cells of the three compounds were refined in the *Pbca* space group, as observed in the analogous $(R-NH_3)_2PbI_4$ compounds, with lattice constants $a = 8.19243$, $b = 8.22189$, and $c = 37.73297$ Å for P_{HXA2} ; $a = 8.19642$, $b = 8.24638$, and $c = 42.34463$ Å for P_{OCA2} ; and $a = 8.18840$, $b = 8.27068$, and $c = 72.44761$ Å for P_{ODA2} .

The use of organic cations of different lengths does not alter the in-plane lattice parameters, a and b , which are approximately constant in the three compounds, their values related to those of the tetragonal and cubic phases of the 3D perovskite $CH_3NH_3PbBr_3$ ($a_{2D} \sim a_{tetragonal}$; $a_{2D} \sim \sqrt{2}a_{cubic}$; $a_{tetragonal} = 8.322$ Å; $a_{cubic} = 5.901$ Å).²⁹ On the contrary, the interlayer spacing increases linearly with increasing the alkyl chain length (n), following the relationship d (Å) = $8.06 + 1.59 \times n$ as previously reported.³⁰ Consequently, the differences between the optical properties of P_{ODA} and the other perovskites cannot be attributed to different structural phases.

3.5 Processability of the P_{ODA} perovskites

The P_{ODA2} solid was dispersed in toluene and then the solvent was removed (Fig. 1, from 1 to 2). This process was repeated three times to demonstrate that the colloidal solution preserved its optical properties and the solid sample exhibited the same XRPD spectrum as the initial sample.

We also checked the possibility to assemble–disassemble the P_{ODA} perovskites reversibly (Fig. 1, from 1 to 3). It is worth mentioning that while (alkyl ammonium)₂PbX₄ perovskite films exhibit a sharp absorption peak, this peak does not exist in a DMF solution,^{9,31} indicative of the reversion of the perovskite to

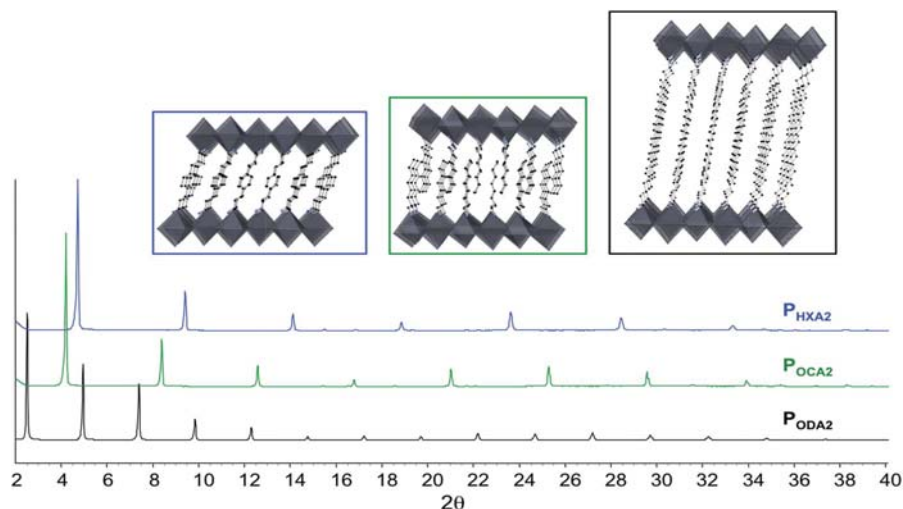


Fig. 4 X-ray diffraction pattern of P_{HXA2} (blue), P_{OCA2} (green), and P_{ODA2} (black) powders and schematic representations of the A_2PbBr_4 perovskite frameworks.

its precursors. Remarkably, we succeeded in rebuilding the $P_{\text{ODA}2}$ perovskite with the same optical features after dispersing it in DMF followed by solvent evaporation.

In addition, the DMF dispersion was spin-coated on a substrate (Fig. 1, from 3 to 5), thus leading to the $P_{\text{ODA}2}$ film.

Moreover, the production of nanoparticles increased hugely and the size of the plaques was smaller than 100 nm when the DMF dispersion was injected into toluene (Fig. 1, from 3 to 4). Fig. 5 shows a TEM image of the isolated material (see details in the Experimental section). PXRD of this nanomaterial ($P_{\text{ODA}2\text{nm}}$) showed its crystallinity (Fig. S19[†]) and Pawley refinement indicates that it has the same orthorhombic phase as $P_{\text{ODA}2}$ ($a = 8.17328$, $b = 8.28443$, and $c = 72.57105$ Å).

$P_{\text{ODA}2\text{nm}}$ emitted in a similar wavelength (at 396 nm, Table 1) to the other $P_{\text{ODA}2}$ materials herein prepared (see absorption and emission spectra in Fig. 6). This evidenced that excitons are strongly localized in the inorganic framework and the optical properties of these materials are dominated by the optical properties of the crystal.

3.6 Stability and photostability of the perovskite samples

Relevant features of hybrid perovskites for their application in devices should be not only with high stability and luminescence, but also with significant photostability.

$P_{\text{ODA}2}$ stored as a solid in the dark and under an air atmosphere preserved its emissive properties for more than six months while $P_{\text{ODA}1}$ became yellowish with time.

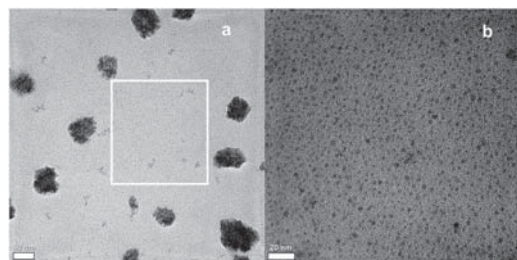


Fig. 5 HRTEM image of $P_{\text{ODA}2\text{nm}}$: (a) scale bar 50 nm; (b) magnified image of white box in (a), scale bar 20 nm.

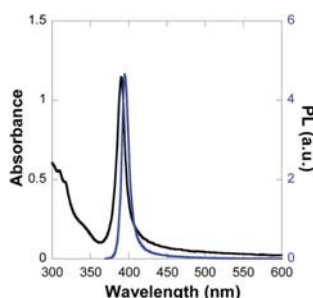


Fig. 6 Absorption (black) and emission (blue, $\lambda_{\text{exc}} = 330$ nm) of colloidal solutions of $P_{\text{ODA}2\text{nm}}$ (0.16 mg mL^{-1}).

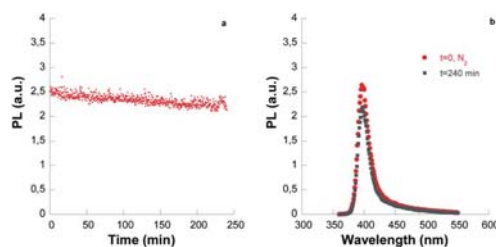


Fig. 7 (a) Photoluminescence of $P_{\text{ODA}2}$ dispersed in toluene as a function of the irradiation time: $\lambda_{\text{exc}} = 330$ nm, PL registered at 397 nm under a nitrogen atmosphere. (b) Photoluminescence spectra before and after 240 minutes of irradiation.

The photostability of the perovskite was evaluated by measuring the evolution of its PL intensity as a function of irradiation time. The colloidal solutions were illuminated using fluorimeter lamps at λ_{exc} at 330 nm in the presence and in the absence of air.

UV irradiation of $P_{\text{ODA}2}$ and $P_{\text{ODA}1}$ under an air atmosphere led to a loss of less than 7% after 200 min illumination (see Fig. 7 for $P_{\text{ODA}2}$). In the case of $P_{\text{OCA}2}$ the loss of emission was also small (Fig. S20[†]). By contrast $P_{\text{HXA}2}$ showed a considerably lower photostability and lost more than 30% of its emissive efficiency (Fig. S20[†]).

4. Conclusions

We have demonstrated here that highly dispersible perovskites with a two-dimensional inorganic framework and (alkyl ammonium)₂PbBr₄ formula can be efficiently prepared by using a 2 : 1 alkyl ammonium bromide/PbBr₂ ratio. In addition, the dual role of the alkyl ammonium salt is shown; it is not only a component of the inorganic framework but also of its organic capping. The length of the alkyl ammonium salt proved to be crucial for the dispersibility and luminescence of the nanomaterial. These materials proved to be easily processed. Thus, (octadecylammonium)₂PbBr₄ (P_{ODA}) perovskites remain stable when solid, they are dispersible in toluene and can be spin-coated on a substrate. Moreover, these perovskites can be disassembled–assembled and they exhibit a high radiative rate constant (up to $80 \times 10^6 \text{ s}^{-1}$) and photostability under UV light. These results are promising for the efficient preparation of highly dispersible 2D-layered perovskites which are of interest in light emitting devices.

Acknowledgements

We thank MINECO (Project CTQ2014-27758, contract granted to S.G-C) and FGUV (R.E.G contract).

Notes and references

- 1 D. B. Mitzi, in *Progress in Inorganic Chemistry*, John Wiley & Sons, Inc., 2007, pp. 1–121.

- 2 P. Gao, M. Gratzel and M. K. Nazeeruddin, *Energy Environ. Sci.*, 2014, **7**, 2448–2463.
- 3 S. Kazim, M. K. Nazeeruddin, M. Grätzel and S. Ahmad, *Angew. Chem., Int. Ed.*, 2014, **53**, 2812–2824.
- 4 S. González-Carrero, R. E. Galian and J. Pérez-Prieto, *Part. Part. Syst. Charact.*, 2015, DOI: 10.1002/ppsc.201400214.
- 5 X. Hong, T. Ishihara and A. V. Nurmikko, *Phys. Rev. B: Condens. Matter Mater. Phys.*, 1992, **45**, 6961–6964.
- 6 K. Pradeesh, J. J. Baumberg and G. Vijaya Prakash, *J. Appl. Phys.*, 2012, **111**, 013511.
- 7 E. Hanamura, *Phys. Rev. B: Condens. Matter Mater. Phys.*, 1988, **38**, 1228–1234.
- 8 Z. Cheng and J. Lin, *CrystEngComm*, 2010, **12**, 2646–2662.
- 9 S. Zhang, P. Audebert, Y. Wei, A. Al Choueiry, G. Lanty, A. Bréhier, L. Galmiche, G. Clavier, C. Boissière, J.-S. Lauret and E. Deleporte, *Materials*, 2010, **3**, 3385–3406.
- 10 Y. Wei, P. Audebert, L. Galmiche, J.-S. Lauret and E. Deleporte, *Materials*, 2014, **7**, 4789–4802.
- 11 S. Ahmad and G. V. Prakash, *J. Nanophotonics*, 2014, **8**, 083892.
- 12 S. Ahmad, P. K. Kanaujia, W. Niu, J. J. Baumberg and G. Vijaya Prakash, *ACS Appl. Mater. Interfaces*, 2014, **6**, 10238–10247.
- 13 S. Ahmad, J. J. Baumberg and G. Vijaya Prakash, *J. Appl. Phys.*, 2013, **114**, 233511.
- 14 D. G. Billing and A. Lemmerer, *New J. Chem.*, 2008, **32**, 1736–1746.
- 15 G. C. Papavassiliou, G. Pagona, N. Karousis, G. A. Mousdis, I. Koutselas and A. Vassilakopoulou, *J. Mater. Chem.*, 2012, **22**, 8271–8280.
- 16 L. C. Schmidt, A. Pertegás, S. González-Carrero, O. Malinkiewicz, S. Agouram, G. Mínguez Espallargas, H. J. Bolink, R. E. Galian and J. Pérez-Prieto, *J. Am. Chem. Soc.*, 2014, **136**, 850–853.
- 17 N. Kitazawa, M. Aono and Y. Watanabe, *Thin Solid Films*, 2010, **518**, 3199–3203.
- 18 K. Pradeesh, K. Nageswara Rao and G. Vijaya Prakash, *J. Appl. Phys.*, 2013, **113**, 083523.
- 19 P. Audebert, G. Clavier, V. Alain-Rizzo, E. Deleporte, S. Zhang, J.-S. Lauret, G. Lanty and C. Boissière, *Chem. Mater.*, 2009, **21**, 210–214.
- 20 N. Kawano, M. Koshimizu, Y. Sun, N. Yahaba, Y. Fujimoto, T. Yanagida and K. Asai, *J. Phys. Chem. C*, 2014, **118**, 9101–9106.
- 21 G. C. Papavassiliou, G. A. Mousdis and I. B. Koutselas, *Monatsh. Chem.*, 2001, **132**, 113–119.
- 22 K. Pradeesh, J. J. Baumberg and G. V. Prakash, *Appl. Phys. Lett.*, 2009, **95**, 173305.
- 23 A. Adenier, M. M. Chehimi, I. Gallardo, J. Pinson and N. Vilà, *Langmuir*, 2004, **20**, 8243–8253.
- 24 W. E. Morgan and J. R. Van Wazer, *J. Phys. Chem.*, 1973, **77**, 964–969.
- 25 S. Chen, T. W. Goh, D. Sabba, J. Chua, N. Mathews, C. H. A. Huan and T. C. Sum, *APL Mater.*, 2014, **2**, 081512.
- 26 I. Saikumar, S. Ahmad, J. J. Baumberg and G. Vijaya Prakash, *Scr. Mater.*, 2012, **67**, 834–837.
- 27 G. Pawley, *J. Appl. Crystallogr.*, 1981, **14**, 357–361.
- 28 A. A. Coelho, in *TOPAS-academic, 4.1 edn*, Coelho Software, Brisbane, Australia, 2007.
- 29 O. Knop, R. E. Wasylshen, M. A. White, T. S. Cameron and M. J. M. V. Oort, *Can. J. Chem.*, 1990, **68**, 412–422.
- 30 Y. Takeoka, K. Asai, M. Rikukawa and K. Sanui, *Bull. Chem. Soc. Jpn.*, 2006, **79**, 1607–1613.
- 31 M. Era, T. Kobayashi, K. Sakaguchi, E. Tsukamoto and Y. Oishi, *Org. Electron.*, 2013, **14**, 1313–1317.

Electronic Supplementary Information

Soranyel Gonzalez-Carrero, Guillermo Mínguez Espallargas, Raquel E. Galian* and Julia Pérez-Prieto*

Absorption and emission spectra of colloidal solutions of P_{ODA1} , P_{OCA1} , and P_{HXA1}	S2
Table S2: Emission lifetimes (τ) and their corresponding contributions (A) to the total signal of the perovskites dispersed in toluene or as a spin-coated film.	S3
<u>TGA Section</u> : TGA heating curves of different perovskite and the precursor for their synthesis.	S5
<u>¹H-RMN Section</u> : ¹ H-RMN (300 MHz) spectrum of P_{ODA1} , P_{ODA2} and their precursor in deuterated DMSO	S8
Quantification of dispersable perovskites A ₂ PbBr ₄ : P_{ODA1} , P_{ODA2} and P_{OCA2} , Table S2-S4	S12
<u>XPS Section</u> : spectra of O _{1s} , C _{1s} , Pb _{4f} , N _{1s} and Br _{3d} for P_{HX2} , P_{OCA2} , and P_{ODA2}	S15
<u>TEM Section</u> : HRTEM images of P_{HXA2} , P_{OCA2} and P_{ODA2} .	S18
<u>XRD Section</u> : Observed and calculated profiles of the X-ray powder diffraction of P_{HX2} , P_{OCA2} , P_{ODA2} and P_{ODA2np}	S19
<u>Photostability Studies</u> : Photoluminescence of P_{HXA2} , P_{OCA2} and P_{ODA2} dispersed in toluene as a function of the irradiation time ($\lambda_{exc} = 330$ nm).	S21

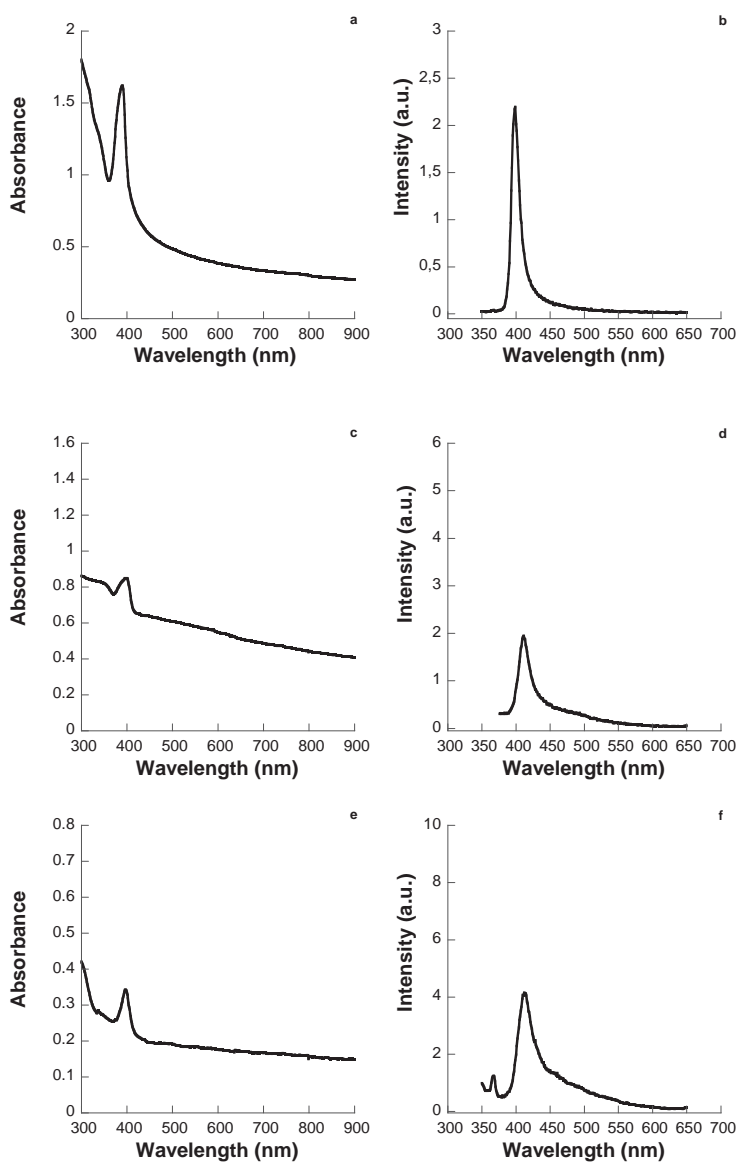


Figure S1. Absorption and emission ($\lambda_{\text{exc}}=330$ nm) spectra of colloidal solutions of P_{ODA1} (1 mg/mL; a,b) P_{OCA1} (0.6 mg/mL; c,d), and P_{HXA1} (0.2 mg/mL; e,f) and in toluene.

Table S1. Emission lifetimes (τ) and their corresponding contributions (A) to the total signal of the perovskites dispersed in toluene or as a spin-coated film.

	χ	PL ^a nm	$\langle\tau_{av}\rangle^b$ ns	τ_1 ns	τ_2 ns	A ₁	A ₂
P_{ODA1}/air	1.19	397	9.345	3.154	30.155	96.975	3.025
P_{ODA1}/N₂	1.28	397	8.840	3.120	31.560	97.580	2.420
Film^c	0.88	398	1.810	0.768	1.929	21.23	78.76
P_{ODA2}/air	1.40	397	4.192	2.773	27.89	99.41	0.592
P_{ODA2}/N₂	1.50	397	3.833	2.650	27.33	99.51	0.486
Film^c	1.29	398	2.18	1.289	2.386	29.70	70.29
P_{HXA2}/air	1.01	408	6.404	2.618	24.48	97.81	2.191
P_{HXA2}/N₂	1.21	408	6.413	2.413	22.15	97.31	2.695
P_{OCA2}/air	0.95	409	3.675	2.615	22.365	99.340	0.659
P_{OCA2}/N₂	1.01	409	5.794	2.670	27.805	98.550	1.454

^a Wavelength of the maximum emission (excitation at 340 nm); ^b τ_{av} average lifetime; ^c Film prepared by spin-coating of toluene dispersion of the perovskite on quartz.

Quantification of dispersable A_2PbBr_4 perovskites

TGA and 1H -NMR analysis of the P_{HXA1} , P_{OCA1} , P_{ODA1} , P_{HXA2} , P_{OCA2} , and P_{ODA2} perovskites after purification and their supernatants (Ss) give valuable information on the composition of these perovskites.

The first loss of weight in the perovskite samples was attributed to the loss of the organic capping of the material, i.e., ODE and ammonium salt (plus OLA in some samples). The second step of the weight loss was ascribed to the loss of the ammonium bromide in the perovskite framework, while the third step is consistent with the loss of the perovskite lead bromide.

In the case of the supernatants, removal of the solvent followed by addition of ethyl ether caused the precipitation of a solid (Ss). In addition, the ether solution was distilled, thus recovering ODE with the ammonium salt (plus OLA in the case of the synthesis of P_{HXA1} , P_{OCA1} , and P_{ODA1}). For comparative purposes, the TGA of the individual precursors (namely HXABr, OCABr, and ODABr ammonium salts) and the corresponding amines, as well as that of ODE, OLA, and lead bromide, were also recorded and are included in TGA section.

Further data on the composition of P_{HXA} , P_{OCA} and P_{ODA} samples were obtained from their 1H -NMR spectra, which gave information on the molar ratio of the organic components (RMN section). In combination with their TGA spectra, the $PbBr_2$ weight percentage present in the isolated mass was calculated. The 1H -NMR spectra of the supernatants were also analysed (spectra not included); the data obtained from them combined with those of the corresponding perovskite samples were consistent with the amount of material used in the preparation of the perovskites.

The molar composition of P_{ODA1} , P_{ODA2} , P_{HXA2} , and P_{OCA2} , as well as the yield of isolated perovskite (estimation based on the mmol of $PbBr_2$ in the perovskite compared to the mmol used in the reaction) are shown in Tables S2-S4.

Thermogravimetric Analysis Section

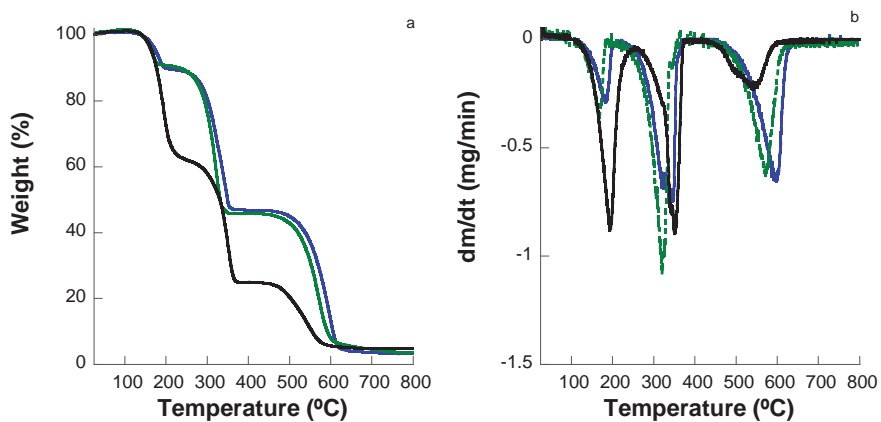


Figure S2. TGA heating curves of P_{HXAl} (-), P_{OCA1} (-) and P_{ODA1} (-) expressed as weight % as a function of applied temperature (a) and the corresponding 1st derivate (b).

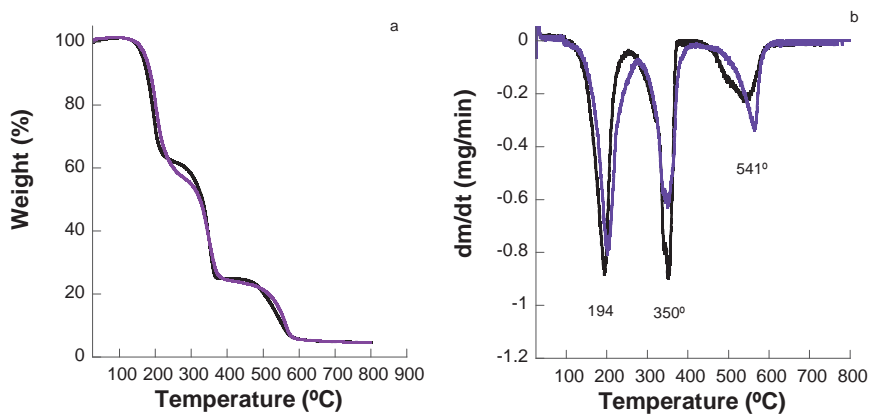


Figure S3. Comparison of TGA heating curves of P_{ODA1} (-) and P_{ODA2} (-) expressed as weight % as a function of applied temperature (a) and the corresponding 1st derivate (b).

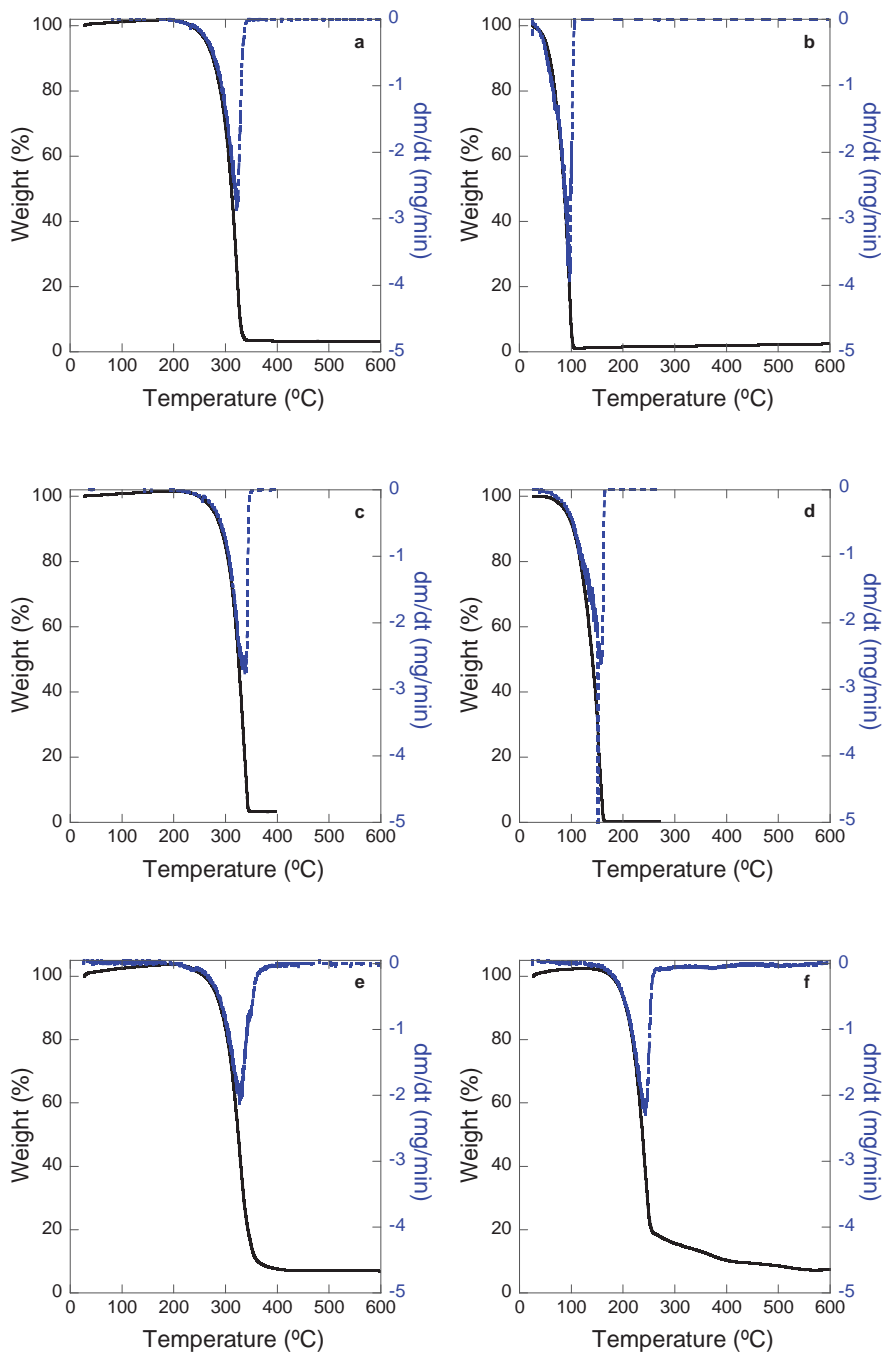


Figure S4. TGA heating curves of **HXABr** (a), hexyl amine **HXA** (b), **OCABr** (c) octylamine **OCA** (d), **ODABr** (e) and octadecylamine **ODA** (f) expressed as weight % as a function of applied temperature and the corresponding 1st derivate.

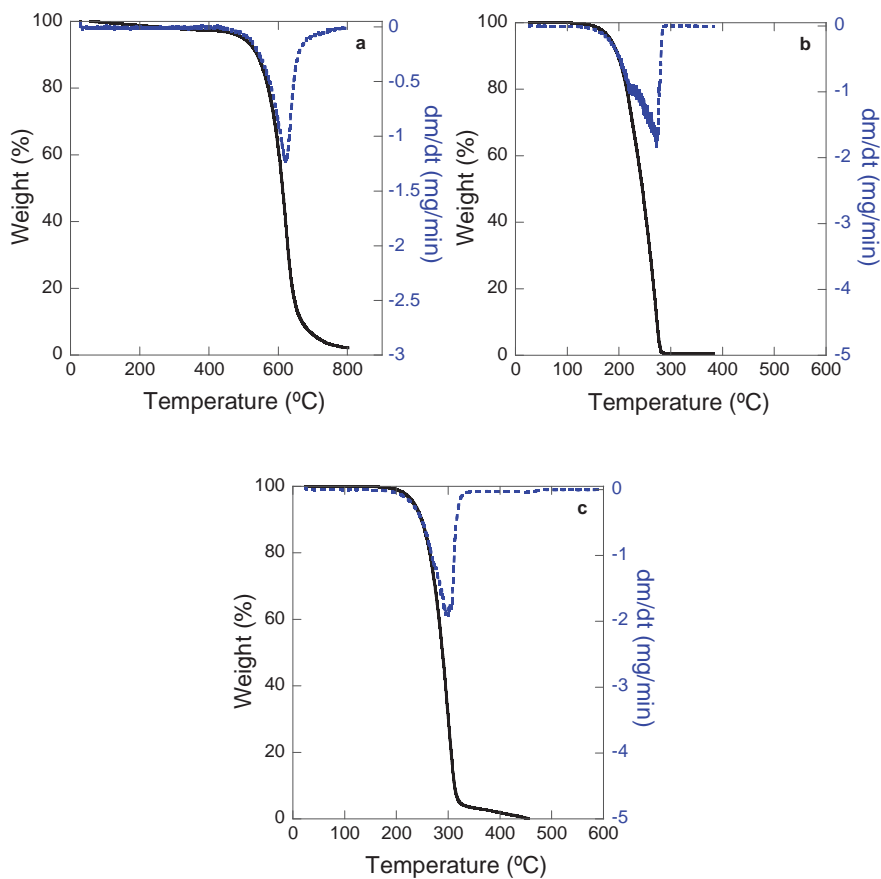


Figure S5. TGA heating curve of lead bromide (a) **ODE** (b) and **OLA** (c) expressed as weight % as a function of applied temperature and the corresponding 1st derivate.

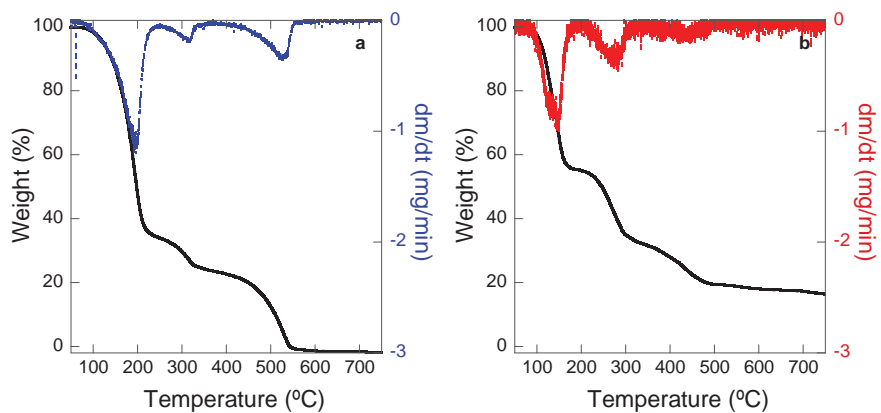


Figure S6. TGA heating curves expressed as weight % as a function of applied temperature and the corresponding 1st derivate of **PODA1 Ss** (a) and **PODA2 Ss** (b)

¹H-RMN section

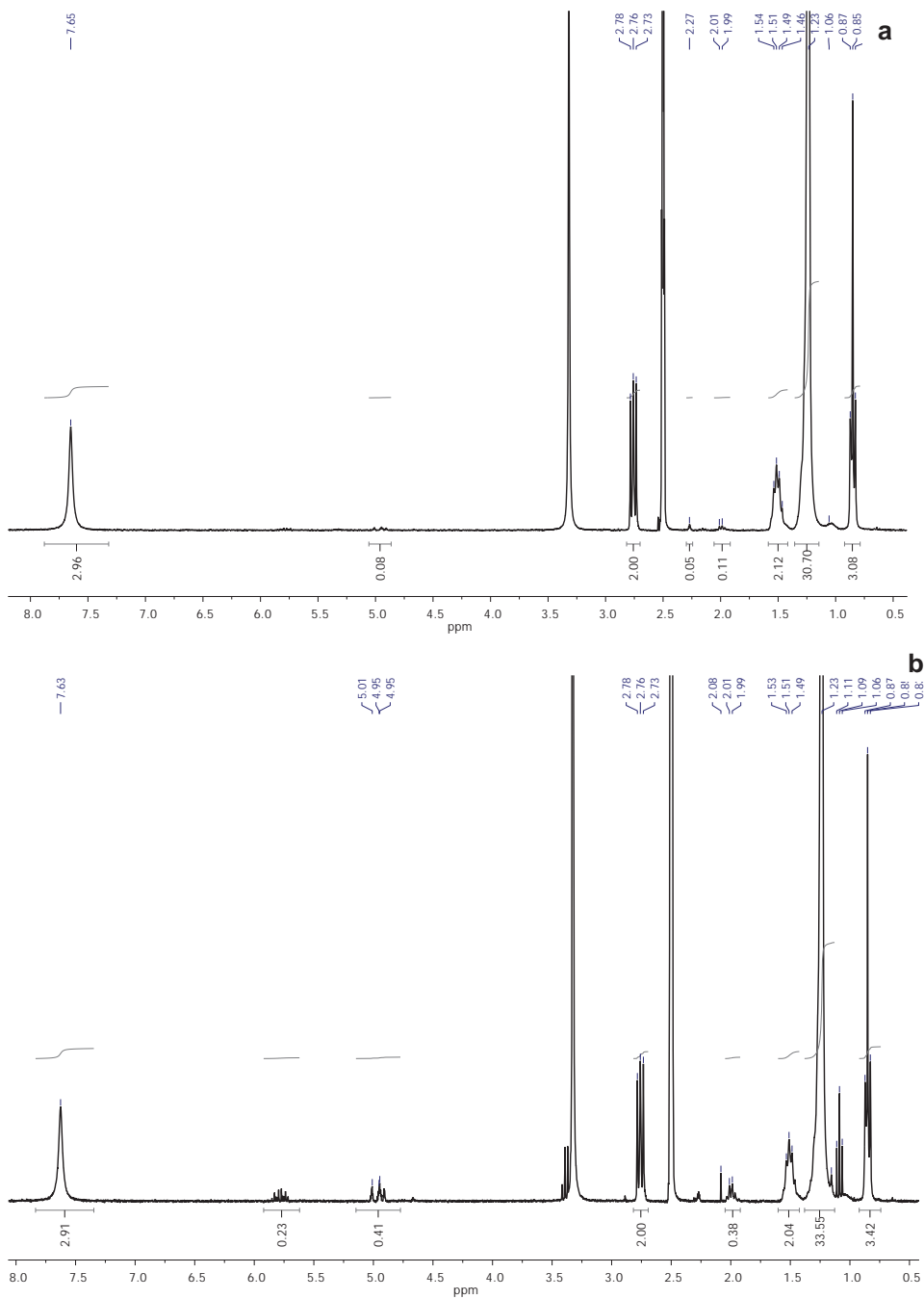


Figure S7. ¹H-RMN (300 MHz) spectrum of **P_{ODA1}** (a) and **P_{ODA2}** (b) in deuterated DMSO.

Octylammonium bromide

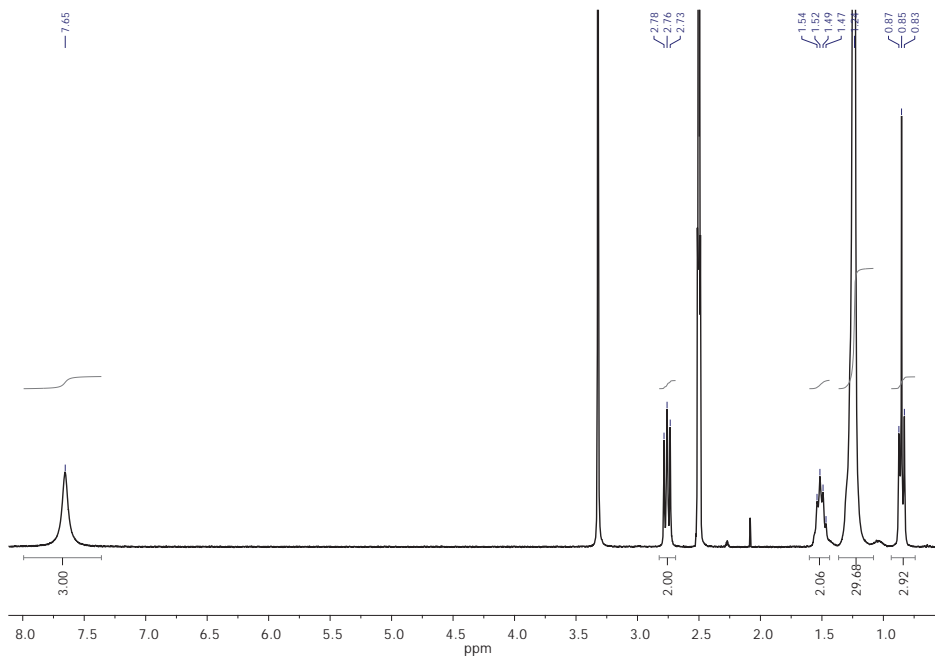


Figure S8. ^1H NMR (300 MHz) spectrum of octylammonium bromide (**ODABr**) in deuterated DMSO.

^1H NMR (300 MHz, d-DMSO) (300 MHz, DMSO) δ 7.65 (s, 3H), 2.76 (t, $J = 7.7$ Hz, 2H), 1.60 – 1.44 (m, 2H), 1.24 (s, 30H), 0.85 (t, $J = 6.7$ Hz, 3H).

Oleic acid

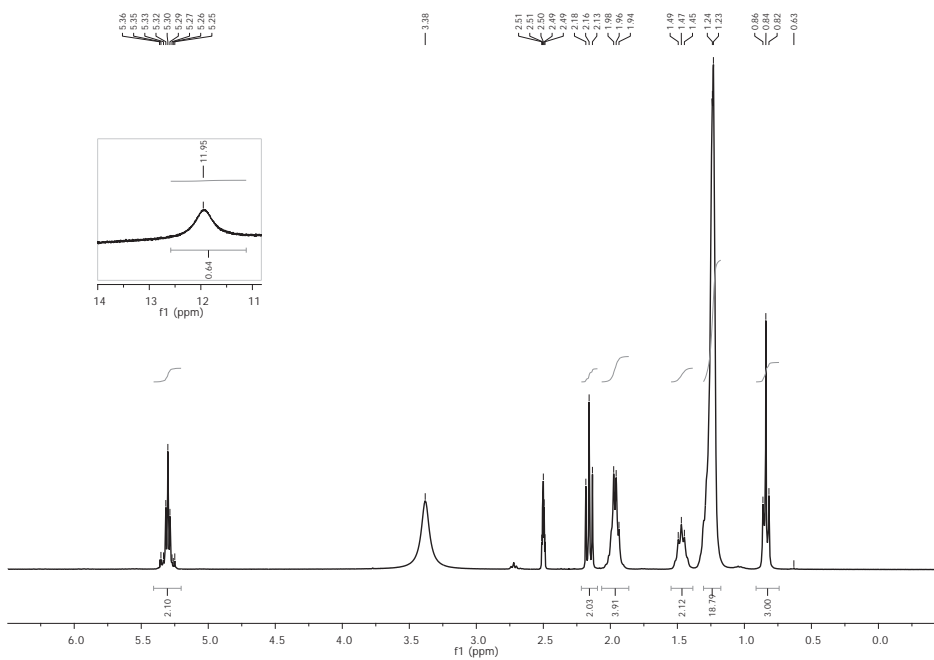


Figure S9. ^1H NMR (300 MHz) spectrum of oleic acid (OLA) in deuterated DMSO.

^1H NMR (300 MHz, d-DMSO) δ 11.95 (s, 1H), 5.41 – 5.20 (m, 2H), 2.16 (t, J = 7.4 Hz, 2H), 2.06 – 1.86 (m, 4H), 1.55 – 1.38 (m, 2H), 1.23 (d, J = 2.3 Hz, 19H), 0.91 – 0.74 (m, 3H).

Octadecene

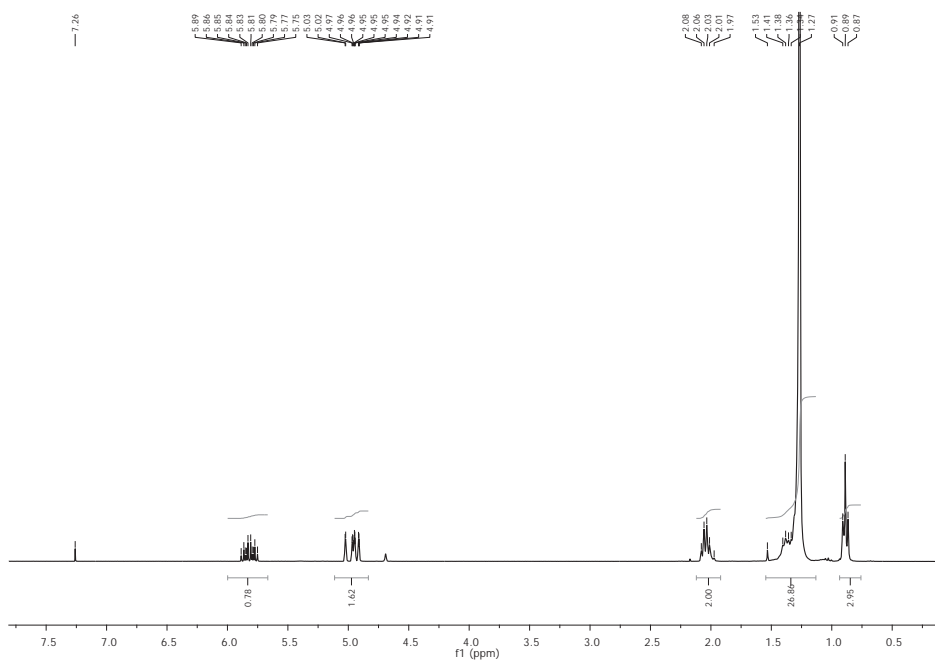


Figure S10. ^1H NMR (300 MHz) spectrum of **ODE** in deuterated CDCl_3 .

^1H NMR (300 MHz, CDCl_3) δ 5.82 (ddt, $J = 16.9, 10.2, 6.7$ Hz, 1H), 5.12 – 4.76 (m, 2H), 2.12 – 1.92 (m, 2H), 1.60 – 0.97 (m, 27H), 0.89 (t, $J = 6.6$ Hz, 3H).

Table S2. Quantification of the component molar ratio in P_{ODA1}

Reagents	Reagents ^a mmol	P_{ODA1}	
		Component ^b mmol	Component/PbBr ₂ ^b Molar ratio
ODABr surfactant	0.20	0.081	175
ODABr framework		0.077	1.86
ODE	6.09	0.004	0.09
OLA	0.26		
PbBr₂	0.10	0.044	1.00

^a Moles used in the synthesis. ^b Moles of each component in the product calculated by TGA and ¹H-RMN; perovskite chemical yield of 44%.

Table S3. Quantification of the component molar ratio in P_{ODA2}

Reagents	Reagents ^a mmol	P_{ODA2}	
		Component ^b mmol	Component/PbBr ₂ ^b Molar ratio
ODABr surfactant	0.10	0.053	1.77
ODABr framework		0.053	1.77
ODE	3.00	0.011	0.36
PbBr₂	0.05	0.030	1.00

^a Moles used in the synthesis. ^b Moles of each component in the product calculated by TGA and ¹H-RMN; perovskite chemical yield of 60%

Table S4. Quantification of the component molar ratio in P_{OCA2}

Reagents	Reagents ^a mmol	P_{OCA2}	
		Component ^b mmol	Component/PbBr ₂ ^b Molar ratio
OCABr surfactant	0.20	0.029	0.40
OCABr framework		0.135	1.82
ODE	6.10	0.003	0.04
PbBr₂	0.10	0.074	1.00

^a Moles used in the synthesis. ^b Moles of each component in the product calculated by TGA and ¹H-RMN; perovskite chemical yield of 74% .

X-Ray Photoelectron Spectroscopy Section

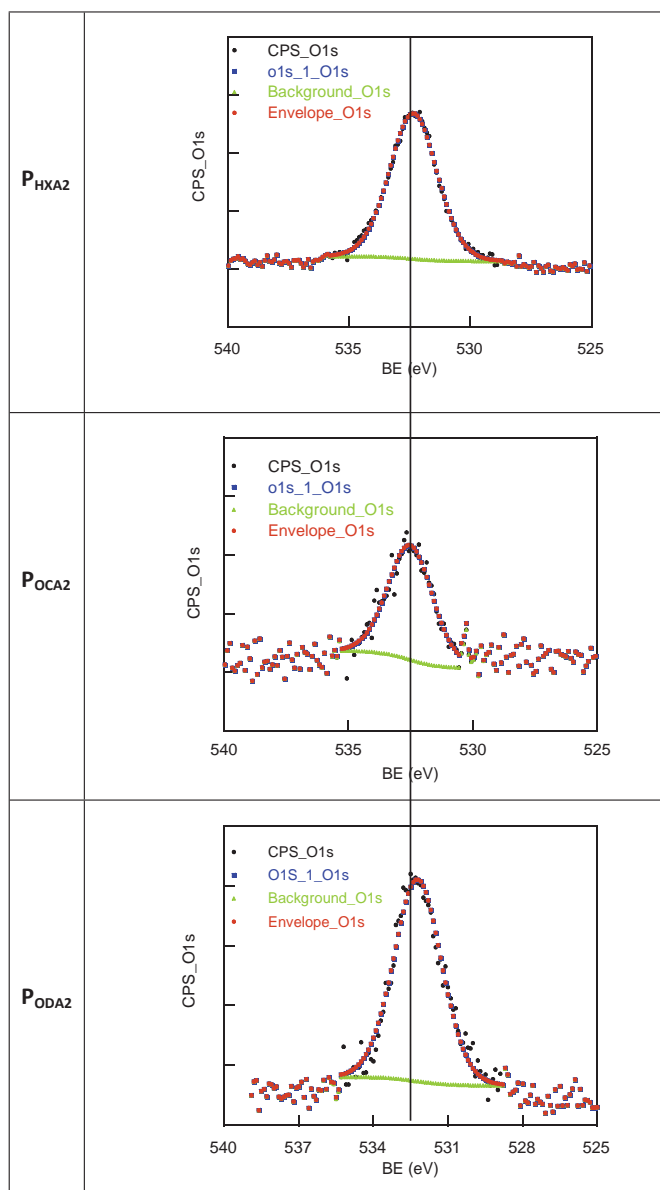


Figure S11. XPS spectra of O_{1s} for P_{HXA2}, P_{OCA2} and P_{ODA2}

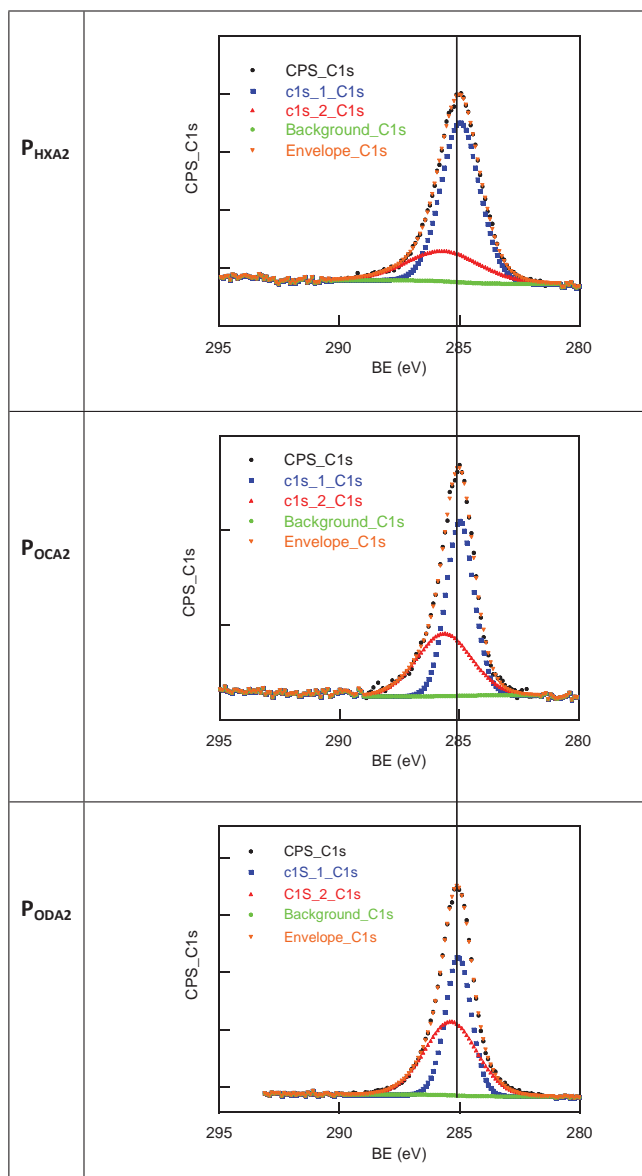


Figure S12. XPS spectra of C_{1s} for P_{HXA2}, P_{OCA2} and P_{ODA2}

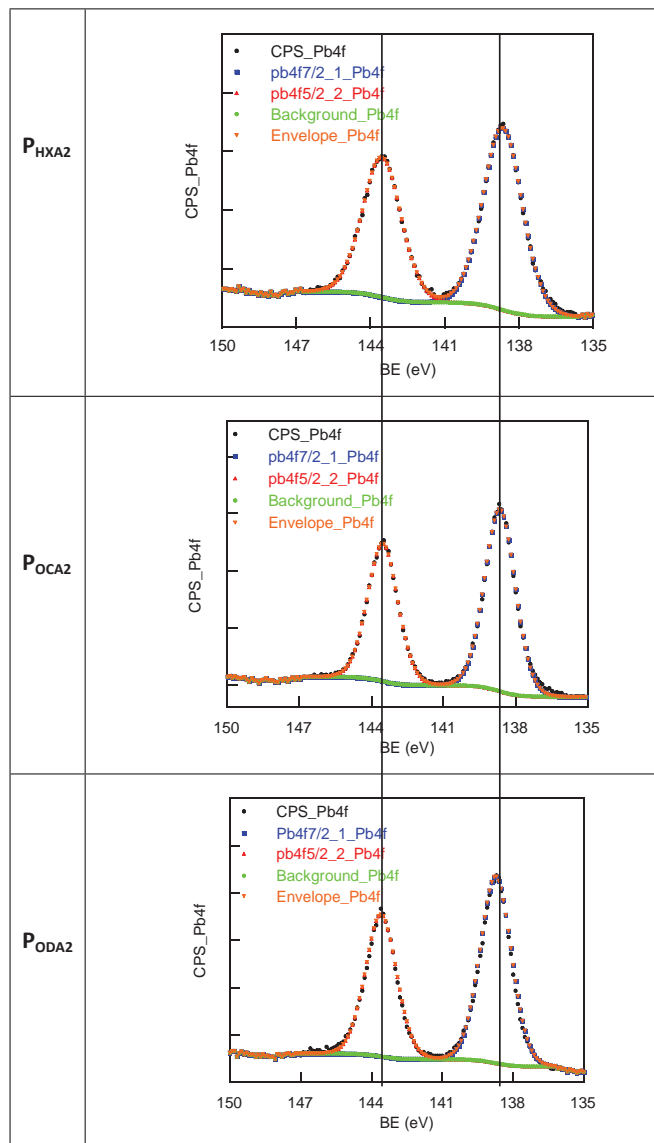


Figure S13. XPS spectra of Pb_{4f} for P_{HXA2}, P_{OCA2} and P_{ODA2}

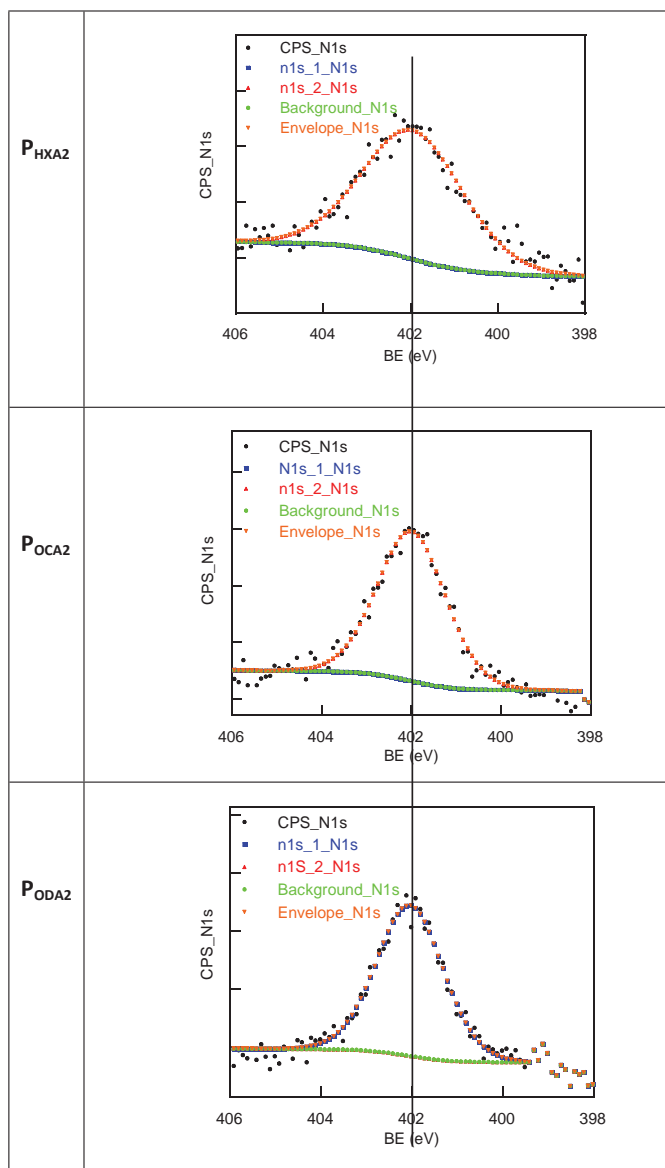


Figure S14. XPS spectra of N_{1s} for P_{HXA2} , P_{OCA2} and P_{ODA2}

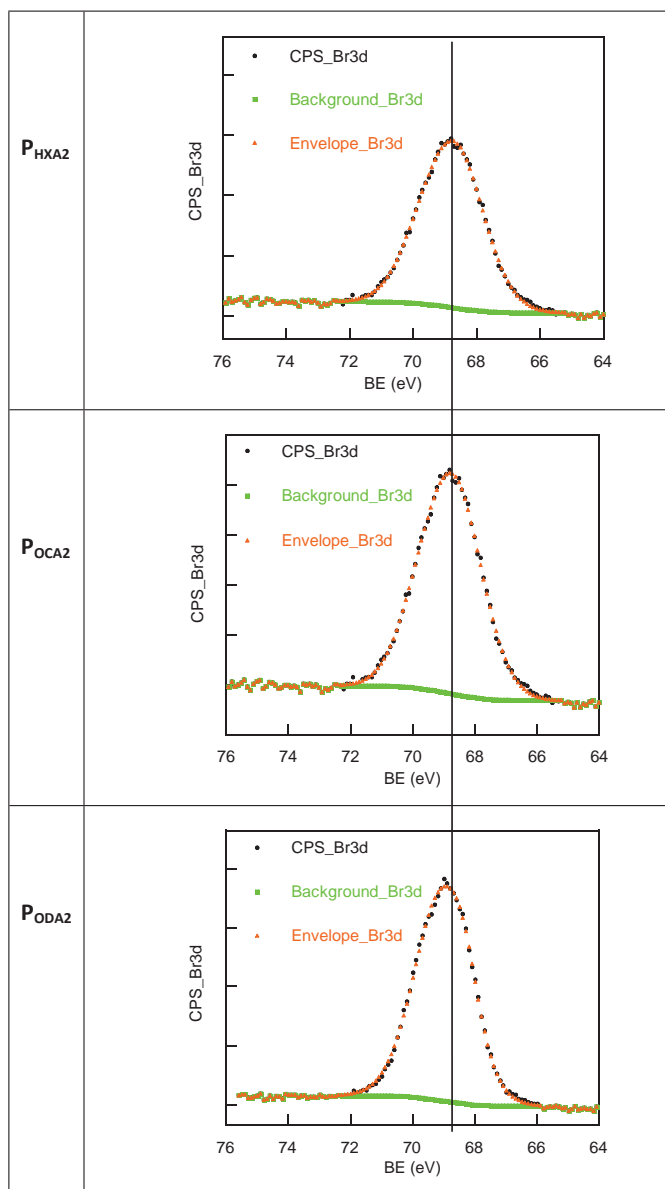


Figure S15. XPS spectra of Br_{3d} for P_{HXA2} , P_{OCA2} and P_{ODA2}

Transmission electron microscopy Section

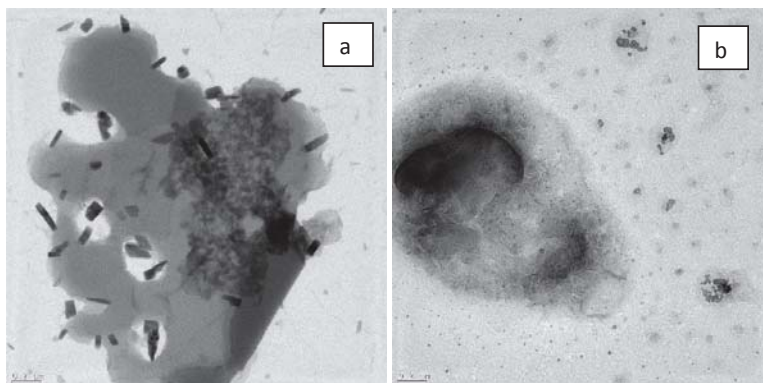


Figure S16. HRTEM of P_{HXA2} (a) and P_{OCA2} (b). Scale bar 0.2 μm .

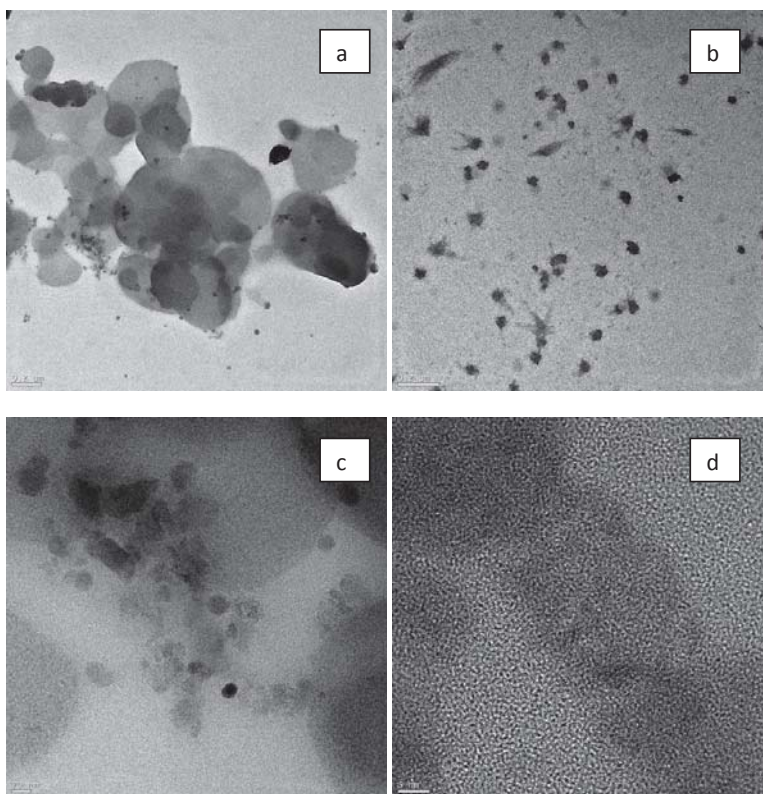


Figure S17. HRTEM of P_{ODA2} in toluene. Scale bar 0.2 μm (a,b), 20 nm (c) and 5 nm (d).

X-ray Diffraction Section

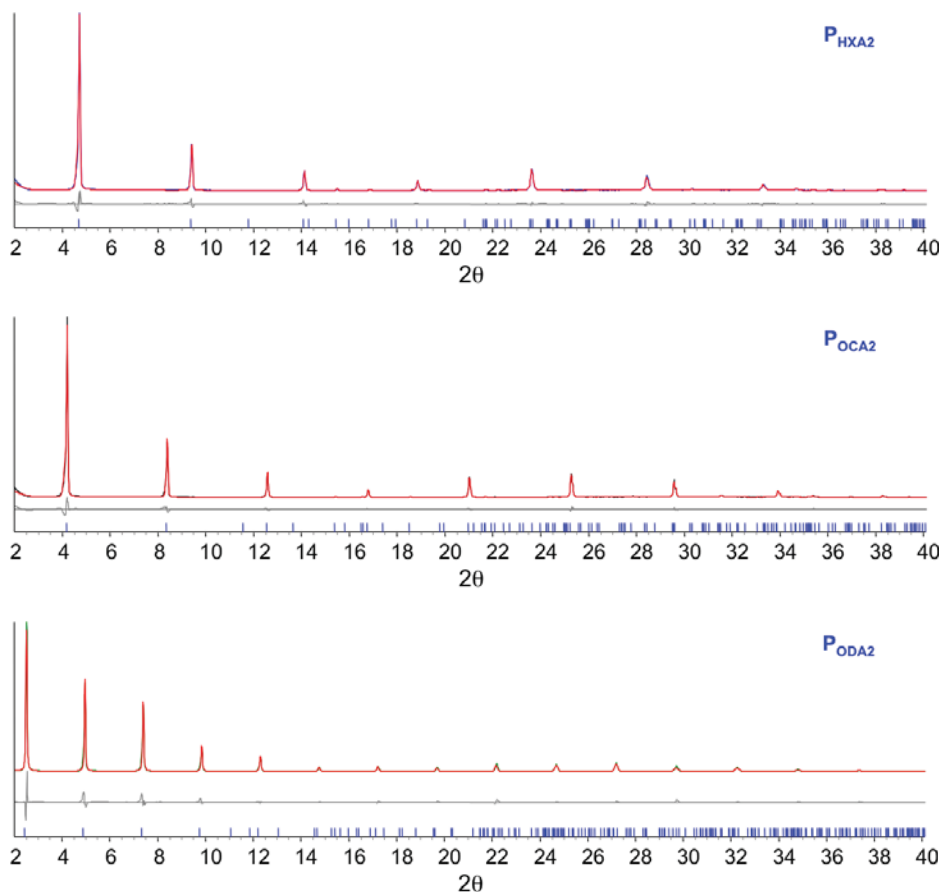


Figure S18. Observed (*blue*) and calculated (*red*) profiles and difference plot [$(I_{obs} - I_{calcd})$] (*grey*) of the X-ray powder diffraction Pawley refinement for P_{HXA2} (top), P_{OCA2} (middle) and P_{ODA2} (bottom) ($\lambda = \text{Cu K}\alpha$, 2θ range 2.0–40.0 °); tick marks indicate peak positions.

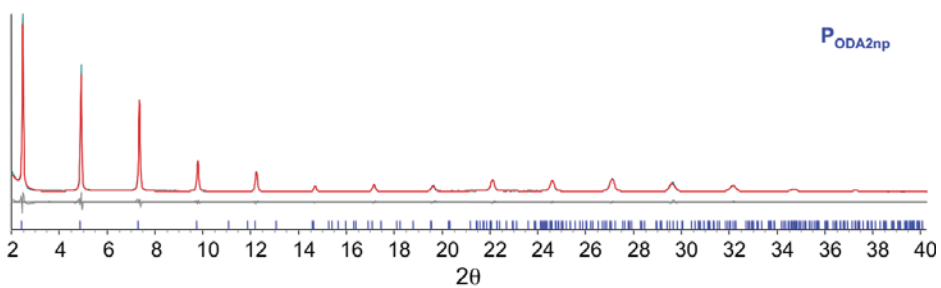


Figure S19. Observed (*blue*) and calculated (*red*) profiles and difference plot [$I_{\text{obs}} - I_{\text{calcd}}$] (*grey*) of the X-ray powder diffraction Pawley refinement after processing, P_{ODA2np} ($\lambda = \text{Cu K}\alpha$, 2θ range 2.0–40.0 °); tick marks indicate peak positions.

Photostability Studies

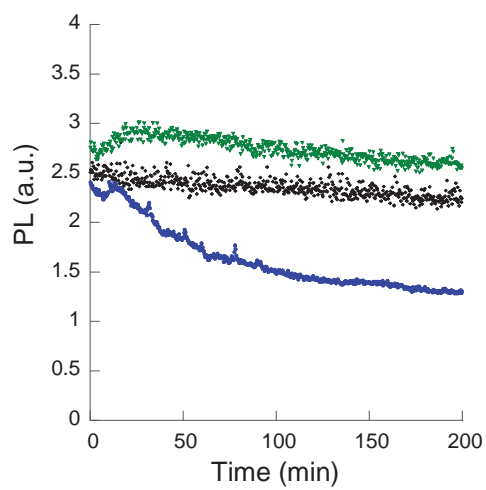


Figure S20. Photoluminescence of **P_{HXA2}** (■), **P_{OCA2}** (▼) and **P_{ODA2}** (◆) dispersed in toluene as a function of the irradiation time ($\lambda_{\text{exc}} = 330$ nm), PL registered at 411, 409, and 397 nm, respectively, under nitrogen atmosphere.

The Luminescence of $\text{CH}_3\text{NH}_3\text{PbBr}_3$ Perovskite Nanoparticles Crests the Summit and Their Photostability under Wet Conditions is Enhanced

Soranyel Gonzalez-Carrero, Laura Francés-Soriano, María González-Béjar, Saïd Agouram, Raquel E. Galian,* and Julia Pérez-Prieto*

Hybrid organic–inorganic lead halide perovskites are of great interest in photovoltaic devices and as luminescent materials for light-emitting devices.^[1] Their photoluminescence (PL) spectrum can be modified via controlled changes in their stoichiometry.^[2] There are many studies exploring the performance of these perovskites, in particular those with the MAPbX_3 ($\text{MA} = \text{CH}_3\text{NH}_3$, $\text{X} = \text{halide}$) stoichiometry, which address their optical gain, quantum yield, and their use as components of optical devices, among other features.^[3] However, there is a demand for enhancing their emissive properties for use in efficient luminescent devices. In addition, there are concerns as to their stability and degradation, which affect their performance.^[4] It has recently been reported that the stability of MAPbI_3 perovskite solar cells can be improved by crystal crosslinking with butylphosphonic acid 4-ammonium chloride.^[5]

Recent studies on the dynamics of the PL of organolead halide MAPbI_3 perovskite films under continuous optical excitation and different atmospheres have suggested competition between photoactivation and photodarkening of their emission.^[6] It was demonstrated that in these perovskites, an initial photoactivation step is followed by a photodarkening stage, which finally becomes the dominant process. Activation of PL has been associated with trap state filling by photogenerated carriers;^[7] the presence of oxygen plays a key role in this process. In addition, photodarkening has been associated with the presence of water in the environment; interestingly, this process seems to be partially reversible with negligible changes in the material absorption spectrum.^[6] It has been suggested that this moisture-related

photodarkening is due to the formation of hydrated species, favored by the photoexcited carriers, weakening the interaction between the organic cation and the PbX_6 octahedra in the framework, thus promoting the formation of complexes with water molecules.^[8]

Crystalline nm-sized MAPbX_3 nanoparticles have recently been prepared and they yield colourful and stable colloidal dispersions.^[9] This makes it possible to prepare thin homogeneous films of these nanoparticles by spin-coating on a quartz substrate. MAPbBr_3 nanoparticles can be prepared with an 88% chemical yield and high PL (83% quantum yield) by fine-tuning the molar ratios of all the components, which either form part of the framework (MABr and PbBr_2) or act as the organic capping (octylammonium bromide and 1-octadecene, ODE).^[9b] The method consists of the induced precipitation of the nanoparticles from the dimethylformamide (DMF)/ODE mixture of all the components by using acetone.

Another interesting strategy to prepare MAPbBr_3 perovskite nanomaterial with high PL (70% quantum yield) is that of the ligand-assisted reprecipitation (LARP) technique reported by Zhong and co-workers.^[9c] This technique consists in the dropwise addition of a DMF solution of the capping ligands (octylamine and oleic acid) and the perovskite precursors (MABr and PbBr_2) into toluene, followed by the discharge of large particles via centrifugation. Rogach and co-workers^[9d] have recently reported the preparation of MAPbBr_3 nanoparticles with a remarkable PL quantum yield (93%) by slight modifications of this strategy. In particular, the DMF solution was added to toluene at 60 °C. They stated that the synthetic yield of MAPbBr_3 nanoparticles by the LARP method is limited due to the formation of bulk material by-products together with the desired nanoparticles.

Encouraged by these results, our aim was to reach the maximum in the emissive efficiency of MAPbBr_3 nanoparticles, while preparing them with a high chemical yield. We envisaged that by injecting a DMF solution containing the proper organic capping, as well as the proper molar ratio between all the components (organic ligand, MABr and PbBr_2), into toluene would produce bright yellow perovskite dispersions.

We report here that MAPbBr_3 perovskite nanoparticles with a PL quantum yield of $\approx 100\%$ can be efficiently prepared (chemical yield of 76%) by using the quasi-spherical

S. Gonzalez-Carrero, L. Francés-Soriano,
Dr. M. González-Béjar, Dr. R. E. Galian,
Prof. J. Pérez-Prieto
Instituto de Ciencia Molecular (ICMol)
Universidad de Valencia
Catedrático José Beltrán 2
46980 Paterna, Valencia, Spain
E-mail: raquel.galian@uv.es; julia.perez@uv.es



Dr. S. Agouram
Departamento de Física Aplicada y Electromagnetismo
Universitat de Valencia
C/Dr. Moliner 50, Burjassot, Valencia 46100, Spain

DOI: 10.1002/smll.201600209

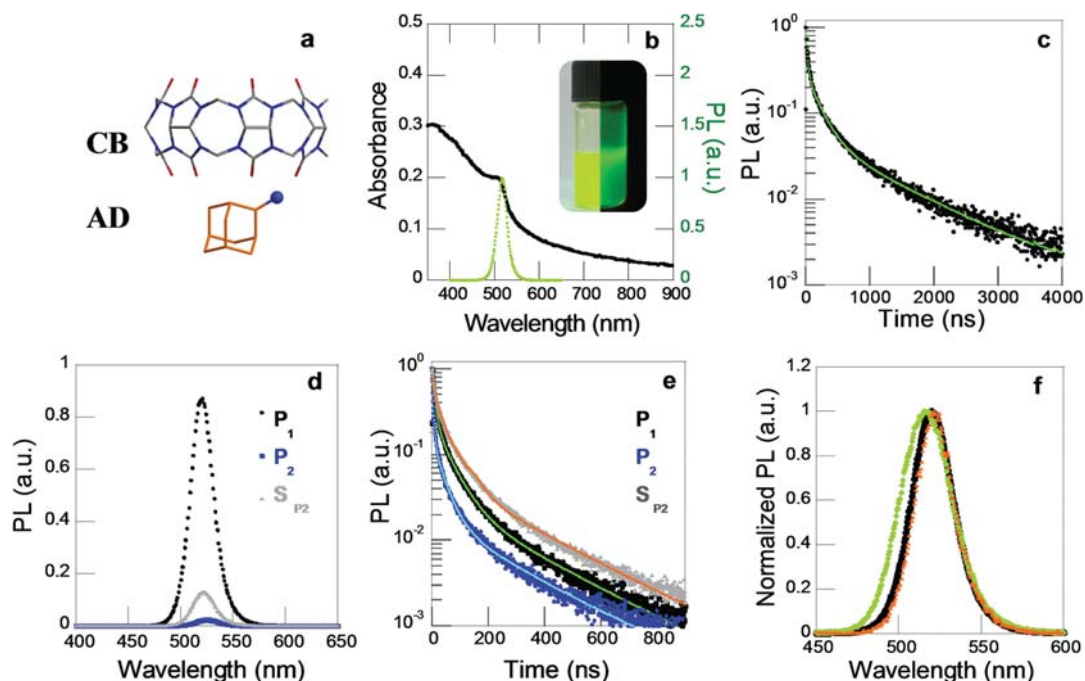


Figure 1. a) Molecular structure of curcubit[7]uril (CB) and 2-adamantylammonium (AD) ligands used in the preparation of the perovskite nanoparticles. b) Absorption (in black) and emission (in green) spectra of P_{AD} ; inset: image of a toluene dispersion of P_{AD} under lab light (left) and UV-light (right). c) Kinetic photoluminescence trace ($\lambda_{exc} = 340$ nm, $\lambda_{em} = 520$ nm) of P_{AD} in aerated toluene. d, e) Emission spectra (d) and kinetic traces (e) of (i) P_{AD} precipitate (P_1) obtained after centrifugation of the initial dispersion at 3000 rpm for 5 min, (ii) the precipitate obtained after centrifugation of supernatant at 9000 rpm for 10 min (P_2), and (iii) the final supernatant (S_{P2}). f) Time-resolved PL spectra of P_{AD} in aerated toluene registered at the maximum of the kinetic PL decay trace (0 ns, in green; 100 ns later, in orange); the black line in this figure represents the PL steady state spectrum.

shaped 2-adamantylammonium bromide (ADBr) as the only capping ligand (**Figure 1**) by fine-tuning the molar ratio between all the components. The photodarkening of these nanoparticles (P_{AD}) under prolonged irradiation, attributed to moisture, can be avoided by the formation of curcubit[7]-uril-adamantyl ammonium host-guest complexes (AD@CB) on the nanocrystal surface (P_{AD-CB}).

First, the preparation of MAPbBr₃ perovskite nanoparticles was addressed using a 1:1, 2:1, and 4:1 molar ratio between the ammonium salts (MABr/ADBr molar ratio of 6:4) and PbBr₂. Briefly, a DMF solution of MABr, ADBr, and PbBr₂ was injected dropwise into toluene while stirring, and the dispersion was further stirred for 1 h (see the Experimental Section for further details). This yielded green luminescent dispersions which, after centrifugation (7000 rpm)

for 4 min, produced a precipitate, which was separated and eventually dispersed in toluene. The nanoparticles obtained by using the 2:1 molar ratio between the ammonium salts and PbBr₂ were the most luminescent (up to ten times more emissive than 1:1) (Figure S1, Supporting Information) and, therefore, only these nanoparticles were fully characterized.

Figure 1b shows the absorption spectrum of P_{AD} and its narrow emission (full width at half maximum, FWHM, of 22 nm) with the maximum at 520 nm, i.e., considerably blue-shifted when compared to that of the bulk material (at ≈ 540 nm). Remarkably, the emission quantum yield of P_{AD} under air was of $\approx 100\%$, **Table 1**. This yield was determined by using a monochromatic light source (150 W) and an integrating sphere and it was corroborated by using two different standard dyes (see details in the Supporting Information). To

Table 1. Photoluminescence data of P_{AD} and P_{AD-CB} .

P	λ^a [nm]	FWHM ^b [nm]	Φ_{PL}^c	τ_1^d [ns]	τ_2^d [ns]	τ_3^d [ns]
P_{AD} Air	520	22	0.99	19.9 (76)	185.2 (20)	1082.0 (4)
P_{AD} N ₂	520	24	0.99	23.1 (73)	205.0 (21.5)	1161.4 (5.5)
P_{AD-CB} Air	519	24	0.89	23.3 (73.5)	201.5 (21.5)	1142.4 (5)
P_{AD-CB} N ₂	519	25	0.82	23.5 (74)	203.7 (21)	1233.7 (5)

^a λ_{exc} 340 nm; ^bFWHM; ^cPL quantum yield; ^dContribution of the component to the total PL in brackets.

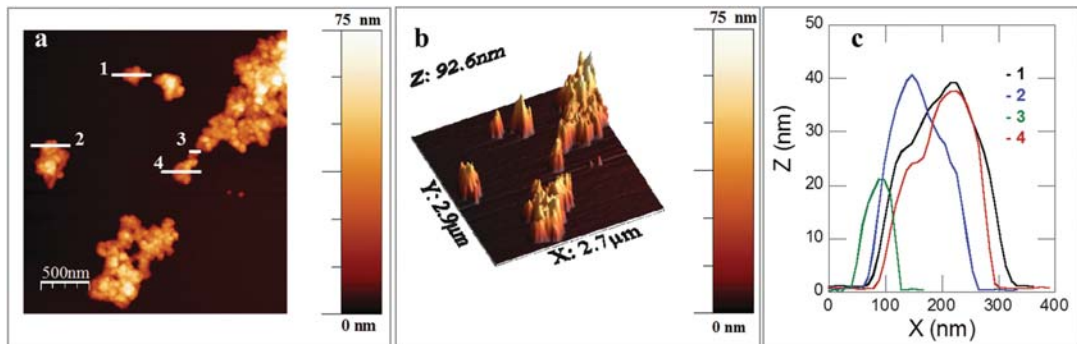


Figure 2. Representative AFM image of P_{AD} showing the presence of aggregates a) 2D view, b) 3D view and c) “height” profile of the aggregates and a nanoparticle identified in (a), see horizontal lines.

date, there is no example in the literature of $MAPbX_3$ perovskites with such emissive efficiency. Moreover, the features of the absorption and emission spectra of colloidal P_{AD} , as well as its emissive efficiency, did not undergo any change after six months at room temperature, thus proving its high chemical stability.

The PL decay of P_{AD} registered at $\lambda_{em} = 520$ nm under both nitrogen and air atmosphere (Figure 1c) was triexponential; the emission lifetimes (τ_i) are shown in Table 1. These data revealed the presence of the typical component with τ of ≈ 20 ns, which can be attributed to the charge carrier recombination of the conduction band electron and the valence band hole, together with two components with an extraordinarily long τ (contributing about 20% and 5%, respectively, to the total PL). The presence of long-lived PL components in colloidal $MAPbBr_3$ spherical nanoparticles is unexpected.^[9c,d] Therefore, we varied the separation method of the perovskite nanoparticles by performing multiple centrifugation/separation steps and analyzed the PL kinetics of the precipitates (termed as P_1 and P_2) and the final supernatant (termed as S_{P_2}); see Figure 1d,e, and Table S1 of the Supporting Information. In addition, we performed variations in the preparation protocol, specifically the precursors were injected into a 16-fold greater toluene volume and, after centrifugation, the PL kinetics of the precipitate (P_3) and the supernatant (S_{P_3}) were analyzed; see experimental details and Figure S2 of the Supporting Information. The absorption and emission spectra of the different samples were similar to those shown in Figure 1b, their luminescence quantum yield was higher than 90% and, though the lifetime of the longest-lived component decreased, it was over 200 ns (Tables S1 and S2, Supporting Information).

Though the absorption and emission features of P_{AD} perovskites are similar to those recently reported for $CH_3NH_3PbBr_3$ quantum dots (QDs),^[10] this is not indicative of the actual shape of the nanocrystals. In fact, it has recently been reported that different shaped $CsPbBr_3$ nanocrystals (spherical QDs, nanocubes, and platelet-like nanoparticles) exhibit the PL peak practically at the same wavelength.^[11] The average PL decay lifetime of these nanocrystals varies from several tens of ns (QDs) to ≈ 1 μ s (platelet-like nanoparticles).

The X-ray powder diffraction (XRPD) pattern of P_{AD} fitted to a single-phase model corresponding to the cubic phase of hybrid organic–inorganic $CH_3NH_3PbBr_3$ and compared well with those reported in the literature for $CH_3NH_3PbBr_3$ nanoparticles (Figure S3, Supporting Information). The crystallite size calculated by the Scherrer equation was 53 ± 5 nm. High resolution transmission electron microscopy (HRTEM) images showed nanoplatelets (around 44×35 nm²), but the perovskite material was unstable under the e-beam (Figure S4, Supporting Information); this behavior has already been reported for μ m-sized $CH_3NH_3PbBr_3$ perovskites.^[12] We were able to identify the formation of spherical Pb nanoparticles at very short times under the beam exposure (Figure S5, Supporting Information).^[13]

Atomic force microscopy (AFM) was then used to gain more information about the size of P_{AD} nanoparticles using samples with different concentrations (from 0.04 to 2 mg mL⁻¹ of P_{AD} in toluene), which were deposited on a silicon wafer and dried under vacuum. **Figure 2** shows a representative AFM image of the highest concentrated sample indicating the presence of large aggregates of nanoparticles, where the measurement of the height profile (≈ 21 nm) of an individual nanoplatelet was feasible; the lateral size of the nanoplatelet was estimated as 60 nm following a method reported in the literature.^[14] The aggregates become smaller with the sample dilution (Figure S6 of the Supporting Information shows small aggregates visualized in the 50-fold diluted sample). The size of the nanoparticles is in good agreement with that visualized in the TEM images and estimated from the XRPD data.

The recombination dynamics of photogenerated charges of lead halide perovskites is still under debate.^[15] A very small Stokes shift between the absorption and emission spectra and the presence of long-lived PL components are features found in platelet-like $CsPbBr_3$ nanoparticles. Their increased PL lifetime has been mainly attributed to exciton radiative recombination in the large crystal.^[11]

The PL spectrum of P_{AD} was registered at the top and at a lower point of the kinetic trace (specifically 0 and 100 ns, respectively, in Figure 1f). The slow decay component exhibited a slightly red-shifted PL peak (at λ_{max} 520 nm)

with respect to that of the fast decay component (band at λ_{max} 517 nm). An in-depth study of the long-lived emission lifetimes of P_{AD} would be interesting, but it is outside the scope of this manuscript.

The composition of P_{AD} was determined by combining thermogravimetric analysis (TGA) and proton nuclear magnetic resonance ($^1\text{H-NMR}$) data. The TGA of P_{AD} was compared with that of individual precursors (MABr, ADBr, and lead bromide, Figure S7, Supporting Information) and it showed a weight loss of $\approx 28\%$ at 330 °C and then of 72% before reaching 600 °C, corresponding to the organic and inorganic components, respectively. The peaks of the first derivative were at 324 and 570 °C.

The molar ratio of the organic components in P_{AD} was quantified by reverting the perovskite back to its precursors after dissolving it in deuterated dimethyl sulfoxide and then analyzing the mixture by $^1\text{H-NMR}$ spectroscopy (see details in the Supporting Information and Figure S8). These studies revealed that the perovskite nanomaterial was obtained in a high chemical yield (76%, Table S3, Supporting Information).

The effect of the reaction temperature on the optical properties of the adamantylammonium-capped perovskites was also analyzed. The synthesis was carried out by injecting dropwise the precursor solution into toluene at 80 °C. The resulting colloidal perovskite nanoparticles ($P_{\text{AD}/80}$) exhibited a slightly red-shifted emission peak (at 524 nm) and a lower PL quantum yield (89%) than P_{AD} (Figure S9, Supporting Information).

The photostability under air of P_{AD} was studied using fluorimeter lamps ($\lambda_{\text{exc}} = 350$ nm) as the light source. The dynamics of the PL of P_{AD} under continuous optical excitation did not show a photoactivation stage, as expected taking into account the perovskite quantum yield of $\approx 100\%$ (Figure 3c). Photodarkening under prolonged irradiation of the perovskite in air atmosphere led to a loss of emission of $\approx 25\%$ after 180 min irradiation. Therefore, though the quasi-spherical shaped ADBr allows the perovskite to reach the maximum emission, it cannot totally stop the photodarkening process under continuous irradiation.

As mentioned above, moisture can be a problem for the (photo)stability of the organolead halide perovskites. Taking into account the good affinity between cucurbituril portals for cations^[16] and the high binding affinity constant of CB with 2-adamantylammonium moiety ($K = 1.00 \pm 0.3 \times 10^{14} \text{ M}^{-1}$);^[17] we envisaged that the preparation of the nanoparticles under the same conditions as P_{AD} but in the presence of CB could be beneficial for the photostability of the resulting nanoparticles. The addition of a small amount of CB (12:1 ADBr/CB molar ratio) to the a DMF solution containing the same concentration of ADBr, MABr, and PbBr_2 as that used in the synthesis of P_{AD} , gave rise to nanoparticles termed as $P_{\text{AD-CB}}$, which were also dispersible in toluene. The XRPD pattern of $P_{\text{AD-CB}}$ also fitted to a single-phase model corresponding to the cubic phase of MAPbBr_3 (Figure S3, Supporting Information), and the crystallite size calculated by the Scherrer equation was of 34 ± 3 nm (i.e., smaller than that estimated for P_{AD}). These nanoparticles showed the same behavior as P_{AD} under the e-beam during the TEM characterisation (Figure S10, Supporting Information).

The composition of $P_{\text{AD-CB}}$ nanoparticles was determined by combining TGA and $^1\text{H-NMR}$ data. The TGA of $P_{\text{AD-CB}}$ shows a weight loss of $\approx 30\%$ before reaching 325 °C, followed by a 6% weight loss before reaching 470 °C, and finally a weight loss of $\approx 64\%$ before reaching 600 °C (Figure S7, Supporting Information). The peaks of the first derivative are at 324, 414, and 566 °C. The first weight loss could be attributed to the loss of MABr plus ADBr salt, whereas the second loss could be attributed to CB. The sublimation of lead bromide occurs at a similar temperature to that found in P_{AD} . The molar ratio of the organic components in $P_{\text{AD-CB}}$ was quantified by following the same strategy as in P_{AD} , i.e., by reverting the perovskite into its components and analyzing the mixture by $^1\text{H-NMR}$ spectroscopy; the ADBr/CB molar ratio was 6.83 (see Figure S8 and Table S4, Supporting Information).

The attachment of CB[7] to the nanoparticle surface was corroborated by attenuated total reflection Fourier transform infrared spectroscopy (ATR-FTIR). Figure S11 of the Supporting Information shows the comparison between the FTIR

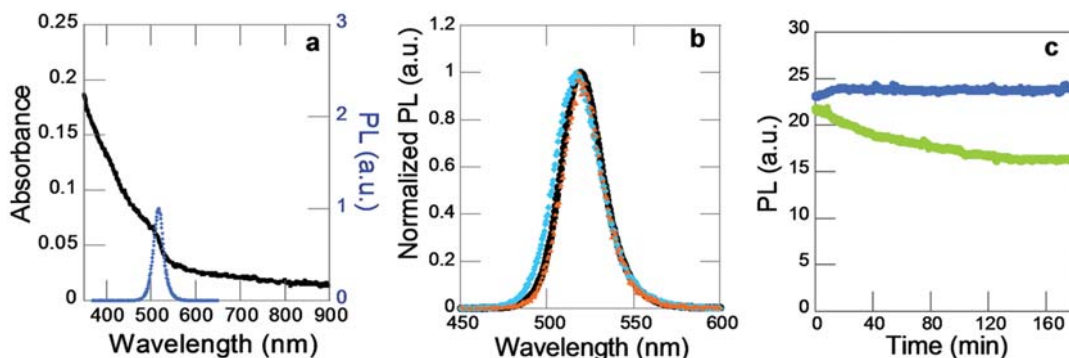


Figure 3. a) Absorption (in black) and emission spectra (in blue) of $P_{\text{AD-CB}}$ in aerated toluene. b) Time-resolved PL spectra of $P_{\text{AD-CB}}$ registered at the maximum of the kinetic PL decay trace (0 ns, in blue; 100 ns later, in orange); the black line represents the PL steady-state spectrum. c) Photoluminescence of P_{AD} (green) and $P_{\text{AD-CB}}$ (blue) dispersed in aerated toluene as a function of irradiation time; ($\lambda_{\text{exc}} = 340$ nm, $\lambda_{\text{em}} = 520$ nm).

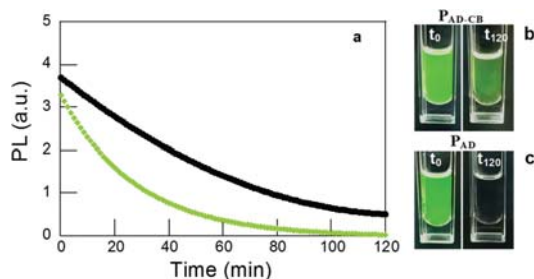


Figure 4. a) Photoluminescence of P_{AD-CB} (in black) and P_{AD} (in green) dispersed in toluene and in contact with water as a function of the irradiation time; $\lambda_{exc} = 350$ nm, PL registered at 520 nm under air atmosphere; b,c) Images are of P_{AD-CB} and P_{AD} colloidal dispersions immediately after addition (left) of water and 120 min afterward (right).

spectra of CB, AD@CB, P_{AD} , and P_{AD-CB} . The strong band assigned to CB $\nu_{as}(C=O)$ stretching vibration was at higher values in P_{AD-CB} (1734 cm^{-1}) than in CB and AD@CB (1710 and 1716 cm^{-1}). These differences corroborate the interaction of the CB with the nanoparticle surface through the carbonyl groups and the C=O stretching at higher values suggests a further deviation from the planarity of the C=O bond compared with the N–C–N plane when the CB anchored to the nanoparticle surface.^[18]

P_{AD-CB} exhibited a high PL (quantum yield of 89.0%) with the maximum at 519 nm, i.e., 1 nm blue-shifted compared to that of P_{AD} (Table 1). The P_{AD-CB} PL decay trace was registered at 519 nm; the PL decay also fitted to a triexponential function of time (the corresponding contributions to the total signal are shown in Table 1). The PL spectrum of P_{AD-CB} was also registered at the same points as previously described for P_{AD} (Figure 3b). In this case, the shift between the spectra was even smaller than in the case of P_{AD} .

The dynamics of the PL of P_{AD-CB} under continuous UV-excitation (Figure 3c) showed an initial photoactivation stage, increasing the emission efficiency of the nanoparticle by 4% in the first 20 min but no further emission changes were detected during the following 160 min. This amazing photostability of the colloid is consistent with similar kinetics for the photoactivation process (due to the presence of oxygen) to that of the photodarkening process, i.e., CB reduces the efficiency of the moisture effect. Moreover, 24 h irradiation decreases the nanoparticle emission by only 13%.

To further compare the better performance of P_{AD-CB} to that of P_{AD} under humid conditions, 0.5 mL of water were injected at the bottom of each cuvette containing 1.5 mL of the corresponding toluene colloid and the evolution of the PL of the perovskite under continuous irradiation ($\lambda_{exc} = 350$ nm) was followed under air atmosphere. **Figure 4** demonstrates the strikingly higher photostability of P_{AD-CB} toluene dispersions even under such drastic conditions (combining direct contact with water and UV-photoirradiation).

In summary, we demonstrate that the luminescence of $CH_3NH_3PbBr_3$ perovskite nanoparticles reaches its maximum by using ADBr as the only capping ligand. These nanoparticles exhibit a luminescence quantum yield of $\approx 100\%$,

thus showing that the nanoparticle surface is properly passivated. Nevertheless, these nanoparticles undergo a considerable photodarkening under prolonged irradiation. The capacity of the adamantyl moiety to form a supramolecular system in the presence of CB produces nanoparticles with an astonishing photostability, while maintaining a strong luminescence. These properties make these materials very promising for developing devices in which excellent PL and photostability are required. Moreover, these nanoparticles are obtained with a high chemical yield.

Experimental Section

Synthesis of P_{AD} Nanoparticles: First, concentrated DMF solutions of the components, 2-adamantylammonium bromide (0.043 M), methylammonium bromide (0.089 M), and lead bromide (0.027 M) were prepared. Then, a precursor solution was prepared by mixing 2-adamantylammonium bromide (50 μ L, 2.18 μ mol), methylammonium bromide (37 μ L, 3.24 μ mol), and lead bromide (100 μ L, 2.7 μ mol) in DMF (MABr: ADBr: PbBr₂ molar ratio of 1.2:0.08:1) and stirred for 15 min. This precursor solution was dropped into toluene (5 mL) and stirred for 1 h. A strong green luminescent dispersion was immediately observed. Then, the dispersion was centrifuged at 7000 rpm (6300 g) by 4 min at 20 °C. The solid obtained was dispersed in toluene (1 mL) and maintained as colloidal dispersion.

Synthesis of P_{AD-CB} Nanoparticles: They were prepared following the same procedure than for P_{AD} , except that after stirring the precursor solution (MABr: ADBr: PbBr₂ mixture) for 15 min, CB (0.18 μ mol, dissolved in DMF) was added, and then the mixture was stirred during 30 min before it was dropped into toluene.

Characterization Methods: the UV–visible spectra of the samples were recorded using a quartz cuvette in an UV–visible spectrophotometer Secoman Uvi Ligh XT5. Steady-state fluorescence spectra were measured at room temperature on an Amnco Browman series 2 Luminescence spectrometer. The PL quantum yields of the colloidal perovskites were measured by using a Hamamatsu C9920-02 absolute PL Quantum Yield Measurement System with monochromatic light source (Xenon Lamp, 150 W) and integrating sphere. Kinetic photoluminescence traces were measured using a Compact photoluminescence lifetime spectrometer C11367, Quantaaurus-Tau, with LED excitation wavelength of 340 nm. Time-resolved PL spectra measurements were made with a Time Master Fluorescence lifetime spectrometer TM-2/2003 from PTI; sample excitation was afforded by PTI's own GL-3300 nitrogen laser at 337 nm (Energy per pulse at 5 Hz of 1.45 mJ).

HRTEM selected area electron diffraction was carried out by using a field emission gun (FEG) TECNAI G2 F20 microscope operated at 200 kV.

The XRPD analyses were performed in a powder diffractometer D8 Avance A25 model Bruker, with a powder diffractometer θ - θ configuration, X-ray tubes on a lineal receiver Cu radiation.

The composition of P_{AD} and P_{AD-CB} was determined by combining TGA and ¹H-NMR data. The attachment of CB to the nanoparticle surface was further corroborated by ATR-FTIR measurements. Further details about experimental procedures and characterization methods are given in the Supporting Information.

Supporting Information

Supporting Information is available from the Wiley Online Library or from the author.

Acknowledgements

The authors thank the Spanish Ministry of Economy and Competitiveness (CTQ2014-60174-P; Maria de Maeztu: MDM-2015-0538; grants to SGC and LFS, and RyC to MGB), and FGUV (REG). The authors also thank Dr. A. Forment for her help in the interpretation of the AFM images.

- [1] S. D. Stranks, H. J. Snaith, *Nat. Nanotechnol.* **2015**, *10*, 391.
- [2] a) S. Gonzalez-Carrero, G. M. Espallargas, R. E. Galian, J. Perez-Prieto, *J. Mater. Chem. A* **2015**, *3*, 14039; b) S. González-Carrero, R. E. Galian, J. Pérez-Prieto, *Part. Part. Syst. Charact.* **2015**, *32*, 709; c) J. H. Noh, S. H. Im, J. H. Heo, T. N. Mandal, S. I. Seok, *Nano Lett.* **2013**, *13*, 1764.
- [3] a) G. Xing, N. Mathews, S. S. Lim, N. Yantara, X. Liu, D. Sabba, M. Grätzel, S. Mhaisalkar, T. C. Sum, *Nat. Mater.* **2014**, *13*, 476; b) G. Li, Z.-K. Tan, D. Di, M. L. Lai, L. Jiang, J. H.-W. Lim, R. H. Friend, N. C. Greenham, *Nano Lett.* **2015**, *15*, 2640; c) F. Deschler, M. Price, S. Pathak, L. E. Klintonberg, D.-D. Jarausch, R. Högler, S. Hüttner, T. Leijtens, S. D. Stranks, H. J. Snaith, M. Atatüre, R. T. Phillips, R. H. Friend, *J. Phys. Chem. Lett.* **2014**, *5*, 1421; d) V. D'Innocenzo, A. R. Srimath Kandada, M. De Bastiani, M. Gandini, A. Petrozza, *J. Am. Chem. Soc.* **2014**, *136*, 17730; e) J. Luo, J.-H. Im, M. T. Mayer, M. Schreier, M. K. Nazeeruddin, N.-G. Park, S. D. Tilley, H. J. Fan, M. Grätzel, *Science* **2014**, *345*, 1593.
- [4] a) W.-J. Yin, J.-H. Yang, J. Kang, Y. Yan, S.-H. Wei, *J. Mater. Chem. A* **2015**, *3*, 8926; b) G. Niu, X. Guo, L. Wang, *J. Mater. Chem. A* **2015**, *3*, 8970.
- [5] X. Li, M. Ibrahim Dar, C. Yi, J. Luo, M. Tschumi, S. M. Zakeeruddin, M. K. Nazeeruddin, H. Han, M. Grätzel, *Nat. Chem.* **2015**, *7*, 703.
- [6] J. F. Galisteo-López, M. Anaya, M. E. Calvo, H. Míguez, *J. Phys. Chem. Lett.* **2015**, *6*, 2200.
- [7] a) S. D. Stranks, V. M. Burlakov, T. Leijtens, J. M. Ball, A. Goriely, H. J. Snaith, *Phys. Rev. Appl.* **2014**, *2*, 034007; b) Y. Tian, A. Merdasa, M. Peter, M. Abdellah, K. Zheng, C. S. Ponceca, T. Pullerits, A. Yartsev, V. Sundström, I. G. Scheblykin, *Nano Lett.* **2015**, *15*, 1603.
- [8] J. A. Christians, P. A. Miranda Herrera, P. V. Kamat, *J. Am. Chem. Soc.* **2015**, *137*, 1530.
- a) L. C. Schmidt, A. Pertegás, S. González-Carrero, O. Malinkiewicz, S. Agouram, G. Míguez Espallargas, H. J. Bolink, R. E. Galian, J. Pérez-Prieto, *J. Am. Chem. Soc.* **2014**, *136*, 850; b) S. Gonzalez-Carrero, R. E. Galian, J. Perez-Prieto, *J. Mater. Chem. A* **2015**, *3*, 9187; c) F. Zhang, H. Zhong, C. Chen, X.-g. Wu, X. Hu, H. Huang, J. Han, B. Zou, Y. Dong, *ACS Nano* **2015**, *9*, 4533; d) H. Huang, A. S. Susha, S. V. Kershaw, T. F. Hung, A. L. Rogach, *Adv. Sci.* **2015**, *2*, 1500194.
- [9] H. Huang, F. Zhao, L. Liu, F. Zhang, X.-g. Wu, L. Shi, B. Zou, Q. Pei, H. Zhong, *ACS Appl. Mater. Interfaces* **2015**, *7*, 28128.
- [10] S. Sun, D. Yuan, Y. Xu, A. Wang, Z. Deng, *ACS Nano* **2016**, *10*, 3648.
- [11] F. Zhu, L. Men, Y. Guo, Q. Zhu, U. Bhattacharjee, P. M. Goodwin, J. W. Petrich, E. A. Smith, J. Vela, *ACS Nano* **2015**, *9*, 2948.
- [12] J. A. Sichert, Y. Tong, N. Mutz, M. Vollmer, S. Fischer, K. Z. Milowska, R. García Cortadella, B. Nickel, C. Cardenas-Daw, J. K. Stolarczyk, A. S. Urban, J. Feldmann, *Nano Lett.* **2015**, *15*, 6521.
- [13] C.-F. Josep, C. Eugenio, F.-A. Alicia, P.-C. Elena, *Nanotechnology* **2014**, *25*, 395703.
- [14] a) H. He, Q. Yu, H. Li, J. Li, J. Si, Y. Jin, N. Wang, J. Wang, J. He, X. Wang, Y. Zhang, Z. Ye, *Nat. Commun.* **2016**, *7*, 10896; b) T. Tachikawa, I. Karimata, Y. Kobori, *J. Phys. Chem. Lett.* **2015**, *6*, 3195.
- [15] K. I. Assaf, W. M. Nau, *Chem. Soc. Rev.* **2015**, *44*, 394.
- [16] S. Moghaddam, C. Yang, M. Rekhasky, Y. H. Ko, K. Kim, Y. Inoue, M. K. Gilson, *J. Am. Chem. Soc.* **2011**, *133*, 3570.
- [17] L. Frances-Soriano, M. Gonzalez-Bejar, J. Perez-Prieto, *Nanoscale* **2015**, *7*, 5140.

Received: January 21, 2016
Revised: July 8, 2016
Published online: August 24, 2016



Supporting Information

for *Small*, DOI: 10.1002/smll.201600209

The Luminescence of $\text{CH}_3\text{NH}_3\text{PbBr}_3$ Perovskite Nanoparticles
Crests the Summit and Their Photostability under Wet
Conditions is Enhanced

*Soranyel Gonzalez-Carrero, Laura Francés-Soriano, María
González-Béjar, Saïd Agouram, Raquel E. Galian,* and Julia
Pérez-Prieto**

Supporting Information

The Luminescence of CH₃NH₃PbBr₃ Perovskite Nanoparticles Crests the Summit and their Photostability under Wet Conditions is Enhanced

Soranyel Gonzalez-Carrero, Laura Francés-Soriano, María González-Béjar, Saïd Agouram, Raquel E. Galian and Julia Pérez-Prieto**

Table of content

Details of experimental procedures	S2
Figure S1. Absorption and emission spectra of P _{AD} colloidal perovskite nanoparticles at different molar ratios between ammonium salts and lead bromide	S4
Table S1. Photoluminescence data of toluene dispersion of P _{AD} precipitate (P ₁), obtained after centrifugation of the initial dispersion, and of the precipitate (P ₂) obtained after centrifugation of the supernatant, and of the final supernatant (S _{p2})	S5
Figure S2. Emission spectra and kinetic traces of P _{AD} precipitate (P ₃) obtained after centrifugation of the initial dispersion (injected into 80 mL of toluene) and the final supernatant (S _{p3}).	S5
Table S2. Photoluminescence data of P _{AD} precipitate (P ₃) obtained after centrifugation of initial dispersion (injected into 80 mL of toluene) and the final supernatant (S _{p3}).	S5
Figure S3. X-ray diffraction pattern P _{AD} and P _{AD-CB} nanoparticles	S6
Figure S4. HRTEM images of P _{AD} showing the formation of platelet-like nanoparticles and the decomposition of the perovskite sample; scale bar 20 nm.	S6
Figure S5. HRTEM images showing the formation of Pb nanoparticles after exposure of P _{AD} of the e-beam for 50s.	S7
Figure S6. AFM analysis of a highly diluted P _{AD} sample	S8
Figure S7. TGA heating curves of P _{AD} , P _{AD-CB} , ADBr, MABr, and lead bromide	S9
Figure S8. ¹ H-NMR of CB, ADBr, P _{AD} and P _{AD-CB} in deuterated DMSO	S10
Table S3. Quantification of the component molar ratio in P _{AD}	S10
Figure S9. HRTEM images, absorption and emission spectra of P _{AD/80} synthesized at 80°C.	S11
Figure S10. HRTEM images of P _{AD-CB} nanoparticles showing its decomposition under the e-beam	S12
Table S4. Quantification of the component molar ratio in P _{AD-CB}	S12
Figure S11. Comparison between the FTIR spectra of CB, AD@CB, P _{AD} and P _{AD-CB}	S13

Experimental Section

Materials

All the reagents used in the synthesis of the perovskites and the ammonium bromides were purchased from Aldrich and used as received. The organic solvents were of spectroscopic grade (Scharlab). Cucurbit[7]uril (99 %) was purchased from Stream Chemicals.

Methylammonium bromide ($\text{CH}_3\text{NH}_3\text{Br}$) and 2-adamantylammonium bromide ($\text{C}_{10}\text{H}_{18}\text{NBr}$) were synthesized by reaction of the corresponding amine in water/HBr, accordingly to the previously reported procedure.^[1]

Characterization Methods

UV-Visible and photoluminescence steady-state studies

UV-visible spectra of the samples were recorded using a quartz cuvette in a UV-visible spectrophotometer secoman Uvi Ligth XT5.

Steady-state fluorescence spectra were measured at room temperature on an Amnico Browman series 2, Luminescence spectrometer, equipped with a Xenon lamp (150 W). The AB2 software (v. 5.5) was used to register the data. All the data were acquired using 1cm×1cm path length quartz cuvettes, using an excitation wavelength of 350 nm.

Photoluminescence quantum yields

The photoluminescence (PL) quantum yield of colloidal perovskite nanoparticles was measured using a Hamamatsu C9920-02 absolute PL Quantum Yield Measurement System with monochromatic light source (150 W) and integrating sphere. The nanoparticles were dispersed in toluene and the excitation wavelength used was 350 nm. Solution of 9,10 diphenylanthracene (DPA, $\Phi_{\text{PL}}=0.91$ in cyclohexane at $\lambda_{\text{exc}}=355$ nm) and fluorescein ($\Phi_{\text{PL}}=0.86$ in NaOH 0.1 M at $\lambda_{\text{exc}}=465$ nm) were used as fluorescence standards for the characterization of QY measuring systems.^[2]

Time-resolved photoluminescence decays

PL decays were measured using a Compact fluorescence lifetime spectrometer C11367, Quantaurus-Tau, with seven types of LED light source (280 nm, 340 nm, 365 nm, 405 nm, 470 nm, 590 nm, 630 nm). Fluorescence lifetime measurement software U11487 was used to register the data. All the data of PL decay of perovskite dispersed in toluene were acquired using 1cm×1cm path length quartz cuvettes, and LED excitation wavelength of 340 nm.

The PL decays of colloidal perovskite nanoparticles P_{AD} and $P_{\text{AD-CB}}$ were fitted with a triexponential function of time (t) equation 1, where τ_i are the decay times and α_i represents the amplitudes of the components.

$$I(t) = \sum_i \alpha_i \left(-\frac{t}{\tau_i}\right) \quad (1)$$

Time-resolved photoluminescence spectra

The time resolved PL spectra measurements were made with a Time Master Fluorescence lifetime spectrometer TM-2/2003 from PTI. Sample excitation was afforded by PTI's own GL-3300 nitrogen laser at 337 nm (Energy per pulse at 5 Hz of 1.45 mJ). These time resolved PL spectra were compared with the steady-state PL spectra measured on a spectrofluorometer PTI (LPS-220B, motor driver MD-5020, Brytebox PTI), equipped with a Xenon lamp (75 W) power supply. The Felix 32 Analysis software was used to register the data. All the data were acquired using 1cm×1cm path length quartz cuvettes and at room temperature.

Microscopy images

Transmission electron microscopy TEM measurements were carried out by using a Field Emission Gun (FEG) TECNAI G2 F20 microscope operated at 200 kV. TEM samples were prepared from a toluene dispersion of the nanoparticles, and a few drops of the resulting suspension were deposited onto a carbon film supported on a copper grid, which was subsequently dried.

The atomic-force microscopy (AFM) analysis of P_{AD} topography images was recorded in tapping mode using a Di NanoScope IVa Controller (resonance frequency of 300 KHz, force constant of 40 N/m). A tip radius (rtip) of 10 nm and tip-to-face angle (γ) of 19.4° were used to estimate the experimental width. The samples were prepared by drop casting of concentrated (2 mg/mL) toluene dispersion and a fiftyfold more diluted sample on silicon wafers. These substrates had been previously sonicated for 10 minutes in a freshly prepared $H_2O_2:NH_4OH:H_2O$ (1:1:2) solution and the process was repeated three times using new solutions. Then, they were sonicated for 10 minutes in milli-Q water twice and dried under a N_2 stream. The AFM images were analysed following a reported methodology.^[3]

X-Ray Power Diffraction (XRPD)

The XRD analyses were performed in a powder diffractometer D8 Avance A25 model Bruker, with a powder diffractometer θ - θ configuration, X-ray tubes on a lineal receiver Cu radiation, and plus DIFFRAC EVA Data assessment program. The diffracted intensities were recorded at room temperature from 2° to 80° 2 θ angles, with a step size of 0.02° and an acquisition time of 38.4 seconds per step.

Nuclear magnetic resonance (¹H-NMR)

The perovskite NPs were transformed into their components by addition of deuterated DMSO. The ¹H-NMR spectra were registered at room temperature in a Bruker DPX300 spectrometer, with a 300 MHz Bruker magnet (7 T). The chemical shifts (δ) are informed in ppm relative to tetramethylsilane (TMS).

Thermogravimetry analysis (TGA)

The TGA was carried out using a Mettler Toledo TGA/SDTA 851e system with an operative temperature range 25-1100 °C and 0.1 microgram sensitivity. The samples were heated from 25 to 800 °C, with an increase of 10 °C /min and under nitrogen flux of 40 mL/ min.

Attenuated total reflection-Fourier transforms infrared spectrometry (ATR-FTIR) measurements

All ATR-FTIR spectra were performed using a FTIR Thermo Nicolet Nexus spectrophotometer at room temperature with 64 scans and a resolution of 4 cm⁻¹ between 400 and 4000 cm⁻¹. CB spectrum was performed depositing the powder directly on the crystal. ADBr@CB, P_{AD} and P_{AD-CB} FTIR spectra were measured depositing a drop of a concentrated solution followed by slowly evaporating the solvent at room temperature. ADBr@CB solution was made in acetonitrile while P_{AD} and P_{AD-CB} solutions were dispersed in hexane.

Variation in the separation method of P_{AD} nanoparticles

Colloidal P_{AD} perovskites were centrifuged at 3000 rpm for 5 minutes at 20 °C and the precipitate (P_1) was separated. The supernatant was centrifuged at 9000 rpm for 10 minutes at 20 °C, leading to a new precipitate (P_2) and supernatant (S_{P2}). The precipitates (P_1 and P_2) were dispersed in toluene and maintained as colloidal dispersions.

In another experiment, the precursor solution was dropped into 80 mL of toluene instead of 5 mL. Then, the dispersion was centrifuged at 7000 rpm for 5 minutes at 20 °C. The precipitate (P_3) was dispersed in toluene (1 mL). The precipitate and the supernatant (S_{P_3}) were analysed.

Analysis of the components in P_{AD} and P_{AD-CB} and their quantification by NMR and TGA

The colloidal P_{AD} and P_{AD-CB} nanoparticles were precipitated by centrifugation at 7000 rpm and the resulting supernatants were analysed by $^1\text{H-NMR}$ spectroscopy and TGA in order to quantify their components. The PbBr_2 content in an aliquot of perovskite material was determined by TGA, which confirmed the absence of unreactive PbBr_2 , which exhibits a shifted TGA curve when compared with that of the PbBr_2 in the perovskite. Then, another aliquot of the perovskite material was reverted back into the precursors by dissolving it in deuterated dimethyl sulfoxide to determine the molar ratio of the organic components of the perovskite. The supernatants were similarly analysed by TG and $^1\text{H-NMR}$. The resulting data made it possible to determine the chemical yield of the perovskite material. The ratio of each component is shown in Tables S1 and S2.

Stability and photostability of P_{AD} and P_{AD-CB} colloidal nanoparticles

The emissive properties of P_{AD} and P_{AD-CB} dispersed in toluene did not change when they were stored in the darkness and under air for six months.

The photostability of P_{AD} and P_{AD-CB} colloidal nanoparticles, in the presence and in the absence of air, was studied by irradiating the samples (λ_{exc} at 350 nm) for 3 h on a spectrofluorometer PTI, equipped with a Xenon lamp (75 W) at room temperature. The Felix 32 Analysis software was used to register the data. All the data were acquired using 1cm \times 1cm path length quartz cuvettes.

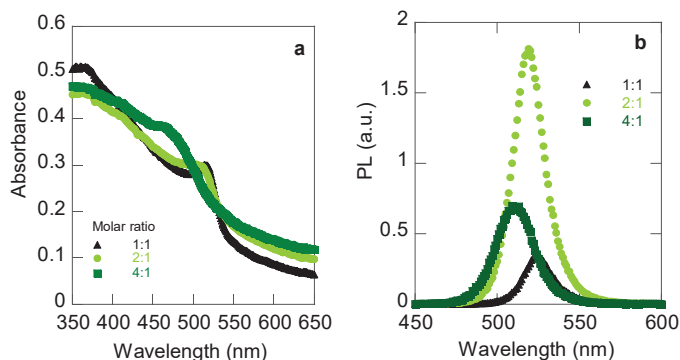


Figure S1. Absorption (a) and emission (b) spectra of P_{AD} colloidal perovskite nanoparticles using 1:1, 2:1 and 4:1 molar ratio between ammonium salts and lead bromide (MABr:ADBr=6:4)

Table S1. Photoluminescence data of toluene dispersion of P_{AD} precipitate (P_1), obtained after centrifugation of the initial dispersion, and of the precipitate (P_2) obtained after centrifugation of the supernatant, and of the final supernatant (S_{P_2})

P_{AD}	λ^a (nm)	τ_{av}	τ_1^b (ns)	τ_2^b (ns)	τ_3^b (ns)
P_1	521	94.7	9.6 (73)	52.5 (24)	243.2 (3)
P_2	523	87.1	4.9 (83)	35.4 (15)	225.5 (2)
S_{P_2}	523	112.8	6.7 (46)	41.5 (49)	247.7 (5)

^{a)} λ_{exc} 340 nm. ^{b)} Contribution of the component to the total PL in brackets.

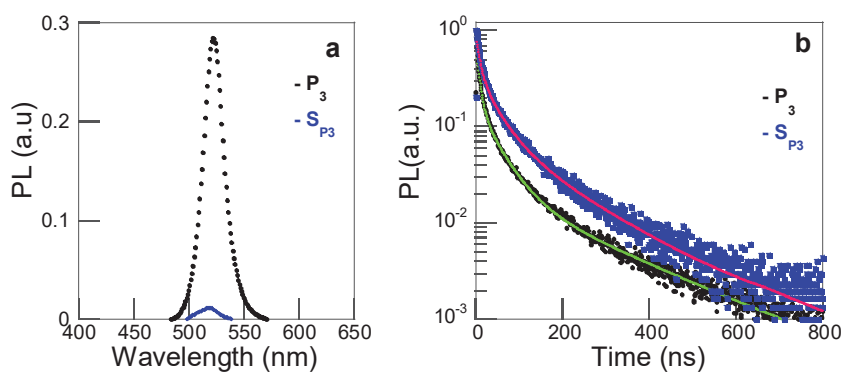


Figure S2. (a) Emission spectra and (b) kinetic traces of P_{AD} precipitate (P_3) obtained after centrifugation of the initial dispersion (injected into 80 mL of toluene) and the final supernatant (S_{P_3}).

Table S2. Photoluminescence data of P_{AD} precipitate (P_3) obtained after centrifugation of initial dispersion (injected into 80 mL of toluene) and the final supernatant (S_{P_3}).

	λ^a (nm)	τ_{av}	τ_1^b (ns)	τ_2^b (ns)	τ_3^b (ns)
P_3	522	82.5	7.6 (79)	44.0 (18)	213.4 (3)
S_{P_3}	520	83.8	8.6 (62)	40.8 (30)	153.7 (8)

^{a)} λ_{exc} 340 nm. ^{b)} Contribution of the component to the total PL in brackets.

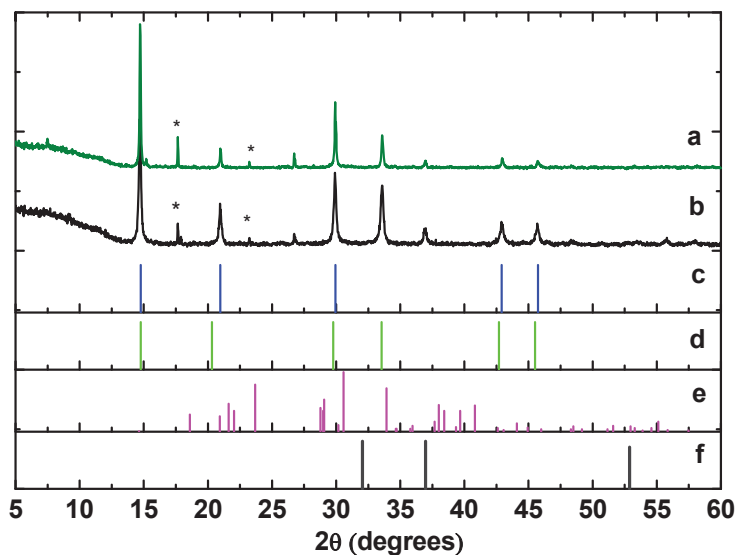


Figure S3. X-Ray Powder diffraction (XRPD) pattern of P_{AD} (a) and $P_{AD/CB}$ (b). Reference lines for specified reflections derived from XRD patterns reported for MAPbX₃ nanoparticles (c, d); ¹⁴¹Pb bromide (d, PDF 05-0608) and lead (d, PDF 00-003-1156). Signals corresponding to ADBr are marked with an asterisk.

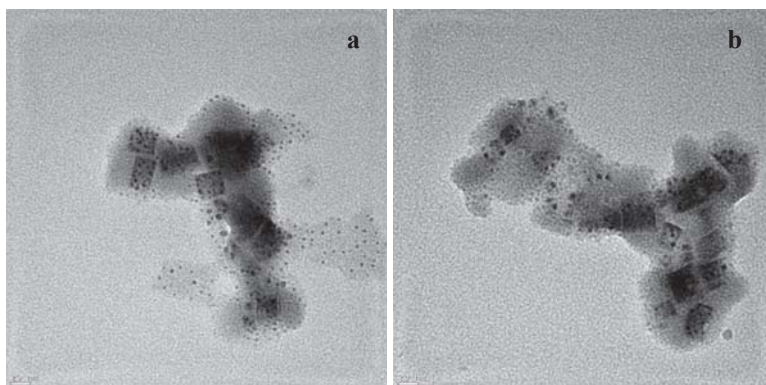


Figure S4. HRTEM images of P_{AD} showing nanoplatforms and the decomposition of the perovskite sample; scale bar 20 nm.

High-resolution TEM (HRTEM) images from a P_{AD} sample

Both high-resolution TEM (HRTEM) and selected area electron diffraction pattern were used to obtain structure information of the synthesised nanoparticles. Figure S5 (a, b) presents a representative TEM image of a P_{AD} sample with its corresponding SAED pattern. We observed a characteristic polycrystalline diffraction pattern which showed well-defined spots distributed in at least 4 diffraction rings. The radius of the electron diffraction ring $r(hkl)$ and the interplanar lattice spacing $d(hkl)$ are related by $r(hkl).d(hkl) = L\lambda$, where $L\lambda = 1$ is the camera constant of the transmission electron microscope. From the electron diffraction pattern, r is measured and the lattice spacing d is determined. The experimental d -values determined from the SAED pattern of P_{AD} sample were found to be: 2.87, 2.49, 1.77 and 1.516 Å corresponding to the planes (111), (200), (220) and (311) respectively, which are indexed as the cubic phase of Pb (JCPDS: 004-0686) with space group Fm3m. It is worth noticing that no diffraction rings corresponding to other compounds are observed.

The single crystalline structure of nanoparticles was also confirmed by the high-resolution TEM image suggesting the nanoparticles were single crystals as indicated clearly by atomic lattice fringes figure S5 (c,d). Direct measurement of spacing in between the crystal fringes visualized in the HRTEM micrograph is 2.86 Å and corresponding to the (111) lattice spacing of Pb, another lattice spacing of 2.46 Å between adjacent lattice planes corresponds to the (200) planes of cubic Pb.

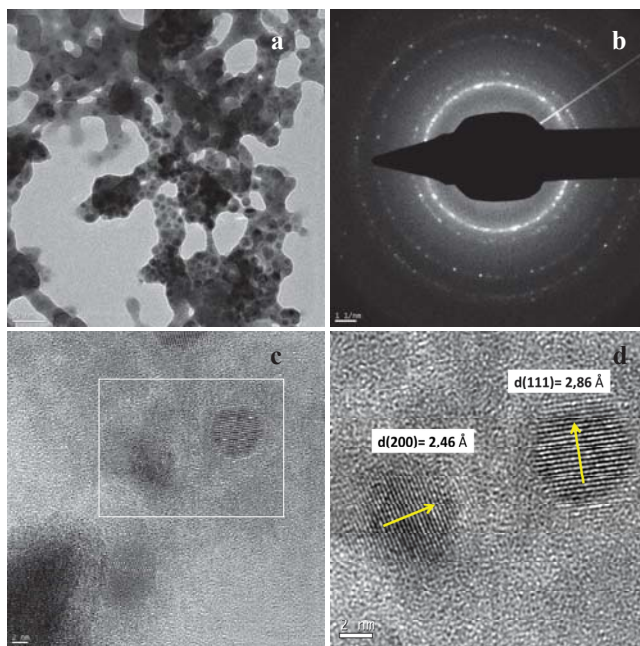


Figure S5. Representative TEM images of P_{AD} sample (a) and the corresponding SAED pattern (b); scale bar 50 nm and 1 nm, respectively. HRTEM images showing the formation of Pb nanoparticles after exposure of P_{AD} to the e-beam for 50s (c); the crystal fringes of the selected area in white (d).

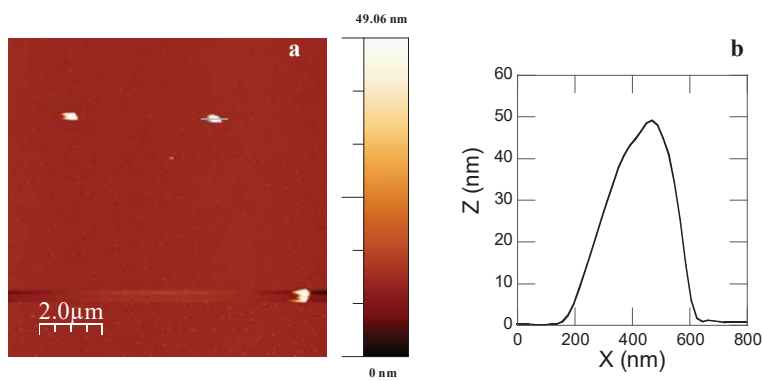


Figure S6. (a) AFM image of a diluted P_{AD} sample (the P_{AD} sample in Figure 2 was diluted by fiftyfold) showing the appearance of smaller aggregates. (b) Line profile of the aggregate identified in (a).

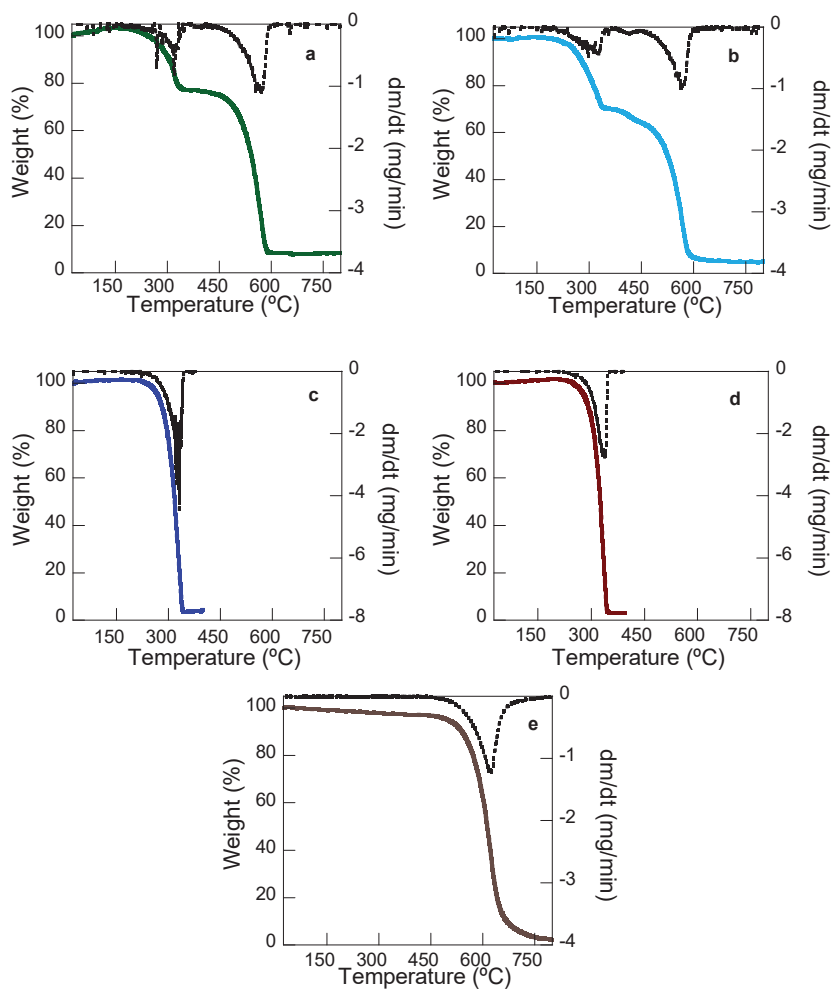


Figure S7. TGA heating curves (-) and the corresponding 1st derivatives (---) of P_{AD} (a), P_{AD-CB} (b) and the precursors ADBr (c), MABr (d) and $PbBr_2$ (e)

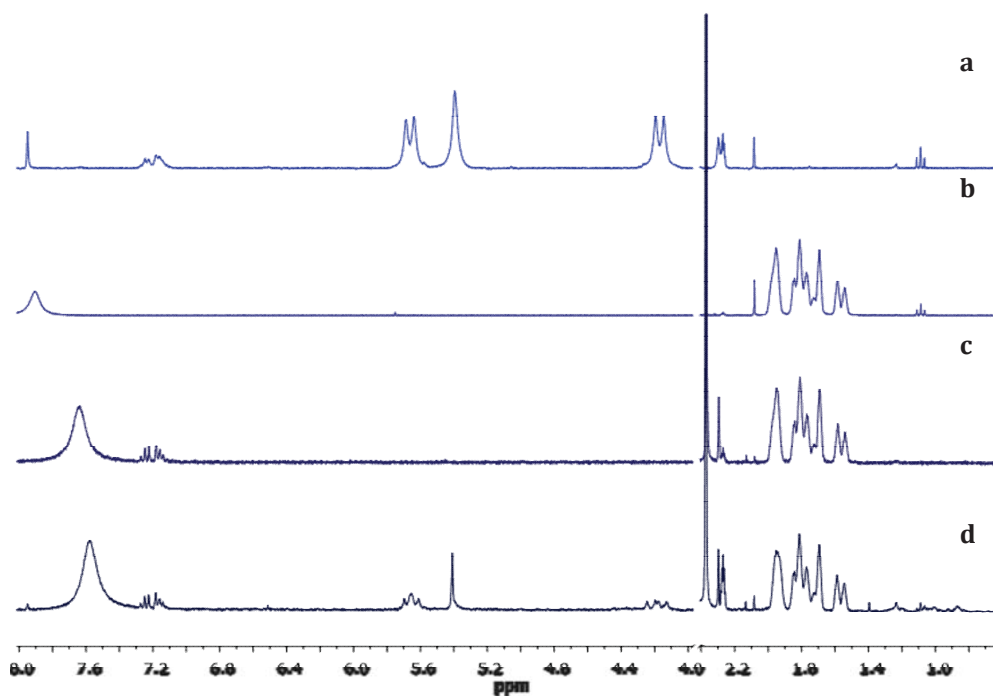


Figure S8. $^1\text{H-NMR}$ spectra of CB (a), ADBr (b), P_{AD} (c) and $\text{P}_{\text{AD-CB}}$ (d) in deuterated DMSO.

Table S3. Quantification of the component molar ratio in P_{AD} by using TGA and $^1\text{H-NMR}$ data

Reagents	Reagents μmol	P_{AD}	
		Component μmol	Component/ PbBr_2^{a} Molar ratio
ADBr	6.9	2.02	0.29
MABr	10.3	4.59	0.68
PbBr_2	8.2	6.86	1.00

^aMol of PbBr_2 calculated by TGA.

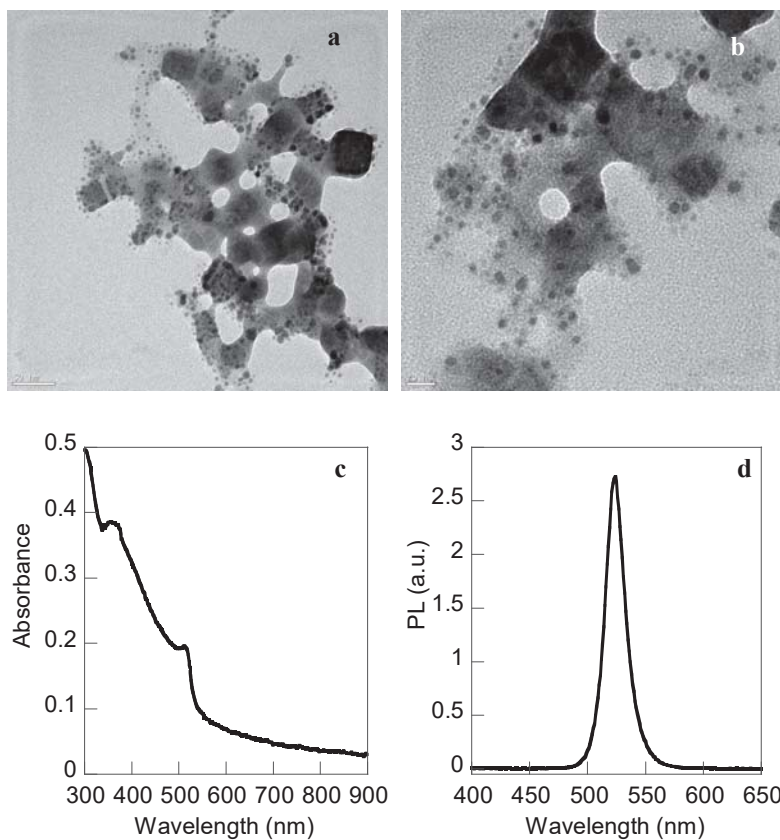


Figure S9. (a,b) HRTEM images (scale bar 50 and 20 nm) of $P_{AD/80}$ nanoparticles at 80°C in toluene, the perovskite decomposes under the e-beam. Absorption (c) and emission (d) spectra of the $P_{AD/80}$ dispersed in toluene.

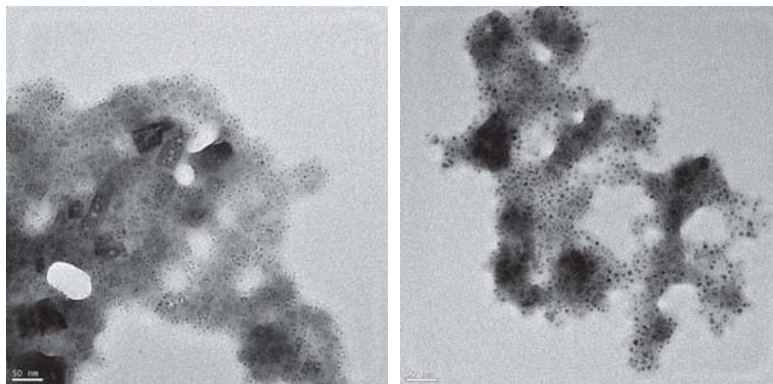


Figure S10. HRTEM images of P_{AD-CB} showing its decomposition under the e-beam; scale bar 50 nm.

Table S4. Quantification of the component molar ratio in P_{AD-CB} by using TGA and 1H -NMR data

Reagents	Reagents μmol	P_{AD-CB}	
		Component μmol	Component/ PbBr_2^a Molar ratio
ADBr	6.54	2.28	0.297
MABr	9.81	5.96	0.770
CB	0.54	0.34	0.045
PbBr₂	8.17	7.66	1.00

^aMol of PbBr_2 calculated by TGA.

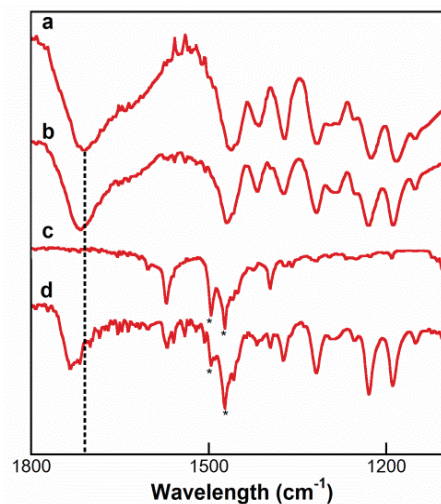


Figure S11. Comparison between the ATR-FTIR spectra of: (a) CB, (b) ADBr@CB, (c) P_{AD} and (d) P_{AD-CB}. The signals corresponding to the remaining hexane are marked with an asterisk (*).

- [1] Aharon, S.; Cohen B. E.; Etgar L., *The Journal of Physical Chemistry C* **2014**, *118*, 17160-17165.
- [2] Suzuki, K.; Kobayashi A.; Kaneko S.; Takehira K.; Yoshihara T.; Ishida H.; Shiina Y.; Oishi S.; Tobita S., *PCCP* **2009**, *11*, 9850-9860.
- [3] Josep, C.-F.; Eugenio C.; Alicia F.-A.; Elena P.-C., *Nanotechnology* **2014**, *25*, 395703.
- [4] a) Kojima, A.; Teshima K.; Shirai Y.; Miyasaka T., *Journal of the American Chemical Society* **2009**, *131*, 6050-6051; b) Zhang, F.; Zhong H.; Chen C.; Wu X.-g.; Hu X.; Huang H.; Han J.; Zou B.; Dong Y., *ACS Nano* **2015**, *9*, 4533-4542.



Cite this: *J. Mater. Chem. C*, 2018, **6**, 6771

Highly photoluminescent, dense solid films from organic-capped $\text{CH}_3\text{NH}_3\text{PbBr}_3$ perovskite colloids†

Soranyel González-Carrero,  Laura Martínez-Sarti, Michele Sessolo, 
Raquel E. Galian  and Julia Pérez-Prieto *

The preparation of densely-packed films from hybrid lead halide perovskite nanocrystals is not trivial, as during assembly into the solid state both the charge transport and photoluminescence can be substantially altered. The objective of the present study was to retain the pre-engineered confined morphologies of hybrid lead halide perovskite nanocrystals in densely-packed solid films by using short organic ligands. Therefore, the roles of the organic ligands would be to provide stable colloids and a good passivation of the nanoparticle surface, as well as to enable the efficient assembly of the nanoparticles in the solid state. We report here an effective and reproducible process to deposit lead halide perovskite nanoparticle films from colloidal $\text{CH}_3\text{NH}_3\text{PbBr}_3$ nanoparticles short organic ligands. Remarkably, we demonstrate that nanoparticle solid films with thicknesses of hundreds of nanometres can retain high photoluminescence, with a quantum yield of 80%, and still sustain charge transport.

Received 20th March 2018,
Accepted 22nd May 2018

DOI: 10.1039/c8tc01344f

rsc.li/materials-c

1. Introduction

Organic-inorganic (hybrid) perovskites exhibit exceptional electronic and optical properties and are of great interest in photovoltaic devices and as luminescent materials for light-emitting devices.^{1–4} Hybrid perovskite films are commonly solution-processed directly from their precursors and consist of polycrystalline materials with many grain boundaries, which may act as recombination centres.⁵ A good passivation of the perovskite films to minimize non-radiative recombination is important to achieve high efficiency in optoelectronic devices.⁶ Passivation of the grain boundaries with species such as chloride ions, pyridine and lead halides can diminish the detrimental effect of the trap states.^{5,7,8} Moreover, it has recently been reported that passivation of the grain boundaries during spin coating of the precursor solution of the $\text{CH}_3\text{NH}_3\text{PbI}_3$ perovskite on a substrate in the presence of excess methylammonium iodide can even facilitate the charge transport in the film.^{8,9} Hybrid lead halide perovskites can be prepared as small-sized nanoparticles (NPs) by using medium-to-long chain alkylammonium halides to enable the confinement of the material to the nanometer scale and their dispersibility in low-to-medium polar organic solvents, as well as to provide high photoluminescence (PL). The challenge is to retain pre-engineered quantum confined structures and properties into nanoparticle

solid films.¹⁰ In particular, ensuring charge transport in perovskite NP films while maintaining high PL can be achieved only in densely-packed NP assemblies.¹¹ Such films can be obtained with perovskite colloids which are well passivated by ligands that can also strongly assemble the NPs at short distances, hence retaining the pre-engineered colloidal morphologies in the solid film. However, organic ligands used in the typical synthesis of colloidal inorganic nanoparticles are usually large and bulky and therefore suppress inter-particle coupling (hindering charge transport) when assembled in solid films. Consequently, several approaches have been used to decrease the inter-particle distance and to enhance charge transport,¹² such as thermal decomposition of the original ligand,^{13,14} and exchange for a smaller or an electrically active one.^{15–17} An alternative strategy is the post-assembly treatment of NP films with a short, compact ligand.^{18,19} The preparation of uniform perovskite NP films with a controlled thickness is essential for their application in light-emitting diodes and solar cells.^{20,21} We hypothesized that the preparation of these NP films with good charge transport properties requires the use of well-passivated NPs, whose organic capping would (i) provide them with a low tendency to aggregate in solution, (ii) enable their assembly in densely-packed nanoparticle films, and (iii) be charge transport-compatible. The high PL and photostability, among the other features, are also essential for their good performance.²² After methylammonium lead bromide ($\text{CH}_3\text{NH}_3\text{PbBr}_3$) colloids were first synthesized in 2014 with a 20% photoluminescence quantum yield (Φ_{PL}), small variations in their preparation and organic capping quickly led to colloidal perovskites with a higher luminescence.^{23–27} In fact, we have recently demonstrated that $\text{CH}_3\text{NH}_3\text{PbBr}_3$ NPs ($\text{P}_{2\text{ADAH-Br}}$) capped with 2-adamantylammonium

Instituto de Ciencia Molecular (ICMol), Universidad de Valencia, Catedrático José Beltrán 2, 46980, Paterna, Valencia, Spain. E-mail: julia.perez@uv.es

† Electronic supplementary information (ESI) available: Additional absorption and emission spectra, SEM images and X-ray diffraction (XRD). See DOI: 10.1039/c8tc01344f

bromide (2ADAH-Br), *i.e.*, with both ions within the 1 nm scale, are highly luminescent (Φ_{PL} ca. 100%).²⁸ We also demonstrated that the capping failed to provide the required steric hindrance between the nanoparticles and, as a consequence, there was considerable aggregation in solution, manifested by an extremely long-lived photoluminescence (average lifetime in hundreds of nano-seconds).^{28,29} To address the preparation of uniform and highly dense perovskite NP solid films, it is imperative to use non-aggregated colloidal nanoparticles. The tendency to aggregate $\text{P}_{2\text{ADAH-Br}}$ nanoparticles is consistent with the considerable van der Waals attraction between adamantyl moieties that can overcome the steric repulsion (this effect is size- and shape-dependent). In fact, they have been used as strongly molecular structure-directing agents.^{30–32} Surface engineering of extraordinarily emissive $\text{P}_{2\text{ADAH-Br}}$ nanoparticles should now be directed towards decreasing their aggregation tendency in solution by interfering slightly in their interaction with the final aim of preparing films with enhanced optical and electronic properties.

We report here that highly photoluminescent colloidal $\text{CH}_3\text{NH}_3\text{PbBr}_3$ perovskites capped with 2-adamantylamine and a short-chain alkanecarboxylic acid show a low tendency to aggregate in solution but can be assembled in densely-packed NP films with controlled thicknesses by centrifugal casting. Electrical measurements using simple multilayer diodes and conductive atomic force microscopy (c-AFM) showed that the ligand in the nanoparticle solid film does not only passivate the grain boundaries well but it also proves to be carrier transport-compatible.

2. Results and discussion

2.1 Surface engineering of the perovskite nanoparticle surface

Our first aim was to determine the effect of the ligand type on the emission lifetime and Φ_{PL} of the $\text{CH}_3\text{NH}_3\text{PbBr}_3$ NPs. In particular, we selected certain ligands in order to screen for the effect of several factors: (i) the shape of the adamantylamine on the NP surface, by comparing 2-adamantylamine (2ADA) with 1-adamantylamine (1ADA); (ii) the length of a linear alkyl-carboxylic acid (with 3, 6, 8, 10 and 18 carbon atoms), and (iii) the use of branched isobutanoic or 1-adamantanecarboxylic acid, a nanometer-sized moiety which is both rigid and virtually stress-free, instead of the Br anion (Fig. 1a).

The preparation of the $\text{CH}_3\text{NH}_3\text{PbBr}_3$ NPs was carried out following a previously described procedure for $\text{P}_{2\text{ADAH-Br}}$.²⁸ Briefly, a DMF precursor solution containing lead bromide and $\text{CH}_3\text{NH}_3\text{Br}$ (1 : 1.1 molar ratio) and organic ligands, specifically 1-ADA or 2-ADA and an alkylcarboxylic acid (0.8 : 9.5 molar ratio), was injected dropwise into toluene while stirring, see the Experimental section for further details. This yielded a green luminescence dispersion, which after centrifugation (7000 rpm) for 7 min, produced a solid which can easily be dispersed in toluene.

$\text{P}_{1\text{ADAH-Br}}$ suspensions showed average PL lifetimes of 37 ns, but they were considerably less luminescent (Φ_{PL} ca. 40%) than $\text{P}_{2\text{ADAH-Br}}$. It is highly probable that the shape of 2ADA facilitates the Br proximity to the nanoparticle surface (better passivation),

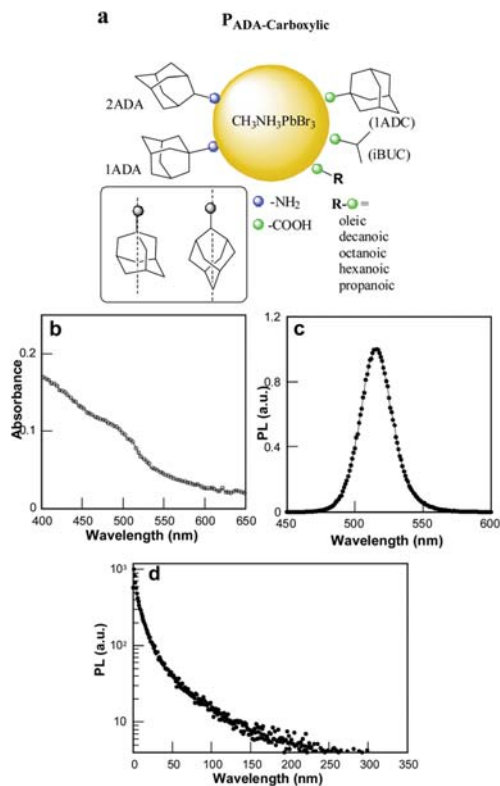


Fig. 1 (a) Schematic representation of $\text{CH}_3\text{NH}_3\text{PbBr}_3$ nanoparticles capped with ADA and carboxylic acid. (b–d) Absorption spectrum (b), PL emission spectrum (c) and PL kinetic decay traces of colloidal $\text{P}_{2\text{ADA-propanoic}}$ nanoparticles (d) in toluene.

while it also favours a strong inter-particle interaction (long lifetime), leading to the formation of undesirable aggregates in solution.

Subsequently, we studied the optical properties of $\text{P}_{2\text{ADA-carboxylic}}$ perovskites which were prepared using alkylcarboxylic acids and adamantylamine (with a carboxylic acid/ADA molar ratio of 12 : 1), with the aim to interfere in the formation of aggregates.

Interestingly, the colloidal nanoparticles with the shortest alkyl-chain carboxylic acid (propanoic acid), $\text{P}_{2\text{ADA-propanoic}}$ showed the desired photophysical features: a high quantum yield (98%), a shorter average PL lifetime τ_{av} (33 ns), and the emission peak wavelength at about 516 nm (with full width at half height, FWHM, of 27 nm), Fig. 1. The photophysical data for the other nanoparticles are described in Tables S1, S2 and Fig. S1, S2 (ESI†).

These findings suggest a positive synergy between the carboxylic acid and 2ADA, while the 2ADA steric hindrance enables a good passivation of the nanoparticle surface, thereby reaching the high Φ_{PL} of $\text{P}_{2\text{ADAH-Br}}$, the anchored carboxylic acid impedes the aggregation of the colloidal nanoparticles. The nanoparticles transform when they are observed using transmission electron

microscopy due to electron-beam-induced damage, as reported before.^{28,33} Scanning electron microscopy (SEM) revealed the formation of the nanoparticles with a diameter of about 22 nm (Fig. S3, ESI[†]).

X-ray photoelectron spectroscopy (XPS) can provide the binding energy (BE) of a core-level electron of an atom in the solid. This energy depends on the potential energy at that position, which in turn depends on the chemical environment of the atom. The Pb 4f XPS spectra (Fig. S4a, ESI[†]) showed two symmetric peaks at 138.1 eV and 143.0 eV, attributed to Pb 4f_{7/2} and Pb 4f_{5/2}, respectively.³⁴ The spin-orbit splitting was 4.9 eV, which agrees with the value reported in the literature.^{24,34} The Br 3d XPS spectrum (Fig. S4b, ESI[†]) showed two peaks at 67.9 eV and 69 eV, which can be assigned to the inner and surface Br anions.^{25,35} The N 1s XPS spectrum (Fig. S4c, ESI[†]) was deconvoluted into two peaks centred at 399.8 eV and 401.5 eV, which can be ascribed to 2-adamantylamine and the methylammonium salt, respectively.^{24,36} The O 1s XPS spectrum (Fig. S4d, ESI[†]) exhibited three peaks. The typical band at 530.0 eV was accompanied by two other peaks at higher energies: the peak at 531.8 eV ascribed to the two nonequivalent oxygen atoms of the carboxylic acid and the peak at 533.4 eV assigned to the two chemically equivalent oxygen atoms of the carboxylate species. The C 1s XPS spectrum (Fig. S4e, ESI[†]) also deconvoluted into three peaks, the peak at 284.6 eV can be assigned to C–C and C–H bonds, while that observed at 285.9 eV can be attributed to the C–N bond of the amine and the C–O bond of the carboxylic acid.²⁴ Finally, the peak at the highest binding energy (288.4 eV) can be assigned to the C=O bond of the propionic acid.³⁶ The quantification of the perovskite components by XPS showed an atomic ratio of 2.7 and 1.1 for Br/Pb and N/Pb, respectively.

2.2 Preparation of nanoparticle solid films

There are several strategies for the preparation of films from the nanoparticles in suspension, such as drop casting and spin coating, and the challenge is to obtain uniform, defect-free films. Though colloidal quantum dots, such as CdSe and PbSe, have been self-assembled successfully into thin films,^{12,37} the same has not been reported widely for hybrid perovskites. The process chosen here was centrifugal casting, which uses centrifugal acceleration to distribute and ultimately cast the material onto a large surface with high control of the thickness (see details in the Experimental section).^{38–40} The substrate (glass slide) was placed at the bottom of a conic centrifuge tube (50 mL) together with 5 mL of freshly-prepared colloids, and the sample was centrifuged for 6 min (Fig. S5, ESI[†]). The nanoparticles in the suspension started to settle and assemble on the substrate. After complete sedimentation of the nanoparticles, the supernatant liquid was removed and the film was dried under a toluene atmosphere at room temperature.

The previously synthesized colloidal P₂ADA-propionic NPs at different concentrations (25, 50, and 100% v/v) in a final volume of 5 mL were used for the preparation of films of different thicknesses (P_{film1}, P_{film2} and P_{film3}, respectively) by centrifugal casting of toluene colloids (see details in the Experimental section).

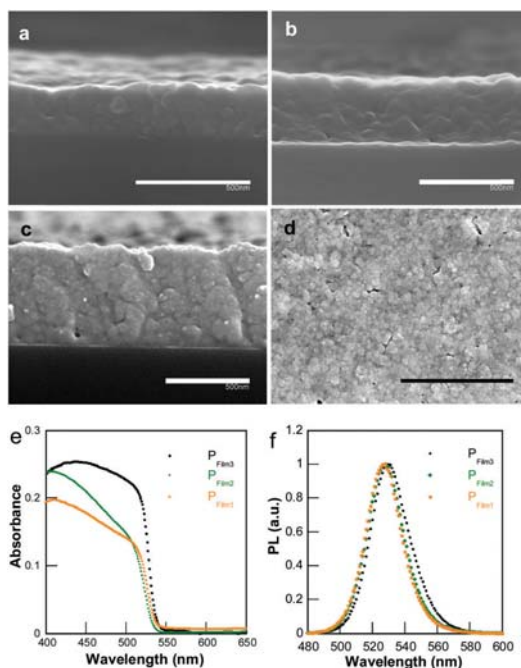


Fig. 2 (a–c) Cross-sectional SEM images of the P₂ADA-propionic NPs solid films on glass with different thicknesses: P_{film1} (a), P_{film2} (b) and P_{film3} (c); scale bar = 500 nm. (d) Top view SEM image of P_{film1} (scale bar of 3 μm). (e and f) Absorption and normalized PL spectra of the P₂ADA-propionic films.

Table 1 Photoluminescence data of the P₂ADA-propionic colloids and of the corresponding films

	Thickness (nm)	λ_{max}^a (nm)	FWHM ^b (nm)	Φ_{PL}^c	τ_{av}^d (ns)
P ₂ ADA-Propionic		516	27	98	33
P _{film1}	260	527	26	80	52
P _{film2}	396	528	26	72	58
P _{film3}	670	529	28	53	93

^a PL peak maximum. ^b Full width at half maximum. ^c PL quantum yield ($\lambda_{\text{exc}} = 365$ nm). ^d Average lifetime. The PL decays, registered at the PL peak maximum, were fitted with a triexponential function.

The cross-sectional SEM images of the films (Fig. 2d–f) show the formation of densely-packed nanoparticle solid films of increasing thicknesses (260 ± 30 nm, 396 ± 28 nm, and 670 ± 44 nm for P_{film1}, P_{film2}, and P_{film3}, respectively). Comparison between the PL parameters of the film series (Table 1) and the colloid showed that (i) the PL emission of the films shifted slightly to a lower energy due to photon recycling; (ii) the peak width of the films was unchanged when compared to that of the colloidal NPs; (iii) the Φ_{PL} of P_{film1} was very high (80%) in spite of its thickness and (iv) its PL lifetime only changed from 33 ns to 52 ns.

Due to the remarkable photophysical properties of P_{film1} and their similarities to those of the colloidal suspensions, we focused the following studies on this particular material. The film showed

a clear band edge cut-off with no apparent excitonic contribution and an optical band gap of about 2.3 eV (Fig. 2e). The energy-dispersive X-ray spectroscopy (EDX) analysis of the film indicated an average Br/Pb molar ratio of 3.1.

The grazing incidence X-ray diffraction (GIXRD) pattern of the NP film showed the typical single-phase model corresponding to the cubic phase (Fig. S6, ESI†), where the diffraction peaks at 14.9°, 21.1°, 30.1°, 33.7°, 43.0° and 45.8° correspond to the (001), (011), (002), (021), (211), (022) and (221) crystallographic planes.⁴¹

2.3 Charge transport and morphology of the nanoparticle solid film (P_{film})

In order to investigate the charge transport properties of the perovskite NP films, we prepared multi-layer diodes using organic semiconductors as charge transport layers. The diodes were prepared on patterned indium tin oxide (ITO) coated glass slides, using poly(3,4-ethylenedioxythiophene)polystyrene sulfonate (PEDOT:PSS) as the hole injection layer, the P_{film} perovskite film, 1,3-bis[3,5-di(pyridin-3-yl)phenyl]benzene (BmPyPhB) as the electron transport layer and Ba (5 nm) and Ag (100 nm) as the cathodes. The device layouts as well as the current density–voltage–luminance (J - V - L) curves are reported in Fig. 3. The electrical characteristics indicate a high-quality diode, as the leakage current (ohmic contact at low applied bias) is very low, indicating a low density of defects in the perovskite NP film. Current injection takes place at about 2 V, when the electroluminescence is also observed. This means that both electrons and holes are injected into, and transported within, the perovskite NP film. We also fabricated reference diodes with the same transport materials but with a spin-coated polycrystalline MAPbBr₃ film as the active layer (thickness of 300 nm). The J - V characteristics of this diode closely resemble that of the device based on the NPs (Fig. 3), suggesting a comparable carrier transport within the two materials. The moderate electroluminescence (about 20 cd m⁻²) can be ascribed to a non-optimal device configuration, *i.e.* a lack of an electron blocking layer in between PEDOT:PSS and the perovskite film, or to spatial inhomogeneities in perovskite morphological and optoelectronic properties.⁴² Conductive atomic force microscopy (c-AFM) allows the simultaneous acquisition of dark conductivity and topographic maps of the same area of a sample.⁴³ Thus we have used c-AFM to study the local electronic properties and morphology of the film

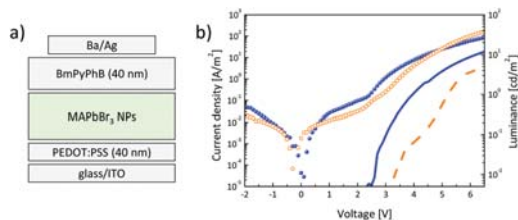


Fig. 3 (a) Device structure and (b) current density (symbols) and luminance (line) vs. the applied bias curve for the multilayer diode using the perovskite NPs (blue) and a reference polycrystalline MAPbBr₃ film (orange) as the electroluminescent materials.

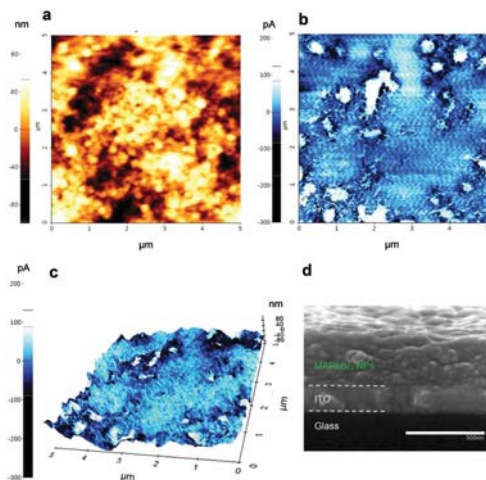


Fig. 4 (a) Topographical AFM; (b) c-AFM images of P_{film1^*} obtained at a bias voltage (-3.5 V) in the dark. (c) 3D topographic and c-AFM images of P_{film1^*} (bias = -3.5 V). AFM image scales: $5 \mu\text{m} \times 5 \mu\text{m}$. (d) Cross-sectional SEM images of P_{film1^*} (scale bar 500 nm).

prepared by the centrifugal casting of colloidal $P_{2\text{ADA-propanoic}}$ NPs onto the ITO-coated glass, using the same volume and concentration of the NP colloid as that used in the preparation of P_{film} . The thickness of the nanoparticle solid film on ITO-coated glass (291 ± 18 nm) was similar to that obtained on the uncoated glass (Fig. 4d).

AFM measurements were performed under dark conditions (*i.e.* only illuminated by the AFM near-IR laser) to avoid any photocarrier generation. Conductive AFM can be carried out either in a conventional contact mode or by a modified protocol in which, at each pixel, the tip approaches the surface, measures the current, retracts from the surface and then moves to the next pixel. As we did not observe any tip-sample deterioration, we performed the measurements using the conventional contact mode. Fig. 4 displays the topographical image of the film over an area of $25 \mu\text{m}^2$ and the corresponding conductive images of the film at a bias voltage of -3.5 V in the dark (Fig. 4a and b, respectively). The brightest and darkest contrast in the topographical image, Fig. 4a, indicates protrusions and depressions in the range of $+80$ nm to -80 nm, respectively, revealing an average root mean square roughness (R_{RMS}) of about 25 nm, which is comparable to that of PbSe quantum dot films (19 nm) of a similar thickness.³⁷

Remarkably, the conductive c-AFM maps also show the presence of large inhomogeneities in the film, with relatively low conductive regions and high conductive domains (Fig. 4b). Such spatial inhomogeneity is probably hindering the homogeneous transport of injected carriers, which would be preferentially transported and would then recombine through the high conductivity regions of the diode. This uneven distribution of charge carriers can cause the inefficient electroluminescence observed here. It is worth noting that the superposition of the

topography with the conductivity map (Fig. 4c) shows only a small correlation between the surface topographical structures and the current intensity, suggesting that the spatial current distribution is not solely associated with the topographical features of the NP solid film (such as the height, *i.e.* film thickness). The high conductive domains are attributed to the high-density regions of NPs with a more efficient connectivity between them. This can be related to the unique properties of the adamantyl moiety, in particular to the strong ADA-ADA interactions, which minimise the inter-particle distance.

3. Conclusions

In summary, we demonstrate here the preparation of highly luminescent (quantum yield of 80%) thin films with arbitrary thicknesses (up to several hundreds of nanometers), consisting of densely-packed hybrid lead bromide nanoparticles. This result was achieved by surface engineering of the NPs through screening for several different ligands. In particular, adamantyl-amine-capped $\text{CH}_3\text{NH}_3\text{PbBr}_3$ nanoparticles can be produced as highly emissive colloids with a low tendency to aggregate when short alkyl chain carboxylic acids are used as co-ligands, and the cooperative action of the ligands can interfere with the inter-particle interactions.

In spite of the thickness of these nanoparticle films, they exhibited good charge transport properties, as shown by conductive atomic force microscopy and electroluminescent measurements. This indicates that short ligands are able to efficiently passivate the perovskite surface, interfering with the nanoparticle aggregation and allowing efficient charge transport.

4. Experimental section

4.1 Materials

All the reagents and solvents used in the synthesis of the perovskites were purchased from Aldrich and used as received. Methylammonium bromide ($\text{CH}_3\text{NH}_3\text{Br}$) was synthesized by the reaction of methylamine with HBr/water .²⁸

4.2 Preparation of the perovskite nanoparticles

The $\text{P}_{2\text{ADA-carboxylic}}$ NPs were prepared following a similar re-precipitation method that we reported previously.²⁸ The precursor solution was prepared by mixing lead bromide (50 mg, 0.136 mmol), methylammonium bromide ($\text{CH}_3\text{NH}_3\text{Br}$, 18 mg, 0.160 mmol), 2-adamantylamine (16.4 mg, 0.108 mmol) and propionic acid (97 μL , 1.30 mmol) in 5 mL of dimethylformamide. The molar ratio of $\text{PbBr}_2:\text{CH}_3\text{NH}_3\text{Br}:2\text{ADA}:\text{propionic acid}$ was 1:1.1:0.8:9.5. Then, 100 μL of the precursor solution was injected drop by drop into toluene (5 mL) while stirring and a strong green luminescence dispersion was immediately observed. The unreactive material was separated by centrifugation at 7000 rpm (6300 g) for 7 minutes at 20 °C. The solid obtained was dispersed in toluene (5 mL) and maintained as colloidal dispersion. The perovskite colloids comprising a different carboxylic ligand were prepared following the same procedure but replacing the propionic

acid with the corresponding alkyl carboxylic acid, preserving the molar ratio between the reagents (Fig. S1 and S2 (ESI[†])).

4.3 Preparation of the nanoparticle solid films

The NP solid films ($\text{P}_{\text{film}1}$, $\text{P}_{\text{film}2}$, and $\text{P}_{\text{film}3}$) were prepared by the centrifugal casting of colloidal $\text{P}_{2\text{ADA-propanoate}}$ NPs, using an Eppendorf Centrifuge 5804 R. Different volumes of the colloid, 1.25 mL ($\text{P}_{\text{film}1}$), 2.5 mL ($\text{P}_{\text{film}2}$) and 5 mL ($\text{P}_{\text{film}3}$), were added to a conical centrifuge tube (50 mL) containing the glass slide substrate (1.5 cm^2) at the bottom, and the final volume of the toluene colloidal dispersion was 5 mL. Then, the sample was centrifuged (6 min at 6000 rpm); the supernatant was pipetted out and the glass substrate with the deposited $\text{CH}_3\text{NH}_3\text{PbBr}_3$ nanoparticle was carefully washed with toluene and allowed to dry under a saturated toluene atmosphere at room temperature. The film on the ITO-coated glass was prepared similarly to $\text{P}_{\text{film}1}$. The substrates were first cleaned ultrasonically in soapy water, then in de-mineralised water and finally in 2-propanol baths. Finally, they were dried under nitrogen and immediately placed into a conic tube.

4.4 Materials characterization

Optical measurements. The UV-Vis spectra of the colloidal samples were recorded using a quartz cuvette in a UV-visible spectrophotometer secoman Uvi Light XT5. The spectra of the UV-Vis films were recorded on a JASCO V-670 spectrometer with a horizontal integrating sphere (PIV-757). Steady-state PL spectra were measured using an Aminco Bowman series 2 Luminescence spectrometer. PL decays were measured using a Compact fluorescence lifetime spectrometer C11367, QuantaTaurus-Tau. PL lifetime measurement software U11487 was used to register the data; the PL decays were fitted with a triexponential function. The PL quantum yield of colloidal NPs and the film was measured using a Hamamatsu C9920-02 absolute PL Quantum Yield Measurement System with a monochromatic light source (150 W) and an integrating sphere. All the PL data of colloidal nanoparticles were measured in toluene, using 1 $\text{cm} \times 1 \text{ cm}$ path length quartz cuvettes, at room temperature and using an excitation wavelength of 365 nm.

Morphological characterization. The top and cross-sectional SEM images of the NP solid films were obtained using a HITACHI S-4800, with a spotlight of field emission (FEG). The images were obtained at 20 kV. The EDX analysis was carried out in a HITACHI S-4800 equipped with an XFlash 5030 Bruker detector using acquisition software QUANTAX 400. The PXRD of the NP solid films was registered using a powder diffractometer D8 Advance A25 (Bruker). The diffracted intensities were recorded at room temperature from 5° to 80° 2 θ angles, with a step size of 0.02° and an acquisition time of 38.4 seconds per step.

4.5 Multi-layer diodes fabrication

Glass substrates with an indium-doped tin-oxide (ITO) coating were subsequently cleaned with a detergent solution, Millipore water, isopropyl alcohol, and then transferred to a UV-ozone chamber for 20 minutes of treatment. Hence they were coated with a 40 nm thick poly(3,4-ethylenedioxythiophene) doped

with the poly(styrenesulfonate) (PEDOT:PSS, Clevis PVP AI 4083 from Heraeus) film in air, and annealed at 150 °C for 15 minutes. After deposition of the nanoparticle films by centrifugal casting, the electron transport (hole blocking) layer (BmPyPhB) and the top metal electrode (5 nm Ba capped with 100 nm Ag) were thermally evaporated in a high vacuum chamber with a base pressure of 10^{-6} mbar. The devices were not encapsulated and were characterized in a nitrogen-filled glove box. The current density and luminance *versus* voltage characteristics were measured using a Keithley 2400 SourceMeter and a photodiode coupled to a Keithley 6485 Picoammeter.

4.6 Conductive atomic force microscopy (c-AFM)

The topographic, current mapping and *I-V* measurements of NP solid films prepared on the ITO-coated glass substrate were measured using an atomic force microscope Park Systems NX20, equipped with Pt-Ir coated Si tips (CONTSCPT, diameter 7 nm), using a resonance frequency of 31.998 kHz and a spring constant of 0.2 N m⁻¹. c-AFM mapping was performed in contact mode at different voltage bias (from ± 0.5 V to ± 4.5 V) and at scan rate of 0.6 Hz. The current is measured directly after the tip using a preamplifier with a gain of 1011 V/A (ULCA). The current and topographic images were taken under ambient conditions and in the dark. Data acquisition was carried out using SmartScan software (version 1.0) and XEI Data Processing and Analysis software (version 4.3.0) Build2 (Park Systems Corp). The NX20 equipment is supported by an Active Vibration Isolation System (AVIS) model AVI-200S/LP (Table Stable Ltd).

Conflicts of interest

There are no conflicts to declare.

Acknowledgements

We thank MINECO (CTQ2014-60174 partially co-financed with FEDER funds, and Maria de Maeztu: MDM-2015-0538; predoctoral grants to S. G. C and L. M.-S.; RyC contract to M. S.) for financial support. We also thank Fátima Linares Ordoñez (Centro de Instrumentación Científica (CIC), University of Granada) for technical support.

References

- M. M. Lee, J. Teuscher, T. Miyasaka, T. N. Murakami and H. J. Snaith, *Science*, 2012, **338**, 643–647.
- H.-S. Kim, C.-R. Lee, J.-H. Im, K.-B. Lee, T. Moehl, A. Marchioro, S.-J. Moon, R. Humphry-Baker, J.-H. Yum, J. E. Moser, M. Grätzel and N.-G. Park, *Sci. Rep.*, 2012, **2**, 591.
- A. Kojima, K. Teshima, Y. Shirai and T. Miyasaka, *J. Am. Chem. Soc.*, 2009, **131**, 6050–6051.
- Y.-H. Kim, H. Cho and T.-W. Lee, *Proc. Natl. Acad. Sci. U. S. A.*, 2016, **113**, 11694–11702.
- L. K. Ono and Y. Qi, *J. Phys. Lett.*, 2016, **7**, 4764–4794.
- X. Li, Y.-B. Zhao, F. Fan, L. Levina, M. Liu, R. Quintero-Bermudez, X. Gong, L. N. Quan, J. Fan, Z. Yang, S. Hoogland, O. Voznyy, Z.-H. Lu and E. H. Sargent, *Nat. Photonics*, 2018, **12**, 159–164.
- R. Long, J. Liu and O. V. Prezhdo, *J. Am. Chem. Soc.*, 2016, **138**, 3884–3890.
- D.-Y. Son, J.-W. Lee, Y. J. Choi, I.-H. Jang, S. Lee, P. J. Yoo, H. Shin, N. Ahn, M. Choi, D. Kim and N.-G. Park, *Nat. Energy*, 2016, **1**, 16081.
- B. Lee, S. Lee, D. Cho, J. Kim, T. Hwang, K. H. Kim, S. Hong, T. Moon and B. Park, *ACS Appl. Mater. Interfaces*, 2016, **8**, 30985–30991.
- A. Swarnkar, A. R. Marshall, E. M. Sanehira, B. D. Chernomordik, D. T. Moore, J. A. Christians, T. Chakrabarti and J. M. Luther, *Science*, 2016, **354**, 92–95.
- C. G. Bischak, E. M. Sanehira, J. T. Pecht, J. M. Luther and N. S. Ginsberg, *Nano Lett.*, 2015, **15**, 4799–4807.
- C. R. Kagan and C. B. Murray, *Nat. Nanotechnol.*, 2015, **10**, 1013–1026.
- M. Drndić, M. V. Jarosz, N. Y. Morgan, M. A. Kastner and M. G. Bawendi, *J. Appl. Phys.*, 2002, **92**, 7498–7503.
- A. W. Wills, M. S. Kang, A. Khare, W. L. Gladfelter and D. J. Norris, *ACS Nano*, 2010, **4**, 4523–4530.
- M. Law, J. M. Luther, Q. Song, B. K. Hughes, C. L. Perkins and A. J. Nozik, *J. Am. Chem. Soc.*, 2008, **130**, 5974–5985.
- D. V. Talapin and C. B. Murray, *Science*, 2005, **310**, 86.
- J. J. Choi, Y.-F. Lim, M. E. B. Santiago-Berrios, M. Oh, B.-R. Hyun, L. Sun, A. C. Bartnik, A. Goedhart, G. G. Malliaras, H. D. Abruña, F. W. Wise and T. Hanrath, *Nano Lett.*, 2009, **9**, 3749–3755.
- A. T. Fafarman, W.-k. Koh, B. T. Diroll, D. K. Kim, D.-K. Ko, S. J. Oh, X. Ye, V. Doan-Nguyen, M. R. Crump, D. C. Reifsnyder, C. B. Murray and C. R. Kagan, *J. Am. Chem. Soc.*, 2011, **133**, 15753–15761.
- M. H. Zarghami, Y. Liu, M. Gibbs, E. Gebremichael, C. Webster and M. Law, *ACS Nano*, 2010, **4**, 2475–2485.
- L. Martinez-Sarti, T. M. Koh, M.-G. La-Placa, P. P. Boix, M. Sessolo, S. G. Mhaisalkar and H. J. Bolink, *Chem. Commun.*, 2016, **52**, 11351–11354.
- A. Perumal, S. Shendre, M. Li, Y. K. E. Tay, V. K. Sharma, S. Chen, Z. Wei, Q. Liu, Y. Gao, P. J. S. Buenconsejo, S. T. Tan, C. L. Gan, Q. Xiong, T. C. Sum and H. V. Demir, *Sci. Rep.*, 2016, **6**, 36733.
- H. Huang, L. Polavarapu, J. A. Sichert, A. S. Sussha, A. S. Urban and A. L. Rogach, *NPG Asia Mater.*, 2016, **8**, e328.
- L. C. Schmidt, A. Pertegás, S. González-Carrero, O. Malinkiewicz, S. Agouram, G. Mínguez Espallargas, H. J. Bolink, R. E. Galian and J. Pérez-Prieto, *J. Am. Chem. Soc.*, 2014, **136**, 850–853.
- S. Gonzalez-Carrero, R. E. Galian and J. Perez-Prieto, *J. Mater. Chem. A*, 2015, **3**, 9187–9193.
- F. Zhang, H. Zhong, C. Chen, X.-G. Wu, X. Hu, H. Huang, J. Han, B. Zou and Y. Dong, *ACS Nano*, 2015, **9**, 4533–4542.
- H. Huang, A. S. Sussha, S. V. Kershaw, T. F. Hung and A. L. Rogach, *Adv. Sci.*, 2015, **2**, 1500194.
- O. Vybornyi, S. Yakunin and M. V. Kovalenko, *Nanoscale*, 2016, **8**, 6278–6283.

- 28 S. Gonzalez-Carrero, L. Francés-Soriano, M. González-Béjar, S. Agouram, R. E. Galian and J. Pérez-Prieto, *Small*, 2016, **12**, 5245–5250.
- 29 V. S. Chirvony, S. González-Carrero, I. Suárez, R. E. Galian, M. Sessolo, H. J. Bolink, J. P. Martínez-Pastor and J. Pérez-Prieto, *J. Phys. Chem. C*, 2017, **121**, 13381–13390.
- 30 J. Krajčovič, A. Kovalenko, P. Heinrichová, M. Vala and M. Weiter, *J. Lumin.*, 2016, **175**, 94–99.
- 31 A. Kovalenko, C. Yumusak, P. Heinrichova, S. Stritesky, L. Fekete, M. Vala, M. Weiter, N. S. Sariciftci and J. Krajcovic, *J. Mater. Chem. C*, 2017, **5**, 4716–4723.
- 32 H. Yan, J. N. Hohman, F. H. Li, C. Jia, D. Solis-Ibarra, B. Wu, J. E. P. Dahl, R. M. K. Carlson, B. A. Tkachenko, A. A. Fokin, P. R. Schreiner, A. Vailionis, T. R. Kim, T. P. Devereaux, Z.-X. Shen and N. A. Melosh, *Nat. Mater.*, 2017, **16**, 349–355.
- 33 J. Shamsi, P. Rastogi, V. Caligiuri, A. L. Abdelhady, D. Spirito, L. Manna and R. Krahné, *ACS Nano*, 2017, **11**, 10206–10213.
- 34 M. Acik, I. K. Park, R. E. Koritala, G. Lee and R. A. Rosenberg, *J. Mater. Chem. A*, 2018, **6**, 1423–1442.
- 35 H. Huang, J. Raith, S. V. Kershaw, S. Kalytchuk, O. Tomanec, L. Jing, A. S. Susha, R. Zboril and A. L. Rogach, *Nat. Commun.*, 2017, **8**, 996.
- 36 M. Lashkor, F. J. Rawson, J. A. Preece and P. M. Mendes, *Analyst*, 2014, **139**, 5400–5408.
- 37 Q. Lin, H. J. Yun, W. Liu, H.-J. Song, N. S. Makarov, O. Isaienko, T. Nakotte, G. Chen, H. Luo, V. I. Klimov and J. M. Pietryga, *J. Am. Chem. Soc.*, 2017, **139**, 6644–6653.
- 38 J. Y. Kim, V. Adinolfi, B. R. Sutherland, O. Voznyy, S. J. Kwon, T. W. Kim, J. Kim, H. Ihee, K. Kemp, M. Adachi, M. Yuan, I. Kramer, D. Zhitomirsky, S. Hoogland and E. H. Sargent, *Nat. Commun.*, 2015, **6**, 7772.
- 39 Y. Kim, E. Yassitepe, O. Voznyy, R. Comin, G. Walters, X. Gong, P. Kanjanaboos, A. F. Nogueira and E. H. Sargent, *ACS Appl. Mater. Interfaces*, 2015, **7**, 25007–25013.
- 40 C. Qin, T. Matsushima, A. S. D. Sandanayaka, Y. Tsuchiya and C. Adachi, *J. Phys. Lett.*, 2017, **8**, 5415–5421.
- 41 T. Baikie, N. S. Barrow, Y. Fang, P. J. Keenan, P. R. Slater, R. O. Piltz, M. Gutmann, S. G. Mhaisalkar and T. J. White, *J. Mater. Chem. A*, 2015, **3**, 9298–9307.
- 42 S. Y. Leblebici, L. Leppert, Y. Li, S. E. Reyes-Lillo, S. Wickenburg, E. Wong, J. Lee, M. Melli, D. Ziegler, D. K. Angell, D. F. Ogletree, P. D. Ashby, F. M. Toma, J. B. Neaton, I. D. Sharp and A. Weber-Bargioni, *Nat. Energy*, 2016, **1**, 16093.
- 43 M. Marrese, V. Guarino and L. Ambrosio, *J. Funct. Biomater.*, 2017, **8**, 7.

ELECTRONIC SUPPLEMENTARY INFORMATION

Highly Photoluminescent, Dense Solid Films from Organic-capped $\text{CH}_3\text{NH}_3\text{PbBr}_3$

Perovskite Colloids

Soranyel Gonzalez-Carrero, Laura Martinez-Sarti, Michele Sessolo, Raquel. E. Galian, Julia Pérez-Prieto*

Instituto de Ciencia Molecular (ICMol), Universidad de Valencia, Catedrático José Beltrán 2, 46980, Paterna, Valencia, Spain.

Corresponding author email: julia.perez@uv.es

Table of Content	
Table S1. Photoluminescence data of $\text{P}_{1\text{ADA-carboxylic}}$ series as colloids	S2
Figure S1. Absorption spectra; PL emission spectra and PL kinetic decay traces of $\text{CH}_3\text{NH}_3\text{PbBr}_3$ nanoparticles capped with 1-ADA and carboxylic acid	S2
Table S2. Photoluminescence data of the $\text{P}_{2\text{ADA-carboxylic}}$ series as colloids	S3
Figure S2. Absorption spectra; PL emission spectra and PL kinetic decay traces of $\text{CH}_3\text{NH}_3\text{PbBr}_3$ nanoparticles capped with 2-ADA and carboxylic acid.	S3
Figure S3. Scanning electron Microscopy (SEM) images of ITO coated Glass and $\text{P}_{2\text{ADA-propanoate}}$ nanoparticles deposited on ITO coated Glass.	S4
Figure S4. XPS spectra corresponding to Pb 4f; Br 3d; N 1s; O 1s and C 1s of $\text{P}_{2\text{ADA-propanoic}}$ nanoparticles.	S5
Figure S5. Schematic representation of the centrifugal casting method used for film preparation.	S6
Figure S6. X-ray diffraction of $\text{P}_{2\text{ADA-propanoic}}$ NP solid film.	S6

Table S1. Photoluminescence data of $P_{1\text{-ADA-carboxylic}}$ series as colloids. Average lifetime, calculate as $\tau_{\text{av}} = \sum A_i \tau_i^2 / \sum A_i \tau_i$; where τ_i are the decay times and A_i represents the amplitudes of the components, values obtained from the fitted PL kinetic decay traces.

	Amine	Carboxylic Acid	$\lambda_{\text{max}}^{\text{a}}$ (nm)	$\Phi_{\text{PL}}^{\text{b}}$	$\tau_{\text{av}}^{\text{c,d}}$ (ns)
1	1-ADA	Oleic acid	521	87	30
2	1-ADA	Decanoic acid	523	81	47
3	1-ADA	Octanoic acid	523	85	116
4	1-ADA	Hexanoic acid	525	82	93
5	1-ADA	Isobutanoic acid	526	78	181
6	1-ADA	Propanoic acid	526	66	125
7	1-ADA	1-Adamantanecarboxylic acid	522	72	78

^a PL maximum wavelength; ^b PL quantum yield; ^c average lifetime, the PL decays, registered at the PL peak maximum, were fitted with a triexponential function of time.

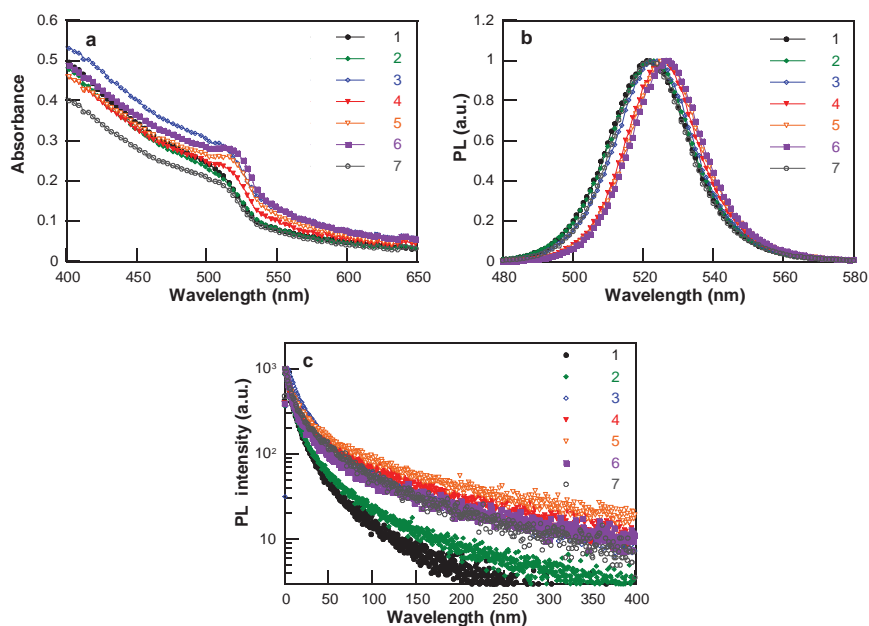
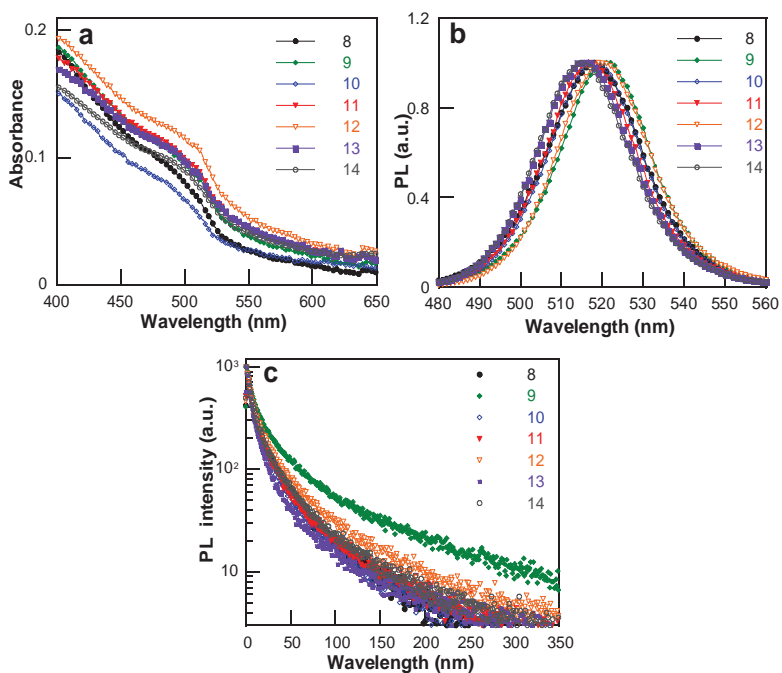


Figure S1. a) Absorption spectra; b) PL emission spectra and c) PL kinetic decay traces of $\text{CH}_3\text{NH}_3\text{PbBr}_3$ nanoparticles capped with 1-ADA and carboxylic acid. See details in table S1.

Table S2. Photoluminescence data of the P_{2ADA-carboxylic} series as colloids

	Amine	Carboxylic Acid	$\lambda_{\text{max}}^{\text{a}}$ (nm)	FWHM ^b (nm)	$\Phi_{\text{PL}}^{\text{c}}$	$\tau_{\text{av}}^{\text{d,e}}$ (ns)
8	2-ADA	Oleic acid	518	26	94	32
9	2-ADA	Decanoic acid	521	26	94	76
10	2-ADA	Octanoic acid	517	26	98	34
11	2-ADA	Hexanoic acid	519	27	96	40
12	2-ADA	Isobutanoic acid	519	27	95	50
13	2-ADA	Propanoic acid	516	27	98	33
14	2-ADA	1-Adamantanecarboxylic acid	516	26	97	41

^a PL peak maximum; ^bfull width at half maximum; ^cPL emission quantum yield; ^daverage lifetime. The PL decays, registered at the PL peak maximum, were fitted with a triexponential function of time.^e

**Figure S2.** a) Absorption spectra; b) PL emission spectra and c) PL kinetic decay traces of CH₃NH₃PbBr₃ nanoparticles capped with 2-ADA and carboxylic acid. See details in table S2.

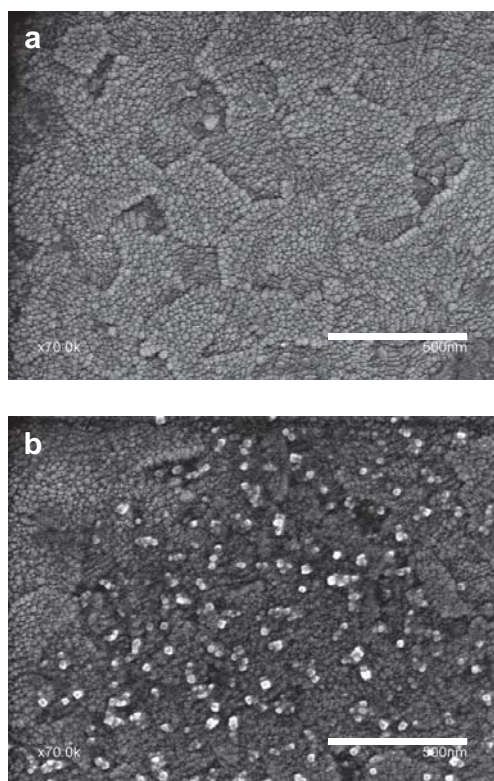


Figure S3. Scanning electron Microscopy (SEM) images of: a) ITO coated Glass and b) P_{ZADA-propanoic} nanoparticles deposited on ITO coated Glass.

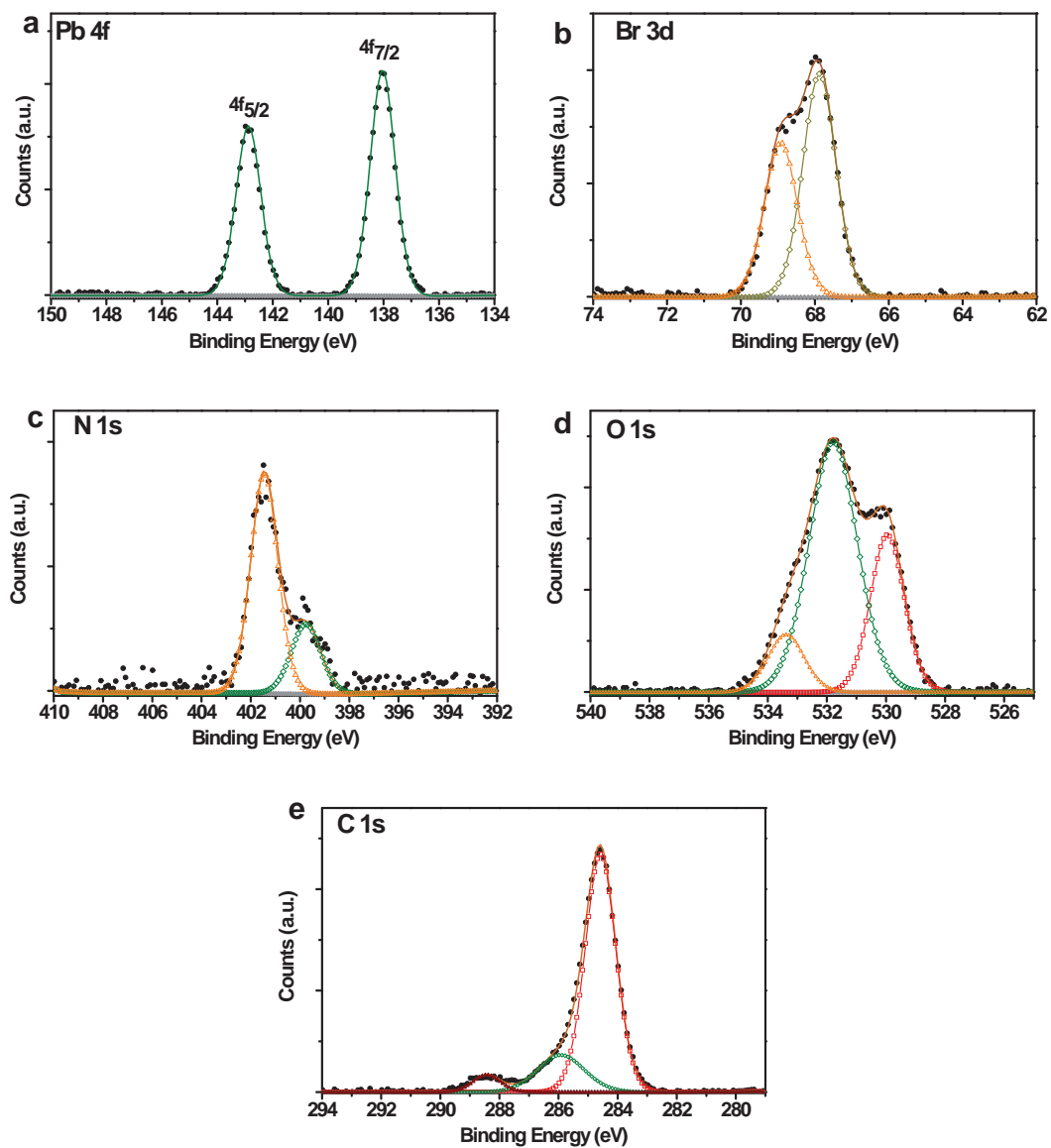


Figure S4. XPS spectra corresponding to: a) Pb 4f; b) Br 3d; c) N 1s; d) O 1s and e) C 1s of P₂ADA-propanoic nanoparticles.

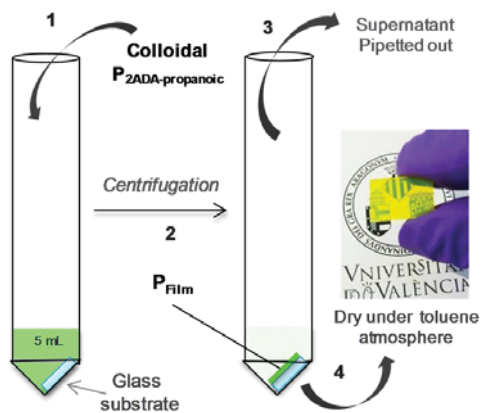


Figure S5. Schematic representation of the centrifugal casting method used for film preparation.

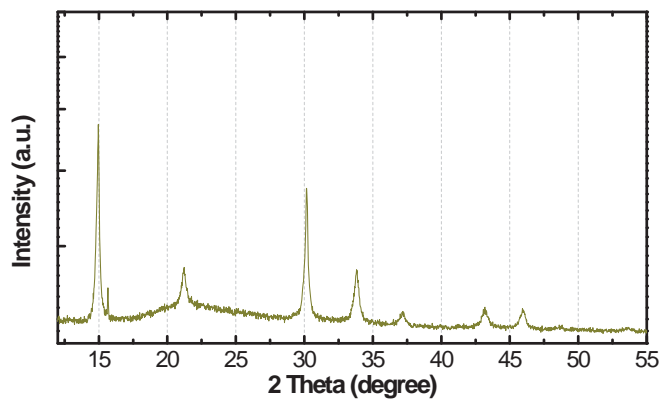


Figure S6. X-ray diffraction of P₂ADA-propanoic NP solid film



Colloids of Naked $\text{CH}_3\text{NH}_3\text{PbBr}_3$ Perovskite Nanoparticles: Synthesis, Stability, and Thin Solid Film Deposition

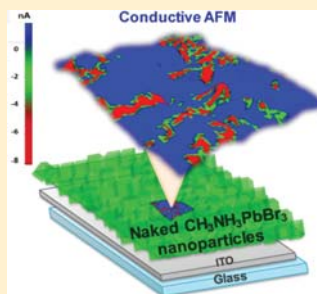
Soranyel Gonzalez-Carrero,[†] Luciana C. Schmidt,^{†,‡} Ignacio Rosa-Pardo,[†] Laura Martínez-Sarti,[†] Michele Sessolo,[†] Raquel E. Galian,^{*,†,§} and Julia Pérez-Prieto^{*,†,§}

[†]ICMOL, Institute of Molecular Science, Universidad de Valencia, Catedrático José Beltrán 2, 46980 Paterna, Valencia, Spain

[‡]INFIQC (UNC-CONICET), Dpto. Química Orgánica, Facultad de Ciencias Químicas, Universidad Nacional de Córdoba, Ciudad Universitaria, X5000HUA Córdoba, Argentina

Supporting Information

ABSTRACT: A novel preparation of lead halide, $\text{CH}_3\text{NH}_3\text{PbBr}_3$, perovskite nanoparticle solid films from colloidal “naked” nanoparticles, that is, dispersible nanoparticles without any surfactant, is reported. The colloids are obtained by simply adding potassium ions, whose counterions are both more lipophilic and less coordinating than bromide ions, to the perovskite precursor solutions ($\text{CH}_3\text{NH}_3\text{Br}/\text{PbBr}_2$ in dimethylformamide) following the reprecipitation strategy. The naked nanoparticles exhibit a low tendency to aggregate in solution, and they effectively self-assembled on a substrate by centrifugation of the colloid, leading to homogeneous nanoparticle solid films with arbitrary thickness. These results are expected to spur further the interest in lead halide perovskites due to the new opportunities offered by these films.



INTRODUCTION

Lead halide perovskites, with the general chemical formula APbX_3 , where A is an organic or inorganic monovalent cation—in particular methylammonium (CH_3NH_3^+ , MA), formamidinium ($\text{HC}(\text{NH}_2)_2^+$), and Cs^+ —and X is the halide anion (Cl^- , Br^- , or I^-), have been extensively studied mainly due to their exceptional optoelectronic properties.^{1–5} These are attractive materials because of their ease of processability for mass production, such as the preparation of conductive films from solutions of perovskite precursors. This strategy can produce some weaknesses in the end product (polycrystallinity, structural, and chemical defects) and often suffers from a lack of reproducibility of the film morphology.

Therefore, there is a great interest in the direct film preparation from colloidal perovskite nanoparticles (NPs), aimed at high reproducibility of the film morphology as well as improvement of their optoelectronic properties. There are important challenges to be overcome for achieving those goals in the case of lead halide perovskites: the preparation of organic ligand-free perovskite NPs with a low tendency to aggregate in solution and the efficient self-assembling of the perovskite NPs on a substrate to lead to conductive NP solid films with controlled thicknesses.

$\text{CH}_3\text{NH}_3\text{PbBr}_3$ colloids were first reported in 2014, by using medium and long alkylammonium bromide as the organic capping to confine the material to the nanometer scale and enable their dispersibility in low-to-medium polar organic solvents.⁶ Since then, the variations in their preparation, use of other ammonium bromides, ammonium carboxylates, instead

of ammonium bromides, and different molar ratios between the reagents have provided high control on their crystallization, composition, shape, size, and, consequently, on their optical performance.^{7–15}

The passivation of the perovskite nanoparticles with organic ligands hampers the preparation of conductive thin films, and consequently there is an increasing interest in developing strategies for synthesizing stable “naked” colloidal nanoparticles. The synthesis of organic ligand-free $\text{CH}_3\text{NH}_3\text{PbX}_3$ colloids is challenging. An interesting two-step approach has recently been reported to prepare $\text{CH}_3\text{NH}_3\text{PbX}_3$ (X = Br, I, and mixture of them) colloids of 100 nm to 1 μm , depending on the nature of X. It consisted of the mixing of PbX_2 NPs of tens of nanometers (prepared by laser ablation) with isopropanol solutions of $\text{CH}_3\text{NH}_3\text{X}$ under vigorous sonication and mild heating.¹⁶ The detection in the PbX_2 NPs of excess of halide as well as carbon material, derived from the solvent (iodobenzene or bromobenzene) decomposition under laser ablation, was suggested to be responsible for the confinement of the PbX_2 material to the nanometer scale.¹⁷ Whereas the carbon materials did not prevent the formation of the hybrid perovskite after addition of the methylammonium halide, the nanoparticle size drastically increased and perovskite particles of hundreds of nanometers were formed.

Received: December 23, 2017

Accepted: January 19, 2018

Published: January 30, 2018

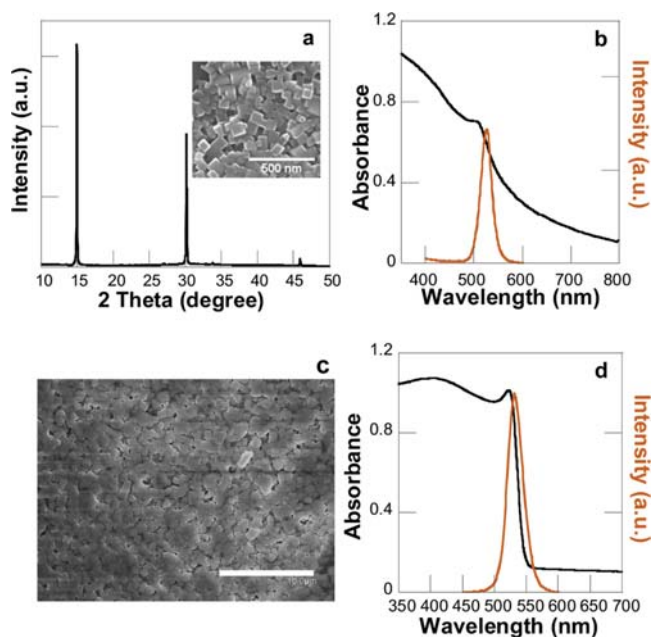


Figure 1. (a) PXRD of MAP@K NPs deposited on quartz revealing its (001) orientation; inset: SEM image of MAP@K NP solid (scale bar: 500 nm). (b) Absorption and emission spectra of MAP@K colloid in ethyl acetate. (c) SEM image of MAP@K_{F3} (scale bar: 10 μm). (d) Absorption and emission spectra of MAP@K_{F3}.

Our aim was to use a simple, one-step procedure to prepare naked CH₃NH₃PbBr₃ colloidal NPs and assemble them in conductive thin films. We devised that the colloids could be directly prepared by using inorganic salts as the confinement agents. We report here an easy preparation method of naked CH₃NH₃PbBr₃ NPs by simply using an excess of CH₃NH₃Br in the perovskite precursor solutions (CH₃NH₃Br/PbBr₂ in dimethylformamide (DMF)) and a potassium salt, whose counterion is both more lipophilic and less coordinating than that of the bromide (specifically, hexafluorophosphate anion PF₆⁻). The purpose was to replace the excess of CH₃NH₃⁺ at the CH₃NH₃PbBr₃ NP surface with K⁺ on the basis of the higher enthalpy formation of KBr than that of CH₃NH₃Br (-394 vs. -259 kJ/mol), with the final aim of producing confined and stable NPs.^{18,19} The NPs self-assembled on a substrate under centrifugation of the colloids to lead to homogeneous and conductive NP films.

RESULTS AND DISCUSSION

The colloidal CH₃NH₃PbBr₃ methylammonium bromide (MAP) NPs were prepared by using the reprecipitation strategy.^{9,11} In brief, a mixture of CH₃NH₃Br, KPF₆, and PbBr₂ in DMF (2:2:1 CH₃NH₃Br/KPF₆/PbBr₂ molar ratio) was used as the precursor solution. An aliquot of this solution was added dropwise to a moderately polar solvent (ethyl acetate) under vigorous stirring to lead to a yellowish dispersion (see details in the [Materials and Methods](#)). After centrifugation, a luminescent yellow solid was separated and was redispersed in ethyl acetate. The colloid was considerably stable and took about 3 h for the complete precipitation of NPs, which were easily redispersed by manual shaking.

To determine the components of the NPs, both the solid and the residual material after solvent evaporation of the supernatant were dissolved in dimethyl sulfoxide (which reverted the perovskite back into its precursors) and they were analyzed by ¹⁹F NMR and ¹H NMR ([Figures S1 and S2](#)). ¹⁹F NMR spectra showed that all of the PF₆⁻ anions were in the supernatant in the form of two different salts. This was consistent with the presence of KPF₆ and CH₃NH₃PF₆ in the supernatant; in fact, the ¹H NMR spectrum of the supernatant showed signals ascribed to the CH₃NH₃⁺ cation.

The powder X-ray diffraction (PXRD) pattern of MAP, [Figure 1a](#), deposited on quartz by a centrifugal strategy²⁰ (see details below) confirmed the exclusive formation of cubic CH₃NH₃PbBr₃ NPs with lattice diffraction peaks at 14.9, 30.1, and 45.9° (weak), which can be assigned to the (001), (002), and (003) crystallographic peaks; thus, the film displayed (001) exclusive orientation.^{21–24} The estimated crystallite size, calculated by Debye–Scherrer equation, was 69 ± 2 nm. The morphology of MAP was studied by scanning electron microscopy (SEM); the images showed the formation of cubic NPs (inset [Figure 1a](#)). The energy dispersive X-ray spectrum ([Figure S3](#)) of the MAP deposited on glass demonstrated the presence of K in the perovskite material, and a K/Pb/Br molar ratio of 0.5:1:3.4 was calculated. Therefore, the perovskite is capped with KBr.

The absorption and emission spectra of the colloidal MAP NPs in ethyl acetate ([Figure 1b](#)) exhibited features of confined material. Thus, the absorption and emission peaks were at about 505 and 525 nm (full-width at half maximum, fwhm = 28 nm), respectively, considerably blue shifted compared to those of bulk CH₃NH₃PbBr₃ (absorption peak at about 540 nm).

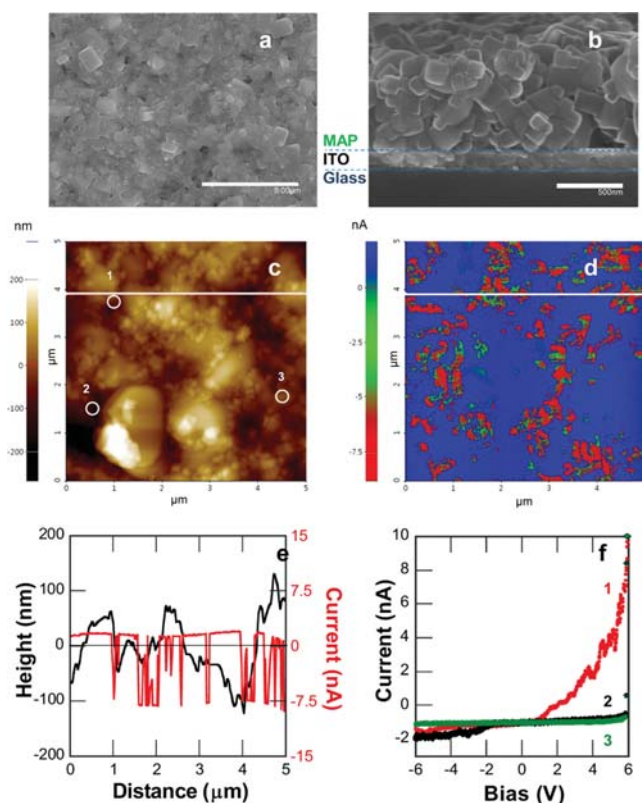


Figure 2. (a) Top and (b) cross-sectional SEM image of MAP@K_{F4} (scale bar 5 μ m and 500 nm, respectively). (c, d) Topographical and conductive AFM images of MAP@K_{F4} (bias = -1.5 V); image scale 5 μ m \times 5 μ m. (e) Cross-sectional profile of height and current along the white line in images (c) and (d). (f) I - V curve as a function of applied bias (+6 to -6 V) under dark conditions for grains marked in the topographic AFM image c.

The UV-visible maximum at 505 nm was attributed to the exciton peak of the colloidal nanoparticles, whereas the absorption observed above 550 nm could correspond to the scattering of different-sized colloidal aggregates present in solution and absent in the solid film.^{11,25} These data corroborated that K⁺ was on the nanoparticle surface; otherwise, the partial substitution of CH₃NH₃⁺ for K⁺ in the crystal structure would provoke a shift in the absorption peak to the UV, among other changes.²⁶ Consequently, these perovskite NPs were termed MAP@K NPs and used for solid film preparation.

The formation of luminescent MAP@K colloids was also observed when using toluene and chlorobenzene in their preparation instead of ethyl acetate (emission peaks at ca. 527 and 525 nm for toluene and chlorobenzene, respectively, Figure S4). However, the NPs remained dispersible for a shorter time (less than 1 h). Therefore, only the stable colloid in ethyl acetate was fully characterized. Photoluminescence (PL) of the MAP@K colloid in ethyl acetate exhibited a quantum yield (Φ_{PL}) of 17% and an average lifetime (τ_{av}) of 29 ns, with a short-lived component of τ_1 3.4 ns (79%) and a long-lived component of τ_2 38 ns (21%).

Control studies were performed to gain further insight into the role of K⁺ in the stability of the MAP@K NPs. The synthesis of MAP colloids was carried out in the absence of KPF₆ under the same experimental conditions. An orange colloidal dispersion, probably assisted by the excess of MA (MA/PbBr₂, 2:1), was obtained, but it exhibited a high tendency to precipitate. After centrifugation, the orange pellet could hardly be redispersed in ethyl acetate. In fact, the colloid was stable for just 5 min, and the pellet precipitate was observed at the bottom of the tube (Figure S5). The absorption spectra of the MAP dispersion showed a poor absorption band and high scattering; these features are typical of bulk MAP material prepared using 1:1 MA/PbBr₂ molar ratio in the absence of organic ligands.⁶ These data demonstrated that K⁺ participated in the stabilization of the hybrid MAP@K NPs, providing considerably stable colloids in a medium polar solvent and preventing the collapse of NPs.

Attempts to prepare densely packed perovskite nanoparticle solid films from the ethyl acetate MAP@K colloid were addressed by using the centrifugal casting method.²⁰ Briefly, freshly prepared MAP@K colloids in ethyl acetate were added to a centrifugal tube with a glass substrate at the bottom, and the sample was centrifuged for 7 min. Then, the supernatant

was pipetted out and the MAP@K NP solid film on the glass substrate (MAP@K_{F1}; see further details in the [Materials and Methods](#)) was allowed to dry at room temperature under ethyl acetate atmosphere. The SEM images showed that the film coverage of the glass substrate was incomplete. Increase of the particle concentration did not result in complete substrate coverage (see MAP@K_{F2} in [Figure S6](#) and details in the [Materials and Methods](#)). Interestingly, a complete coverage of the glass substrate was obtained by using a mixture of ethyl acetate and toluene in the centrifugation step; see the SEM image of the film, MAP@K_{F3}, in [Figure 1c](#). The film showed an absorption peak at 526 nm and a narrow and slightly red-shifted emission peak at 530 nm (fwhm = 30 nm) compared to that of the MAP@K colloid in ethyl acetate ([Figure 1b](#)). The film showed a Φ_{PL} of 7% and a τ_{av} of 97 ns, which fit to three components (τ_1 8.1 ns (60%), τ_2 40.2 ns (31%), and τ_3 170.5 ns (9%)).²⁷

The colloidal dispersion and solid film prepared from MAP@K were stable for at least 1 month when stored in closed-amber vials.

Conductive atomic force microscopy (c-AFM) measurements were carried out in the dark using the PinPoint conductive mode to study the local electronic properties and morphology of an MAP@K NP solid film prepared by centrifugal casting on indium tin oxide (ITO)²⁰-coated glass (termed MAP@K_{F4}). [Figure 2a,b](#) shows the top and cross-sectional SEM images of MAP@K_{F4} and demonstrates the formation of a densely packed nanoparticle solid film of 881 ± 78 nm thickness (see the [Materials and Methods](#) and [Figure S7](#) for further details).

The topographical image (area of $25 \mu\text{m}^2$) of MAP@K_{F4}, [Figure 2c](#), showed protrusions and depressions in the range of +100 to -100 nm (average roughness of 75 nm). The contrast c-AFM image ([Figure 2d](#)) revealed a spatial distribution of high and low current magnitude regions, represented in red and blue, respectively. The cross-sectional profile image of height and current along the white line in the topographic and current AFM image ([Figure 2e](#)) exhibits high magnitude current domains, between -8.4 and 2.1 nA (average current magnitude -0.447 nA). The c-AFM measurement showed that the vertical current transport was heterogeneous on the nanometer scale, as reported in c-AFM studies of $\text{CH}_3\text{NH}_3\text{PbX}_3$ films prepared by spin-coating the solution of perovskite precursors.^{28–30} Remarkably, the conductivity observed in MAP@K_{F4} was of high magnitude.

The local dark current versus bias (I - V) of MAP@K_{F4} ([Figure 2d](#)) was measured at specific locations from the topographic AFM image, identified as round marks in [Figure 2c](#) (bias at 6 to -6 V). The local I - V response exhibits a diode behavior, previously observed for millimeter-sized MAPbBr₃ crystals.^{31,32} Thus, a linear ohmic region at low voltages, where the traps are partially filled; a step-up in current at intermediate voltages, where the traps are filled with injected carriers; and an abrupt increase in current at high voltages, where the carriers move freely, were observed (see curve 1 in [Figure 2f](#)). The high conductive domains may be attributed to high-density regions of NPs dispersed in the film with an effective electrical connectivity between them. The charge transport was further investigated at a larger scale by depositing the NP films onto interdigitated indium tin oxide²⁰ electrodes, with an electrode gap of $20 \mu\text{m}$ ([Figure S8a](#)). The current density versus voltage (J - V) curve in the dark shows current injection in both reverse and forward bias, with current up to 100 nA at voltages as low

as 5 V. The transport properties are comparable to those of a polycrystalline MAPbBr₃ film obtained by direct spin-coating of the precursor solution ([Figure S8b](#)). Interestingly, when measuring the sample under 1 sun illumination, we observed an increase in the current (up to 5 \times) and a shift in the J - V curve toward positive bias. The latter effect might originate from a separation of the photogenerated electron-hole pairs. However, considering that the device lacks charge selective contacts and that no photovoltage can be observed under illumination, the shift in the J - V characteristics is probably due to the intrinsic photoconductivity of the perovskite film.

CONCLUSIONS

In summary, we present here an easy preparation method of colloidal stable naked $\text{CH}_3\text{NH}_3\text{PbBr}_3$ perovskites by adding a potassium salt to the solution of perovskite precursors. The K⁺ cations on the NP surface stabilize the nanomaterial and the colloid and enable the efficient assembly of nanoparticles on substrates to lead to densely packed, semiconducting nanoparticle solid films.

MATERIALS AND METHODS

Materials. Lead bromide (99.999%), methylamine (40% in water), potassium hexafluorophosphate ($\geq 99\%$), bromidic acid, and the solvents used were purchased from Sigma-Aldrich and used as received. Methylammonium bromide ($\text{CH}_3\text{NH}_3\text{Br}$) was synthesized by reaction of the corresponding amine in water/HBr.

Synthesis of Colloidal MAP@K. The precursor solution was prepared by mixing PbBr₂ (25 mg, 0.068 mmol), MABr (15.3 mg, 0.14 mmol), and KPF₆ (25 mg, 0.14 mmol) in 2.5 mL of dimethylformamide. The molar ratio between the components PbBr₂/MABr/KPF₆ was 1:2:2. Then, 100 μL was added dropwise into 10 mL of ethyl acetate under vigorous stirring. Immediately after, the yellowish reaction was centrifuged at 7000 rpm for 7 min. The supernatant was discarded, and the precipitate was redispersed in 5 mL of ethyl acetate.

Preparation of MAP@K_{F1} NP Solid Film. Colloidal MAP@K used for the preparation of NP solid films was prepared following the above-mentioned method. The precursor solution was prepared mixing PbBr₂ (25 mg, 0.068 mmol), MABr (15.3 mg, 0.14 mmol), and KPF₆ (25 mg, 0.14 mmol) in 2.5 mL of dimethylformamide. An aliquot, specifically 100 μL , of this solution was added dropwise into 10 mL of ethyl acetate under vigorous stirring.

Then, the MAP@K colloid (10 mL) was added to a conical centrifuge tube (50 mL), which had the glass slide substrate at its bottom, and the mixture was centrifuged for 7 min at 8000 rpm. Finally, the supernatant was pipetted out and the glass substrate with the deposited MAP@K was allowed to dry in ethyl acetate atmosphere, at room temperature.

Preparation of MAP@K_{F2}. The NP solid film was prepared following the method described above for MAP@K_{F1} but using a mixture of two MAP@K colloids (10 mL each).

Preparation of MAP@K_{F3}. The NP solid film was prepared following the above-mentioned method for MAP@K_{F2} but adding 10 mL of toluene to 20 mL of MAP@K colloid before the centrifugation step.

Preparation of MAP@K_{F4}. The NP solid film was prepared following the above-mentioned method for MAP@K_{F3} but using an ITO-glass-coated substrate.

The glass substrates used were cleaned ultrasonically in water-soap, demineralized water, and 2-propanol baths. Then, they were dried under nitrogen and immediately placed into a conic centrifugal tube. Centrifugation was carried out in an Eppendorf Centrifuge 5804 R.

Preparation of Polycrystalline MAPbBr₃. The precursor solution was prepared mixing PbBr₂ and MABr (1:2 ratio, respectively) in dimethylformamide to a total concentration of 100 mg/mL. The solution was spin-coated at 3000 rpm for 60 s. The as-prepared layers were annealed on a hot plate at 90 °C for 30 min in a nitrogen atmosphere glovebox.

Optical Measurement. UV–visible spectra of the samples were recorded using a quartz cuvette in a UV–visible spectrophotometer secoman Uvi Ligh XT5. The UV–vis spectra of NP solid films were recorded in a JASCO V-670 spectrometer with a horizontal integrating sphere (PIV-757). Steady-state PL spectra were measured on an Amnicon Browman series 2 Luminescence spectrometer, equipped with a xenon lamp (150 W). AB2 software (version 5.5) was used to register the data. The photoluminescence (PL) quantum yields of colloidal MAP@K (in ethyl acetate) and film were measured using a Hamamatsu C9920-02 absolute PL quantum yield measurement system with monochromatic light source (150 W) and integrating sphere. All of the data were acquired using 1 cm × 1 cm path length quartz cuvettes, at room temperature, using an excitation wavelength of 365 nm.

PL decays were measured using a Compact fluorescence lifetime spectrometer C11367, Quantaaurus-Tau. Fluorescence lifetime software U11487 was used to register the data. All of the data of PL decay of perovskite dispersed in ethyl acetate were acquired using 1 cm × 1 cm path length quartz cuvettes and light-emitting diode excitation wavelength of 365 nm. The PL decays of colloidal perovskite nanoparticles were fitted with a triexponential function. The average lifetimes (τ_{av}) were calculated as $\tau_{av} = \sum A_i \tau_i^2 / \sum A_i \tau_i$ where τ_i are the decay times and A_i represents the amplitudes of the components, values obtained from the fitted PL kinetic decay traces.

Morphology Characterization. The layer thickness was determined with a mechanical profilometer (Ambios XP-1). Scanning electron microscope²⁹ images of NP solid films were obtained using a HITACHI S-4800 with a spotlight of field emission gun. Images were acquired at 20 kV. Elemental analysis was performed on HITACHI S-4800 equipped with XFlash 5030 Bruker detector and acquisition software QUANTAX 400. The PXRD analyses of NP solid films were performed in powder diffractometer D8 Advance A25 model Bruker, with a powder diffractometer θ – θ configuration, and X-ray tubes on a lineal receiver Cu radiation. Plus DIFFRAC EVA Data assessment program was used to register the data. The diffracted intensities were recorded at room temperature from 5 to 80° 2 θ angles (step size of 0.02°).

Conductive Atomic Force Microscopy (c-AFM). The topographic, current mapping, and I – V measurements of NP solid film, MAP@K_{F4}, were registered in dark and at room temperature, in atomic force microscope Park Systems NX20, equipped with Pt–Ir-coated Si tips (CONTSCPt, diameter 7 nm) and using PinPoint conductive mode. The gentle PinPoint mode allowed acquiring reproducible and reliable topography and c-AFM images of the MAP@K_{F4} film surface, instead of contact mode. This PinPoint mode operates in an approach–retract manner. Experimentally, the tip was approached over a period of 2 ms to achieve an interaction force of 0.24 nN; the force was held constant while the current was registered (2

times) at 17 kHz. Then, the tip retracted over a period of 2 ms and moved to the next pixel, Figure S7. The control height (set to 0.15 μ m) at constant force was also recorded to generate a simultaneous topographic image. Different voltage biases were applied (from ± 1.5 to ± 5.5 V) using a scan rate of 0.23 Hz. The PinPoint mode is significantly different from the tapping mode because the contact mode tip used is not oscillating and the tip retracts and approaches each pixel rather than adjusting the tip height to maintain a constant oscillation amplitude, resulting in highly reproducible images. The current is measured directly after the tip using a preamplifier with a gain of 1011 V/A (ULCA). Data acquisition was carried out using SmartScan software (version 1.0) and XEI Data Processing and Analysis software (version 4.3.0) Build2 (Park Systems Corp). The NX20 equipment is supported by active vibration isolation system model AVI-200S/LP (Table Stable Ltd). The I – V images were performed using a current compliance of 10 nA and sample bias from +6 to –6 V with a period of 1.0 s.

Lateral Transport Measurements. The substrates used for these measurements were prepatterned interdigitated ITO electrodes (Naranjosubstrates) coated on glass. The current density–voltage (J – V) characteristics were obtained using a Keithley 2400 source measure unit. The electrical characterization was performed in the dark and under illumination using a solar simulator by Abet Technologies (model 10500 with an AM1.5G xenon lamp as the light source). The current density was calculated taking into account the channel width and film thickness.

■ ASSOCIATED CONTENT

5 Supporting Information

The Supporting Information is available free of charge on the ACS Publications website at DOI: 10.1021/acsomega.7b02052.

Additional information: NMR, absorption and emission spectra, SEM images, energy dispersive X-ray spectroscopy analysis, and J – V curve measurements (PDF)

■ AUTHOR INFORMATION

Corresponding Authors

*E-mail: raquel.galian@uv.es (R.E.G.).

*E-mail: julia.perez@uv.es (J.P.-P.).

ORCID

Soranyel Gonzalez-Carrero: 0000-0003-2430-4458

Luciana C. Schmidt: 0000-0001-7059-3938

Michele Sessolo: 0000-0002-9189-3005

Raquel E. Galian: 0000-0001-8703-4403

Julia Pérez-Prieto: 0000-0002-5833-341X

Notes

The authors declare no competing financial interest.

■ ACKNOWLEDGMENTS

We thank MINECO (CTQ2014-60174 cofinanced with FEDER funds, Maria de Maeztu: MDM-2015-0538; predoctoral grants to S.G.-C. and L.M.-S.; RyC grant to M.S.) for financial support. We also thank the Centro de Instrumentación Científica (CIC) of University of Granada for technical support in the c-AFM measurement using Park System equipment.

REFERENCES

- (1) Kojima, A.; Teshima, K.; Shirai, Y.; Miyasaka, T. Organometal Halide Perovskites as Visible-Light Sensitizers for Photovoltaic Cells. *J. Am. Chem. Soc.* **2009**, *131*, 6050–6051.
- (2) Lee, M. M.; Teuscher, J.; Miyasaka, T.; Murakami, T. N.; Snaith, H. J. Efficient Hybrid Solar Cells Based on Meso-Superstructured Organometal Halide Perovskites. *Science* **2012**, *338*, 643–647.
- (3) González-Carrero, S.; Galian, R. E.; Pérez-Prieto, J. Organometal Halide Perovskites: Bulk Low-Dimension Materials and Nanoparticles. *Part. Part. Syst. Charact.* **2015**, *32*, 709–720.
- (4) Manser, J. S.; Christians, J. A.; Kamat, P. V. Intriguing Optoelectronic Properties of Metal Halide Perovskites. *Chem. Rev.* **2016**, *116*, 12956–13008.
- (5) Fu, A.; Yang, P. Organic-inorganic perovskites: Lower threshold for nanowire lasers. *Nat. Mater.* **2015**, *14*, 557–558.
- (6) Schmidt, L. C.; Pertegás, A.; González-Carrero, S.; Malinkiewicz, O.; Agouram, S.; Mínguez Espallargas, G.; Bolink, H. J.; Galian, R. E.; Pérez-Prieto, J. Nontemplate Synthesis of $\text{CH}_3\text{NH}_3\text{PbBr}_3$ Perovskite Nanoparticles. *J. Am. Chem. Soc.* **2014**, *136*, 850–853.
- (7) Gonzalez-Carrero, S.; Galian, R. E.; Perez-Prieto, J. Maximizing the emissive properties of $\text{CH}_3\text{NH}_3\text{PbBr}_3$ perovskite nanoparticles. *J. Mater. Chem. A* **2015**, *3*, 9187–9193.
- (8) Zhang, F.; Zhong, H.; Chen, C.; Wu, X.-g.; Hu, X.; Huang, H.; Han, J.; Zou, B.; Dong, Y. Brightly Luminescent and Color-Tunable Colloidal $\text{CH}_3\text{NH}_3\text{PbX}_3$ ($X = \text{Br}, \text{I}, \text{Cl}$) Quantum Dots: Potential Alternatives for Display Technology. *ACS Nano* **2015**, *9*, 4533–4542.
- (9) Huang, H.; Susha, A. S.; Kershaw, S. V.; Hung, T. F.; Rogach, A. L. Control of Emission Color of High Quantum Yield $\text{CH}_3\text{NH}_3\text{PbBr}_3$ Perovskite Quantum Dots by Precipitation Temperature. *Adv. Sci.* **2015**, *2*, No. 1500194.
- (10) Huang, H.; Polavarapu, L.; Sichert, J. A.; Susha, A. S.; Urban, A. S.; Rogach, A. L. Colloidal lead halide perovskite nanocrystals: synthesis, optical properties and applications. *NPG Asia Mater.* **2016**, *8*, No. e328.
- (11) Gonzalez-Carrero, S.; Francés-Soriano, L.; González-Béjar, M.; Agouram, S.; Galian, R. E.; Pérez-Prieto, J. The Luminescence of $\text{CH}_3\text{NH}_3\text{PbBr}_3$ Perovskite Nanoparticles Crests the Summit and Their Photostability under Wet Conditions is Enhanced. *Small* **2016**, *12*, 5245–5250.
- (12) Vybornyi, O.; Yakunin, S.; Kovalenko, M. V. Polar-solvent-free colloidal synthesis of highly luminescent alkylammonium lead halide perovskite nanocrystals. *Nanoscale* **2016**, *8*, 6278–6283.
- (13) Levchuk, I.; Osvet, A.; Tang, X.; Brandl, M.; Perea, J. D.; Hoegl, F.; Matt, G. J.; Hock, R.; Batentschuk, M.; Brabec, C. J. Correction to Brightly Luminescent and Color-Tunable Formamidinium Lead Halide Perovskite FAPbX_3 ($X = \text{Cl}, \text{Br}, \text{I}$) Colloidal Nanocrystals. *Nano Lett.* **2017**, *17*, 3993.
- (14) Lu, C.-H.; Hu, J.; Shih, W. Y.; Shih, W.-H. Control of morphology, photoluminescence, and stability of colloidal methylammonium lead bromide nanocrystals by oleylamine capping molecules. *J. Colloid Interface Sci.* **2016**, *484*, 17–23.
- (15) Teunis, M. B.; Johnson, M. A.; Muhoberac, B. B.; Seifert, S.; Sardar, R. Programmable Colloidal Approach to Hierarchical Structures of Methylammonium Lead Bromide Perovskite Nanocrystals with Bright Photoluminescent Properties. *Chem. Mater.* **2017**, *29*, 3526–3537.
- (16) Lamberti, F.; Litti, L.; De Bastiani, M.; Sorrentino, R.; Gandini, M.; Meneghetti, M.; Petrozza, A. High-Quality, Ligands-Free, Mixed-Halide Perovskite Nanocrystals Inks for Optoelectronic Applications. *Adv. Energy Mater.* **2017**, *7*, No. 1601703.
- (17) Amendola, V.; Polizzi, S.; Meneghetti, M. Laser Ablation Synthesis of Gold Nanoparticles in Organic Solvents. *J. Phys. Chem. B* **2006**, *110*, 7232–7237.
- (18) Pedley, J. B. *Thermochemical Data and Structures of Organic Compounds*. Thermodynamics Research Center: College Station, TX, 1994.
- (19) Lide, D. R. *CRC Handbook of Chemistry and Physics*, 85th ed.; Taylor & Francis, 2004.
- (20) Kim, J. Y.; Adinolfi, V.; Sutherland, B. R.; Voznyy, O.; Kwon, S. J.; Kim, T. W.; Kim, J.; Ihee, H.; Kemp, K.; Adachi, M.; Yuan, M.; Kramer, I.; Zhitomirsky, D.; Hoogland, S.; Sargent, E. H. Single-step fabrication of quantum funnels via centrifugal colloidal casting of nanoparticle films. *Nat. Commun.* **2015**, *6*, No. 7772.
- (21) Chen, F.; Zhu, C.; Xu, C.; Fan, P.; Qin, F.; Gowri Manohari, A.; Lu, J.; Shi, Z.; Xu, Q.; Pan, A. Crystal structure and electron transition underlying photoluminescence of methylammonium lead bromide perovskites. *J. Mater. Chem. C* **2017**, *5*, 7739–7745.
- (22) Baikie, T.; Barrow, N. S.; Fang, Y.; Keenan, P. J.; Slater, P. R.; Piltz, R. O.; Gutmann, M.; Mhaisalkar, S. G.; White, T. J. A combined single crystal neutron/X-ray diffraction and solid-state nuclear magnetic resonance study of the hybrid perovskites $\text{CH}_3\text{NH}_3\text{PbX}_3$ ($X = \text{I}, \text{Br}$ and Cl). *J. Mater. Chem. A* **2015**, *3*, 9298–9307.
- (23) Peng, W.; Wang, L.; Murali, B.; Ho, K.-T.; Bera, A.; Cho, N.; Kang, C.-F.; Burlakov, V. M.; Pan, J.; Sinatra, L.; Ma, C.; Xu, W.; Shi, D.; Alarousu, E.; Goriely, A.; He, J.-H.; Mohammed, O. F.; Wu, T.; Bakr, O. M. Solution-Grown Monocrystalline Hybrid Perovskite Films for Hole-Transporter-Free Solar Cells. *Adv. Mater.* **2016**, *28*, 3383–3390.
- (24) Zhang, Z.-Y.; Wang, H.-Y.; Zhang, Y.-X.; Li, K.-J.; Zhan, X.-P.; Gao, B.-R.; Chen, Q.-D.; Sun, H.-B. Size-dependent one-photon- and two-photon-pumped amplified spontaneous emission from organometal halide $\text{CH}_3\text{NH}_3\text{PbBr}_3$ perovskite cubic microcrystals. *Phys. Chem. Chem. Phys.* **2017**, *19*, 2217–2224.
- (25) Chirvony, V. S.; González-Carrero, S.; Suárez, I.; Galian, R. E.; Sessolo, M.; Bolink, H. J.; Martínez-Pastor, J. P.; Pérez-Prieto, J. Delayed Luminescence in Lead Halide Perovskite Nanocrystals. *J. Phys. Chem. C* **2017**, *121*, 13381–13390.
- (26) Tarasova, A. Y.; Isaenko, L. I.; Kesler, V. G.; Pashkov, V. M.; Yeliseyev, A. P.; Denysyuk, N. M.; Khyzhun, O. Y. Electronic structure and fundamental absorption edges of KPb_2Br_5 , $\text{K}_0.5\text{Rb}_0.5\text{Pb}_2\text{Br}_5$, and RbPb_2Br_5 single crystals. *J. Phys. Chem. Solids* **2012**, *73*, 674–682.
- (27) Zhang, X.; Liu, H.; Wang, W.; Zhang, J.; Xu, B.; Karen, K. L.; Zheng, Y.; Liu, S.; Chen, S.; Wang, K.; Sun, X. W. Hybrid Perovskite Light-Emitting Diodes Based on Perovskite Nanocrystals with Organic-Inorganic Mixed Cations. *Adv. Mater.* **2017**, *29*, No. 1606405.
- (28) Moerman, D.; Eperon, G. E.; Precht, J. T.; Ginger, D. S. Correlating Photoluminescence Heterogeneity with Local Electronic Properties in Methylammonium Lead Tribromide Perovskite Thin Films. *Chem. Mater.* **2017**, *29*, 5484–5492.
- (29) Kutes, Y.; Zhou, Y.; Bosse, J. L.; Steffes, J.; Pature, N. P.; Huey, B. D. Mapping the Photoresponse of $\text{CH}_3\text{NH}_3\text{PbI}_3$ Hybrid Perovskite Thin Films at the Nanoscale. *Nano Lett.* **2016**, *16*, 3434–3441.
- (30) Lee, B.; Lee, S.; Cho, D.; Kim, J.; Hwang, T.; Kim, K. H.; Hong, S.; Moon, T.; Park, B. Evaluating the Optoelectronic Quality of Hybrid Perovskites by Conductive Atomic Force Microscopy with Noise Spectroscopy. *ACS Appl. Mater. Interfaces* **2016**, *8*, 30985–30991.
- (31) Shi, D.; Adinolfi, V.; Comin, R.; Yuan, M.; Alarousu, E.; Buin, A.; Chen, Y.; Hoogland, S.; Rothenberger, A.; Katsiev, K.; Losovyj, Y.; Zhang, X.; Dowben, P. A.; Mohammed, O. F.; Sargent, E. H.; Bakr, O. M. Low trap-state density and long carrier diffusion in organolead trihalide perovskite single crystals. *Science* **2015**, *347*, 519.
- (32) Yang, K.; Li, F.; Veeramalai, C. P.; Guo, T. A facile synthesis of $\text{CH}_3\text{NH}_3\text{PbBr}_3$ perovskite quantum dots and their application in flexible nonvolatile memory. *Appl. Phys. Lett.* **2017**, *110*, No. 083102.

Supporting Information

Colloids of naked $\text{CH}_3\text{NH}_3\text{PbBr}_3$ perovskite nanoparticles: synthesis, stability and thin solid film deposition

Soranyel Gonzalez-Carrero[†] Luciana C. Schmidt,^{†,‡} Ignacio Rosa-Pardo,[†] Laura Martinez-Sarti,[†] Michele Sessolo,[†] Raquel E. Galian^{†,*} and Julia Pérez-Prieto^{†,*}

Figure S1. ^{19}F NMR spectra of MAP@K NPs (a), supernatant (b) and KPF_6 (c) in deuterated DMSO.	S2
Figure S2. ^1H NMR spectra of MAP@K (a) and supernatant (b) in deuterated DMSO. The signal marked with an asterisk corresponds to CH_3 signals of CH_3NH_3^+ .	S3
Figure S3. Energy dispersive X-ray spectrum of MAP@K NP solid film.	S4
Figure S4. Absorption and emission spectra of colloidal MAP@K NPs synthesized in toluene (a) and chlorobenzene (b).	S5
Figure S5. (a) Absorption spectra of colloidal MAP@K and MAP bulk in ethyl acetate. Photos of colloidal MAP@K (yellow) and MAP bulk (orange) dispersions taken immediately (b) and 5 minutes (c) after their redispersion in ethyl acetate.	S6
Figure S6. SEM images of MAP@K _{F1} (a) and MAP@K _{F2} (b). Scale bar 10 μm .	S7
Figure S7. Simplified diagram of conductive AFM in PinPoint conductive mode.	S8
Figure S8. J-V curves measured in the dark and under 1 sun illumination for (a) a 400 nm thick perovskite NPs film and (b) a 90 nm thick polycrystalline MAPbBr ₃ layer, both deposited onto interdigitated ITO electrodes (gap 20 μm).	S9

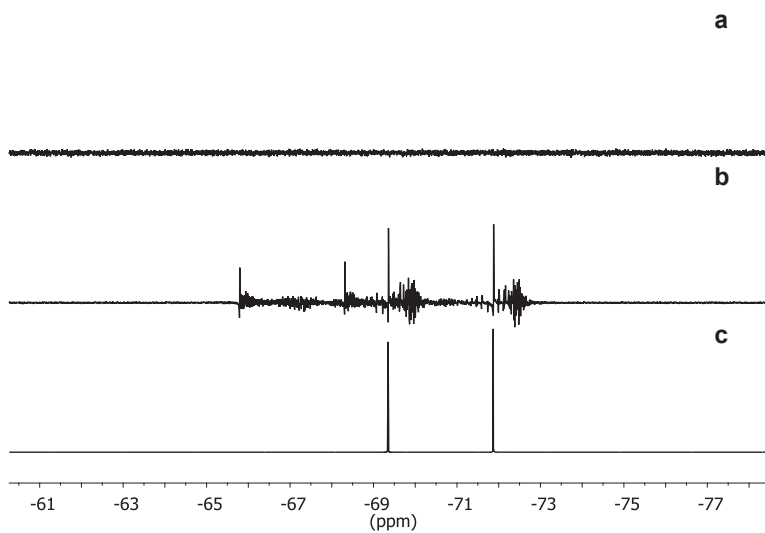


Figure S1. ^{19}F NMR spectra of MAP@K NPs (a), supernatant (b) and KPF_6 (c) in deuterated DMSO. It has to be taking into account that under these conditions the perovskite reverts back into its precursors.

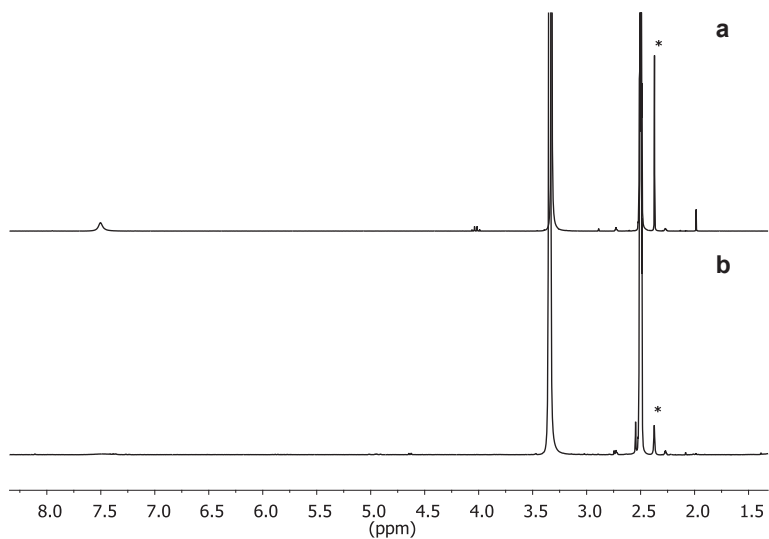


Figure S2. ^1H NMR spectra of MAP@K (a) and supernatant (b) in deuterated DMSO. The signal marked with an asterisk corresponds to CH_3 signals of CH_3NH_3^+ . It has to be taking into account that under these conditions the perovskite reverts back into its precursors.

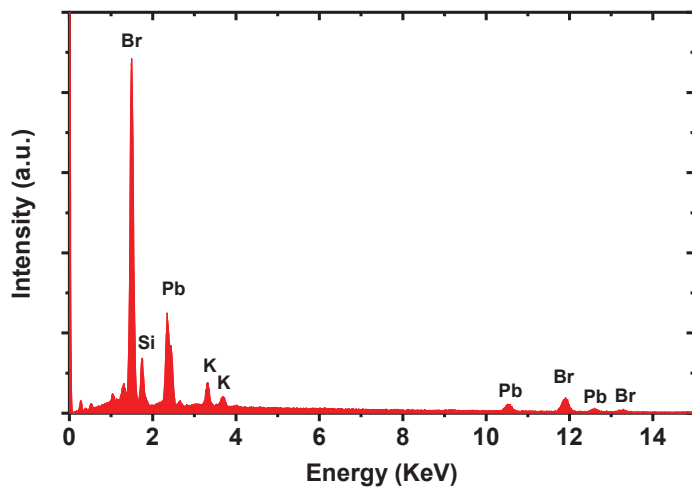


Figure S3. Energy dispersive X-ray spectrum of MAP@K NP solid film.

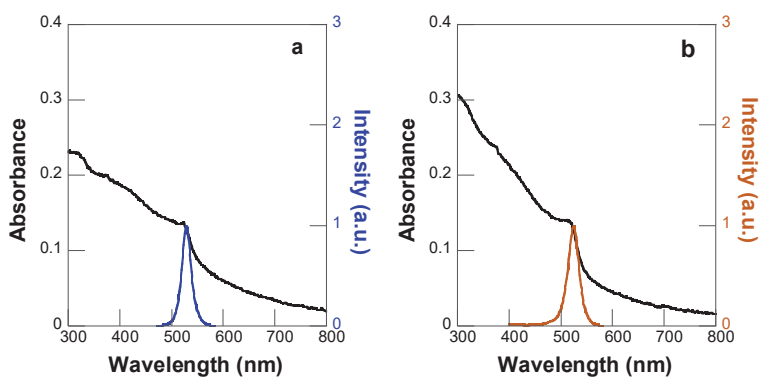
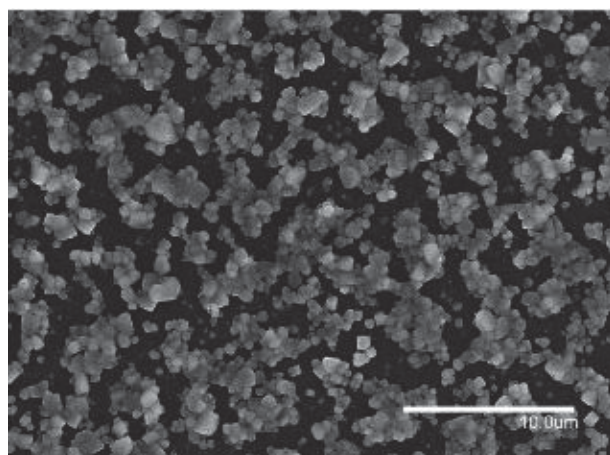


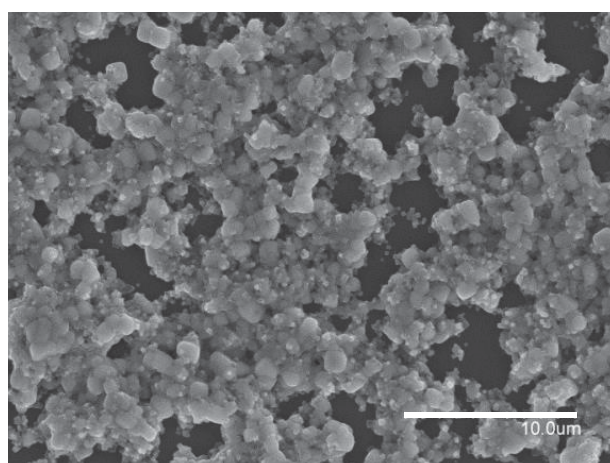
Figure S4. Absorption and emission spectra of colloidal MAP@K NPs synthesized in toluene (a) and chlorobenzene (b).



Figure S5. (a) Absorption spectra of colloidal MAP@K and MAP bulk in ethyl acetate. Images of colloidal MAP@K (yellow) and MAP (orange) dispersions taken (b) immediately and (c) 5 minutes after their redispersion in ethyl acetate.



a



b

Figure S6. SEM images of MAP@K_{F1} (a) and MAP@K_{F2} (b). Scale bar 10 μm.

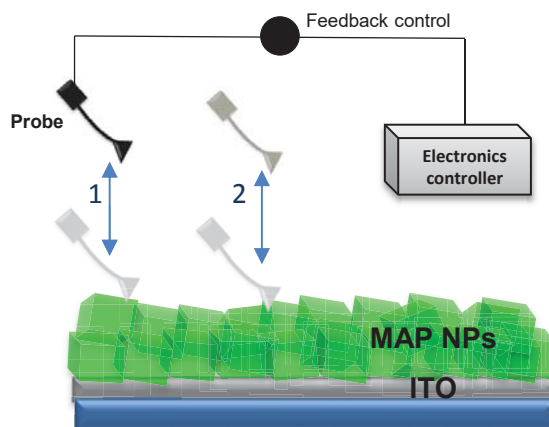


Figure S7. Simplified diagram of conductive AFM in PinPoint conductive mode, which the tip approach to the surface of the sample until a predefined threshold point is reached and then retract at each pixel point.

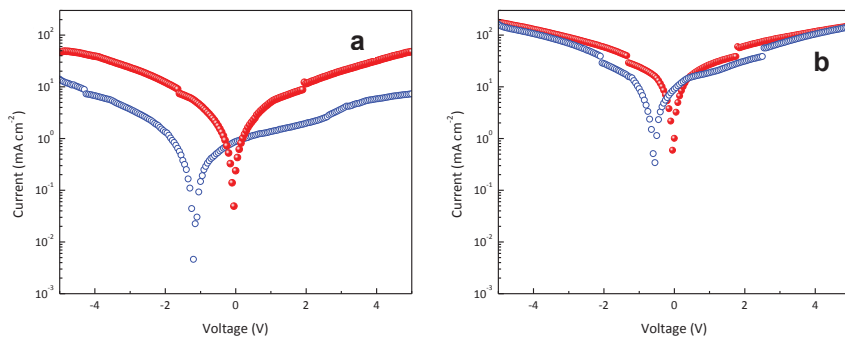


Figure S8. J-V curves measured in the dark and under 1 sun illumination for (a) a 400 nm thick perovskite NPs film and (b) a 90 nm thick polycrystalline MAPbBr₃ layer, both deposited onto interdigitated ITO electrodes (gap 20 μm). Blue symbols indicate dark measurements while the red symbols correspond to J-V curves recorded under illumination.

List of Abbreviation

A

AD	Adamantylammonium
ADA	Adamantylamine
ADBr	Adamantylammonium bromide
AFM	Atomic force microscopy
ATR-FTIR	Attenuated Total Reflection-Fourier Transform Infrared spectroscopy

B

BmPyPhB	1,3-bis[3,5-di(pyridin-3-yl)phenyl]benzene
---------	--

C

CB	Cucurbit[7]uril
----	-----------------

E

EA	Ethylammonium
EABr	Ethylammonium bromide
E _g	Exciton binding energy
EL	Electroluminescence

F

FFT	Fast fourier transform
FTO	Fluorine doped Tin Oxide
fwhm	Full width at half maximum

H

HA	Hexylammonium
HABr	Hexylammonium bromide
HOIP	Hybrid organic-inorganic metal halide perovskites
HRTEM	High resolution transmission electron microscopy

I

ITO	Indium tin oxide
-----	------------------

J

LARP	Ligand assisted re-precipitation method
LED	Light-emitting diode
λ_{em}	Emission wavelength
λ_{exc}	Excitation wavelength

M

MA	Methylammonium
----	----------------

N

NMR	Nuclear Magnetic Resonance
-----	----------------------------

O

OA	Octylammonium
OABr	Octylammonium bromide
ODA	Octadecylammonium
ODABr	Octadecylammonium bromide
ODE	1-Octadecene
OLA	Oleic acid

P

P	Perovskite
PCE	Power conversion efficiency
PEDOT:PSS	Poly(3,4-ethylenedioxythiophene): poly(styrenesulfonate)
PL	Photoluminescence
PLQY	Photoluminescence Quantum Yield
pTPD	Poly[N,N'-bis(4-butylphenyl)-N,N'-bis(phenyl)-benzidine]
PXRD	Powder X-ray diffraction

R

RMS	Root mean square roughness
-----	----------------------------

S

SEM	Scanning Electron Microscopy
SPPO13	2,7-bis(diphenylphosphoryl)-9,9'-spirobi[fluorene]

T

τ_{av}	Average photoluminescence Lifetime
TEM	Transmission electron microscopy
TGA	Thermogravimetric Analysis

U

UV-vis	Ultraviolet-visible
--------	---------------------

X

XPS	X-ray photoelectron spectroscopy
-----	----------------------------------